A More Transparent Infrared Window

Eli J. Mlawer[1], Jeana Mascio[2], David D. Turner[3], Vivienne H. Payne[4], Connor Flynn[5], and Robert Pincus[6]

[1]Atmospheric & Environmental Research
[2]Atmospheric and Environmental Research, Inc.
[3]NOAA Earth System Research Laboratory
[4]Jet Propulsion Laboratory, California Institute of Technology
[5]University of Oklahoma
[6]Columbia University

April 16, 2024

Abstract

The infrared window region (780-1250 cm-1, 12.8 to 8.0 μm) is of great importance to Earth's climate due to its high transparency and thermal energy. We present here a new investigation of the transparency of this spectral region based on observations by interferometers of downwelling surface radiance at two DOE Atmospheric Radiation Measurement program sites. We focus on the dominant source of absorption in this region, the water vapor continuum, and derive updated values of spectral absorption coefficients for both the self and foreign continua. Our results show that the self continuum is too strong in the previous version of Mlawer-Tobin_Clough-Kneizys-Davies (MT_CKD) water vapor continuum model, a result that is consistent with other recent analyses, while the foreign continuum is too weak in MT_CKD. In general, the weaker self continuum derived in this study results in an overall increase in atmospheric transparency in the window, although in atmospheres with low amounts of water vapor the transparency may slightly decrease due to the increase in foreign continuum absorption. These continuum changes lead to a significant decrease in downwelling longwave flux at the surface for moist atmospheres and a modest increase in outgoing longwave radiation. The increased fraction of surface-leaving radiation that escapes to space leads to a notable increase (~5-10%) in climate feedback, implying that climate simulations that use the new infrared window continuum will show somewhat less warming than before. This study also points out the possibly important role that aerosol absorption may play in the longwave radiative budget.

A More Transparent Infrared Window

Eli J. Mlawer (mlawer@aer.com)[1]
Jeana Mascio[1]
David D. Turner[2]
Vivienne E. Payne[3]
Connor J. Flynn[4]
Robert Pincus[5]

Affiliations
[1]Atmospheric and Environmental Research, Lexington, Massachusetts
[2]NOAA/Global Systems Laboratory, Boulder, Colorado
[3]Jet Propulsion Laboratory, California Institute of Technology, Pasadena, California
[4]University of Oklahoma School of Meteorology, Norman, Oklahoma
[5]Lamont-Doherty Earth Observatory, Columbia University, Palisades, New York

Key points:

- Analysis of ground-based radiance observations indicates that the infrared window region is more transparent than had been thought
- The derived water vapor self continuum is 10-30% weaker than previously thought, while the foreign continuum is substantially stronger
- The revised H_2O continuum results in a 5-10% increase in climate feedback and a large change to the radiative budget for moist atmospheres

Abstract

The infrared window region (780-1250 cm^{-1}, 12.8 to 8.0 μm) is of great importance to Earth's climate due to its high transparency and thermal energy. We present here a new investigation of the transparency of this spectral region based on observations by interferometers of downwelling surface radiance at two DOE Atmospheric Radiation Measurement program sites. We focus on the dominant source of absorption in this region, the water vapor continuum, and derive updated values of spectral absorption coefficients for both the self and foreign continua. Our results show that the self continuum is too strong in the previous version of Mlawer-Tobin_Clough-Kneizys-Davies (MT_CKD) water vapor continuum model, a result that is consistent with other recent analyses, while the foreign continuum is too weak in MT_CKD. In general, the weaker self continuum derived in this study results in an overall increase in atmospheric transparency in the window, although in atmospheres with low amounts of water vapor the transparency may slightly decrease due to the increase in foreign continuum absorption. These continuum changes lead to a significant decrease in downwelling longwave flux at the surface for moist atmospheres and a modest increase in outgoing longwave radiation. The increased fraction of surface-leaving radiation that escapes to space leads to a notable increase (~5-10%) in climate feedback, implying that climate simulations that use the new infrared window continuum will show somewhat less warming than before. This study also points out the possibly important role that aerosol absorption may play in the longwave radiative budget.

Plain Language Summary

The spectral region in the infrared from 780-1250 cm^{-1} (12.8 to 8.0 μm) is referred to as a window due to its transparency – in this region, thermal radiation emitted by the surface can pass relatively unimpeded through the atmosphere, allowing Earth to cool. The limited amount of atmospheric absorption that does occur in this region is primarily due to water vapor, in particular an absorption mechanism termed the water vapor continuum. The strength of water vapor continuum absorption in the infrared window therefore has important consequences for Earth's climate. This study provides a new evaluation of water vapor continuum absorption in the infrared window from an analysis of spectrally resolved measurements of downwelling surface radiances. Our results indicate that for most atmospheres the strength of water vapor continuum absorption is less than had been previously thought due to reduced absorption related to the interactions of water vapor molecules with other water vapor molecules, i.e. the water vapor self continuum. The derived water vapor continuum changes allow the Earth to cool ~5-10% better than had previously been thought, and climate simulations that use the revised infrared window continuum will show somewhat less warming than before.

1. Introduction

Atmospheric absorption in the infrared window (780-1250 cm^{-1}, 12.8 to 8.0 μm) plays an important role in Earth's radiation budget and climate, a consequence of this spectral region's high thermal energy, relative transparency, and the properties of its most important source of absorption, the water vapor self continuum. The self continuum is a weak absorber under typical atmospheric conditions, but its strength increases quadratically with water vapor abundance so under moist conditions self continuum absorption can result in significant atmospheric opacity. The importance of the infrared window region and the dominance of the water vapor self continuum absorption in this region make it imperative that the properties of this absorber be known with high certainty so that atmospheric applications that depend on window absorption can be regarded with confidence. This study presents the result of a new radiative closure analysis (Mlawer and Turner, 2016; Shepherd et al., 2003) of water vapor continuum absorption in the infrared window.

Longwave radiation that escapes to space (outgoing longwave radiation or OLR) is a critical component of the Earth's radiation budget. Most of the thermal radiation emitted by the Earth's surface is absorbed by the atmosphere, which then emits thermal radiation at its own temperature, which typically is less than the surface temperature. An exception to this general behavior occurs in spectral regions that are relatively transparent in clear skies, in which the warm radiation emitted by the surface is only slightly attenuated and therefore escapes the atmosphere. These spectral regions are called "windows" -- the most important with respect to Earth's thermal radiation is the infrared window. For six reference atmospheres, Table 1 shows the total surface flux emitted by the surface, the surface flux in spectral regions in which the total vertical optical depth is less than 1, and the fraction of this "transparent-region" flux that is in the infrared window. These values indicate that only a limited amount of the surface flux has the potential to escape to space, and a large fraction of that amount is in the infrared window.

As has been shown in recent studies (e.g. Seeley and Jeevanjee, 2021; Jeevanjee et al., 2021; Koll and Cronin, 2018), the infrared window plays a crucial role in climate and climate feedback. These studies show that at typical current surface temperatures the infrared window is the primary spectral region in which the radiation that escapes to space can change as the planet adjusts to an energy imbalance, such as is being currently precipitated by anthropogenic increases in greenhouse

Reference atmosphere	Precipitable water vapor (cm)	Total surface flux (W/m^2)	Surface flux for OD < 1	Fraction of OD < 1 flux in IR window
Tropical	4.1	451.62	155.56	0.98
Midlatitude summer	2.9	420.03	171.19	0.97
US standard	1.4	387.41	199.71	0.85
Subarctic summer	2.1	382.15	158.48	0.96
Midlatitude winter	0.9	309.34	178.37	0.74
Subarctic winter	0.4	247.16	165.62	0.60

Table 1. For six reference atmospheres: total upwelling longwave flux at the surface, precipitable water vapor, upwelling flux in the portion of the longwave that are sufficiently transparent (vertical optical depth < 1) so that a significant fraction of the radiation emitted by the surface reaches the top of the atmosphere, and the fraction of the transparent-region surface flux that is in the IR window region. Surface emissivity is assumed to be unity.

gases. As an illustration of this effect, the change in OLR for a simplistic version of current warming is shown in Fig. 1: a 1 K increase in tropospheric temperatures is applied to a baseline profile, with relative humidity values and the tropospheric column amounts of all other species are left unchanged in the perturbed profile. The results indicate that the change in OLR is primarily in the infrared window.

The infrared window is also critically important with respect to downwelling and net flux at the surface. In opaque spectral regions, the downwelling flux arriving at the surface typically is emitted at a temperature close to the surface temperature, resulting in a small net flux at the surface. As shown in Fig. 2, in the infrared window emitted downwelling radiation that reaches the surface is significantly smaller than the upwelling radiation, leading to a large net flux. The net flux divergence, which drives radiative cooling and heating, is also of unique importance in this window. The quadratic dependence on water vapor abundance of the self continuum optical depths leads to large relative gradients in optical depth in the lower atmosphere, and therefore large radiative flux divergences. Due to this effect, for moist atmospheres around 75% of the longwave cooling rate near the surface occurs in the window (Mlawer et al., 1997).

Section 2 provides background information on water vapor continuum absorption in the infrared window. Section 3 presents information about the radiometric measurements used in this study, the radiative transfer model calculations used to compare with these measurements, and details about how the atmospheric properties used in the calculations were obtained. Section 4 contains details about how the measurement-calculation differences were analyzed and then utilized to derive self and foreign continuum coefficients in the infrared window, as well as a specification of the self continuum temperature dependence. Section 5 compares the derived results to results obtained in previous studies and section 6 discusses the impact of the new window water vapor continuum results on atmospheric applications. Section 7 provides a summary and discussion.

2. The Water Vapor Continuum in the Infrared Window

We provide here background information concerning our understanding of water vapor continuum absorption in the infrared window and its development over the last several decades, including its treatment in the Mlawer-Tobin_Clough-Kneizys-Davies (MT_CKD) water vapor continuum

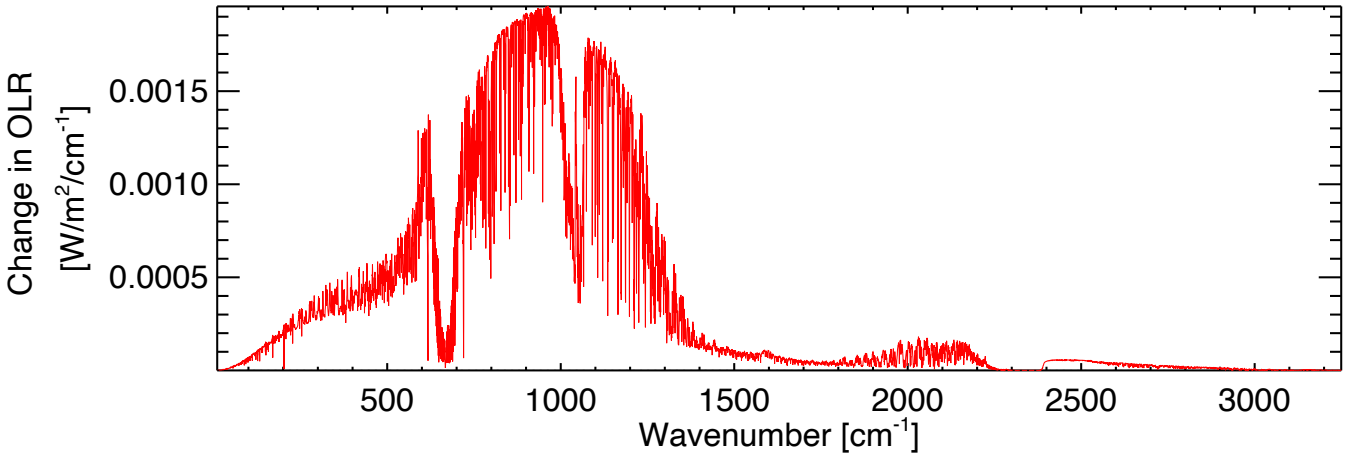

144 **Fig. 1.** Change in OLR due to a 1 K increase in tropospheric temperatures in the mid-latitude summer
145 atmosphere with relative humidity left unchanged.

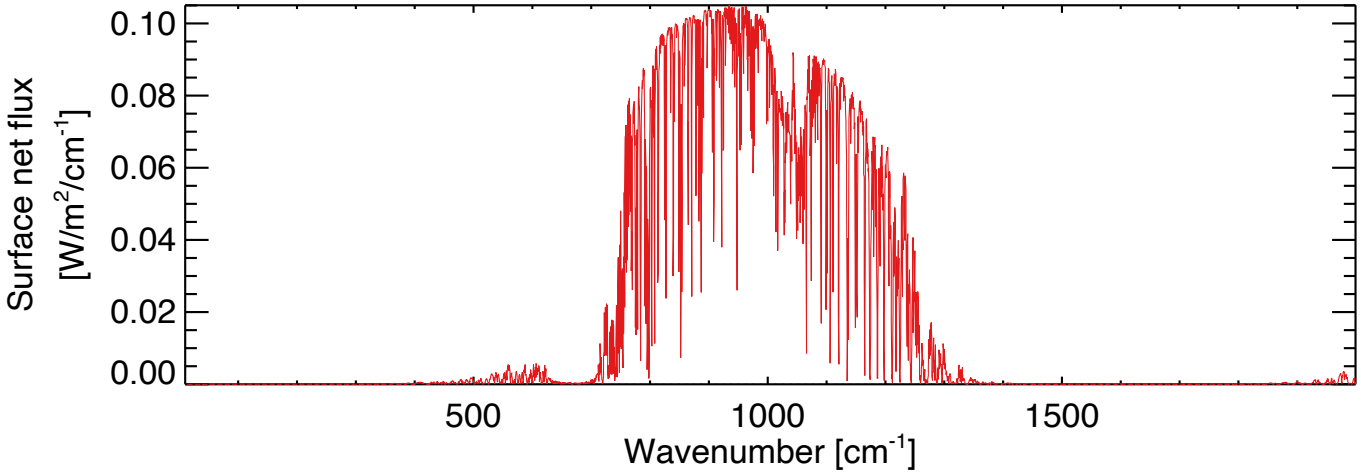

146 **Figure 2.** Magnitude of longwave surface net flux for the mid-latitude summer atmosphere.
147

model (Mlawer et al., 2023; Mlawer et al., 2012), the primary source used in the community to specify water vapor continuum absorption in this spectral region. For reference, self and foreign continuum optical depths from the current version of MT_CKD (v4.1.1) are shown in Fig. 3 for six reference profiles. In recent years, self continuum absorption in the infrared window had been thought to be fairly well known, with the most recent laboratory measurement of the self continuum in this region (Baranov et al., 2008) agreeing well at atmospheric temperatures with the MT_CKD continuum model, which is based on a recent field study (Turner et al., 2004). However, a review of studies of the self continuum absorption in this region over the last several decades shows cracks in this consensus.

The specification of the window self continuum in the original version of the Clough-Kneizys-Davies (CKD) continuum model (see Figs. 3 and 5 of Clough et al., 1989 – Note: the caption of Fig. 3 in Clough et al., 1989, erroneously states that the broadening pressure is 1013 mb, when it actually is 26.7 mb), the predecessor to the MT_CKD model, was based on the laboratory results of Burch (1982). These CKD values can be seen in Fig. 4a and are also shown along with the Burch (1982) measurements in Fig. 4b. Burch and collaborators subsequently significantly revised their experimental values, with the new lower continuum absorption coefficients (also shown in Fig. 4b) ascribed to "minor changes in experimental techniques employed in the recent work" (Burch and Alt, 1984). These improved experimental values were used as the basis for an updated

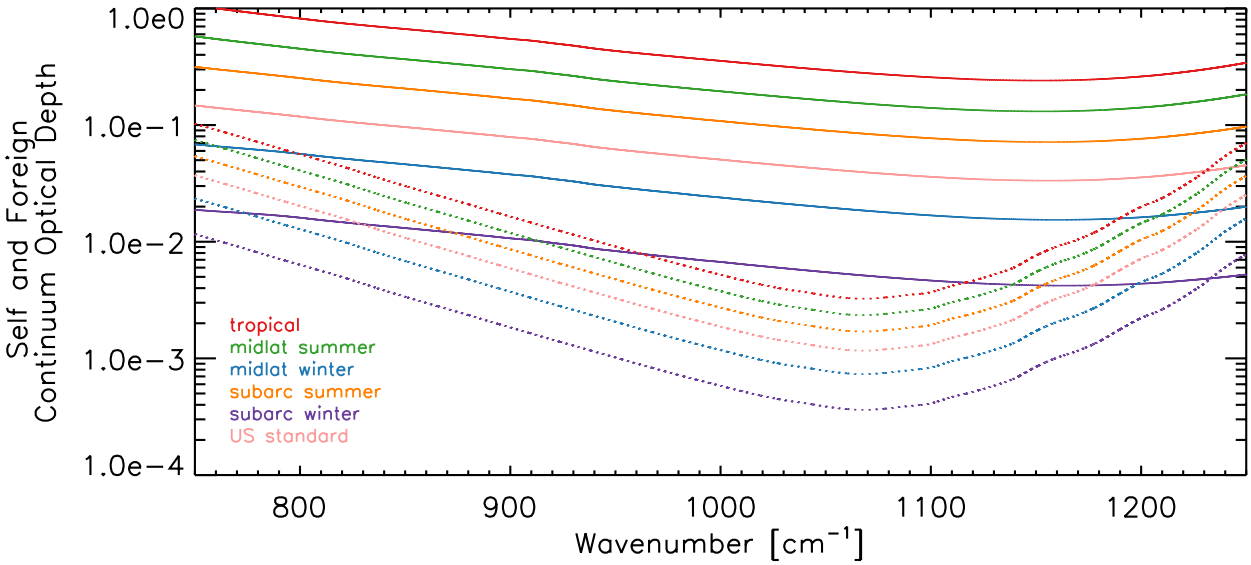

Fig 3. Optical depths due to the MT_CKD_4.1.1 water vapor self (solid) and foreign (dotted) continua for a vertical path for six reference atmospheric profiles.

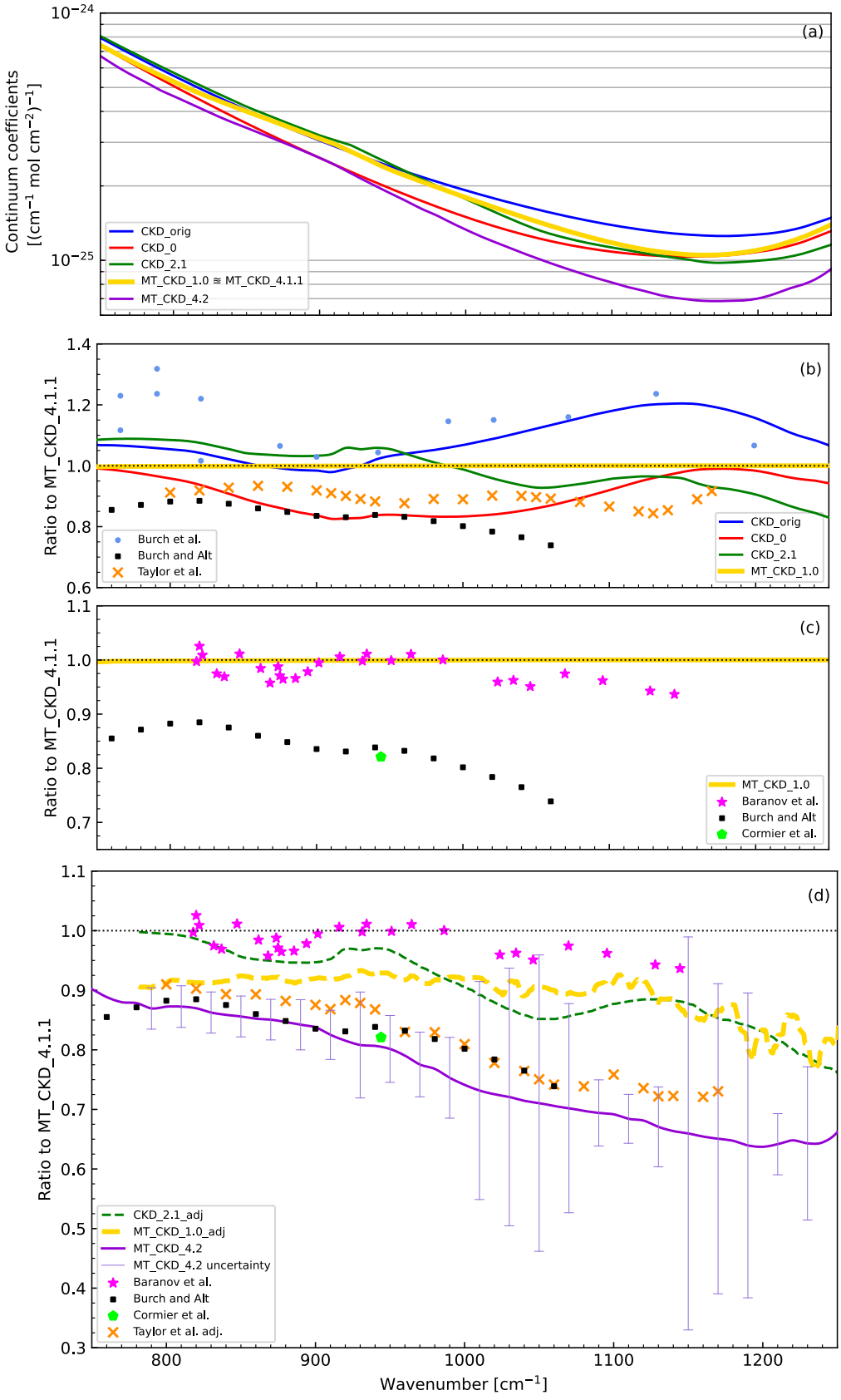
(a)
Continuum coefficients [(cm^{-1} mol cm^{-2})$^{-1}$]
10^{-24}
10^{-25}
CKD_orig
CKD_0
CKD_2.1
MT_CKD_1.0 ≅ MT_CKD_4.1.1
MT_CKD_4.2
(b)
Ratio to MT_CKD_4.1.1
Burch et al.
Burch and Alt
Taylor et al.
CKD_orig
CKD_0
CKD_2.1
MT_CKD_1.0
(c)
Ratio to MT_CKD_4.1.1
MT_CKD_1.0
Baranov et al.
Burch and Alt
Cormier et al.
(d)
Ratio to MT_CKD_4.1.1
CKD_2.1_adj
MT_CKD_1.0_adj
MT_CKD_4.2
MT_CKD_4.2 uncertainty
Baranov et al.
Burch and Alt
Cormier et al.
Taylor et al. adj.
Wavenumber [cm^{-1}]

169

Fig. 4. Various perspectives on the water vapor self continuum in the infrared window. (a) Water vapor self continuum coefficients for five versions of the CKD and MT_CKD continuum. The yellow curve is the self continuum at the beginning of this study, MT_CKD_4.1.1, and the purple curve shows the result of this study, MT_CKD_4.2; (b) Overview of the self continuum in ~2004. Shown as ratios with respect to MT_CKD_4.1.1 are several previous versions of CKD and MT_CKD as well as two sets of laboratory measurements (blue circles and black squares)and the result from the Taylor et al. field campaign (orange X's); (c) Key evaluations of the self continuum before this study are shown as ratios with respect to MT_CKD_4.1.1; (d) Overview of the self continuum after this study. Shown as ratios with to MT_CKD_4.1.1 are the most recent laboratory measurements from three groups (pink stars, black squares, and green pentagon) and the results from three field studies (Taylor et al., 2003, orange X's; CKD_2.1 (green dashed curve), which was motivated by Westwater et al., 1995); MT_CKD_1.0 (yellow dashed curve), which was motivated by Turner et al., 2004) that have been adjusted to account for a stronger foreign continuum (as described in the text) than had been used in the respective original analyses. The purple curve shows the significant decrease in the self continuum that is derived in this study, MT_CKD_4.2 – note that in some regions the corresponding derived error (purple vertical lines with end caps) is significant.

version of the CKD model (CKD_0, see Fig. 7 of Clough et al., 1989). The next update of consequence to the CKD window self continuum occurred about a decade later as a result of analyses of Fourier transfer infrared (FTIR) spectrometer measurements in the tropics (Westwater et al., 1995; Han et al., 1997), which resulted in an increase in the window self continuum in version 2.1 of CKD (shown in Fig. 4a,b). A few years later, an analysis by Turner et al. (2004) using measurements by the Atmospheric Emitted Radiance Interferometer (AERI; Knuteson et al., 2004 a,b) deployed at the Southern Great Plains (SGP; Sisterson et al., 2016) site of Atmospheric Radiation Measurement (ARM) program (Turner & Ellingson, 2016) demonstrated that the window self continuum in CKD needed modification, which led to the values in this region adopted in the first version of the MT_CKD continuum model, MT_CKD_1.0 (Mlawer et al., 2012), also shown in Fig. 4. Fig. 4b also presents the results of a field study of the self continuum by Taylor et al. (2003).

With respect to laboratory measurements of the window self continuum, there was a gap of almost 20 years between the measurements of Burch and subsequent studies. A 2005 laboratory study by Cormier et al. supported a significantly lower continuum absorption coefficient than in MT_CKD_1.0. These measurements were performed using the accurate cavity ring down technique but were only at a single spectral point and contradicted the results from a study by the same group (Cormier et al., 2002) a few years earlier. A subsequent laboratory study using an FTIR (Baranov et al., 2008), mentioned above, showed good agreement with MT_CKD at typical atmospheric temperatures, although significant disagreements were seen with respect to the model's temperature dependence of the self continuum in this region (Fig. 5). The self continuum coefficients derived in Baranov et al. (2008) are shown in Fig. 4c. Also shown in this figure are the laboratory measurements by Burch (1982) – these measurements, and not those from Burch and Alt (1984), were shown in Fig. 8 of Baranov et al. (2008), which drove home that there was agreement between specifications of the window self continuum at room temperature (with the exception of the Cormier et al., 2005, study). However, a conclusion that a consensus existed at this time between laboratory and field studies of the window self continuum is flawed.

To see why, a closer consideration of window self continuum studies based on field measurements is required. There is an important distinction between the window self continuum values based on

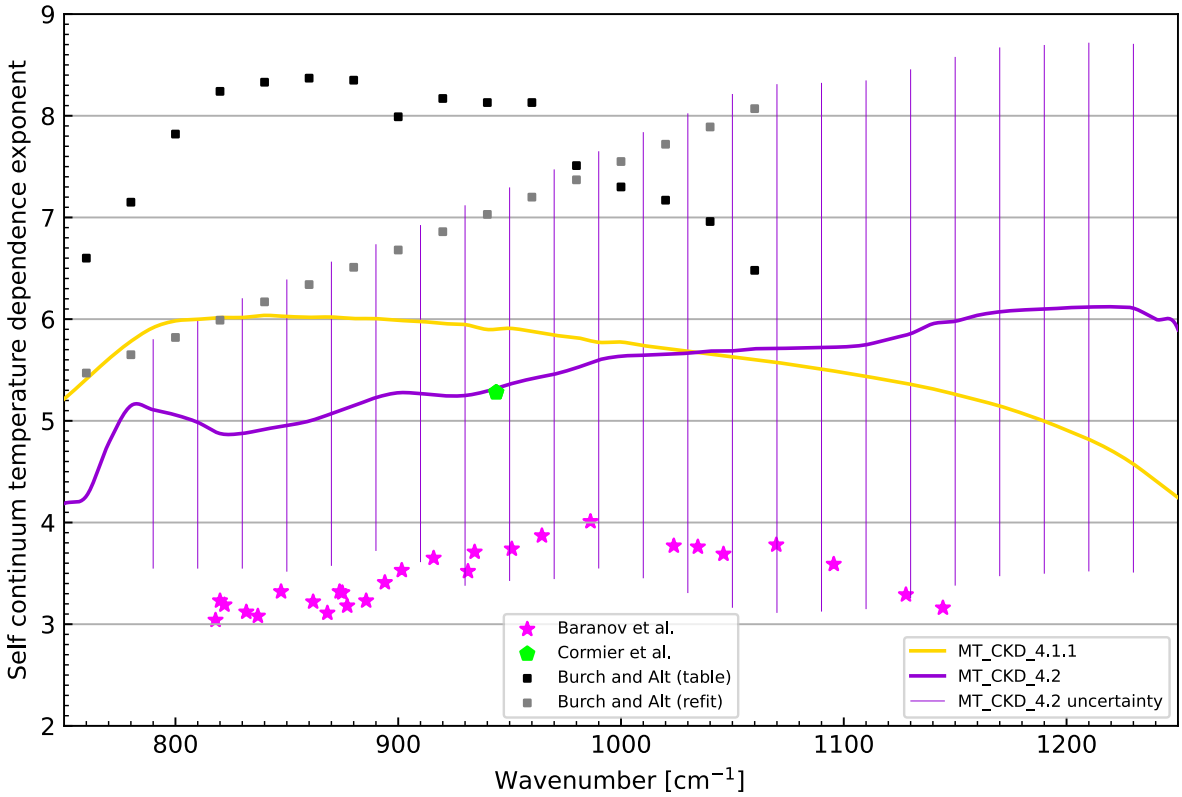

Fig. 5. The temperature exponent of self continuum coefficients from 750-1250 cm^{-1} from several laboratory studies (various symbols), the previous version of MT_CKD, v4.1.1 ≅ v1.0 (yellow curve), and the version derived in this study, MT_CKD_4.2 (purple curve), with estimated uncertainties shown in vertical purple lines without end caps.

field studies (i.e. those that motivated the development of CKD_2.1 and MT_CKD_1.0, as shown in Fig. 4b) and those based on laboratory studies (Fig. 4c). Laboratory studies utilize cells that contain pure water vapor, while the atmospheric paths relevant to field studies are comprised of mostly air (primarily nitrogen and oxygen) with a small fraction of water vapor. Therefore, field studies have a dependence on the water vapor foreign continuum in the window, while laboratory studies typically do not. Although the foreign continuum is much weaker than the self continuum in the window (Fig. 3), significantly inaccurate values assumed for the foreign continuum can still have an impact on the derived self continuum in analyses of field observations. Therefore, the evolution of window foreign continuum values, while interesting in its own right given the objectives of the current study, is also key to a proper understanding of past studies of window self continuum absorption.

The original CKD foreign continuum values (Clough et al., 1989) in the window were based on Burch (1982), which supported the conclusion that the foreign continuum was a very weak absorber in this region (Fig. 6). A major increase in the window foreign continuum came about with advent of MT_CKD (Mlawer et al., 2012), which resulted not from new foreign continuum measurements in this region but rather as a consequence of constraining the model's derived line shape parameters to fit the foreign continuum behavior from 500-750 cm^{-1} in its predecessor version, CKD_v2.4.1. These increased MT_CKD foreign continuum coefficients in the window were subsequently shown to be consistent with field observations by Turner et al. (2004). Even with this increase, foreign continuum absorption in this region remained rather weak compared to the self continuum. The laboratory measurement of Cormier et al. (2005) at 944 cm^{-1}, however, supported a much higher level of foreign continuum absorption, and was followed by a more extensive study (measurements at numerous points between 800-1250 cm^{-1}) by Baranov and Lafferty (2012). As can be seen in Fig. 6, the Baranov and Lafferty (2012) study indicated that the foreign continuum was ~2-4 times greater than MT_CKD_1.0, although the reported strength was about half as large as specified in Cormier et al. (2005). Given the relative optical depths of the window foreign and self continua shown in Fig. 3, assuming a 2-4 times larger foreign continuum would have an appreciable effect on the self continuum absorption derived in a field study.

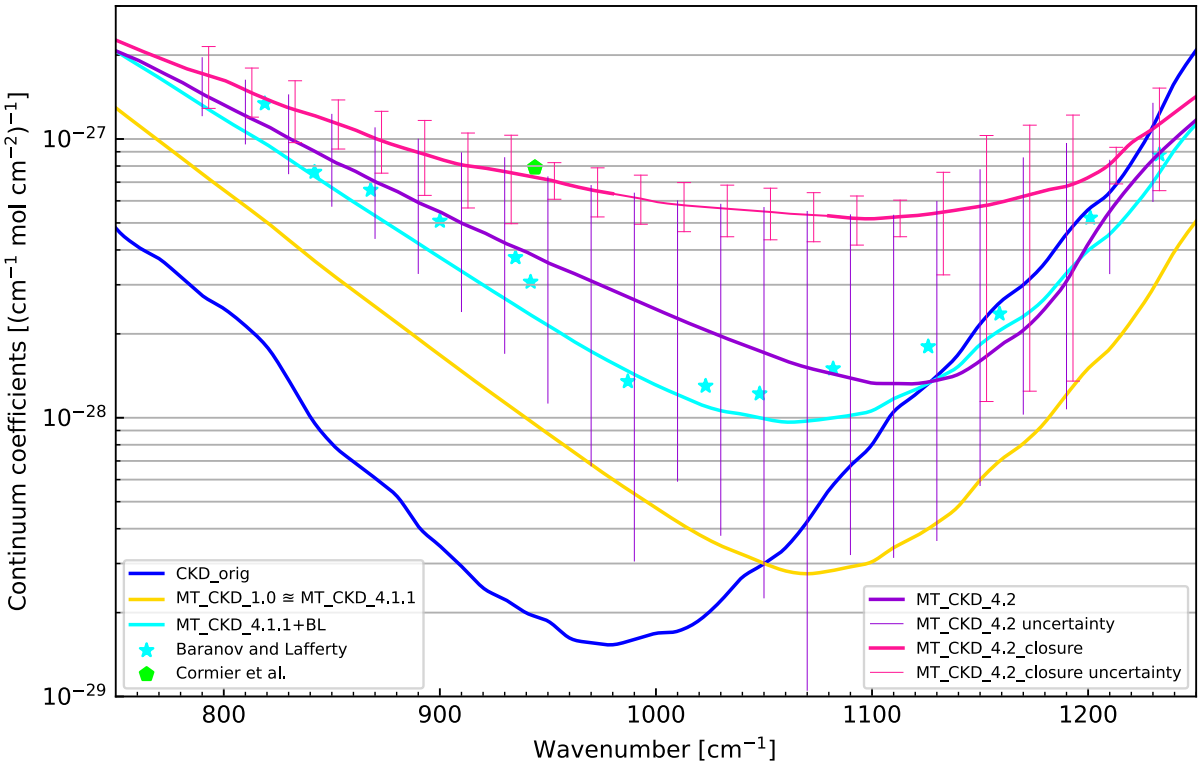

Fig. 6. Water vapor foreign continuum coefficients from 750-1250 cm^{-1} for the original version of the CKD model (blue curve), the current version of the MT_CKD model (v4.1.1, which is equivalent to MT_CKD_1.0, yellow curve), the laboratory results from Baranov and Lafferty (2012, cyan stars) and Cormier et al. (2005, green pentagon), and a version of MT_CKD (v4.1.1+BL, cyan curve) that was adjusted to be consistent with the Baranov and Lafferty (2012) results. The foreign continuum derived in this study, MT_CKD_4.2, is shown in purple, with associated uncertainty values shown with vertical lines without end caps. The pink curve shows the foreign continuum (MT_CKD_4.2_closure) needed to obtain radiative closure with the SGP observations used in this study. Error bars based on the SGP data set are pink vertical lines (slightly offset in the x-direction for clarity) with end caps.

Given that the window foreign continuum derived in Baranov and Lafferty (2012) is much larger than the corresponding foreign continuum values assumed in previous analyses of field observations, it is instructive to understand to what extent the self continuum values derived in previous field studies would have been affected had a stronger foreign continuum been utilized instead in these studies. To evaluate this, we modify the current version of MT_CKD such that the window foreign continuum coefficients are increased to be generally consistent with the Baranov and Lafferty (2012) values. This modified foreign continuum version is shown as MT_CKD_4.1.1+BL in Fig 6. We use this modified version to estimate (method described in Appendix 1) the change in the self continuum values that would have been obtained in three prior field studies had a greater foreign continuum been assumed rather than the values that actually were used in these studies. These reconsidered self continuum values are shown in Fig. 4d as MT_CKD_1.0_adj, CKD_2.1_adj, and Taylor_adj (which, respectively, are based off the studies of Turner et al., 2004, Westwater et al., 1995/Han et al., 1997, and Taylor et al., 2003). We also include on this figure the self continuum laboratory results of Cormier et al. (2005), Baranov et al. (2008), and Burch and Alt (1984), which improved upon the previous measurements by the Burch group.

The overall impression given by Fig. 4d is murkier than in Fig. 4c (or in Fig. 8 of Baranov et al., 2008), but the observational evidence clearly allows the possibility that the window self continuum is significantly weaker than in current MT_CKD. The diversity of values shown suggests, however, that there is no consensus for the strength of the window self continuum. The main motivation for this current study is to bring some clarity to this question of great importance.

3. Elements of the Comparison

Our analysis of water vapor continuum absorption in the infrared window is based on comparisons between clear-sky radiance measurements by the AERI and corresponding calculations by the Line-By-Line Radiative Transfer Model (LBLRTM; Clough et al., 2005) that utilize as input a combination of in situ measurements, retrieved quantities, and model output to specify the atmospheric properties in the radiating column above the AERI.

Our radiative closure analysis is based on observations taken at two sites operated by the ARM program. The primary data set is more than two years of observations (March 2016 - October 2018) from the ARM SGP site, the world's largest and most extensive climate research facility. The SGP site consists of in situ and remote-sensing instrument clusters and has been collecting data since it was established in 1993. Also used in this study are observations from the ARM Observations and Modeling of the Green Ocean Amazon (GoAmazon; Martin et al., 2016) campaign (MAO), held from January 2014 through November 2015 in Manaus, Brazil, at an altitude of about 50 meters. Due to MAO's tropical location the median PWV amount for the profiles used in our analysis is far greater than for SGP (Fig. 7) and provide an excellent dataset for validating the self and foreign continuum derived from SGP observations.

We provide here details about each of the three elements involved in this radiative closure study.

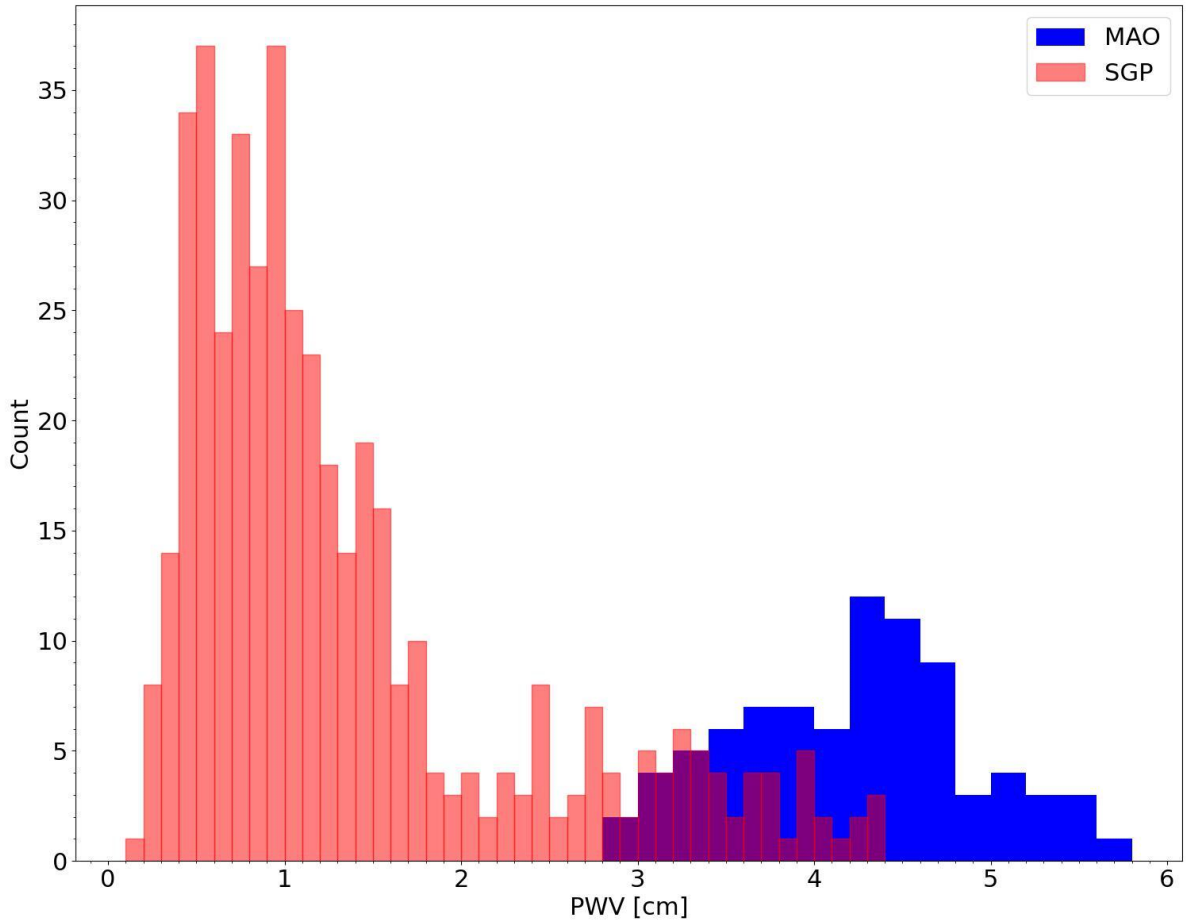

Fig. 7. Precipitable water vapor amounts for the cases used in this study.

3.1 Radiometric Measurements

The AERI, a Fourier transform infrared interferometer that was designed specifically for the ARM program (Turner et al., 2016), measures downwelling spectrally resolved infrared radiance from 550-3000 cm^{-1}. A zenith-looking AERI, deployed at an altitude of 320 m, has been providing operational radiance measurements at SGP since 1995, observing radiances emitted downward by the atmosphere for a large range of water vapor column amounts (PWVs). It uses two detectors to have sensitivity to radiance in the 3.3 to 19 μm band, and the maximum optical path delay provides a spectral resolution of 0.5 cm^{-1}. The instrument regularly views two well-characterized blackbodies, which are operated at ambient temperature and 60 °C, respectively. These blackbody observations, together with a correction for the detector's non-linearity, allows the instrument to measure downwelling spectral infrared radiance with a radiometric accuracy better than 1% of the ambient radiance. Additionally, a calibrated metrology laser and corrections for the finite field-of-

view of the instrument provides the spectral calibration for the observed radiance. Details on the instrument and its calibration method are provided in Knuteson et al. (2004a, b).

The signal observed from the sky is calibrated using the ambient and hot blackbody views using the complex arithmetic technique proposed by Revercomb et al. (1988). However, careful analysis has shown that there can still exist a slight positive bias to the observed sky radiance; this is most easily seen in extremely dry clear sky scenes (Delamere et al., 2010; Turner, 2003). Initially, the source of this bias was assumed to be something in the foreoptics (e.g., some scattered light), and Delamere et al. (2010) assumed that there was a small fraction (order 0.1%) of ambient radiation scattered into the sky observations. However, extensive analysis across multiple AERI systems, including a detailed examination during a particular low radiance condition, ruled out all contributions from the foreoptics (e.g., scattered radiation, polarization) and the Revercomb calibration method rules out phase issues. A new hypothesis was formulated suggesting that emission from the aft optics is not accounted for in the calibration. The functional form of an aft optics correction would be the same as used in Delamere et al. (2010), with the contribution from the "offending" temperature being that of the aft optics. For this study, the observations did not definitively support either an issue with the foreoptics or the aft optics, so no bias correction was applied.

Fig. 8 shows average AERI radiances from observations used in this study for different PWV ranges.

3.2 Model Calculations

Radiance calculations by LBLRTM_v12.15.1 are used in our radiative closure analysis, which focuses on the 780-1280 cm^{-1} region. Absorption line parameters used in these calculations utilize the line file version AER_v3.8.1 and continuum absorption is specified by MT_CKD_4.1.1 (for our baseline calculations). (These models and databases are available at https://github.com/AER-RC, the GitHub repository of the AER Radiation and Climate Group.) We also perform LBLRTM calculations for which the water vapor continuum is changed to MT_CKD_4.1.1+BL. All calculations used in this study include all relevant absorption due to water vapor, carbon dioxide

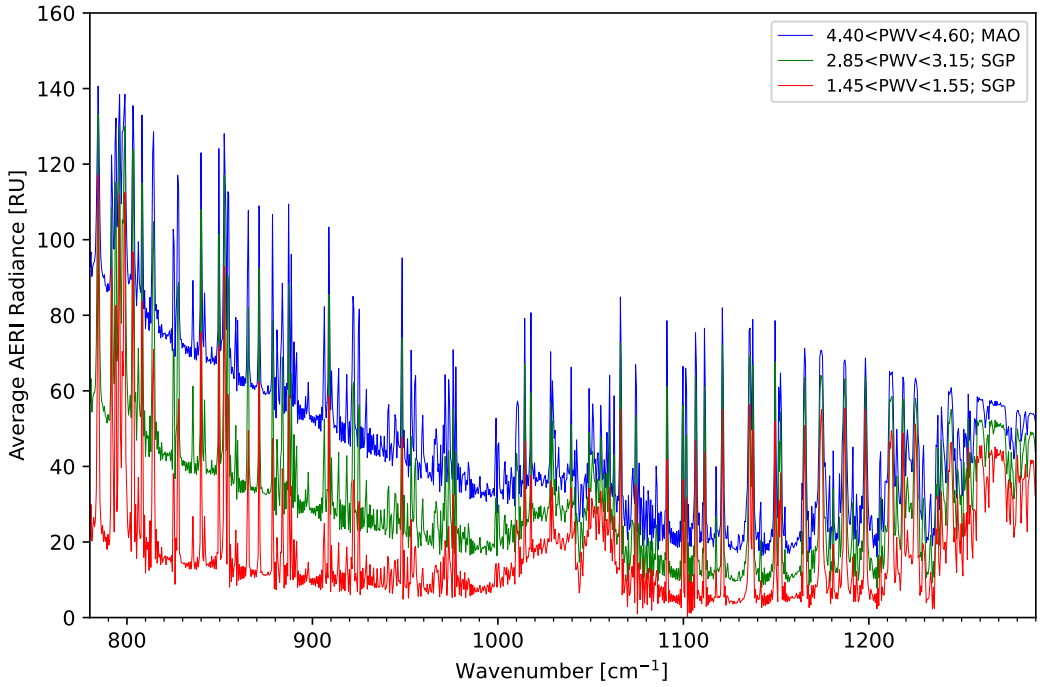

Fig. 8. Average AERI radiances used in this study from MAO (blue curve) and for two PWV bins at SGP (red and green curves). A "radiance unit" (RU) is 1 mW / (m^2 sr cm^{-1}).

(including first-order line coupling), ozone, nitrous oxide, methane (first-order line coupling), ammonia, CCl4, CFC-11, CFC-12, HNO_3, HCFC-22, and PAN.

The MT_CKD water vapor continuum model (Mlawer et al., 2023; Mlawer et al., 2012) provides water vapor self and foreign continuum coefficients (cm^2/molecule/cm^{-1}) every 10 cm^{-1} from 0-20,000 cm^{-1}. To obtain continuum coefficients in between the stored values, a cubic interpolation using the four closest stored values is performed. Absorption coefficients C_x (cm^2/molecule) can be obtained by multiplying the continuum coefficients $\tilde{C}_x$ by the radiation term R:

$$C(\nu, T, \rho_x) = \tilde{C}_x(\nu, T, \rho_x)\, R(\nu, T) \qquad (1)$$

where ν is the wavenumber, T is the temperature, the subscript 'x' denotes either 'self' or 'foreign', and the radiation term R is given by

$$R(\nu, T) = \upsilon \tanh\left(\frac{hc\upsilon}{2kT}\right), \qquad (2)$$

where h is Planck's constant, c is the speed of light, and k is Boltzmann's constant. The dependence on density implied by the notation for $\tilde{C}_x$ is given by

$$\tilde{C}_x(\nu, T, \rho_x) = \tilde{C}_x\left(\nu, T, \rho_{x,ref}\right)\left(\frac{\rho_x}{\rho_{x,ref}}\right) \quad (3)$$

where ρ is the density of the gaseous molecules interacting with water vapor in the respective process (i.e. water vapor for the self continuum; all gaseous molecules except for water vapor for the foreign continuum) and the reference density at which coefficients are stored corresponds to a pressure of 1013 mbar and a temperature of 296K. The optical depth of the self or foreign continuum is given by the product of the absorption coefficient C_x and the water vapor column amount W (molecules/cm^2):

$$\tau_x(\nu, T, \rho_x) = W(H_2O)\, C(\nu, T, \rho_x). \quad (4)$$

The temperature dependence of the self continuum coefficients in the MT_CKD model is given by

$$\tilde{C}_s(\nu, T) = \tilde{C}_s(\nu, 296K)\, (296/T)^{n(\nu)} \quad (5)$$

where n is a wavenumber-dependent dimensionless parameter and the density dependence of the coefficients has been suppressed for clarity. The foreign continuum coefficients are assumed to not be dependent on temperature.

More details about this formulation can be found in Mlawer et al. (2023).

3.3. Input to the Model

Multiple observations are used to create the profiles used as input to the model calculations. The foundation for the temperature and water vapor profiles are observations by radiosondes (hereafter sondes), which were usually launched four times daily during our study period at SGP and twice a day at MAO. However, sonde measurements are not directly used as input to the radiative transfer calculations in our analysis. The sonde launch location at SGP is ~250 m from where the AERI is deployed so its measured temperatures and humidity values in the lowest several hundred meters cannot provide the needed accuracy for our closure study, and sonde humidity measurements have

well known accuracy issues (Turner et al., 2016). For our study, we use the TROPoe (Turner & Löhnert, 2014) physical retrieval algorithm to retrieve profiles of temperature and humidity that provide closure with the sonde profiles, the AERI radiance observations between 538 and 722 cm^{-1} (i.e., regions of the spectrum wherein the water vapor line shape and continuum absorption have undergone validation (Delamere et al., 2010; Mlawer et al., 2019), and the brightness temperatures at 23.8 and 31.4 GHz from a microwave radiometer (MWR; Cadeddu et al., 2013). For this study, the TROPoe retrieval utilizes the latest version of the MT_CKD continuum (Mlawer et al., 2023) and the AER line file, ensuring that its water vapor spectroscopy from 538-722 cm^{-1} includes recent upgrades.

The TROPoe algorithm is a 1-dimensional variational retrieval approach using the optimal estimation framework. It has been extensively modified to include a wide number of measurements (with their uncertainties) from different instruments in the observation vector (Turner & Blumberg, 2019; Turner & Löhnert, 2021). A prior dataset is used to constrain the retrieval; for the SGP, sonde launches from over 10 years were used to create seasonal priors, whereas all the sondes launched during the Go-Amazon field campaign were used to create the single yearly prior for the MAO site. Ultimately, the retrieval finds the solution (i.e., the retrieved thermodynamic profiles) that provides the best fit with all the observations (i.e., sonde, AERI radiances, and MWR brightness temperatures) and the prior (within their uncertainties). The TROPoe retrieval is run at the sonde launch time.

The TROPoe profiles only extend to 17 km, as that is the maximum height of the prior dataset used to constrain the retrieval. Above 17 km, water vapor values are taken from reference atmospheric profiles (U.S. standard for SGP, tropical for MAO) (Anderson et al., 1986). For temperature, Modern-Era Retrospective analysis for Research and Applications, Version 2 (MERRA-2; Randles et al., 2017) profiles are used above 17 km.

Below, in the uncertainty analysis (section 4.5) of the water vapor continuum absorption parameters derived in this study, an alternative data set of temperature and water vapor profiles is also considered. This specification directly uses the sonde-measured temperature and water vapor profiles in which the sonde water vapor measurements are scaled such that agreement is attained

between the 23.8 GHz measurement of the collocated MWR and a corresponding radiative transfer calculation (Turner et al., 2016). This method to specify the thermodynamic profile has been previously used in similar radiative closure studies (e.g. Turner et al., 2004; Mlawer and Turner, 2016). For the SGP cases used in this study, the ratios of the PWV values of the TROPoe-derived and sonde profiles are shown in Fig. 9. Also shown in this figure are the ratios of the PWV values of the TROPoe-derived and MWR-scaled sonde profiles.

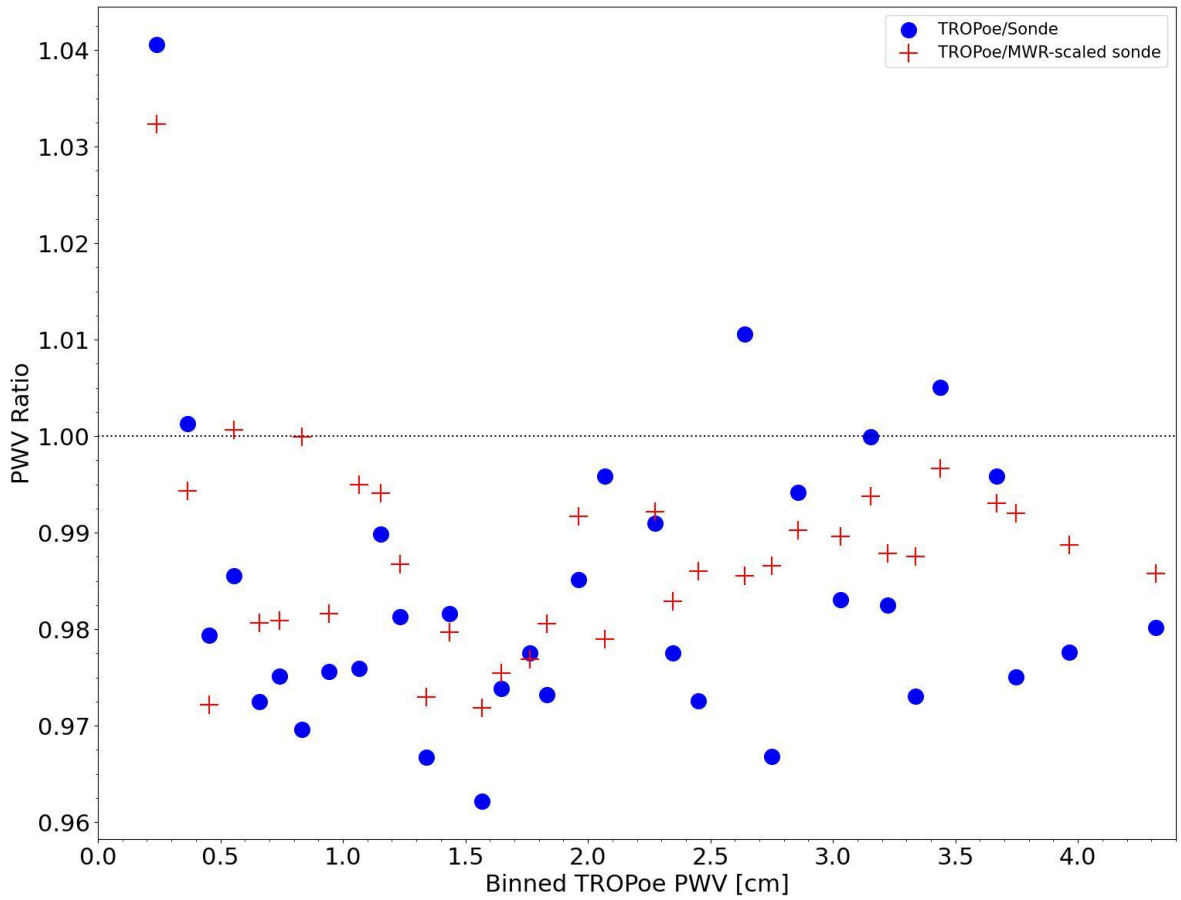

Fig. 9. Ratios of PWV derived from TROPoe retrieval to the sonde-measured (blue circles) and MWR-scaled (red plus symbols) PWVs at SGP.

The profiles of trace gas abundances that are used in the radiative transfer calculations are obtained from multiple sources. MERRA-2 profiles corresponding to the SGP and MAO locations are used to specify ozone. For CO_2, N_2O, CH_4, HCOOH, HNO_3, and PAN, monthly climatologies are used that were originally developed for the NASA Aura satellite project and updated over time by the Tropospheric Emission Spectrometer (TES; Worden et al., 2007) and TRopospheric Ozone and its Precursors from Earth System Sounding (TROPESS; Fu et al., 2013) teams. For four other

446 molecules (CCl4, CFC-11, CFC-12, and HCFC-22), abundance values from the NOAA
447 Halocarbons and other Atmospheric Trace Species (HATS) program
448 (https://gml.noaa.gov/hats/flask/flasks.html) are used. All other molecular profiles are specified
449 using the reference values stored in LBLRTM (U.S. standard atmosphere for SGP, tropical
450 atmosphere for MAO).
451
452 **4. Results of Measurement-Calculation Comparisons**
453 ***4.1. Case and channel selection***
454 More than 3000 sondes were launched at SGP during our study period. For each sonde, AERI
455 measurements within a 35-minute window associated with each sonde launch (t-5 to t+30 minutes)
456 are averaged. Given the large number of sondes and the many AERI channels in the targeted
457 spectral region (780-1280 cm^{-1}), we can be selective with respect to the AERI radiance
458 measurements we use in the study to minimize the possibility that our analysis is affected by
459 clouds, insensitivity to water vapor continuum absorption, and trace gas uncertainty.
460
461 To avoid cloud contamination, we remove from our analysis all cases where a cloud might be
462 contributing to the downwelling infrared radiance using two tests: the cloud liquid water path
463 retrieved by TROPoe is less than 2 g/m^2, and the magnitude of the standard deviation of the 900
464 cm^{-1} radiance observation over the 35-minute window is less than 0.3 RU. This initial screening
465 removes AERI spectra that fail either of these tests for the presence of clouds, resulting in 453
466 AERI spectra being identified as clear-sky observations.
467
468 Our analysis of the water vapor continuum focuses on AERI channel measurements that are
469 sensitive to the strength of water vapor continuum absorption. These spectral elements are
470 identified by evaluating the sensitivities of all AERI channels to a change in continuum strength.
471 We first compute the change in spectral radiances for all clear AERI cases due to a small
472 perturbation in the self continuum, then bin these sensitivity values in 10 cm^{-1} spectral bins and
473 five PWV ranges. For each spectral bin and PWV range, we classify each channel in all AERI
474 cases as either "sensitive" or "insensitive" by computing a threshold between the two classes based
475 on minimizing the combined variance in both classes (Otsu, 1979). AERI channels that are
476 classified as "sensitive" for at least 50% of the cases in at least three of the five PWV ranges are

used in the SGP analysis, and the other channels are not considered further in our retrieval of water vapor continuum coefficients.

Given the very low optical depths associated with the foreign continuum (Fig. 3), a small error in the specification of trace gas abundances can impact the determination of foreign continuum coefficients from the AERI measurements. Any such error in the foreign continuum may then cascade through the analysis, impacting the accuracy of the derived self continuum. To identify AERI channels that may be non-trivially impacted by inaccurate specification of trace gas abundances, the uncertainty for each abundance value is required. In this analysis, we use a conservative estimate of ~2 ppm for CO_2, while the uncertainty in the total column amount of N_2O is estimated as 1% and CH4 as 0.02 ppmv. For HNO_3 and PAN, the uncertainty was calculated as the standard deviation of the monthly values for this location in the climatologies. For NH_3 and HCOOH, we use estimated uncertainties of 50%. For ozone, following Wargan et al. (2017) the stratospheric and tropospheric uncertainties are estimated as 8% and 21%, respectively. For CCl4, CFC-11, CFC-12, and HCFC-22, the uncertainty is set to be consistent with the variance of the respective source value in the HATS database. Using the uncertainty values for all trace gases, a sensitivity study is performed corresponding to an AERI observation associated with a moderate PWV value (2.15 cm) and spectral differences are computed between a baseline calculation in which the trace gases are at their standard abundances and a perturbed calculation in which these abundances are increased by their respective uncertainties. The results from these calculations are shown in Fig. 10a. For a chosen uncertainty threshold value of 0.075 RU, we consider water vapor continuum coefficients derived at spectral points for which the sensitivity to trace gas abundances exceeds this threshold to be less reliable, while those AERI channels below this threshold and thus showing less sensitivity to trace gas uncertainty are considered more reliable. Certain figures in this paper (Figs. 10, 12, 13, and 14) distinguish between these two categories of AERI channels through the use of large circles (greater confidence) and small circles (lesser confidence). (The uncertainty threshold is significantly exceeded throughout the ozone band from 980-1080 cm^{-1} and radiative closure results in this spectral region are not presented in this study to avoid confusion.)

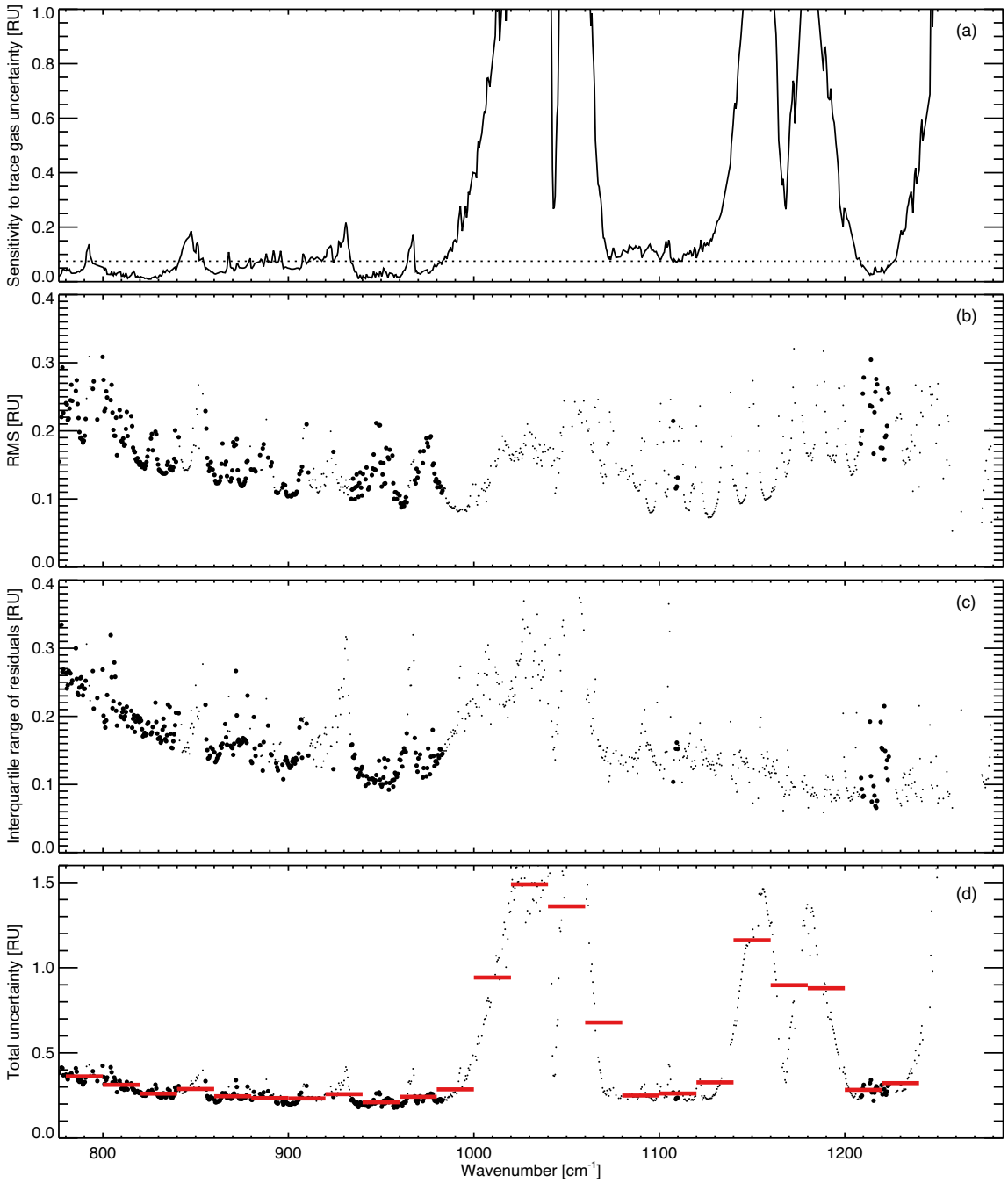

Fig. 10. For AERI channels from 780-1280 cm^{-1}: (a) Difference in calculated radiances due to the changes to abundances of trace gases described in the text. The analysis in this study at spectral locations for which this change is less than the horizontal dotted line shown are viewed with greater confidence; (b) RMS differences between radiances calculated with profiles utilized in this study and reasonable alternate profiles (as described in text); (c) Interquartile range of measurement-calculation differences for all PWV bins; (d) Total spectral uncertainty of measurement-calculation residuals (black circles) and RMS of uncertainties in 20 cm^{-1} regions (red horizontal lines).

4.2. Initial analysis

For each selected AERI channel, the residuals between the AERI radiance measurements and corresponding LBLRTM calculations are grouped into 0.1 cm PWV bins. Since the values of some residuals in each bin can differ greatly from the median residual in that bin, we eliminate the impact of possible outliers only considering the results in a PWV bin for cases that have a residual between the 25th and 75th quartiles. The mean of this "inner half" of cases is computed for all PWV bins (for each set of LBLRTM calculations considered in this study).

The behavior of these binned mean residuals as a function of PWV is shown in Fig. 11 for three AERI channels. Results are shown for LBLRTM calculations that use MT_CKD_4.1.1 (black) and MT_CKD_4.1.1+BL (green; description in section 2). The dependence of the residuals on PWV, fit with a quadratic function for each channel, indicates that the measurement data set is not consistent with the LBLRTM calculations for either of these specifications of self and foreign water vapor continuum absorption. Furthermore, the behavior of the residuals as a function of optical depth suggests that more atmospheric opacity is needed in the calculation for low PWV amount, while the opacity is overestimated for higher PWV values. Other channels in the infrared window show similar results.

The medians (over PWV bins) of the inner half mean residuals for calculation using MT_CKD_4.1.1 (black) and MT_CKD_4.1.1+BL (green) are shown in the top panel of Fig. 12 for each AERI channel analyzed. Although MT_CKD_4.1.1 appears to provide reasonable results, the results in this panel are misleading. As for the three channels shown in Fig. 11, a quadratic curve is fit to the values of binned mean residuals vs. PWV for all AERI channels. The linear and quadratic coefficients of the fit for each channel are shown in the bottom two panels, respectively, of Fig. 12. Reasonable overall agreement between the measured and calculated radiances would result in residuals that would have little dependence on PWV -- the values in each of the bottom two panels of Fig. 12 would be more-or-less zero (i.e. follow the panel's x-axis). This is not the case for either version of LBLRTM available prior to this study.

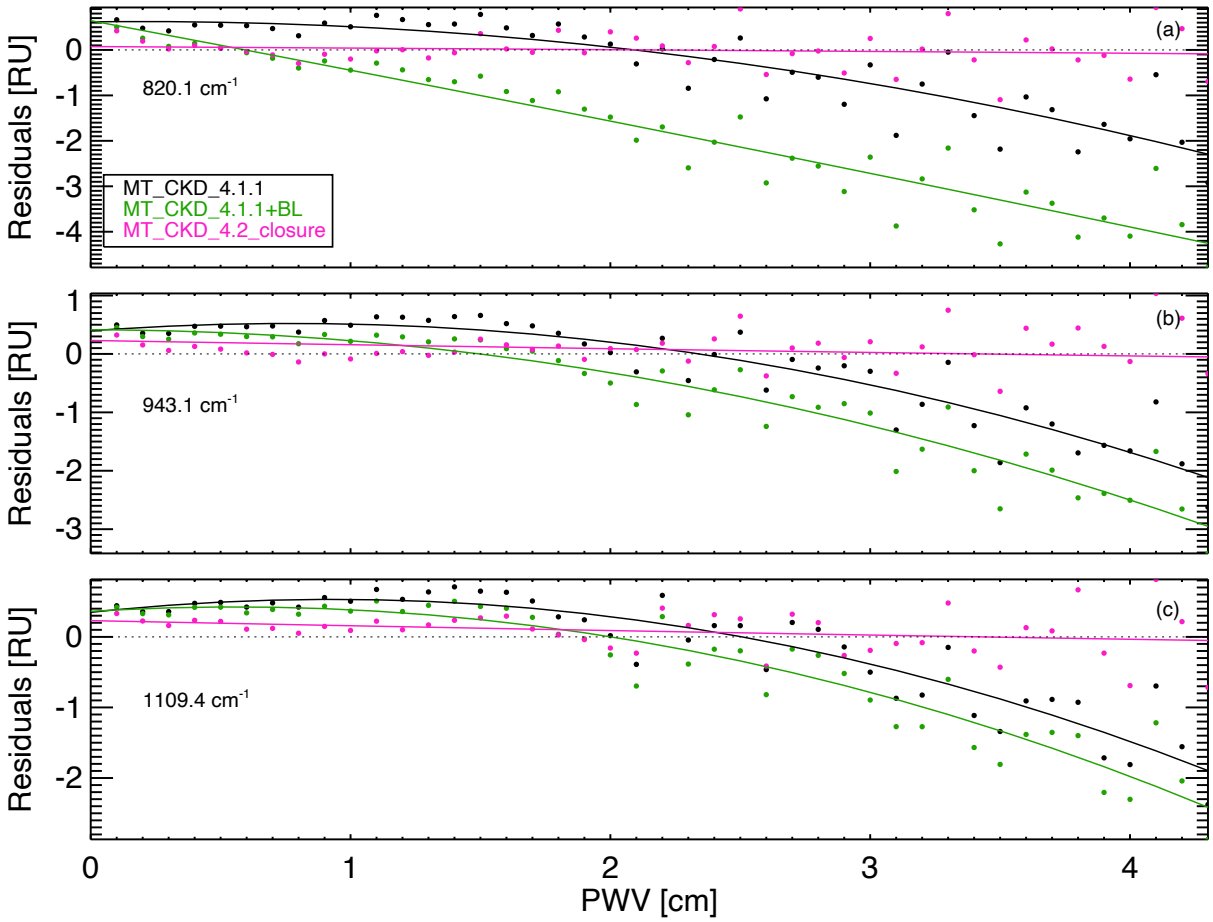

Fig 11. Residuals between AERI measurements at SGP and corresponding LBLRTM calculations as a function of PWV for three AERI channels in the infrared window. The black symbols are for LBLRTM calculations that use MT_CKD_4.1.1, the green symbols correspond to the use of MT_CKD_4.1.1+BL, and the pink symbols result from using the continuum derived in this study, MT_CKD_4.2_closure. Quadratic fits to these residuals are shown as curves in corresponding colors. Cases are binned by PWV and analyzed as described in the text.

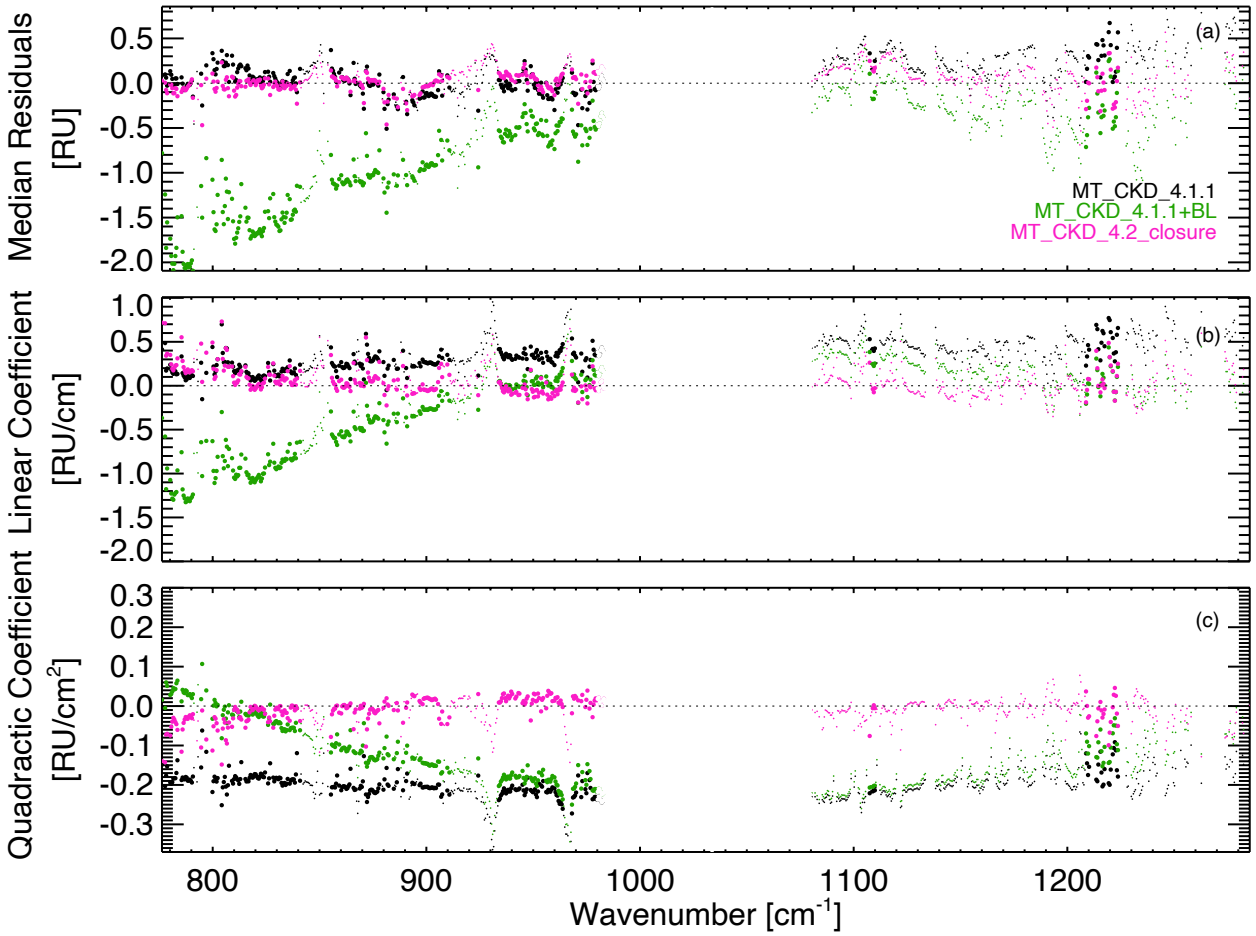

551 **Fig. 12.** Comparison between AERI measurements at SGP and corresponding LBLRTM calculations for
552 the spectral region 780-1280 cm^{-1}: (upper) Median of the PWV-binned residuals. The residual for each
553 spectral point in a PWV bin is computed as the mean of the "inner half" of all residuals in that bin, as
554 described in the text. The black symbols are for LBLRTM calculations that use MT_CKD_4.1.1, the green
555 symbols correspond to MT_CKD_4.1.1+BL, and the pink symbols result from using the continuum derived
556 in this study, MT_CKD_4.2_closure; (middle) Linear coefficient of the quadratic fit to the residuals as a
557 function of PWV; (bottom) Quadratic coefficient of the quadratic fit to the residuals as a function of PWV.
558 The distinction between large and small circles in all panels is explained in the text.
559

560 Since the foreign continuum depends linearly and the self continuum quadratically on the water
561 vapor amount, there is some validity in associating the behavior of the linear fit coefficient shown
562 in Fig. 12b with an inaccurate specification of the foreign continuum and the behavior of the
563 quadratic coefficient (Fig. 12c) with the self continuum. However, due to the dependence of each
564 on pressure, and hence on the water vapor profile and not simply on PWV, and the dependence of
565 the self continuum coefficients on temperature, such an association is not exact. A modification in
566 the specification of either continuum source will lead to changes in both the linear and quadratic

fit coefficients, so improvements to the results shown in Fig. 12 can follow only from a simultaneous analysis of the foreign and self continua.

4.3 Retrieval of Self and Foreign Continua

Our SGP AERI dataset, with its large number of cases and wide range of PWV values, is ideal for retrieving self and foreign continuum coefficients in the infrared window. The wide range of temperatures that characterize the water vapor profiles associated with these AERI observations also may possibly allow the derivation of coefficients that characterize the temperature dependence of the self continuum. Continuum properties determined in the analysis of SGP cases are then validated using AERI measurements from MAO. Due to the high PWV amounts for the MAO cases, this validation is especially informative with respect to the properties of the crucial self continuum.

The retrieval of water vapor continuum properties in the infrared window begins with baseline LBLRTM calculations of downwelling surface radiances for all the cases in the SGP AERI data set. These initial LBLRTM calculations utilize MT_CKD_4.1.1+BL (i.e. corresponding to the green results in Fig. 12), although the retrieval results are fairly insensitive to this choice. Using the measurement-calculation residuals, for each AERI channel between 780-1280 cm^{-1} a least-squares retrieval is performed of three independent variables -- two linear scale factors, one each for the self and foreign continuum coefficients used in the LBLRTM calculations, and a scale factor for the exponent of the self continuum temperature dependence. The sensitivities of the residuals to changes in the retrieved continuum properties (i.e. the Jacobian) used in the retrieval are obtained from additional sets of LBLRTM calculations in which each of these three properties is perturbed by a small amount. In the methodology, we apply the PWV binning discussed above. That is, at each spectral point a single residual and corresponding sensitivities are computed for each PWV bin by averaging the "inner half" of the residuals for all the cases in that bin. With this, each least-square retrieval operates on 43 (the number of PWV bins) measurement-calculation residuals. A three-variable retrieval is run to obtain scale factors for the self continuum, foreign continuum, and temperature exponent of the self continuum. Fig. 13 shows the results of this retrieval.

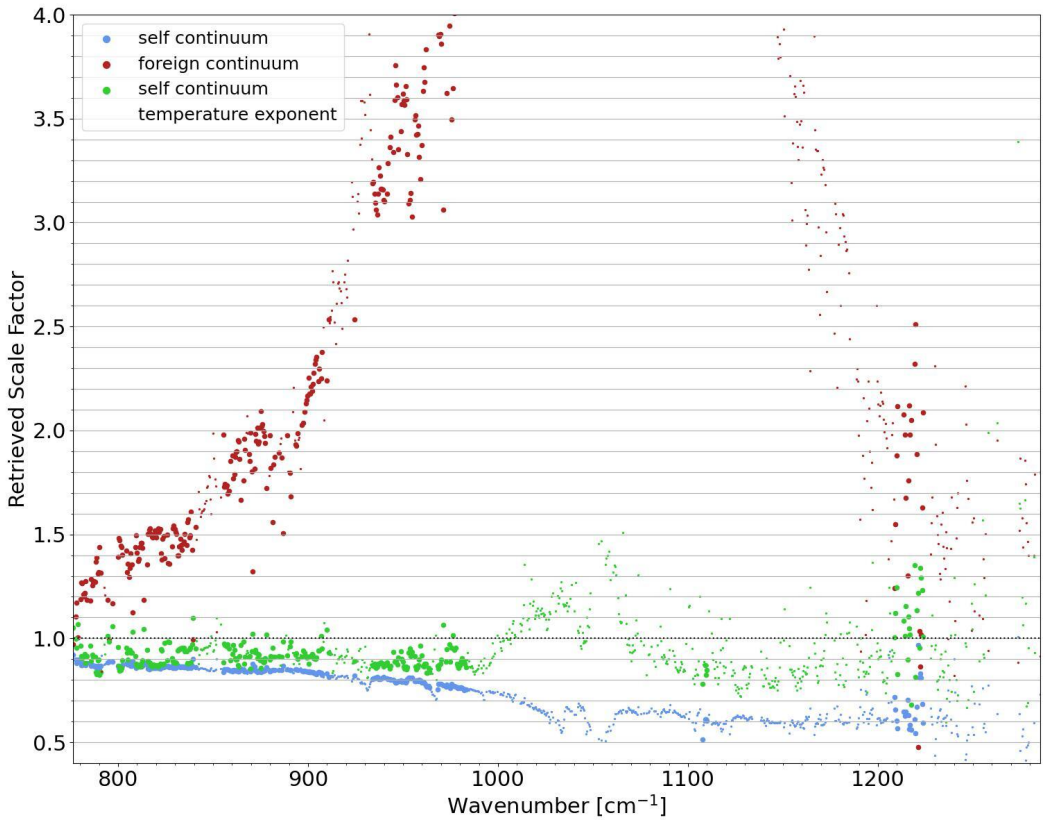

598 **Fig. 13.** Scale factor values (relative to MT_CKD_4.1.1+BL) obtained from the initial retrieval step
599 described in the text for the self continuum (blue), foreign continuum (red), and self continuum temperature
600 exponent (green). The distinction between large and small circles is the same as in Fig 12.
601

602 Using these results, an interim revised version of the MT_CKD water vapor continuum is created
603 by smoothing the retrieved spectral coefficients, interpolating through the ozone band region, and
604 blending the retrieved values into the continuum values in neighboring regions. Then the entire
605 retrieval process is repeated, including new sensitivity calculations using the interim MT_CKD
606 version. This process is iterated several times until the properties until no further smoothly varying
607 change in the continuum parameters could further improve the results (i.e. the median residuals
608 and the linear and quadratic coefficients of the fit of the residuals with respect to PWV).
609

610 The median values of the measurement-calculation residuals using the final retrieved continuum
611 coefficients and temperature dependence (MT_CKD_4.2_closure) are shown in pink in Fig. 12a.
612 As before, a quadratic function is fit to these residuals at each spectral point and the fit coefficients
613 are shown in Fig. 12b and c. Fig. 11 shows in pink the quadratic fit for MT_CKD_4.2_closure for
614 the same example AERI channels shown in this figure for prior versions of MT_CKD. These

figures indicate that the properties of the residuals between the SGP AERI measurements and LBLRTM residuals are greatly improved when MT_CKD_4.2_closure is used in the calculations compared to previous continuum versions. This improvement has resulted from increasing the atmospheric opacity for low PWV cases (roughly PWV < 2 cm) while decreasing it for higher PWVs.

4.4 Validation using AERI observations from MAO

As validation, LBLRTM calculations using several versions of MT_CKD are performed for the MAO AERI cases. The median residuals corresponding to these calculations are shown in Fig. 14. As for the SGP analysis above, these medians are computed from the inner half mean residuals of each PWV bin. (Each MAO PWV bin has a width of 0.2 cm.) As for SGP, no bias correction is applied to the MAO AERI measurements. (For the warm and moist conditions of MAO, any such correction would have only a small impact.) Due to the limited range of PWV values in the MAO dataset, quadratic functions are not fit to the residuals. It is clear from Fig. 14 that the residuals using MT_CKD_4.2_closure are greatly improved compared to previous continuum versions.

The self and foreign continuum coefficients retrieved from the SGP AERI measurements in this study are shown (MT_CKD_4.2_closure) in purple in Figs. 4d and pink in Fig. 6, respectively. The retrieved temperature exponents of the self continuum are shown in Fig. 5 (purple). Detailed discussion of these results is provided in section 5.

4.5 An adjustment to the retrieved foreign continuum

The continuum coefficient retrieval described above did not include the spectral region from 990-1070 cm^{-1}, which has significant ozone absorption. In Fig. 6, a reasonable spectral continuation of the AERI-derived coefficients across this region is shown with a thin pink curve segment. The overall flatness of the foreign continuum coefficients in the 900-1150 cm^{-1} region does not agree with the corresponding relative behavior of the coefficients derived by Baranov and Lafferty (2012) or that of MT_CKD_4.1.1, both of which have much smaller continuum coefficients in the middle of this region (~ 1070 cm^{-1}) than at its endpoints. For MT_CKD_4.1.1, this deep well is a

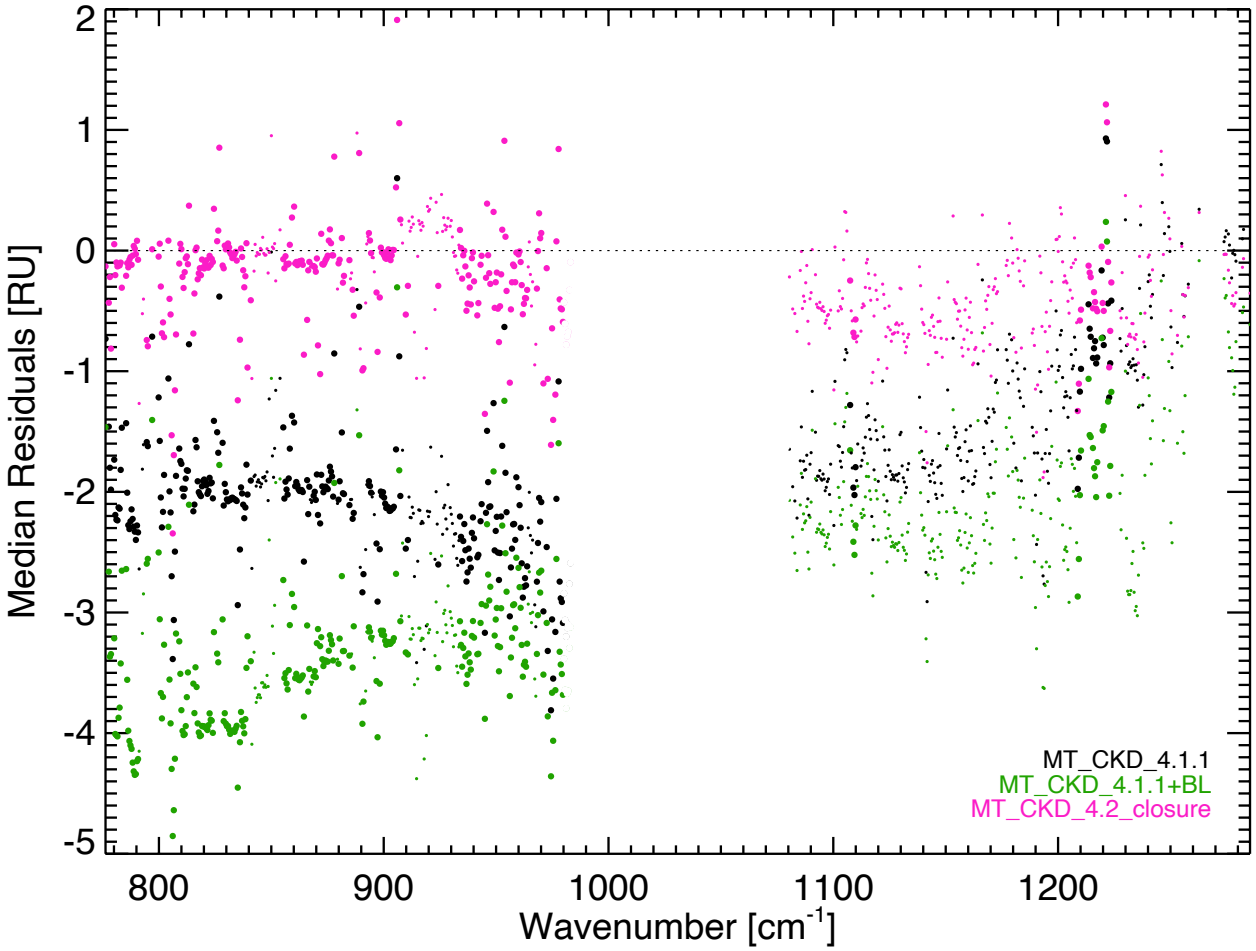

644 **Fig. 14.** Median of the PWV-binned residuals between AERI measurements at MAO and corresponding
645 LBLRTM calculations for the spectral region 780-1280 cm-1. The residual for each spectral point in a PWV
646 bin is computed as the mean of the "inner half" of all residuals in that bin, as described in the text. Residuals
647 are shown for MT_CKD_4.1.1 (black), MT_CKD_4.1.1+BL (green), and MT_CKD_4.2_closure (pink).
648 The distinction between large and small circles is the same as in Fig 12.
649

650 natural consequence of the assumption that the continuum in this region is due to the sum of
651 transitions centered hundreds of wavenumbers away from this window region (e.g. at 100 cm^{-1}),
652 with the continuum absorption from each transition decaying rapidly with increasing wavenumber
653 far (e.g. 800-1000 cm^{-1}) from its center. Based on its generally flat behavior from 900-1150 cm^{-1},
654 we conclude that the MT_CKD_4.2_closure (pink) curve in Figure 6 likely does not represent the
655 actual behavior of the foreign continuum in this region.
656
657 The optical depths in this region from the MT_CKD_4.2_closure foreign continuum are small.
658 Fig. 15a shows the derived foreign continuum optical depths at 980 cm^{-1} for all the cases in the

659 SGP data set. For a PWV of 2 cm, this optical depth is ~0.03. At SGP, if there existed an
660 atmospheric constituent with a small optical depth that scaled somewhat linearly with PWV, then
661 the impact in our analysis of such a constituent would be to inflate the derived foreign continuum
662 optical depth above the actual foreign continuum, and this artificial inflation would
663 disproportionately affect the derived foreign continuum most where it is smallest, i.e. the 980-1120
664 cm^{-1} region.
665
666 We now explore the possibility that the presence of aerosol in the skies over SGP can lead to such
667 an overestimation of the foreign continuum in our analysis. We obtain retrievals of aerosol optical
668 depth (AOD) with two markedly different approaches. We analyze periods coincident with the
669 daytime cases in our data set, and assume that the daytime result are representative of the entire
670 data set.
671
672 The first approach is to retrieve aerosol optical depth (AOD) and aerosol refractive index (RI)
673 within one hour of the AERI observations at SGP used in our analysis from the Aerosol Robotic
674 Network (AERONET; Dubovik & King, 2000). We estimate the AOD at ~1000 cm^{-1} (10 μm) from
675 AERONET observations at shortwave infrared (longest wavelength observed is 1640 nm) and
676 visible wavelengths coupled with assumptions about aerosol composition. We assume that the
677 AOD at longer wavelengths is dominated by contributions from an external mixture of coarse-
678 mode aerosols composed of deliquescent aerosol (produced through hygroscopic growth) and
679 mineral dust. The RI of deliquescent aerosol converges with that of water, 1.3 at 1640 nm and 1.2
680 +0.05i at 10 μm. The RI of dust depends on the composition, which is assumed to be iron-
681 oxide/hematite, a common soil component for the SGP region, having an index of refraction of
682 about 1.6 at 1640 nm and 2+0.02i at 10 μm. We allow the retrieved real part of the RI which spans
683 the range from 1.3 to 1.6 um to dictate the relative fraction of deliquescent aerosol to dust, and
684 thus infer the effective RI of the external mixture at 10 μm. Lastly, we use Mie scattering theory
685 to extend the measured AOD from shorter wavelengths out to ~10 μm. Clearly, the deliquescent
686 components should have a positive dependence on relative humidity and PWV, a fact that is borne
687 out in Fig. 15b. It is also intriguing and comfortingly consistent that the aerosol Angstrom exponent

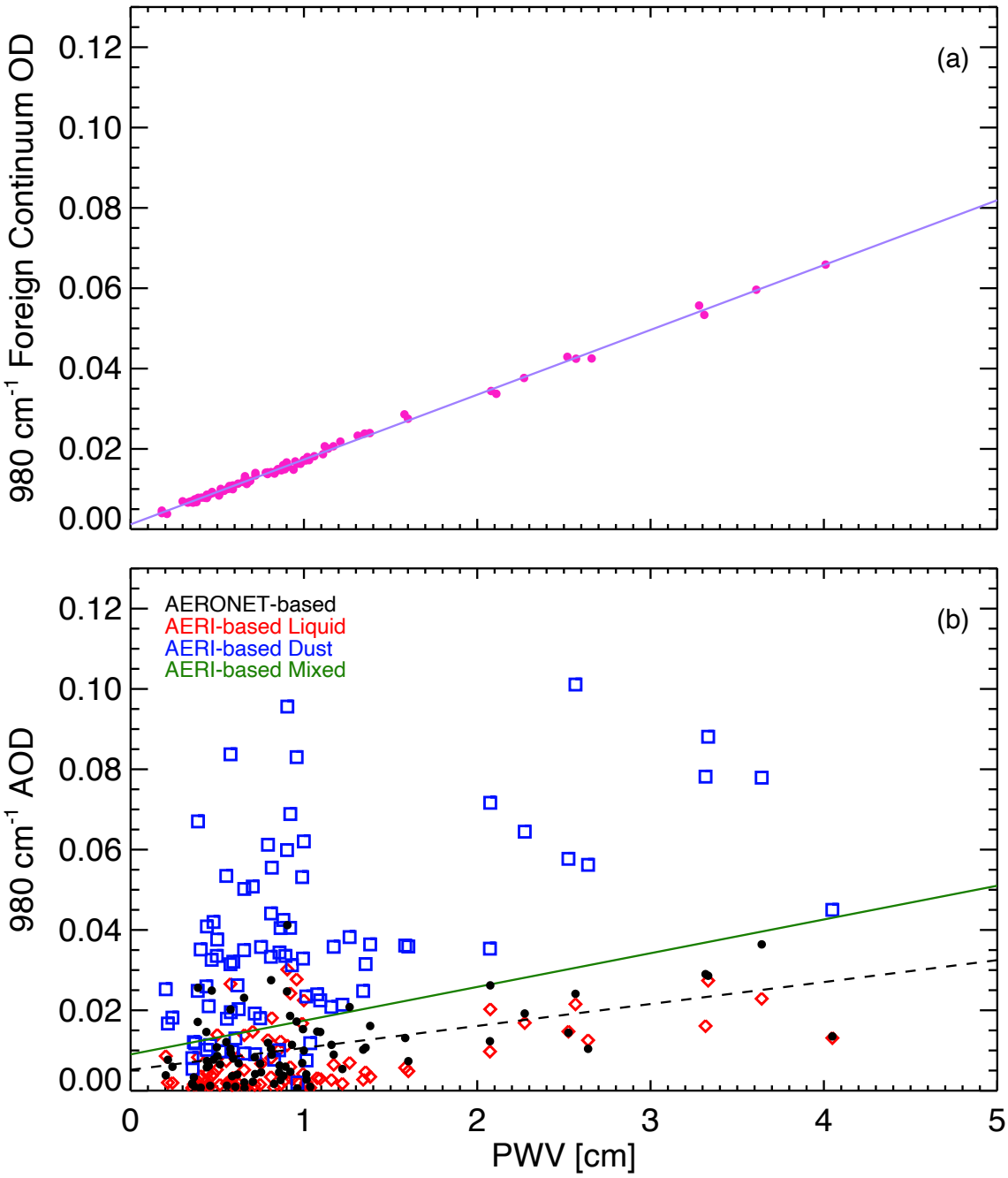

688 **Fig 15**. As a function of PWV for the daytime SGP AERI cases analyzed in this study: (a) Foreign
689 continuum optical depths from MT_CKD_4.2_closure; (b) Aerosol optical depths at 980 cm^{-1} derived from
690 AERONET measurements assuming a combination of a deliquescent aerosol and mineral dust (black points
691 with dashed black fitted line), retrievals from AERI observations at 2500-2860 cm^{-1} assuming a hydrated
692 sulfate aerosol (modeled as liquid, red diamonds), retrievals from AERI observations at 2500-2860 cm^{-1}
693 assuming montmorillonite spheres (dust, blue squares), and a 74/26 combination of the liquid and dust
694 aerosol assumptions, respectively (green linear fit, individual values not shown for figure clarity). Positive
695 correlation with PWV is seen for all modeled aerosols.

696 which typically varies between +2 to 0 for shorter wavelengths that are observed by the AERONET
697 system, to be moderately negative (-0.65) over the 1000-1100 cm^{-1} spectral range, driven by
698 changes in the refractive indices that vary notably in the longer wavelength range while being
699 virtually constant at shorter wavelengths.
700
701 The AODs values obtained from this analysis are shown as black circles in Fig. 15b. The results
702 in Fig. 15 show the estimated aerosol optical depth at 980 cm^{-1} is approximately half of the derived
703 foreign continuum optical depth. The aerosol optical depths scale reasonably linearly with PWV,
704 a consequence of the hygroscopicity of ambient aerosol whereby aerosols increase in size through
705 uptake of water vapor from the atmosphere, supporting the inference that the presence of aerosols
706 could have impacted our retrieval of foreign continuum coefficients.
707
708 The second approach to retrieve AOD uses the downwelling radiance observations made by the
709 AERI in the 2500-2860 cm^{-1} (3.5-4.0 μm) spectral region. Since at 2500-2860 cm^{-1} the
710 downwelling AERI radiance observation is dominated by scattered solar radiation during the
711 daytime, in this analysis we use only the daytime AERI samples that coincide with the AERONET
712 observations used in the first approach. We apply the physical-iterative Mixed-phase Cloud
713 Retrieval Algorithm (MIXCRA; Turner, 2005) to these AERI observations assuming that the
714 "cloud" was composed of aerosol particles (as was done in Turner 2008). We apply MIXCRA
715 with two distinct assumptions for aerosol type, one modeling the aerosol as liquid droplets
716 (representing a hydrated sulfate aerosol, shown as red diamonds in Fig. 15b) and the other
717 assuming montmorillonite spheres (i.e. dust, blue squares in Fig. 15b). The Interagency Monitoring
718 of Protected Visual Environments (IMPROVE; Malm et al., 1994) project provides measurements
719 of the mass of sulfate and soil particles that have diameters less than 2.5 μm. Using IMPROVE
720 data from Stilwell, OK (the closest IMPROVE site to ARM SGP during 2016-2018), over our
721 analysis period the mean ratio of the sulfate (liquid) aerosol mass to the sum of the sulfate and soil
722 mass was 0.74. We thus estimate the AOD at 980 cm^{-1} using $0.74 * AOD_{liquid} + 0.26 * AOD_{dust}$,
723 which yields somewhat higher AOD results (green line in Fig. 15b) as a function of PWV as the
724 first method that was based on AERONET observations.
725

These AOD estimates establish that it is plausible that the presence of aerosols has impacted the determination of the MT_CKD_4.2_closure foreign continuum coefficients shown in Fig. 6. However, the assumptions about aerosol properties made in the analyses above are quite speculative and the actual aerosol optical depths in the infrared window may differ significantly from those we derived. The possibility that our continuum coefficient retrieval has been impacted by aerosols leaves us with two choices, each of which has positive aspects and flaws. We could ignore this likely contamination of our derived foreign continuum (MT_CKD_4.2_closure in Fig. 6) and its problematic flat spectral behavior, and provide these foreign continuum coefficients in the next release of MT_CKD. This choice, when used in concert with our derived self continuum, would provide radiative closure with the AERI observations used in this study, but likely only because the water vapor continuum in this region inappropriately included some absorption that is actually due to aerosols. The other choice is to use the analysis above to make an estimate of the aerosol contribution to the derived foreign continuum, subtract this initial estimate of this aerosol contamination from MT_CKD_4.2_closure, and then use the MT_CKD line shape methodology (Mlawer et al., 2012) to compute foreign continuum coefficients that are in reasonable agreement with this difference. By construction, this option will have relative spectral behavior in the middle of the window that is similar to the behavior in MT_CKD_4.1.1 (also similar to that measured by Baranov and Lafferty, 2012), but will no longer provide closure with the AERI measurements since calculations using this foreign continuum would be missing optical depth unless a user explicitly included longwave aerosols in their calculation. Another drawback of this approach stems from the realization that any estimate of aerosol absorption in the infrared window would be highly uncertain, which would lead to significant uncertainty in the foreign continuum derived after the aerosol contribution is removed from the MT_CKD_4.2_closure foreign continuum.

Given this difficult choice, we feel that it is important for the MT_CKD continuum model to provide our best estimate of the actual foreign continuum despite the inherent uncertainty of the approach used to derive it. Therefore, we choose to derive the new foreign continuum for MT_CKD_4.2 by accounting for the estimated contribution of aerosols. Given that the use of MT_CKD_4.2 will not result in radiative closure, we will also provide the MT_CKD_4.2_closure foreign continuum as an alternate foreign continuum choice for users of MT_CKD.

In Appendix 2, we discuss the approach used to derive a specification of the foreign continuum in the infrared window that is consistent with both a) the closure analysis described in section 3.2 interpreted in light of the aerosol absorption analysis above (i.e. in Fig. 15b) and b) the relative spectral behavior of the foreign continuum in this region given by the MT_CKD line shape calculation. This derivation uses the MT_CKD line shape formalism to compute foreign continuum coefficients from 780-1250 cm^{-1} that, once subtracted from the coefficients in MT_CKD_4.2_closure, is roughly consistent with the properties (AOD and Angstrom exponent in the infrared window) of the aerosol absorption derived from the AERONET measurements.

The foreign continuum coefficients (labeled as MT_CKD_4.2) that result from this aerosol-removing procedure are shown as a purple curve in Fig. 6. Since a similar line shape formalism was used to derive these coefficients as was done for MT_CKD_1.0 (virtually the same as MT_CKD_4.1.1), the MT_CKD_4.2 coefficients also have a minimum near 1100 cm^{-1}. The spectral behavior of the MT_CKD_4.2 coefficients now more closely resemble the Baranov and Lafferty (2012) measurements than the derived coefficients before the assumed impact of aerosols was accounted for. This agreement with an independent measurement of foreign continuum absorption provides a measure of confidence that the aerosol adjustment has some validity.

Given the modification made to the foreign continuum to obtain MT_CKD_4.2 from MT_CKD_4.2_closure, a few observations are worth pointing out. First, calculations using MT_CKD_4.2 do not provide radiative closure with either the SGP or MAO AERI observations. As shown in Fig. 12, impressive agreement between the observations and calculations is obtained using MT_CKD_4.2_closure, but this closure to some extent is due to the assumed inclusion of the radiative effects of aerosols in that continuum version. Removing that contribution, as has been done to construct MT_CKD_4.2, destroys that radiative closure. Therefore, a comparison between the observations and calculations using MT_CKD_4.2 is not informative and we do not include those results on Fig. 12. Second, the strong agreement shown in Fig. 14 between the MAO AERI measurements and calculations using MT_CKD_4.2_closure occurs even though that continuum version is assumed to include the impact of aerosols at SGP. This is possibly due to reasonably similar aerosol loading at SGP and MAO, both continental sites, and the reduced relative radiative impact of aerosols at MAO compared to SGP given the higher PWV amounts at MAO. Third,

some consideration should be given to the results for MT_CKD_4.1.1 and MT_CKD_4.1.1+BL in Fig. 12 in light of the need for the aerosol adjustment detailed above. In both cases, the foreign coefficients in the infrared window in these continuum versions were not derived from field studies, so they could not have been impacted by aerosols in the same way that the MT_CKD_4.2_closure coefficients are assumed to have been. The window self continuum used in these calculations (the same in both versions) was derived by Turner et al. (2004), a radiative closure field study at SGP. It is reasonable that atmosphere opacities in this previous study were affected by a similar aerosol loading as in the current study, and that the self continuum coefficients derived in Turner et al. (2004) implicitly include the radiative effects of the aerosols. Therefore, no further adjustment to these versions is needed to evaluate the behavior of their associated residuals, and it is fair to compare them to those obtained using MT_CKD_4.2_closure, as is done in Fig. 12.

4.6 Uncertainty analysis

The determination of the uncertainties in our retrieved values of self continuum coefficients, foreign continuum coefficients, and the temperature dependence of the self continuum in the infrared window is challenging. Consideration must be given to typical uncertainties in radiative closure studies, such as those due to the radiometric instrument and the specification of the atmospheric profile, as well as complexities in this study such as the consideration of the role of aerosols in the derivation of the foreign continuum. We here provide an analysis of key sources of uncertainty in our derived continuum values.

Our uncertainty analysis is based on the realization that the set of retrieved continuum values (self, foreign, and temperature dependence of self) in MT_CKD_4.2_closure at a spectral point is not the only combination of continuum values that would provide suitable agreement between the observed and calculated radiances. The retrieved values in most small spectral windows (e.g. 10 cm^{-1}, the spacing at which MT_CKD stores continuum coefficients) show some variability (see Fig. 13), as do the final residuals shown in Fig. 12. Therefore, we must consider to what extent the retrieved continuum values can be modified while maintaining "good agreement" between the measurements and calculations. How we define "good agreement" must reflect the uncertainties in both the measurements and calculations. Therefore, we must first analyze individual factors that

lead to uncertainty in the spectral residuals, and then combine these factors to get a total spectral uncertainty. Then, at each spectral point the total uncertainty in the radiance residuals provides a foundation for evaluating other sets of possible retrieved continuum values – if the residuals generally stay within this uncertainty for all PWV bins for a given set of continuum values, then these alternate values are considered plausible. Using this approach, we can find limits past which good agreement is no longer possible, therefore defining the uncertainty in each continuum parameter.

Sources of uncertainty in the radiance residuals arise from the uncertainty in a) the specification of trace gas abundances, b) the temperature and water vapor profiles, and c) the AERI radiance measurements. The method used to determine the uncertainty due to the trace gas specification is discussed above and is shown in Fig. 10a. The uncertainty due to temperature and water vapor profiles is evaluated through the use of a reasonable alternate specification of these profiles, given by sonde measurements in which the measured water vapor profile has been scaled to attain agreement with the brightness temperature measured by a collocated microwave radiometer. This approach to specifying the temperature and water vapor profiles in radiative closure studies has often been utilized in past analyses (e.g. Turner et al., 2004; Mlawer and Turner, 2016; Turner et al., 2016). Fig. 10b shows the spectral RMS differences between calculations that use these alternate profiles and those that use the profiles employed in the analysis described above. Finally, the AERI uncertainty is assigned a value of 0.1 RU based on the random error spectra of the instrument, as estimated by the calibration equation used in its processing (Revercomb et al., 1988; Knuteson et al, 2004b).

In addition to these contributions to the uncertainty in the residuals, it is clear from Fig. 11 that the variability of the final (pink) residuals as a function of PWV adds an additional challenge in determining what constitutes agreement between measurements and calculations for given continuum parameters. To account for this uncertainty, we compute the interquartile differences of the binned residuals for each spectral point, which is shown in Fig. 10c, and include this as an additional term in the uncertainty calculations.

We assume that these four sources of uncertainty in the residuals are independent and add these values in quadrature at each spectral point to get the spectrum of total uncertainty, shown as balck circles in Fig. 10d. Given that the determination of continuum coefficients enforces a degree of spectral smoothness on the coefficients, rather than considering the spectral uncertainty shown in Fig. 10d we group the uncertainty values in 20 cm^{-1} intervals. We take a conservative approach in assigning the final uncertainty value in each interval by using the RMS of the spectral values, which are also shown in Fig. 10d.

Now we compute alternate sets of continuum coefficients at each spectral point to determine the maximum that each continuum coefficient can be perturbed while keeping the residuals as a function of PWV within the uncertainty in the residuals computed above. We illustrate this procedure for the self continuum. First, all self continuum coefficients in MT_CKD_4.2_closure are increased, in turn, by 5,10, 20, and 30%. For each perturbation, we then follow the procedure detailed in Sec. 4.2 to derive optimal spectral values for the foreign continuum and the temperature dependence of the self continuum. For illustration, quadratic fits to the resulting residuals from these optimal perturbations are shown in Fig. 16 as a function of PWV for all spectral elements in the 20 cm^{-1} bins that contain the wavenumbers in Fig. 11, as well as the 1200-1220 cm^{-1} bin. (The wavenumber corresponding to each curve shown is not identified since this analysis is being performed collectively for the spectral elements grouped in each interval.) As an example, Fig. 16b shows that, for the 940-960 cm^{-1} region, the coefficients obtained starting with a 5% perturbation to the self continuum result in the residuals staying within the unshaded region, which corresponds to the radiance uncertainty in this region. That is, a 5% perturbation to the self continuum results in measurement-calculation agreement (as defined above). In contrast, the curves corresponding to a 10% perturbation do not remain withing the unshaded region, so a 10% change to the self continuum does not lead to agreement. Based on the set of perturbation calculations, for this spectral region we determine that the self continuum uncertainty is 7%. We perform this analysis for all 20 cm^{-1} bins – the resulting self continuum uncertainty values are shown as thin purple error bars on the MT_CKD_4.2 curve in Fig. 4.

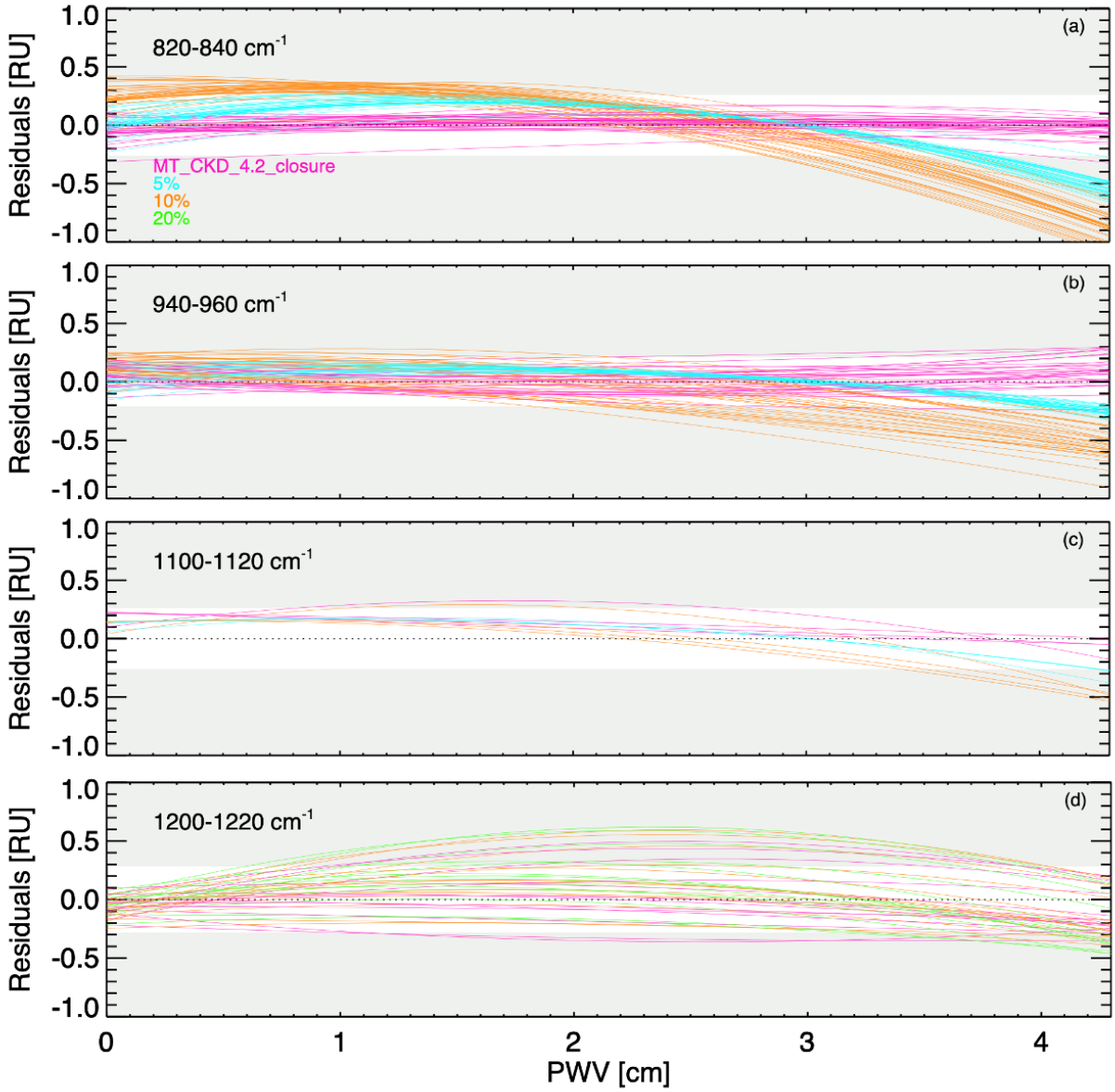

878 **Fig. 16.** For four example 20 cm^{-1} spectral regions, quadratic fits to the residuals are shown for
879 MT_CKD_4.2 closure (pink) and variations in which the self continuum has been increased by 5% (cyan),
880 10% (orange), and 20% (green), with the foreign continuum and self continuum temperature dependence
881 rederived for each perturbation (as described in text). Curves are shown for the spectral elements
882 corresponding to the large circles in Fig. 12 and not all colored curves are shown on all panels for clarity.
883 The regions shaded gray on each panel are outside of the total uncertainty for the respective panels. The set
884 of colored curves that do not typically stay within the unshaded region shows that the corresponding
885 perturbation to the self continuum is greater than the self continuum uncertainty in these regions.
886

887
888 We repeat this procedure starting with a series of foreign continuum perturbations, determining
889 optimal spectral values for the self continuum and the temperature dependence of the self for each
890 perturbation. An analysis similar to the one described above for the self continuum results in the
891 foreign continuum uncertainty values shown in Fig. 6 for MT_CKD_4.2_closure in the 20 cm^{-1}
892 spectral bins. Note that in some spectral regions (primarily the ozone-dominated region from 980-
893 1080 cm^{-1}) this method is not able to determine a reliable uncertainty value for the foreign
894 continuum due to the large uncertainty in the residuals and combined behavior of the self and self
895 temperature dependence in response to the foreign perturbations. In this region, we compute an
896 uncertainty by combining the uncertainty at its boundaries (i.e. 970 and 1090 cm^{-1}) with the
897 difference in continuum values resulting from alternate reasonable ways to span the gap in
898 retrieved (i.e MT_CKD_4.2_closure) foreign continuum values from 980-1080 cm^{-1}. We discuss
899 below the uncertainty associated with the MT_CKD_4.2 foreign continuum coefficients.
900
901 Finally, we follow this procedure beginning with a series of perturbations to the temperature
902 dependence of the self continuum, determining optimal spectral values for the self and foreign
903 continuum. However, in all spectral bins this method is not able to derive reliable estimates of the
904 uncertainty in the self temperature dependence. Even though the AERI datasets used in our study
905 are not able to effectively constrain the self continuum temperature dependence, below we
906 consider the results of other studies to determine rough estimates of the uncertainty in the
907 MT_CKD_4.2 temperature dependence parameters.
908
909 The continuum parameters derived from the AERI measurements are not independent – for
910 example, an increase in the derived self continuum value at a spectral point would necessitate a
911 lower associated foreign continuum value in order to maintain overall radiative closure at that
912 point. Therefore, for the uncertainty analysis it is informative to understand how these two
913 continuum values co-vary. We therefore perform a retrieval of the foreign continuum value for a
914 small perturbation to the self continuum (with the temperature dependence kept fixed). Fig. 17
915 shows the ratio of the foreign and self continuum changes in these retrievals for the window region.
916 Consideration of the uncertainty in either of these quantities should be done in the context of their
917 combined behavior.

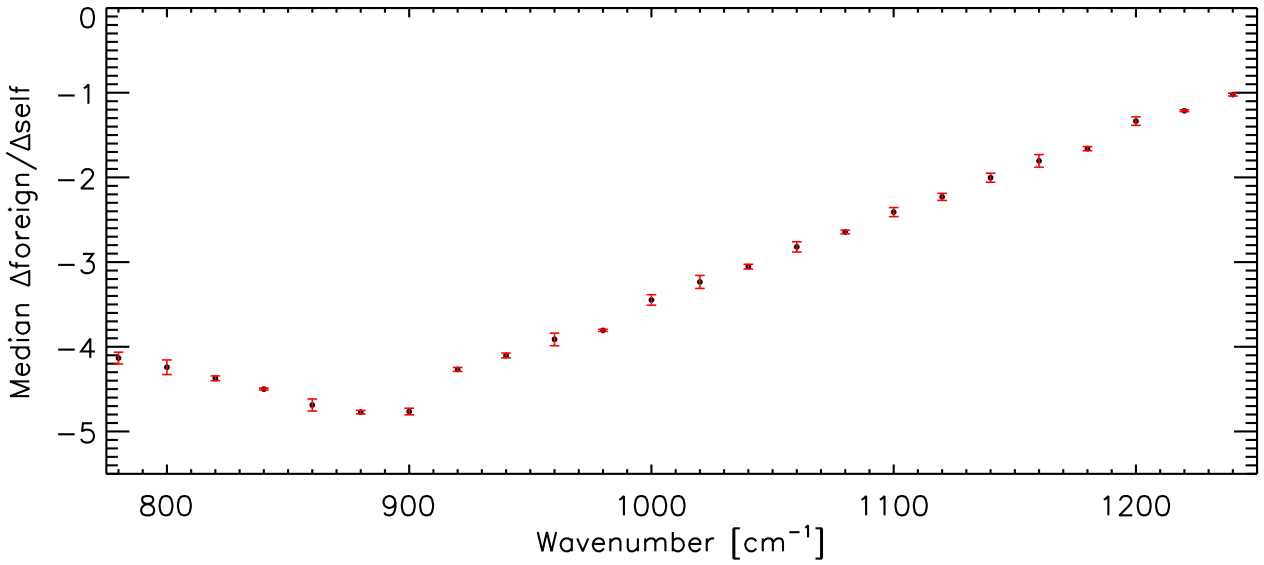

Figure 17. Ratio of change in derived foreign continuum value to a small perturbation in the self continuum value.

The derivation above of uncertainty values for the MT_CKD_4.2_closure foreign continuum coefficients does not directly apply to the MT_CKD_4.2 foreign continuum, which was derived using information other than the AERI measurements at SGP and MAO. The method used to derive these foreign continuum coefficients was quite speculative, involving a) the MT_CKD_4.2_closure foreign continuum coefficients, b) 'best guess' estimates of the aerosol optical properties in the infrared window, and c) a calculation using the MT_CKD line shape formulation constrained to foreign continuum values outside the infrared window and those inferred in the window from a) and b). The highly conjectural nature of this approach presents large challenges from using it alone to determine reasonable uncertainty estimates. Instead, we use all available information (MT_CKD_4.2 closure uncertainties, analysis of the method used to derive MT_CKD_4.2 foreign continuum, and the laboratory measurements shown in Fig. 6) to provide users of MT_CKD with a rough estimate of the uncertainty of MT_CKD_4.2 in specifying water vapor foreign continuum absorption in this region. The upper limit of the uncertainty must reflect the possibility that the impact of aerosols on the derivation of foreign continuum is negligible, so the corresponding uncertainty values are determined by the difference between MT_CKD_4.2 and MT_CKD_4.2_closure (accounting for its own uncertainty). Reassuringly, even though this uncertainty estimate did not consider the single-frequency measurement of Cormier et al. (2005), the upper envelope of the MT_CKD_4.2 uncertainty estimates (shown with

939 thin purple vertical bars in Fig. 6) allow the possibility that the foreign continuum is as great as
940 that value. With respect to the lower limit of the MT_CKD_4.2 uncertainty, we explicitly consider
941 the results from the Baranov and Lafferty (2012) study, which is generally lower than the
942 MT_CKD_4.2 coefficients but clearly represent possibly valid values. We compute the uncertainty
943 by adding in quadrature: a) the difference between MT_CKD_4.2 and MT_CKD_4.1.1+BL and
944 b) the uncertainty in the coefficients determined in Baranov and Lafferty (2012). The resulting
945 MT_CKD_4.2 uncertainty estimates are generally consistent with the results we would have
946 attained in our study had we adjusted the MT_CKD_4.2_closure coefficients to account for the
947 impact of aerosol optical depths somewhat greater than we actually assumed (i.e. consistent with
948 the relative aerosol loading of the green line compared to the black line in Fig. 15b). In Fig. 6, we
949 denote MT_CKD_4.2 foreign continuum uncertainty estimates with open-ended vertical lines to
950 contrast the broader perspective used to determine these values with the AERI-based uncertainty
951 estimates used for the MT_CKD_4.2_closure foreign coefficients, which are denoted as (pink)
952 vertical lines with end caps. To conclude, MT_CKD users should be aware of possible
953 considerable uncertainties when utilizing MT_CKD_4.2 foreign continuum coefficients.
954
955 With a similar perspective, we also consider all available information to determine rough
956 uncertainty estimates for the MT_CKD_4.2 temperature dependence exponents, which are not able
957 to be effectively constrained by the AERI measurements used in this study. The upper limit of the
958 uncertainty needs to include the (refit) values from the Burch and Alt (1984) study (accounting for
959 that study's uncertainty) since we view its results with confidence due to the close agreement of
960 its derived self continuum coefficients with those from the current study. (See Fig. 4.) When
961 considering the lower limit of possible values of the temperature dependence exponents, we do not
962 consider the values derived by Baranov et al. (2008) with great confidence since the self continuum
963 coefficients determined in that work do not agree with those derived in the current study. As a
964 result, there is little information to go on to constrain the lower uncertainty limit. We therefore
965 define the uncertainty bars to be equal in the positive and negative directions (adjusted to ignore
966 the bump in the MT_CKD_4.2 exponents centered at 780 cm^{-1}).
967
968 **5. Analysis of MT_CKD_4.2**

969 Fig. 4a shows the final self continuum coefficients (MT_CKD_4.2) derived in this study along
970 with previous versions of the continuum model. With MT_CKD_4.1.1 used as a reference, Fig. 4d
971 shows the relative spectral behavior of MT_CKD_4.2 (and its uncertainty), the most recent
972 laboratory measurements from three groups, previous versions of CKD and MT_CKD based on
973 field studies that have been adjusted (as described in section 2) to account for a larger foreign
974 continuum than utilized in their respective original derivations, and the similarly adjusted results
975 from the field study by Taylor et al. (2003). Although these self continuum specifications do not
976 all agree, it can be argued the evidence clearly suggests that MT_CKD_4.1.1 is too strong across
977 the entire infrared window. For wavenumbers less than 900 cm^{-1}, most of the results shown agree
978 that the self continuum is 8-15% weaker than MT_CKD_4.1.1. Exceptions to this are the study of
979 Baranov et al. (2008) and the adjusted coefficients of CKD_2.1, which is based on the Westwater
980 et al. (1995) study. The adjustment made to CKD_2.1 only accounts for a change in the foreign
981 continuum, but another significant bias in the Westwater et al. (1995) results likely is present. The
982 type of sonde used in the calculations in that study to specify the water vapor fields were
983 subsequently shown to have a dry bias of 4-8% due to contamination of the relative humidity
984 sensor by the packaging (Wang et al. 2002; Turner et al. 2003). Given the squared dependence of
985 the self continuum on water vapor abundance, a rough estimate suggests that the self continuum
986 coefficients derived in that study were likely too high by at least 8%. As a result, the CKD_2.1_adj
987 curve in Fig. 4d likely needs to be shifted downward by that amount to account for this bias. Given
988 that, all results shown in Fig. 4d for 780-900 cm^{-1} exhibit agreement except for a single outlier
989 result by Baranov et al. (2008). The good agreement of these self continuum specifications persists
990 over the rest of infrared window with the exception of MT_CKD_1.0_adj, which is based on the
991 adjusted results of the Turner et al. (2004) study. It is encouraging that the accurate cavity ring
992 down measurement by Cormier et al. (2005) agrees within the tight uncertainty bound of the
993 current study. In spectral regions in which the uncertainty estimates of the current study are small,
994 the results of the current study are in agreement with all laboratory measurements by Burch and
995 Alt (1984) and most of the adjusted values from the Taylor et al. (2003) field analysis.
996
997 The MT_CKD_4.2 foreign continuum coefficients, which have been adjusted to account for the
998 presence of aerosols at SGP as described above, are shown in Fig. 6. Since its behavior near its
999 minimum results from a similar line shape calculation as MT_CKD_1.0, it is not surprising that

1000 the shapes of these two continuum versions are similar in this region. However, MT_CKD_4.2 is
1001 ~5 times greater than its predecessor in the 960-1150 cm^{-1} region, and 2-4 times greater in the
1002 regions of the infrared window outside this minimum region, i.e. where the continuum is stronger
1003 and the AERI observations provide a greater constraint. In these regions, the MT_CKD_4.2
1004 uncertainty estimates do not include the MT_CKD_1.0 (equivalent to MT_CKD_4.1.1)
1005 coefficients. Despite the quite speculative approach used to adjust the derived foreign continuum
1006 for aerosols, there is some correspondence of these continuum values with the Baranov and
1007 Lafferty (2012) experimental values. By construction, the MT_CKD_4.2 uncertainty estimates
1008 include the Baranov and Lafferty (2012) values.
1009
1010 The self continuum temperature dependence exponents derived in this study are shown in Fig. 5.
1011 As can be seen in Fig. 13, the retrieval of this exponent for 780-980 cm^{-1} shows less variability
1012 than at higher wavenumbers in the region analyzed. Also shown in Fig. 5 are the exponents in
1013 MT_CKD_4.1.1 as well as values derived from the laboratory studies of Baranov et al. (2008),
1014 Cormier et al. (2005), and Burch and Alt (1984). (It is important to note that the exponents shown
1015 on this figure for these studies are for the continuum coefficients as defined in MT_CKD, which
1016 are specified for a reference density and do not include the radiation term.) The Burch and Alt
1017 (1984) study is represented by two sets of alternate temperature exponent values, one based on the
1018 data in the table provided in that work associated with its Fig. 2 and one based on our analysis of
1019 the plotted values in its Fig. 2. It is clear from Fig. 5 that there is no consensus between the
1020 specifications of the self continuum temperature exponents that are displayed. The MT_CKD_4.2
1021 values are in excellent agreement at the single location analyzed in Cormier et al. (2005) and are
1022 closer than MT_CKD_4.1.1 to the Baranov et al. (2008) values in the region where the AERI
1023 analysis is most definitive. Above 980 cm^{-1}, the MT_CKD_4.2 exponents diverge from the
1024 Baranov et al. (2008) values, but there is some suggestion in Fig. 13 that a justifiable choice could
1025 have been made to decrease the MT_CKD_4.2 exponents further, thereby bringing them in closer
1026 agreement to Baranov et al. (2008). Our inability to determine uncertainty values for the exponents
1027 based on the AERI analysis alone reflects that a wide range of exponent values are able (after
1028 adjustments to the self and foreign coefficients) to provide radiative closure with the observations
1029 within the uncertainty in the residuals. Therefore, the exponent values shown in Fig. 5 should be

considered numerical values that optimize the radiative closure results rather than an attempt at a definitive determination of the spectral behavior of a physical quantity.

6. Impact

6.1 Broadband fluxes and heating rates

The impact of the modified water vapor continuum in MT_CKD_4.2 on broadband radiative fluxes (Fig. 18) depends strongly on the moisture content of a profile. (See Table 1 for PWV values.) For dry winter profiles, the continuum modifications cause a modest decrease in upward flux and an increase in downward flux from the increased opacity due to the larger foreign continuum, which outweighs the decrease in the self continuum. The difference in downwelling flux sharply increases at ~800 mb for the tropical or summer profiles (Fig. 18d). In the tropical atmosphere, for example, the downwelling flux at the surface decreases by more than 4 W/m^2 as a result of the overall decrease in atmospheric opacity in the IR window caused by the 10-30% decrease in the dominant water vapor self continuum. The magnitude of the change in upwelling flux (Fig. 18c) due to the use of MT_CKD_4.2 is much smaller than for the downwelling flux since the radiating temperature of lower atmosphere, the region in which the self continuum emits radiation, does not differ too greatly from the surface temperature. Therefore, decreased absorption of surface-emitted radiation by the self continuum in MT_CKD_4.2 is partially compensated by its decreased emission of the lower atmosphere at a (typically) slightly lower temperature. Nevertheless, the upwelling radiation does increase by ~0.7 W/m^2 in the mid-troposphere and 0.5 W/m^2 at the top of the tropical atmosphere, with smaller but still notable increases for atmospheres with moderate PWV values.

The analysis in this study shows that the total atmospheric opacity in the infrared window is less than had previously been thought, but the exact partitioning between the water vapor continuum and aerosols, i.e. the difference between MT_CKD_4.2 and MT_CKD_4.2_closure, is quite uncertain. Fig. 19, which shows the analogous results to those in Fig. 18 for calculations using MT_CKD_4.2_closure, may better reflect the impact on fluxes resulting from this study since all sources of opacity in the infrared window are accounted for. In drier conditions the increase in atmospheric opacity in MT_CKD_4.2_closure results in an increase in downwelling flux at the surface, consistent with the change in the measurement-calculation residuals (e.g. Fig. 11) for

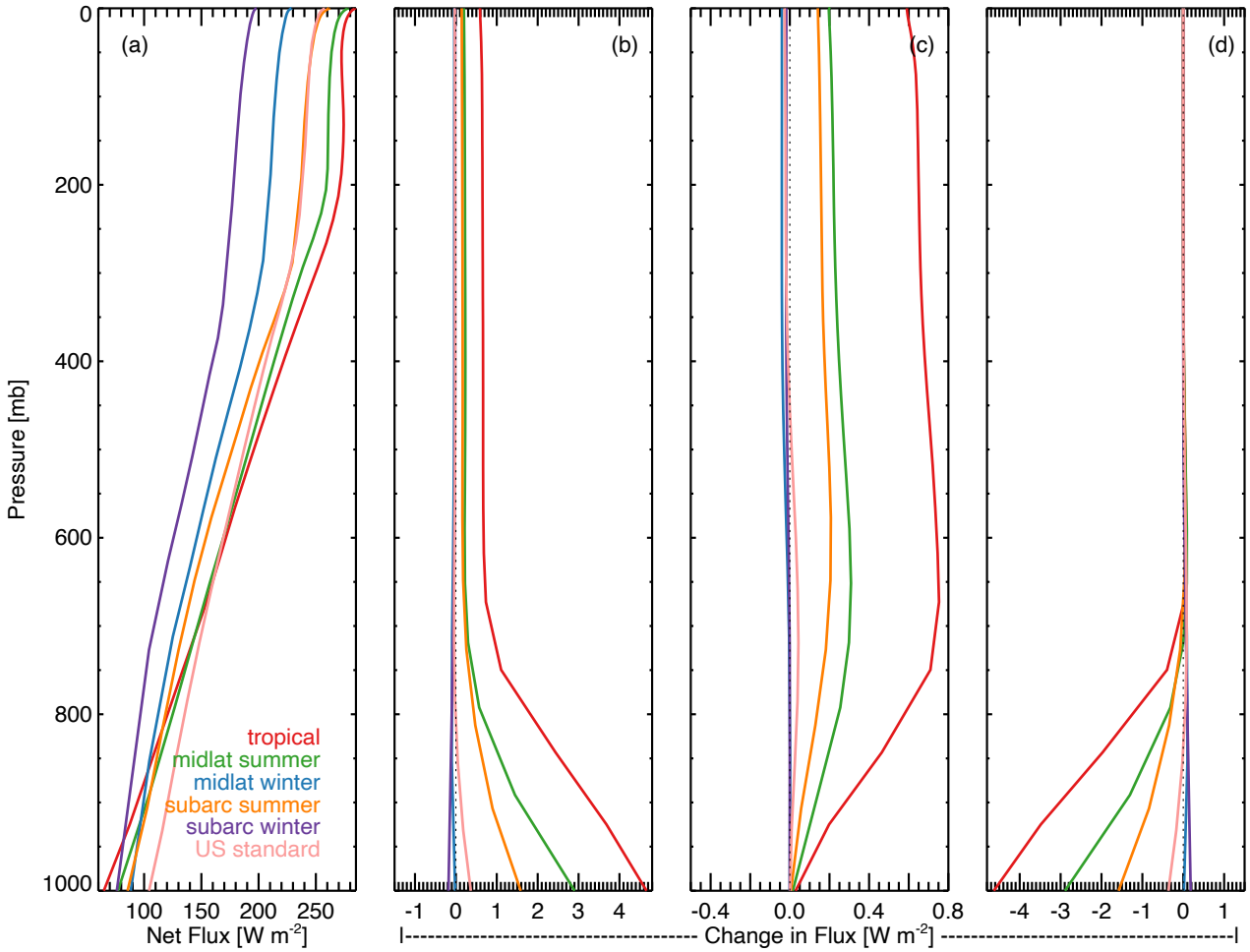

Fig. 18. For six standard atmospheres: (a) longwave net flux from LBLRTM calculations using MT_CKD_4.1.1; (b) Difference in net flux between calculations that use MT_CKD_4.2 and calculations that use MT_CKD_4.1.1; (c) Difference in upward flux between MT_CKD_4.2 and MT_CKD_4.1.1; (d) Difference in downward flux between MT_CKD_4.2 and MT_CKD_4.1.1.

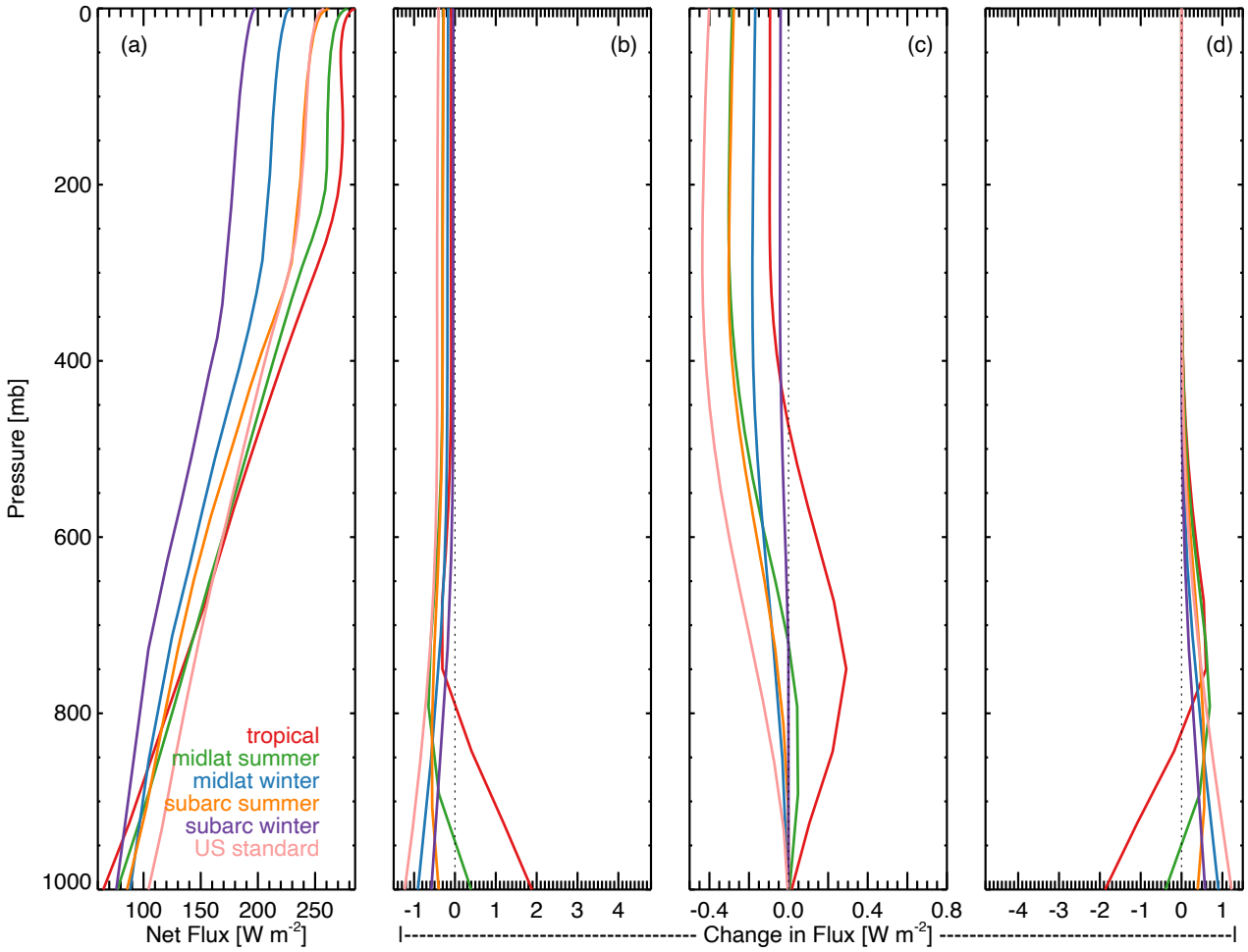

1066 **Fig. 19**. Same as Fig. 18, but differences in (b) through (d) are for calculations that use
1067 MT_CKD_4.2_closure and those that use MT_CKD_4.1.1.
1068

similarly low PWVs. For higher PWV cases, the decreased overall absorption, driven by the decrease in the optical depth of the dominant self continuum, results in a decrease in surface downwelling flux. For upwelling flux at TOA, all cases shown in Fig. 19 show a decrease due to the continuum changes. Even for moist cases in which the magnitude of the increase in foreign continuum optical depth is less than the decrease in the self continuum, the change in foreign continuum results in an upwelling flux difference of larger magnitude since foreign continuum emission occurs higher in the atmosphere, i.e. at temperatures that differ more with respect to the surface temperature than the self continuum emission temperature. Crucially, the impact on fluxes may be very different when the aerosol properties (*e.g.* loading) differ greatly from the aerosols at the location analyzed in this study since the presumed contribution of aerosols is included in the foreign continuum in these calculations.

Fig. 20 shows the difference in longwave heating rates due to modifications in MT_CKD_4.2. The largest changes occur in moist atmospheres, with the heating rates increasing (less cooling) by ~5% in the lower layers of the atmospheres. Fig. S1 presents analogous results for MT_CKD_4.2_closure.

6.2 Top of the atmosphere brightness temperature

Fig. 21 shows the change in the brightness temperature at the top of the atmosphere between LBLRTM calculations that use MT_CKD_4.2 and those that use MT_CKD_4.1.1. These differences increase with the PWV of the atmospheric profile, with maximum of ~+0.3 K for the tropical atmosphere, and do not show a great deal of spectral variability throughout the infrared window. This suggests that use of the new continuum version will lead to a non-trivial change in surface temperatures retrieved using satellite radiances in the infrared window. Fig. S2 provides analogous results for MT_CKD_4.2_closure. For all but the moistest of the profiles shown, the change in brightness temperature is negative due to the additional absorption provided by the aerosol assumed to be included in the foreign continuum.

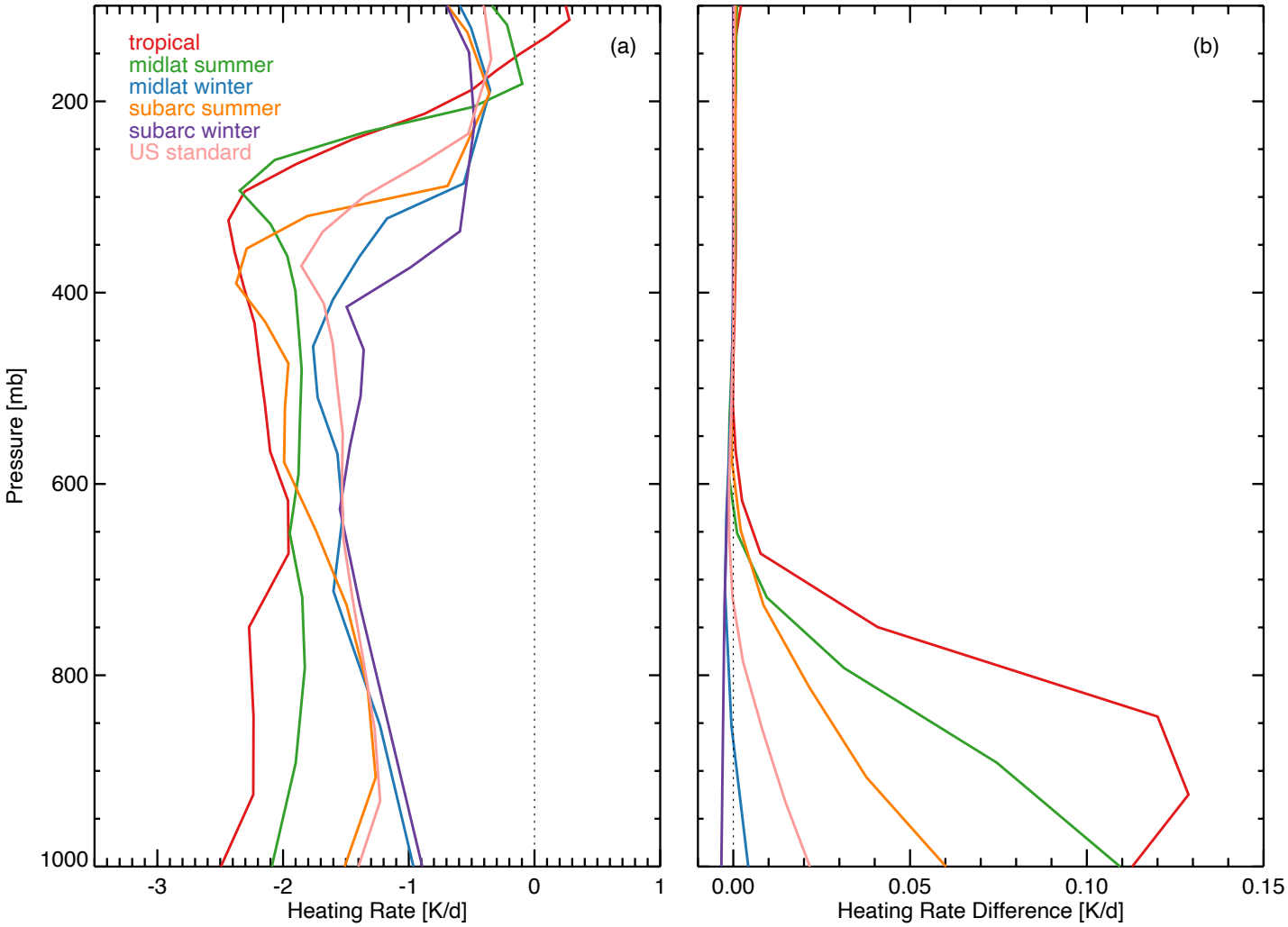

1097 **Fig. 20.** For six standard atmospheres: (a) longwave heating rates from LBLRTM calculations using
1098 MT_CKD_4.1.1 and (b) difference in heating rates between calculations that use MT_CKD_4.2 and
1099 calculations that use MT_CKD_4.1.1.
1100

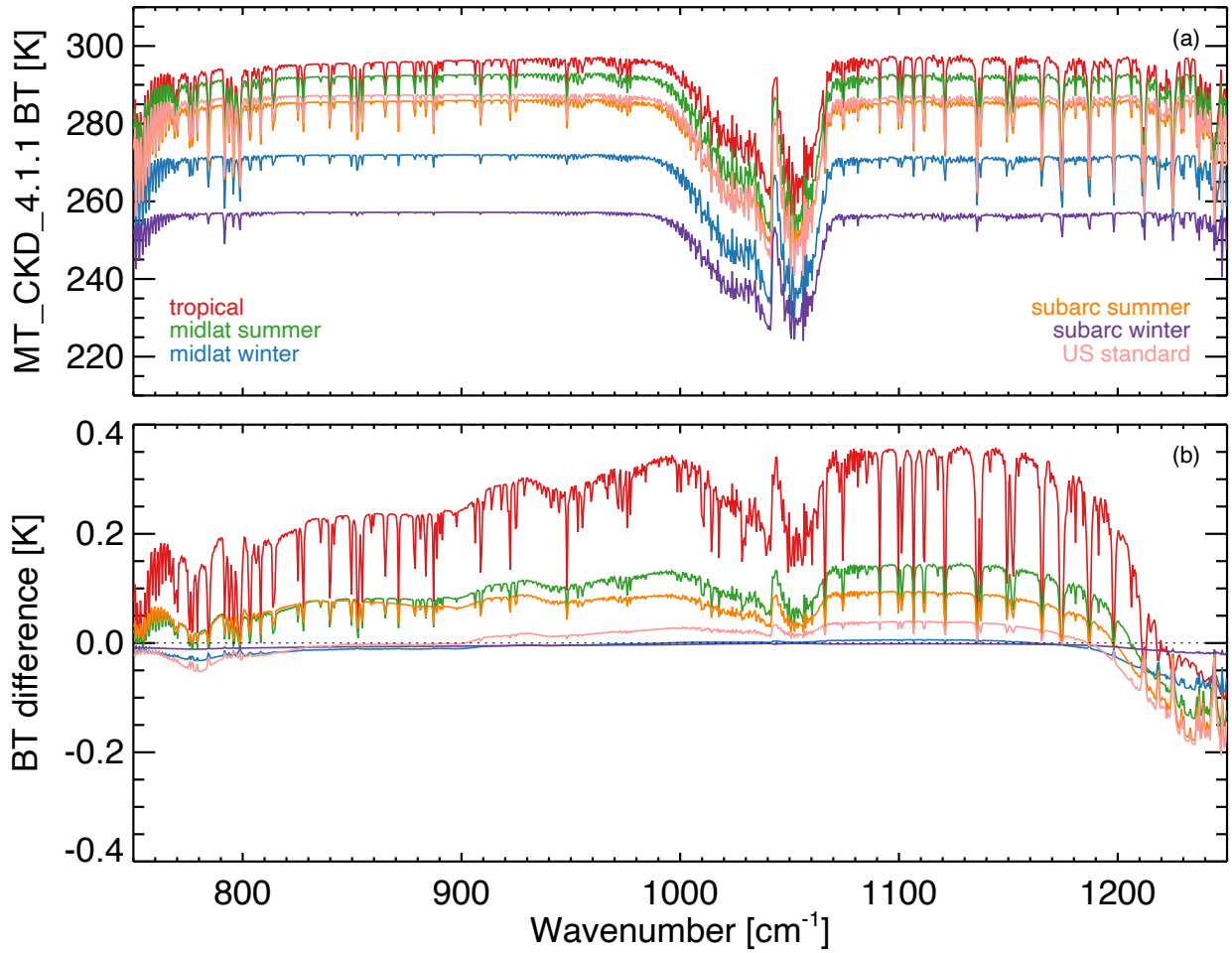

Fig. 21. For six standard atmospheres: (a) brightness temperatures calculated with LBLRTM with MT_CKD_4.1.1 and (b) brightness temperature differences between calculations that use MT_CKD_4.2 and calculations that use MT_CKD_4.1.1.

5.3 Climate considerations

Since only a small fraction of the radiative forcing due to carbon dioxide and methane occurs in the infrared window, the change in the water vapor continuum derived in this work will result in an insignificant change in these forcings. Therefore, no relevant results are shown here.

We assess the impact of the new continuum and resulting opacity change in the infrared window on climate feedbacks with radiative calculations for idealized atmospheric profiles (see, e.g. Koll and Cronin, 2018) using a range of surface temperatures from 240-340K (in 5K increments). Atmospheric temperatures follow a moist adiabat until reaching 220K (defined as the tropopause); temperatures above the tropopause are fixed at 220K. Relative humidity in the troposphere is 75%

and carbon dioxide and ozone concentrations are based on the U.S. Standard atmosphere (ozone concentrations are zero above the tropopause and rescaled in the troposphere to ensure the same total column amount at all surface temperatures). The change in flux between consecutive surface temperatures is interpreted as the climate feedback. Fig. 22 shows this feedback as determined with the existing water vapor continuum (v4.1.1, dashed curves) and with the newly derived continuum (v4.2, solid curves). Differences are shown in the lower panels. Changes to the continuum, and the resulting decrease in atmospheric opacity in the infrared window, induce an increase in climate feedback of ~5% at current surface temperature (~290K), rising to greater than 10% for a surface temperature of ~300K.

The colored curves in Fig. 22 show the contributions of key spectral regions to the total climate feedback. (For this figure, we have slightly expanded the spectral region defined as the window to include the entire region in which the continuum has been modified in this study.) At current Earth temperatures, the infrared window (green) is the spectral region with by far the largest climate feedback. Secondary contributions to the total climate feedback are also provided by infrared water vapor absorption bands, the CO_2 ν_2 band at 15 μm (600-750 cm^{-1}), and the main infrared ozone band at 9.6 μm (1000-1070 cm^{-1}). The climate feedback in the infrared window region decreases with surface temperature due to the increase in atmospheric opacity in moister atmospheres. This opacity increase is rapid due to the dominant role of the water vapor self continuum in the window region and its quadratic dependence on water vapor concentration. The decrease in the climate feedback in the infrared window for higher surface temperatures is partially compensated for by increases in the climate feedback in water vapor absorption bands and the CO_2 band, which has the largest contribution for surface temperatures larger than ~307K.

Fig. 22 shows the significant increase in climate feedback in the infrared window due to the continuum changes derived in this study. The reduced opacity in the revised water vapor continuum results in the climate feedback in the infrared window becoming negative at a temperature 3K greater than before this revision. Our calculations do not extend to sufficiently high temperatures for the climate feedback for the complete longwave region (black curve) to become negative (i.e. runaway greenhouse), but Fig. 22 suggests that the revised continuum implies that runaway greenhouse conditions will occur on Earth at a slightly higher temperature

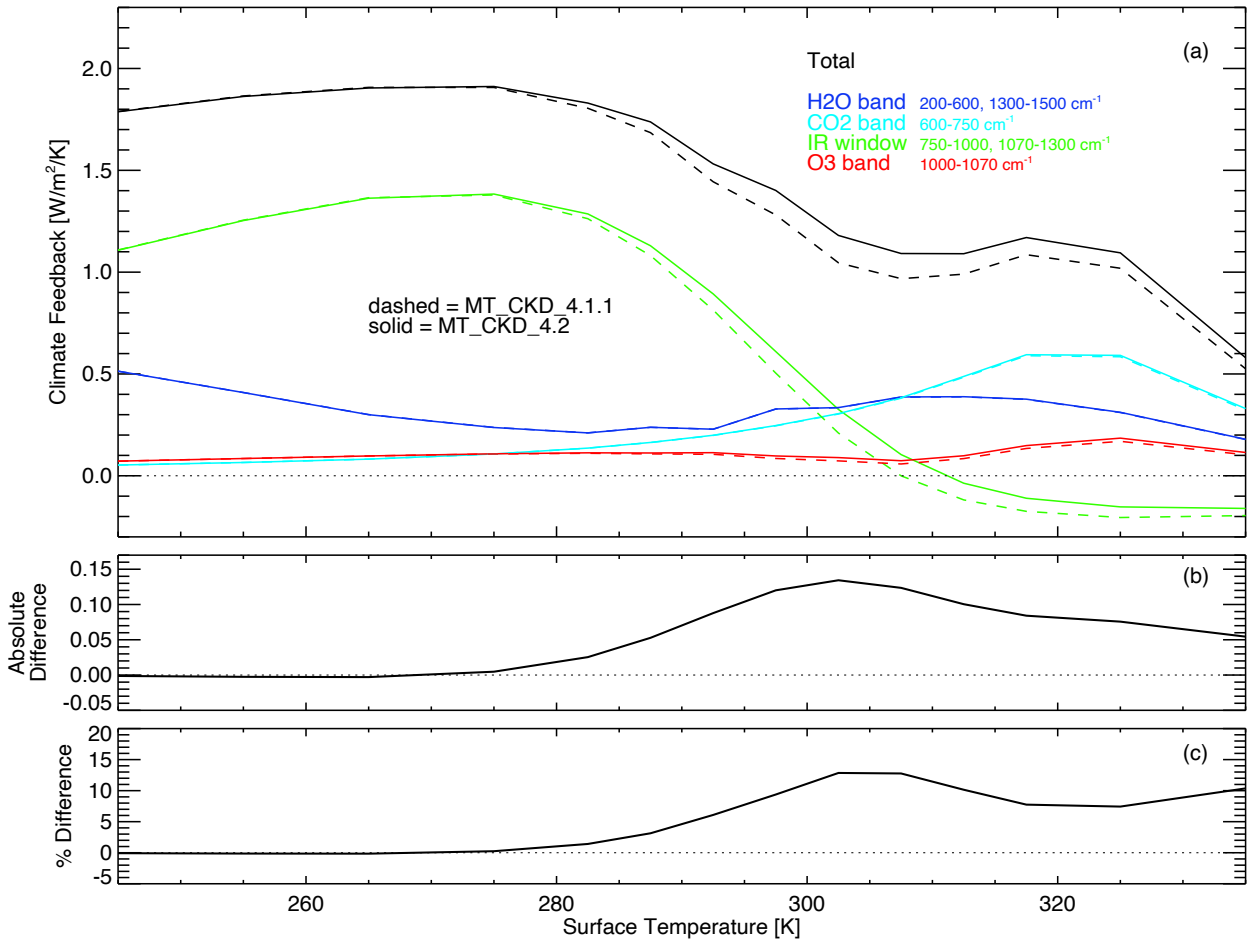

1146 **Fig 22.** As a function of surface temperature in moist adiabat profiles (as described in text), (a) climate
1147 feedback for full longwave region (black), water vapor absorption bands (blue), CO_2 ν_2 band (cyan),
1148 infrared window (green), and ozone band (red). Solid curves use revised continuum (MT_CKD_4.2) in the
1149 calculations while dashed curves use previous continuum (MT_CKD_4.1.1); (b) for full longwave, climate
1150 feedback differences between calculations using MT_CKD_4.2 and MT_CKD_4.1.1; and (c) percentage
1151 differences in climate feedback between calculations using MT_CKD_4.2 and MT_CKD_4.1.1. Climate
1152 feedback is defined as the change in TOA flux per unit change in surface temperature.
1153

than had been previously thought. (Analogous results to those presented in Fig. 22 can be seen in Fig. S3 for MT_CKD_4.2_closure.)

Fig. 23 shows spectrally-resolved climate feedbacks computed with MT_CKD_4.2 (panel b) and the difference with respect to MT_CKD_4.1.1 (panel c); analogous results for MT_CKD_4.2_closure are shown in Fig. S4. Since the changes to the continua decrease absorption due to the self continuum, which is the dominant source of opacity in this region, with the new continuum the climate feedback is increased throughout the vast majority of the infrared window region. The exception is in the region 1200-1300 cm^{-1} for low surface temperatures (i.e. lower PWV values) where, under these conditions, the increased absorption due to the revised foreign continuum can outweigh the impact of the reduced self continuum, leading to a decrease in opacity and a slight increase in climate feedback. Fig. 23c indicates that the change in climate feedback varies spectrally and with surface temperature, a result of the varying spectral behavior of the continuum changes and atmospheric opacity for the different surface temperatures. Additional discussion about the climate feedback results in Figs. 22 and 23 is provided in the supplementary material.

Changes resulting from the new continuum formulation to the surface net radiative flux (defined positive upwards), key to processes such as evaporation, are shown in Fig. 24 as a function of surface temperature for these moist adiabat calculations; spectral results are shown in Fig. S5. Analogous results for MT_CKD_4.2_closure are shown in Fig. S6 and Fig. S7, respectively. The results in Fig. 24 reflect a balance between the increase in upwelling surface flux with increasing surface temperature and an increase in downwelling surface flux due to the increased atmospheric temperature and water vapor loadings associated with the increased surface temperature. At low surface temperature, the low water vapor amounts lead to the former term being larger, so the "surface climate feedback" shown is positive. When the surface temperature is larger than 270K, the impact of the increase in atmospheric opacity associated with a greater surface temperature becomes increasing large, leading to a negative surface climate feedback. The magnitude of this feedback, dominated by the infrared window region, continues to increase with surface temperature until ~300K. At higher temperatures, the most opaque part of this region (~800 cm^{-1}) has become sufficiently opaque so that its surface net flux is small and, therefore, the change in

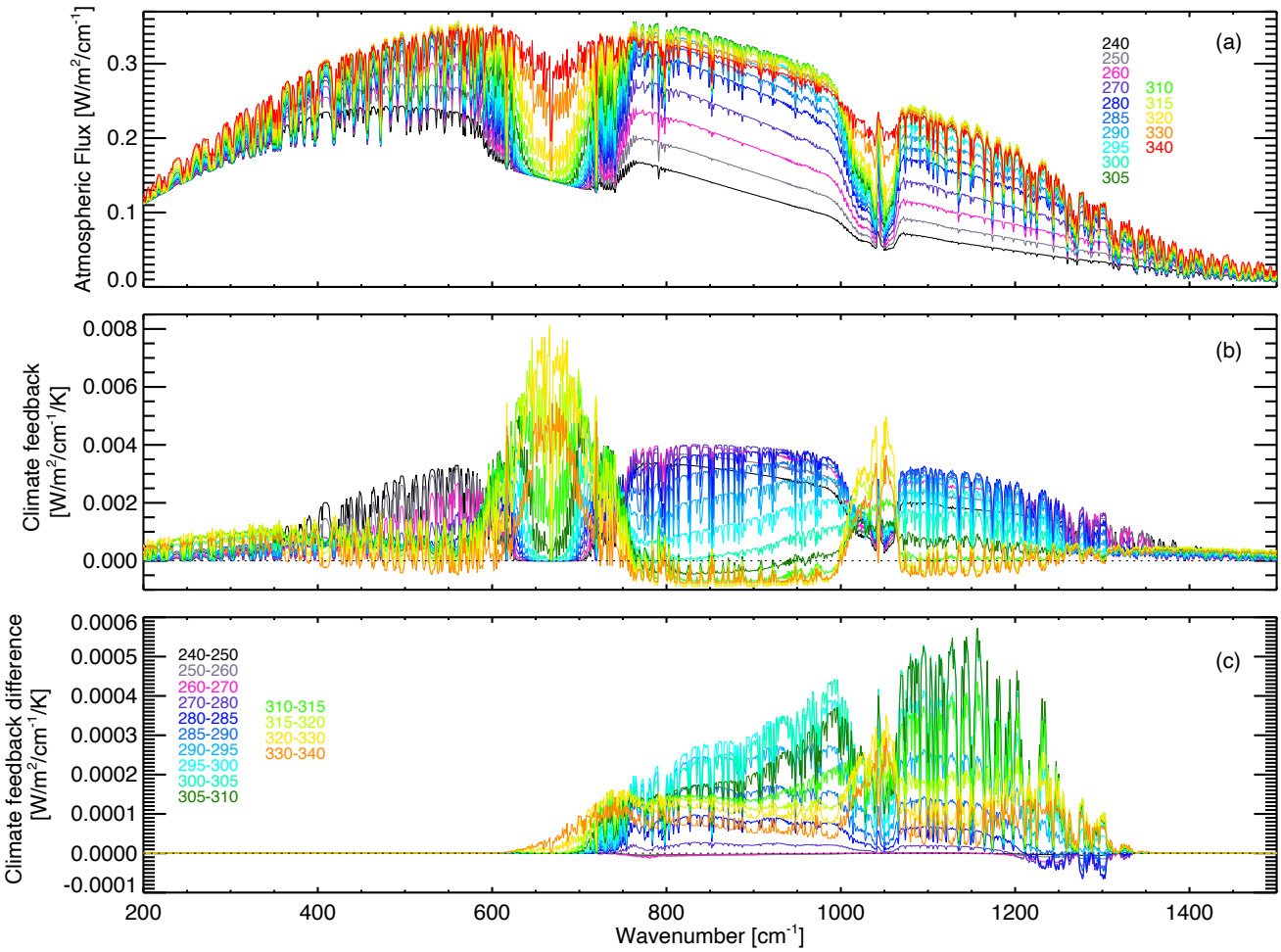

1185 **Fig 23.** For various surface temperatures (colored curves) in moist adiabat profiles (as described in text):
1186 (a) TOA longwave flux calculated using MT_CKD_4.2; (b) spectral behavior of climate feedback
1187 calculated for the temperature ranges denoted on panel (c); and (c) spectral climate feedback differences
1188 between calculations using MT_CKD_4.2 and MT_CKD_4.1.1.

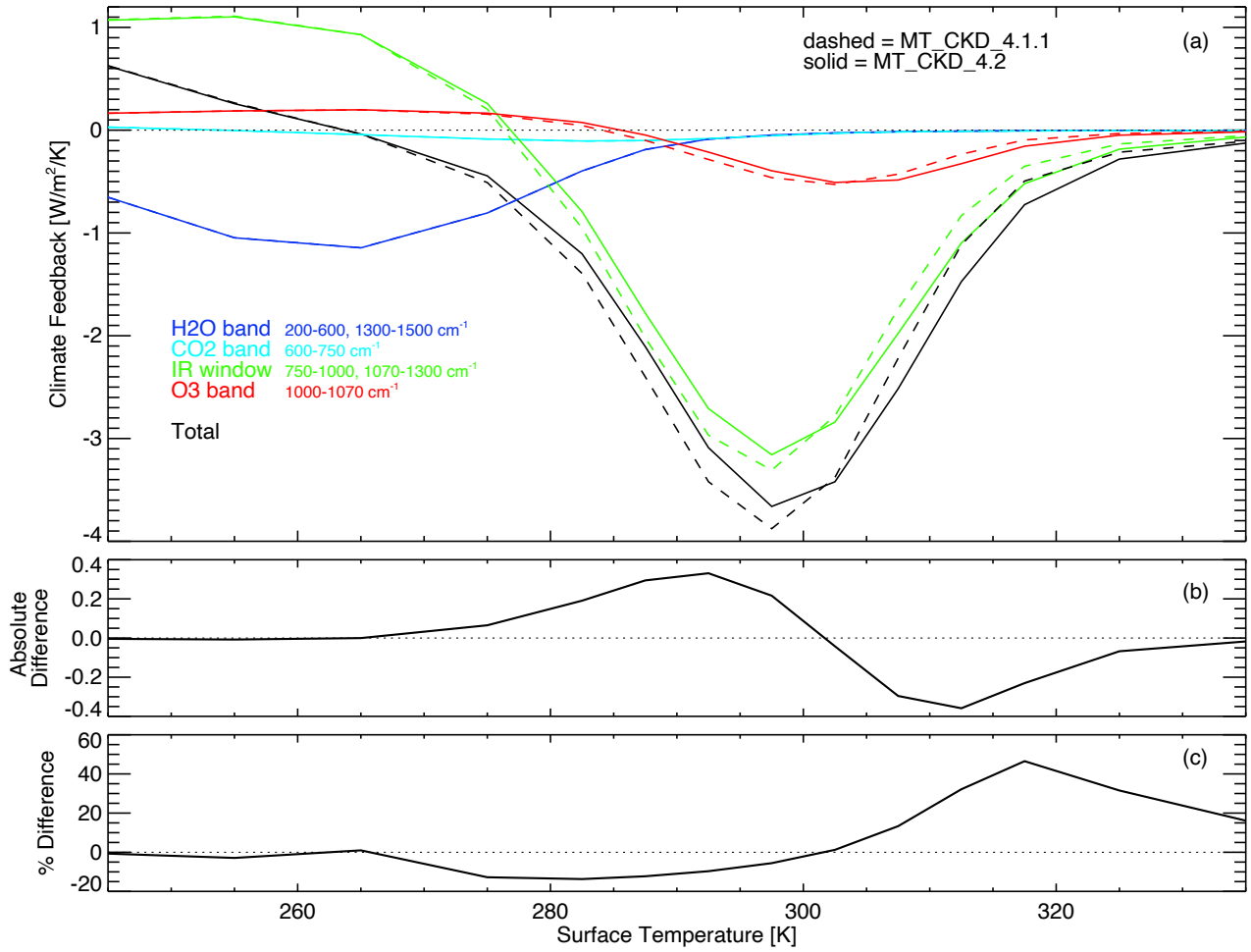

Fig 24. Similar to Fig. 22 but for the surface instead of TOA. Surface climate feedback is defined as the change in surface net flux (defined as positive upward) per unit change in surface temperature.

surface net flux values resulting from a change in surface temperature decreases. These spectral regions stop contributing appreciably to the surface climate feedback, and the overall magnitude starts to decrease. This trend continues as the surface temperature increases until the surface net flux approaches zero, as does the surface climate feedback.

The impact of the changes to the infrared window continuum is to decrease the magnitude of the surface climate feedback for lower surface temperatures, where the trend in surface climate feedback is due to the increase in surface downwelling flux due to the increased atmospheric opacity – the decrease in the self continuum slows down this trend. Conversely, for higher temperatures, the decrease in self continuum opacity decelerates the trend of the surface net flux approaching zero, thereby leading to an increase in the magnitude of the surface climate forcing.

For completeness, the Supplemental Materials includes analogous figures (both for MT_CKD_4.2 and 4.2_closure) for the atmospheric net flux (TOA minus surface net flux) for the moist adiabat calculations, change in atmospheric net flux due to the change in surface temperature ("atmospheric climate feedback"), and changes in this feedback due to the revised water vapor continuum in the infrared window (Figs. S8-S11).

7. Conclusion and discussion

This study provides a new determination of the strength of water vapor continuum absorption in the infrared atmospheric window, which, despite its importance to climate, has not been the subject of many observational studies in the last two decades. Our results are consistent with several recent analyses that indicate that the self continuum, the dominant source of atmospheric absorption in this spectral region, is too strong in MT_CKD_4.1.1. In general, the weaker self continuum derived here results in an overall increase in atmospheric transparency in the window in MT_CKD_4.2 compared to MT_CKD_4.1.1. However, the transparency in atmospheres with low amounts of water vapor, which is high, may slightly decrease due to the increase in foreign continuum absorption derived in this study. These continuum changes lead to a significant decrease in downwelling longwave flux at the surface for moist atmospheres as well as a modest increase in OLR. The increased fraction of surface-leaving radiation that escapes to space leads to a notable increase (~5-10%) in the clear-sky climate feedback.

The diversity of the continuum values derived in previous studies is striking, and the high uncertainty of some of the continuum values we have derived means that our study cannot resolve all remaining uncertainties of significance to Earth's radiative budget and climate. This is especially the case for the foreign continuum and the temperature dependence of the self continuum, but also for the self continuum in certain spectral regions (e.g. 1150-1200 cm^{-1}). This reality points to the need for further accurate laboratory studies of the water vapor continuum in the atmospheric window. Within the last year, an important step in this direction has occurred. Motivated by a presentation of preliminary results from this study (Mlawer et al., 2022), the Campargue group at the University of Grenoble Alpes undertook a measurement of the self continuum at ~1185 cm^{-1} using the accurate technique of optical feedback cavity ring down

spectroscopy. The results of this study (Fournier et al., 2023; F23) are consistent with our result that there is a need for a significant reduction in the strength of the MT_CKD_4.1.1 self continuum in this region, although the decrease derived in our study is greater than in F23. The two results agree within the uncertainties associated with our determination of the self continuum in this region. Measurements of the self continuum were performed in F23 over a limited range of temperatures (296-308 K), which resulted in the determination that the temperature dependence is much weaker than the value we have implemented in MT_CKD_4.2. Given that our study determined that the self continuum temperature dependence could assume a wide range of values while still allowing radiative closure with AERI measurements, this is not surprising. There is a clear need for additional accurate laboratory studies of the self continuum across the full atmospheric window, as well as its temperature dependence and the strength of foreign continuum absorption.

The foreign continuum analysis in this study also demonstrates the need for further laboratory studies of this source of atmospheric absorption. In this study, we posit that our derivation of foreign continuum absorption includes a contribution from aerosols and determine the spectrally dependent fraction of the absorption due to the foreign continuum vs. aerosols through a highly speculative approach. Despite the resulting substantial uncertainty inherent our methodology, our results point out the possibly important role that aerosol absorption may play in the longwave radiative budget, which we hope will prompt further study.

Appendix 1

The method to estimate the "adjusted" self continuum values shown in Fig. 4d for three previous field studies is described here. Using the SGP dataset described in Section 3, we retrieved self continuum values (see section 4.2 for the description of the methodology) using the MT_CKD_4.1.1+BL foreign continuum. For our reconsideration of the Turner et al. (2004) study, we used the entire dataset to estimate the change in derived self continuum values due to the modified foreign continuum, while for the tropical analyses upon which CKD_2.1 was based (Westwater et al., 1995; Han et al., 1997) we used only the most moist cases in the SGP dataset. These revised self continuum values are shown in Fig. 4d as MT_CKD_1.0_adj and CKD_2.1_adj, respectively. Also shown in this figure are the self continuum values derived in a field study by Taylor et al. (2003), which assumed the CKD_2.4 foreign continuum, and corresponding self continuum values that are estimated as the values that would have been obtained had the larger MT_CKD_4.1.1+BL foreign continuum values been assumed instead (denoted as "Taylor_adj").

Appendix 2

Based on a) the foreign continuum value at 980 cm^{-1} from a revised line shape fit (similar to the one used to derive MT_CKD_1.0 as described in Mlawer et al., 2012) applied to the foreign continuum coefficients in MT_CKD_4.1.1 from 500-800 cm^{-1} and b) the value of the foreign continuum at 980 cm^{-1} in MT_CKD_4.2_closure, we estimate that the actual foreign continuum is a little more than half of the retrieved foreign continuum at 980 cm^{-1}, and assume that aerosols are responsible for the remaining fraction. This split between foreign continuum and aerosol is weighted more to the foreign continuum than is implied by Fig. 15, but is within the uncertainty of the aerosol optical depth estimates in panel b of that figure. The first step in the procedure to account for the estimated impact of aerosols on the derived spectral foreign continuum coefficients is to compute the spectral fraction of the derived continuum due to aerosol optical depths. To do this, the spectral dependence of the aerosol optical depth is assumed to be given by a derived Angstrom exponent of -0.647 while the combined foreign and aerosol optical depth is given by MT_CKD_4.2_closure. Using this ratio, the estimated aerosol contribution is removed from the derived foreign continuum coefficients, yielding an estimate of the actual foreign continuum coefficients (i.e. with aerosol removed). It is important to note that since no coefficients were derived from 990-1070 cm^{-1}, this gap remains in these estimated pure continuum coefficients.

These coefficients are then used as constraints in a new fit of the same line shape formalism that was used to derive MT_CKD_1.0. The new fit is aimed at providing values for the foreign continuum in the gap as well as in neighboring spectral regions that are impacted greatly by aerosols (given our assumption) and, therefore, the derived foreign continuum coefficients in those regions cannot be considered very definitive (e.g. 1080-1150 cm^{-1}). The main priorities in the fitting effort are to match the following properties of the constraining foreign continuum coefficients: a) the overall slope of the coefficients from 800-980 cm-1 and b) the coefficient values in spectral regions closest to the gap in which the actual foreign continuum value are thought to be responsible for more than 60% of the AERI-derived foreign continuum coefficients (960-980 $cm^{-1}$and 1220-1230 cm^{-1}). The continuum coefficients resulting from this fit are the final foreign continuum coefficients in the targeted spectral region; in neighboring spectral regions the coefficients from the fit are smoothly merged with the constraining coefficients (i.e. AERI-derived), resulting in the final foreign water vapor coefficients from this AERI analysis (780 - 1250 cm^{-1}). In spectral regions just outside of this range, these coefficients are transitioned into the existing MT_CKD_4.1.1 foreign continuum coefficients in spectral regions (< 600 cm^{-1}, > 1400 cm^{-1}) in which the coefficients have been determined in previous observation-based analyses.

Acknowledgements

The primary support for this project at AER was provided by Atmospheric Systems Research (ASR) program of the U.S. Department of Energy under contract number DE-SC0018296. Additional support for the analysis and dissemination of the results were provided by the NASA U.S. Participating Investigator program under contract number 80NSSC21K1038 and the National Science Foundation under award number 1916927. Support at NOAA was provided by ASR contract 89243019SSC000034. We thank the DOE Atmospheric Radiation Measurement program for the observations upon which this study is based and for their excellent data archive. AER authors are indebted to Karen Cady-Pereira, Matt Alvarado, and Rick Pernak for helpful advice. Part of this research was carried out at the Jet Propulsion Laboratory, California Institute of Technology, under a contract with NASA (80NM0018D0004).

Open Research

Data availability.

All SGP and MAO observations used in this study were obtained from https://www.arm.gov/data. The LBLRTM radiative transfer model can be accessed from https://github.com/AER-RC/LBLRTM and the MT_CKD continuum model from https://github.com/AER-RC/MT_CKD. The LBLRTM input files derived from ARM observations that are used in this study can be found in a tar file that can be downloaded from Zenodo (https://zenodo.org/records/10909710). The Zenodo file also contains all aerosol-related data used in our analysis, as well as the code (Python) used to retrieve the self and foreign continuum coefficients and the self continuum temperature exponents from the measurement-calculation residuals. Additional supporting information is also available in this tar file. All analysis and plots were executed using Python 3.9.7 and IDL Version 8.4.

Supporting information

Additional text and data can be found in *mlawer_ir-window_supporting_information.pdf*.

References

Anderson, G. P., Clough, S. A., Kneizys, F. X., Chetwynd, J. H., & Shettle, E. P. (1986). AFGL atmospheric constituent profiles (0.120 km). (No. AFGL-TR-86-0110). Air Force Geophysics Lab, Hanscom, AFB, MA. Retrieved from http://www.dtic.mil/docs/citations/ADA175173

Baranov, Y.I., Lafferty W.J., Ma Q., & Tipping R.H. (2008). Water vapor continuum absorption in the 800-1250 cm^{-1} spectral region at temperatures from 311 to 363K. *J Quant Spectrosc Radiat Transf*., 109, 2291–2302.

Baranov, Y.I & Lafferty W.J. (2012). The water vapor self- and water–nitrogen continuum absorption in the 1000 and 2500 cm^{-1} atmospheric windows. *Philos Trans R Soc A*, 370, 2578–2589.

Burch, D.E. (1982). Continuum absorption by H2O. *AFGL-TR-81-0300*. 46 pp. Air Force Geophys. Lab., Hanscom AFB, MA. http://dx.doi. org/10.1117/12.931899

Burch, D.E. & Alt, R.L. (1984). Continuum absorption by H_2O in the 700-1200 cm^{-1} and 2400-2800 cm^{-1} windows. *AFGL-TR-84-0128*, 32 pp., Air Force Geophys. Lab., Hanscom AFB, MA.

Cadeddu, M. P., Liljegren, J. C., & Turner, D. D. (2013). The Atmospheric radiation measurement (ARM) program network of microwave radiometers: instrumentation, data, and retrievals. *Atmos. Meas. Tech.,* 6, 2359–2372. https://doi.org/10.5194/amt-6-2359-2013

Clough, S.A., Kneizys, F.X., & Davies, R.W. (1989). Line shape and the water vapor continuum. *Atmos. Res*., 23, 229. https://doi.org/10.1016/0169-8095(89)90020-3

Clough, S.A., Shephard, M.W., Mlawer, E.J., Delamere, J.S., Iacono, M.J., Cady-Pereira, K., Boukabara, S., & Brown, P.D (2005). Atmospheric radiative transfer modeling: A summary of the AER codes. *J. Quant. Spectrosc. Radiative Trans*., 91, 233-244.

Cormier J.G., Hodges J.T., & Drummond, J.R. (2005). Infrared water vapour continuum absorption at atmospheric temperatures. *J. Chem. Phys.,* 122:114309. http: //doi.org/10.1063/1.1862623

Cormier, J.G, Ciurylo, R., & Drummond, J.R. (2002). Cavity ringdown spectroscopy measurements of the infrared water vapor continuum. *J. Chem. Phys*., 116, 1030.

Delamere, J.S., Clough, S.A., Payne, V., Mlawer, E.J., Turner, D.D., & R. Gamache (2010). A far-infrared radiative closure study in the Arctic: Application to water vapor. *J. Geophys. Res*., 115, D17106. doi:10.1029/2009JD012968

Dubovik, O. & King, M.D. (2000). A flexible inversion algorithm for retrieval of aerosol optical properties from Sun and sky radiance measurements. *J. Geophys. Res.*, 105, 20,673-20,696.

Feng, J., Paynter, D., & Menzel, R. (2023). How a stable greenhouse effect on Earth is maintained under global warming. *Journal of Geophysical Research: Atmospheres*, 128, e2022JD038124. https://doi.org/10.1029/2022JD038124

Fournier, Q., Kassi, S., Mondelain, D., Fleurbaey, H., Georges, R., & Campargue, A. (2024), The water vapor self-continuum absorption at 8.45 μm by optical feedback cavity ring down spectroscopy. *J. Quant. Spectr. Rad. Trans.,* 315. http://dx.doi.org/10.2139/ssrn.4607109

Fu, D., Worden, J.R.. Liu, X., Kulawik, S.S., Bowman, K.W. & Natraj, V. (2013). Characterization of ozone profiles derived from Aura TES and OMI radiances. *Atmos. Chem. Phys.*, 13(6), 3445–3462. doi:10.5194/acp-13-3445-2013

Han, Y., Shaw, J.A., Churnside, J.H., Brown, P.D., & Clough, S.A. (1997). Infrared spectral measurements in the tropical Pacific atmosphere. *J. Geophys. Res.*, 102, 4353-4356.

Harries, J., Carli, B., Rizzi, R., Serio, C., Mlynczak, M., Palchetti, L., et al. (2008), The far-infrared Earth, *Rev. Geophys.*,46, RG4004. doi:10.1029/2007RG000233

Jeevanjee, N., Koll, D. D., & Lutsko, N. (2021). "Simpson's law" and the spectral cancellation of climate feedbacks. *Geophysical Research Letters*, 48(14), e2021GL093699. https://doi.org/10.1029/2021gl093699

Koll, D. D., Jeevanjee, N., & Lutsko, N. J. (2023). An analytic model for the clear-sky longwave feedback. *Journal of the Atmospheric Sciences*, 80(8), 1923-1951.

Koll, D. D., & Cronin, T. W. (2018). Earth's outgoing longwave radiation linear due to H_2O greenhouse effect. *Proceedings of the National Academy of Sciences*, 115(41), 10293–10298. https://doi.org/10.1073/pnas.1809868115

Knuteson, R.O, Revercomb. H.E., Best, F.A., Ciganovich, N.C., Dedecker, R.G., Dirkx, T.P., et al. (2004a) Atmospheric Emitted Radiance Interferometer. Part I: Instrument design. *J. Atmos. Oceanic Technol.*, **21**, 1763-1776. https://doi.org/10.1175/JTECH-1662.1

Knuteson, R.O, Revercomb. H.E., Best, F.A., Ciganovich, N.C., Dedecker, R.G., Dirkx, T.P., et al. (2004b): Atmospheric Emitted Radiance Interferometer. Part II: Instrument performance. *J. Atmos. Oceanic Technol.*, **21**, 1777-1789. https://doi.org/10.1175/JTECH-1663.1

McKim, B. A., Jeevanjee, N., & Vallis, G. K. (2021). Joint dependence of longwave feedback on surface temperature and relative humidity. *Geophysical Research Letters*, 48(18), e2021GL094074. https://doi.org/10.1029/2021gl094074

Martin S.T., Artaxo, P., Machado, L., Manzi, A.O.,Souza, R.A., Schumacher, C. et al. (2016). The Green Ocean Amazon Experiment (GoAmazon2014/5) Observes Pollution Affecting Gases, Aerosols, Clouds, and Rainfall over the Rain Forest. *Bulletin of the American Meteorological Society*, 98(5), 10.1175/bams-d-15-00221.1

Malm, W. C., Sislerm J. F., Huffmann, D., Eldred, R. A., & Cahill, T. A. (1994). Spatial and seasonal trends in particle concentration and optical extinction in the United States. *J. Geophys. Res.*, 99, 1347–1370. https://doi.org/10.1029/93JD02916

Mlawer, E.J. & Turner, D.D. (2016). Spectral radiation measurements and analysis in the ARM program. *Meteorol Monogr*, 57 14.1-14.17. doi:10.1175/ AMSMONOGRAPHS-D-15-0027.1

Mlawer, E.J., Cady-Pereira, K.E., Mascio, J., & Gordon, I.E. (2023). The inclusion of the MT_CKD water vapor continuum model in the HITRAN molecular spectroscopic database. *J. Quant. Spectr. Rad. Trans.,* 306. https://doi.org/10.1016/j.jqsrt.2023.108645

Mlawer, E.J., Payne, V.H., Moncet. J.-L., Delamere, J.S., Alvarado, M.J., Tobin, D.C (2012). Development and recent evaluation of the MT_CKD model of continuum absorption. *Philos Trans R Soc A*, 370, 2520–56. doi:10.1098/rsta. 2011.0295

Mlawer, E.J., Taubnam, S.J., Brown, P.D., Iacono, M.J., and Clough, S.A. (1997). RRTM, a validated correlated-k model for the longwave. *J. Geophys. Res*., 102, 16663-16682.

Mlawer, E.J., Turner, D.D., Paine, S.N., Palchetti, L., Bianchini, G., Payne, V.H., et al. (2019). Analysis of water vapor absorption in the far-infrared and submillimeter regions using surface radiometric measurements from extremely dry locations. *J Geophys Res Atmos,* 124,8134–60. doi:10.1029/2018JD029508

Otsu, N. (1979). A threshold selection method from gray-level histograms. *IEEE Transactions on Systems, Man, and Cybernetics*. 9 (1): 62–66. doi:10.1109/TSMC.1979.4310076. S2CID 15326934

Randles, C. A., da Silva, A. M., Buchard, V., Colarco, P. R., Darmenov, A., Govindaraju, R., et al. (2017). The MERRA-2 Aerosol Reanalysis, 1980 onward. Part I: System description and data assimilation evaluation. *J. Climate*, 30(17), 6823–6850. https://doi.org/10.1175/JCLI-D-16-0613.1

Revercomb, H.E., Buijs, H., Howell, H.B., LaPorte, D.D., Smith, W.L., and Sromovsky, L.A. (1988). Radiometric calibration of IR Fourier transform spectrometers: Solution to a problem with the high-resolution interferometer sounder. *Appl. Opt.*, 27, 3210-3218.

Revercomb, H.E., Turner, D.D., Tobin, D.C., Knuteson, R.O., Feltz, W.F., Barnard, J. et al. (2003) The Atmospheric Radiation Measurement Program's water vapor intensive observation periods: overview, initial accomplishments, and future challenges. *Bull. Amer. Meteor. Soc.*, **84**, 217-236

Seeley, J. T., & Jeevanjee, N. (2021). H_2O windows and CO_2 radiator fins: A clear-sky explanation for the peak in equilibrium climate sensitivity. *Geophysical Research Letters*, 48(4), e2020GL089609. https://doi.org/10.1029/2020gl089609

Shephard, M.W., Goldman, A., Clough, S.A., Mlawer, E.J. (2003) Spectroscopic improvements providing evidence of formic acid in AERI-LBLRTM validation spectra. *J. Quant. Spectr. Rad. Trans.,* 82, 383-390. https://doi.org/10.1016/S0022-4073(03)00164-X.

Simpson, G. (1928). Some studies in terrestrial radiation. *Memoirs of the Royal Meteorological Society*, 2(16), 69–95.

Sisterson, D.L, Peppler, R.A., Cress, T.S., Lamb, P.J., and Turner, D.D. (2016). The ARM Southern Great Plains (SGP) site. *The Atmospheric Radiation Measurement Program: The First 20 Years*, *Meteor. Monograph. Amer. Meteor. Soc.,* 57, 6.1-6.14, DOI:10.1175/AMSMONOGRAPHS-D-16-0004.1

Slingo, A. and Webb, M.J. (1997), The spectral signature of global warming. *Quarterly Journal of the Royal Meteorological Society*, 123(538), 293–307. https://doi.org/10.1002/qj.49712353803

Taylor, J.P., Newman, S.M., Hewison, T.J., & McGrath, A. (2003). Water vapour line and continuum absorption in the thermal infrared – reconciling models and observations *Quart. J. Roy. Meteorol. Soc.,* 129 (2003),2949-2969. 10.1256/qj.03.08

Turner, DD., 2003: Microphysical properties of single and mixed-phase Arctic clouds derived from ground-based AERI observations. Ph.D. Dissertation, University of Wisconsin-Madison, 167 pp. Available from https://search.library.wisc.edu/catalog/999951770902121

Turner, D.D. (2005). Arctic mixed-phase cloud properties from AERI-lidar observations: Algorithm and results from SHEBA. *J. Appl. Meteor.,* 44, 427-444.

Turner, D.D. (2008). Ground-based retrievals of optical depth, effective radius, and composition of airborne mineral dust above the Sahel. *J. Geophys. Res.,* 113, E00E03, doi:10.1029/2008JD010054

Turner, D.D., Tobin, D.C., Clough, S.A., Brown, P.D., Ellingson, R.G., Mlawer, E.J. et al. (2004). The QME AERI LBLRTM: A closure experiment for downwelling high spectral resolution infrared radiance. *J. Atmos. Sci*., 61, 2657-2675.

Turner, D.D. & Blumberg, W.G. (2019). Improvements to the AERIoe thermodynamic profile retrieval algorithm. *IEEE Selected Topics Appl. Earth Obs. Remote Sens.*, 12, 1339-1354, doi:10.1109/JSTARS.2018.2874968

Turner, D.D. & Ellingson, R.G. Eds., 2016: *The Atmospheric Radiation Measurement (ARM) Program: The First 20 Years*. Meteor. Monograph, **57**, American Meteorological Society

Turner, D. D. & Löhnert, U. (2014). Information content and uncertainties in thermodynamic profiles and liquid cloud properties retrieved from the ground-based Atmospheric Emitted Radiance Interferometer (AERI). *J. Appl. Meteor. Climatol.*, **53**, 752-771, doi:10.1175/JAMC-D-13-0126.1

Turner, D.D. & Löhnert, U. (2021). Ground-based temperature and humidity profiling: Combining active and passive remote sensors. *Atmos. Meas. Technol*., 14, 3033-3048, doi:10.5194/amt-14-3033-2021

Turner, D.D. & Mlawer, E.J. (2010). Radiative heating in underexplored bands campaigns (RHUBC). *Bull. Amer. Meteor. Soc*., *91*, 911-923. doi:10.1175/2010BAMS2904.1.

Turner, D.D., Lesht, B.M. Clough, S.A., Liljegren, J.C., Revercomb, H.E., & Tobin, D.C. (2003). Dry bias and variability in Vaisala radiosondes: The ARM experience. *J. Atmos. Oceanic Technol.*, **20**, 117-132.

Turner, D.D., Mlawer, E.J. & H.E. Revercomb (2016). Water vapor observations in the ARM program. *The Atmospheric Radiation Measurement Program: The First 20 Years*. Meteor. Monograph, 57, Amer. Meteor. Soc., 13.1-13.18, doi:10.1175/AMSMONOGRAPHS-D-15-0025.1

Wang, J., Cole, H.L., Carlson, D.J., Miller, E.R. & Beirle, K. (2002). Corrections of humidity measurement errors from the Vaisala RS80 radiosonde – application to TOGA COARE data. *J. Atmos. Oceanic Technol.*, **19**, 981-1002

Wargan, K., Labow, G., Frith, S., Pawson, S., Livesey, N., & Partyka, G. (2017). Evaluation of the ozone fields in NASA's MERRA-2 reanalysis. *Journal of Climate*, 30, 2961–2988. https://doi.org/10.1175/JCLI-D-16-0699.1

Westwater, E., Churnside, J., Shaw, J., Snider, J.B., Gage, K.S., Han, Y., Ecklund, W. et al. (1995). Ground-based remote sensor observations during the PROBE experiment in the tropical western Pacific. 882 - 886 vol.2. 10.1109/IGARSS.1995.521086

Worden, H.M., Logan, J.A., Worden, J.R., Beer, R., Bowman, K., Clough, S.A. et al. (2007). Comparisons of Tropospheric Emission Spectrometer (TES) ozone profiles to ozonesondes: Methods and initial results, *J. Geophys. Res.,* 112, D03309. doi:10.1029/2006JD007258

A More Transparent Infrared Window

Eli J. Mlawer (mlawer@aer.com)[1]
Jeana Mascio[1]
David D. Turner[2]
Vivienne E. Payne[3]
Connor J. Flynn[4]
Robert Pincus[5]

Affiliations
[1]Atmospheric and Environmental Research, Lexington, Massachusetts
[2]NOAA/Global Systems Laboratory, Boulder, Colorado
[3]Jet Propulsion Laboratory, California Institute of Technology, Pasadena, California
[4]University of Oklahoma School of Meteorology, Norman, Oklahoma
[5]Lamont-Doherty Earth Observatory, Columbia University, Palisades, New York

Key points:

- Analysis of ground-based radiance observations indicates that the infrared window region is more transparent than had been thought
- The derived water vapor self continuum is 10-30% weaker than previously thought, while the foreign continuum is substantially stronger
- The revised H_2O continuum results in a 5-10% increase in climate feedback and a large change to the radiative budget for moist atmospheres

Abstract

The infrared window region (780-1250 cm^{-1}, 12.8 to 8.0 μm) is of great importance to Earth's climate due to its high transparency and thermal energy. We present here a new investigation of the transparency of this spectral region based on observations by interferometers of downwelling surface radiance at two DOE Atmospheric Radiation Measurement program sites. We focus on the dominant source of absorption in this region, the water vapor continuum, and derive updated values of spectral absorption coefficients for both the self and foreign continua. Our results show that the self continuum is too strong in the previous version of Mlawer-Tobin_Clough-Kneizys-Davies (MT_CKD) water vapor continuum model, a result that is consistent with other recent analyses, while the foreign continuum is too weak in MT_CKD. In general, the weaker self continuum derived in this study results in an overall increase in atmospheric transparency in the window, although in atmospheres with low amounts of water vapor the transparency may slightly decrease due to the increase in foreign continuum absorption. These continuum changes lead to a significant decrease in downwelling longwave flux at the surface for moist atmospheres and a modest increase in outgoing longwave radiation. The increased fraction of surface-leaving radiation that escapes to space leads to a notable increase (~5-10%) in climate feedback, implying that climate simulations that use the new infrared window continuum will show somewhat less warming than before. This study also points out the possibly important role that aerosol absorption may play in the longwave radiative budget.

Plain Language Summary

The spectral region in the infrared from 780-1250 cm^{-1} (12.8 to 8.0 μm) is referred to as a window due to its transparency – in this region, thermal radiation emitted by the surface can pass relatively unimpeded through the atmosphere, allowing Earth to cool. The limited amount of atmospheric absorption that does occur in this region is primarily due to water vapor, in particular an absorption mechanism termed the water vapor continuum. The strength of water vapor continuum absorption in the infrared window therefore has important consequences for Earth's climate. This study provides a new evaluation of water vapor continuum absorption in the infrared window from an analysis of spectrally resolved measurements of downwelling surface radiances. Our results indicate that for most atmospheres the strength of water vapor continuum absorption is less than had been previously thought due to reduced absorption related to the interactions of water vapor molecules with other water vapor molecules, i.e. the water vapor self continuum. The derived water vapor continuum changes allow the Earth to cool ~5-10% better than had previously been thought, and climate simulations that use the revised infrared window continuum will show somewhat less warming than before.

1. Introduction

Atmospheric absorption in the infrared window (780-1250 cm^{-1}, 12.8 to 8.0 μm) plays an important role in Earth's radiation budget and climate, a consequence of this spectral region's high thermal energy, relative transparency, and the properties of its most important source of absorption, the water vapor self continuum. The self continuum is a weak absorber under typical atmospheric conditions, but its strength increases quadratically with water vapor abundance so under moist conditions self continuum absorption can result in significant atmospheric opacity. The importance of the infrared window region and the dominance of the water vapor self continuum absorption in this region make it imperative that the properties of this absorber be known with high certainty so that atmospheric applications that depend on window absorption can be regarded with confidence. This study presents the result of a new radiative closure analysis (Mlawer and Turner, 2016; Shepherd et al., 2003) of water vapor continuum absorption in the infrared window.

Longwave radiation that escapes to space (outgoing longwave radiation or OLR) is a critical component of the Earth's radiation budget. Most of the thermal radiation emitted by the Earth's surface is absorbed by the atmosphere, which then emits thermal radiation at its own temperature, which typically is less than the surface temperature. An exception to this general behavior occurs in spectral regions that are relatively transparent in clear skies, in which the warm radiation emitted by the surface is only slightly attenuated and therefore escapes the atmosphere. These spectral regions are called "windows" -- the most important with respect to Earth's thermal radiation is the infrared window. For six reference atmospheres, Table 1 shows the total surface flux emitted by the surface, the surface flux in spectral regions in which the total vertical optical depth is less than 1, and the fraction of this "transparent-region" flux that is in the infrared window. These values indicate that only a limited amount of the surface flux has the potential to escape to space, and a large fraction of that amount is in the infrared window.

As has been shown in recent studies (e.g. Seeley and Jeevanjee, 2021; Jeevanjee et al., 2021; Koll and Cronin, 2018), the infrared window plays a crucial role in climate and climate feedback. These studies show that at typical current surface temperatures the infrared window is the primary spectral region in which the radiation that escapes to space can change as the planet adjusts to an energy imbalance, such as is being currently precipitated by anthropogenic increases in greenhouse

Reference atmosphere	Precipitable water vapor (cm)	Total surface flux (W/m^2)	Surface flux for OD < 1	Fraction of OD < 1 flux in IR window
Tropical	4.1	451.62	155.56	0.98
Midlatitude summer	2.9	420.03	171.19	0.97
US standard	1.4	387.41	199.71	0.85
Subarctic summer	2.1	382.15	158.48	0.96
Midlatitude winter	0.9	309.34	178.37	0.74
Subarctic winter	0.4	247.16	165.62	0.60

Table 1. For six reference atmospheres: total upwelling longwave flux at the surface, precipitable water vapor, upwelling flux in the portion of the longwave that are sufficiently transparent (vertical optical depth < 1) so that a significant fraction of the radiation emitted by the surface reaches the top of the atmosphere, and the fraction of the transparent-region surface flux that is in the IR window region. Surface emissivity is assumed to be unity.

gases. As an illustration of this effect, the change in OLR for a simplistic version of current warming is shown in Fig. 1: a 1 K increase in tropospheric temperatures is applied to a baseline profile, with relative humidity values and the tropospheric column amounts of all other species are left unchanged in the perturbed profile. The results indicate that the change in OLR is primarily in the infrared window.

The infrared window is also critically important with respect to downwelling and net flux at the surface. In opaque spectral regions, the downwelling flux arriving at the surface typically is emitted at a temperature close to the surface temperature, resulting in a small net flux at the surface. As shown in Fig. 2, in the infrared window emitted downwelling radiation that reaches the surface is significantly smaller than the upwelling radiation, leading to a large net flux. The net flux divergence, which drives radiative cooling and heating, is also of unique importance in this window. The quadratic dependence on water vapor abundance of the self continuum optical depths leads to large relative gradients in optical depth in the lower atmosphere, and therefore large radiative flux divergences. Due to this effect, for moist atmospheres around 75% of the longwave cooling rate near the surface occurs in the window (Mlawer et al., 1997).

Section 2 provides background information on water vapor continuum absorption in the infrared window. Section 3 presents information about the radiometric measurements used in this study, the radiative transfer model calculations used to compare with these measurements, and details about how the atmospheric properties used in the calculations were obtained. Section 4 contains details about how the measurement-calculation differences were analyzed and then utilized to derive self and foreign continuum coefficients in the infrared window, as well as a specification of the self continuum temperature dependence. Section 5 compares the derived results to results obtained in previous studies and section 6 discusses the impact of the new window water vapor continuum results on atmospheric applications. Section 7 provides a summary and discussion.

2. The Water Vapor Continuum in the Infrared Window

We provide here background information concerning our understanding of water vapor continuum absorption in the infrared window and its development over the last several decades, including its treatment in the Mlawer-Tobin_Clough-Kneizys-Davies (MT_CKD) water vapor continuum

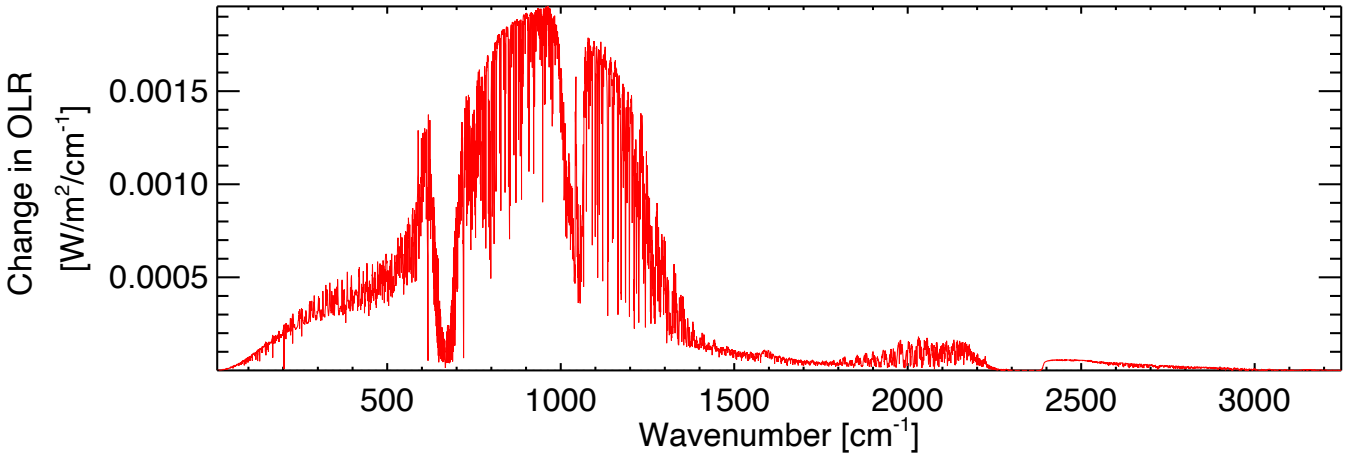

144 **Fig. 1.** Change in OLR due to a 1 K increase in tropospheric temperatures in the mid-latitude summer
145 atmosphere with relative humidity left unchanged.

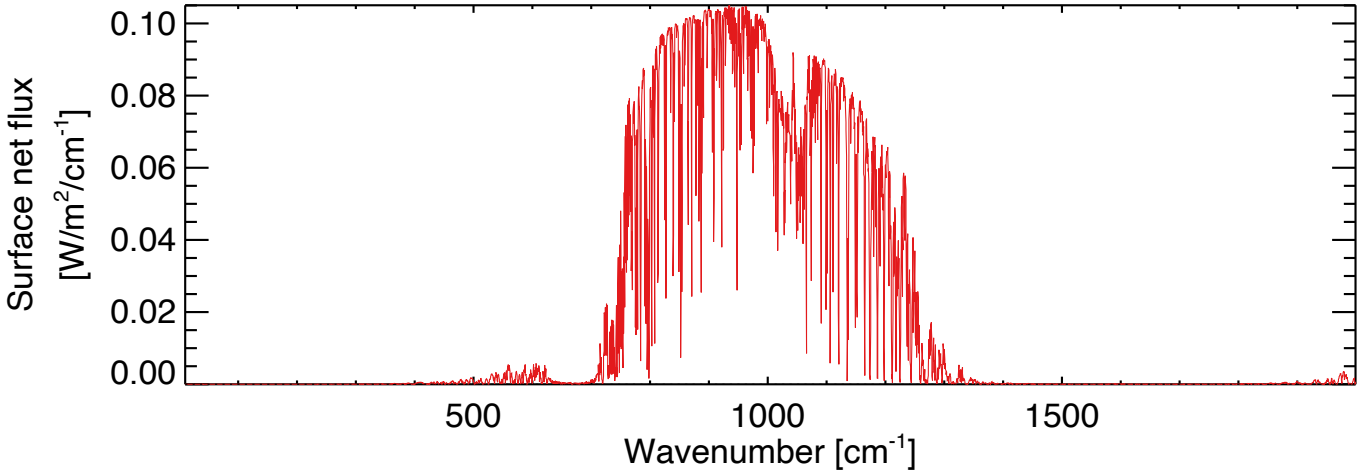

146 **Figure 2.** Magnitude of longwave surface net flux for the mid-latitude summer atmosphere.
147

model (Mlawer et al., 2023; Mlawer et al., 2012), the primary source used in the community to specify water vapor continuum absorption in this spectral region. For reference, self and foreign continuum optical depths from the current version of MT_CKD (v4.1.1) are shown in Fig. 3 for six reference profiles. In recent years, self continuum absorption in the infrared window had been thought to be fairly well known, with the most recent laboratory measurement of the self continuum in this region (Baranov et al., 2008) agreeing well at atmospheric temperatures with the MT_CKD continuum model, which is based on a recent field study (Turner et al., 2004). However, a review of studies of the self continuum absorption in this region over the last several decades shows cracks in this consensus.

The specification of the window self continuum in the original version of the Clough-Kneizys-Davies (CKD) continuum model (see Figs. 3 and 5 of Clough et al., 1989 – Note: the caption of Fig. 3 in Clough et al., 1989, erroneously states that the broadening pressure is 1013 mb, when it actually is 26.7 mb), the predecessor to the MT_CKD model, was based on the laboratory results of Burch (1982). These CKD values can be seen in Fig. 4a and are also shown along with the Burch (1982) measurements in Fig. 4b. Burch and collaborators subsequently significantly revised their experimental values, with the new lower continuum absorption coefficients (also shown in Fig. 4b) ascribed to "minor changes in experimental techniques employed in the recent work" (Burch and Alt, 1984). These improved experimental values were used as the basis for an updated

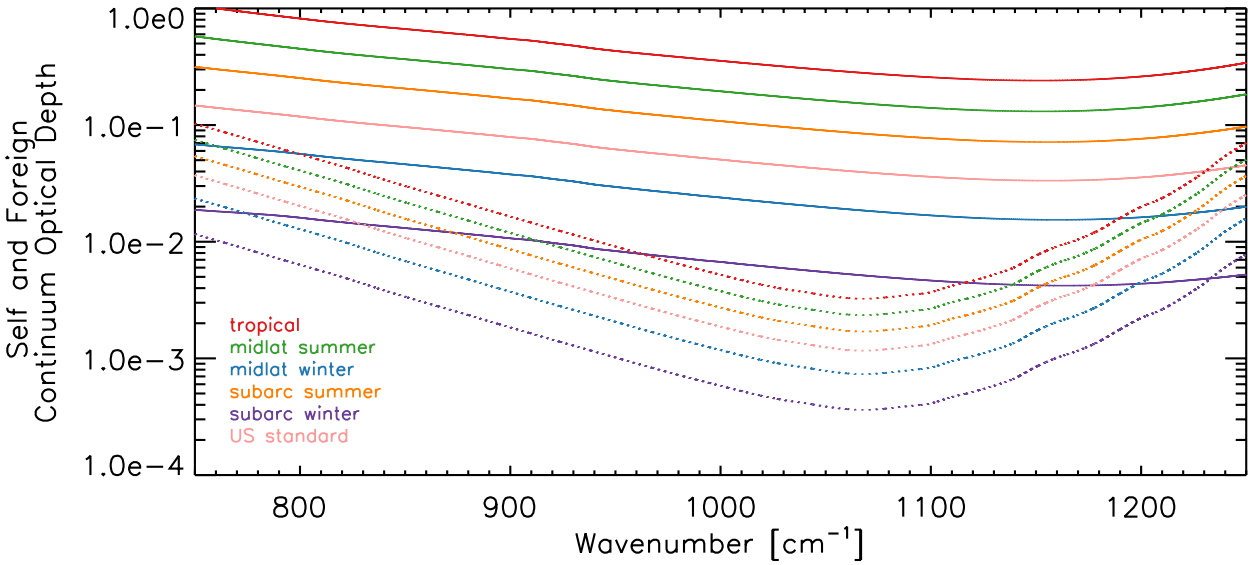

Fig 3. Optical depths due to the MT_CKD_4.1.1 water vapor self (solid) and foreign (dotted) continua for a vertical path for six reference atmospheric profiles.

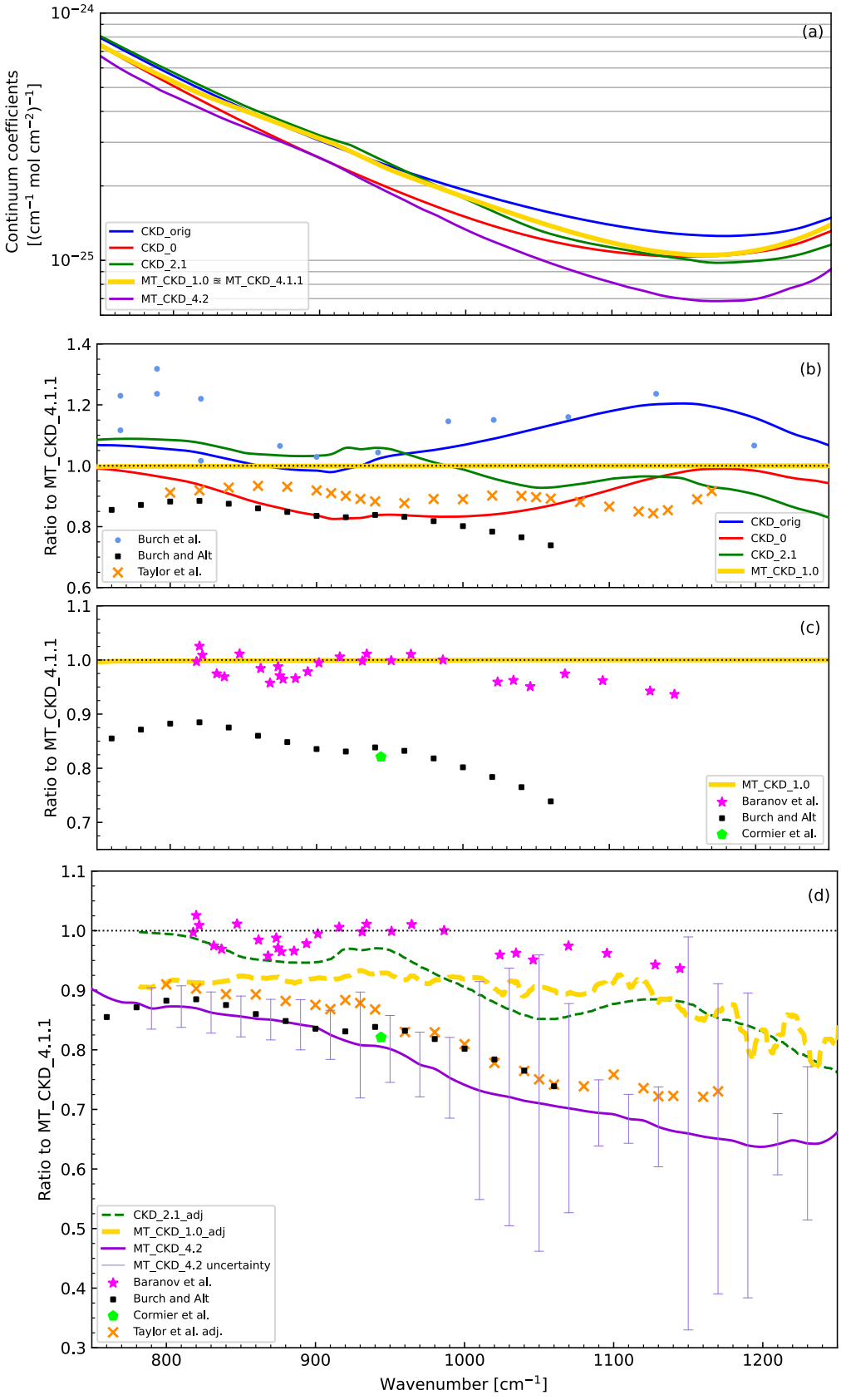
(a)
Continuum coefficients [(cm^{-1} mol cm^{-2})$^{-1}$]
10^{-24}
10^{-25}
CKD_orig
CKD_0
CKD_2.1
MT_CKD_1.0 ≅ MT_CKD_4.1.1
MT_CKD_4.2
(b)
Ratio to MT_CKD_4.1.1
Burch et al.
Burch and Alt
Taylor et al.
CKD_orig
CKD_0
CKD_2.1
MT_CKD_1.0
(c)
Ratio to MT_CKD_4.1.1
MT_CKD_1.0
Baranov et al.
Burch and Alt
Cormier et al.
(d)
Ratio to MT_CKD_4.1.1
CKD_2.1_adj
MT_CKD_1.0_adj
MT_CKD_4.2
MT_CKD_4.2 uncertainty
Baranov et al.
Burch and Alt
Cormier et al.
Taylor et al. adj.
Wavenumber [cm^{-1}]

169

Fig. 4. Various perspectives on the water vapor self continuum in the infrared window. (a) Water vapor self continuum coefficients for five versions of the CKD and MT_CKD continuum. The yellow curve is the self continuum at the beginning of this study, MT_CKD_4.1.1, and the purple curve shows the result of this study, MT_CKD_4.2; (b) Overview of the self continuum in ~2004. Shown as ratios with respect to MT_CKD_4.1.1 are several previous versions of CKD and MT_CKD as well as two sets of laboratory measurements (blue circles and black squares)and the result from the Taylor et al. field campaign (orange X's); (c) Key evaluations of the self continuum before this study are shown as ratios with respect to MT_CKD_4.1.1; (d) Overview of the self continuum after this study. Shown as ratios with to MT_CKD_4.1.1 are the most recent laboratory measurements from three groups (pink stars, black squares, and green pentagon) and the results from three field studies (Taylor et al., 2003, orange X's; CKD_2.1 (green dashed curve), which was motivated by Westwater et al., 1995); MT_CKD_1.0 (yellow dashed curve), which was motivated by Turner et al., 2004) that have been adjusted to account for a stronger foreign continuum (as described in the text) than had been used in the respective original analyses. The purple curve shows the significant decrease in the self continuum that is derived in this study, MT_CKD_4.2 – note that in some regions the corresponding derived error (purple vertical lines with end caps) is significant.

version of the CKD model (CKD_0, see Fig. 7 of Clough et al., 1989). The next update of consequence to the CKD window self continuum occurred about a decade later as a result of analyses of Fourier transfer infrared (FTIR) spectrometer measurements in the tropics (Westwater et al., 1995; Han et al., 1997), which resulted in an increase in the window self continuum in version 2.1 of CKD (shown in Fig. 4a,b). A few years later, an analysis by Turner et al. (2004) using measurements by the Atmospheric Emitted Radiance Interferometer (AERI; Knuteson et al., 2004 a,b) deployed at the Southern Great Plains (SGP; Sisterson et al., 2016) site of Atmospheric Radiation Measurement (ARM) program (Turner & Ellingson, 2016) demonstrated that the window self continuum in CKD needed modification, which led to the values in this region adopted in the first version of the MT_CKD continuum model, MT_CKD_1.0 (Mlawer et al., 2012), also shown in Fig. 4. Fig. 4b also presents the results of a field study of the self continuum by Taylor et al. (2003).

With respect to laboratory measurements of the window self continuum, there was a gap of almost 20 years between the measurements of Burch and subsequent studies. A 2005 laboratory study by Cormier et al. supported a significantly lower continuum absorption coefficient than in MT_CKD_1.0. These measurements were performed using the accurate cavity ring down technique but were only at a single spectral point and contradicted the results from a study by the same group (Cormier et al., 2002) a few years earlier. A subsequent laboratory study using an FTIR (Baranov et al., 2008), mentioned above, showed good agreement with MT_CKD at typical atmospheric temperatures, although significant disagreements were seen with respect to the model's temperature dependence of the self continuum in this region (Fig. 5). The self continuum coefficients derived in Baranov et al. (2008) are shown in Fig. 4c. Also shown in this figure are the laboratory measurements by Burch (1982) – these measurements, and not those from Burch and Alt (1984), were shown in Fig. 8 of Baranov et al. (2008), which drove home that there was agreement between specifications of the window self continuum at room temperature (with the exception of the Cormier et al., 2005, study). However, a conclusion that a consensus existed at this time between laboratory and field studies of the window self continuum is flawed.

To see why, a closer consideration of window self continuum studies based on field measurements is required. There is an important distinction between the window self continuum values based on

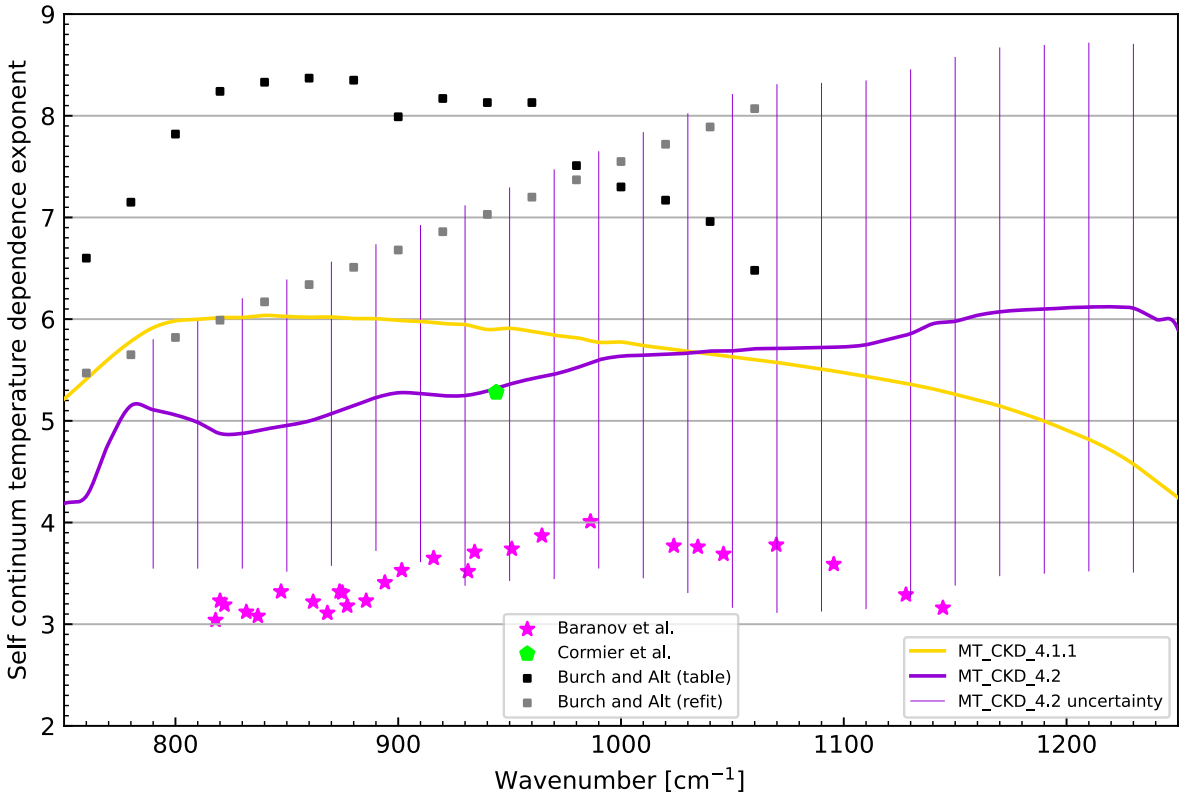

Fig. 5. The temperature exponent of self continuum coefficients from 750-1250 cm^{-1} from several laboratory studies (various symbols), the previous version of MT_CKD, v4.1.1 ≅ v1.0 (yellow curve), and the version derived in this study, MT_CKD_4.2 (purple curve), with estimated uncertainties shown in vertical purple lines without end caps.

field studies (i.e. those that motivated the development of CKD_2.1 and MT_CKD_1.0, as shown in Fig. 4b) and those based on laboratory studies (Fig. 4c). Laboratory studies utilize cells that contain pure water vapor, while the atmospheric paths relevant to field studies are comprised of mostly air (primarily nitrogen and oxygen) with a small fraction of water vapor. Therefore, field studies have a dependence on the water vapor foreign continuum in the window, while laboratory studies typically do not. Although the foreign continuum is much weaker than the self continuum in the window (Fig. 3), significantly inaccurate values assumed for the foreign continuum can still have an impact on the derived self continuum in analyses of field observations. Therefore, the evolution of window foreign continuum values, while interesting in its own right given the objectives of the current study, is also key to a proper understanding of past studies of window self continuum absorption.

The original CKD foreign continuum values (Clough et al., 1989) in the window were based on Burch (1982), which supported the conclusion that the foreign continuum was a very weak absorber in this region (Fig. 6). A major increase in the window foreign continuum came about with advent of MT_CKD (Mlawer et al., 2012), which resulted not from new foreign continuum measurements in this region but rather as a consequence of constraining the model's derived line shape parameters to fit the foreign continuum behavior from 500-750 cm^{-1} in its predecessor version, CKD_v2.4.1. These increased MT_CKD foreign continuum coefficients in the window were subsequently shown to be consistent with field observations by Turner et al. (2004). Even with this increase, foreign continuum absorption in this region remained rather weak compared to the self continuum. The laboratory measurement of Cormier et al. (2005) at 944 cm^{-1}, however, supported a much higher level of foreign continuum absorption, and was followed by a more extensive study (measurements at numerous points between 800-1250 cm^{-1}) by Baranov and Lafferty (2012). As can be seen in Fig. 6, the Baranov and Lafferty (2012) study indicated that the foreign continuum was ~2-4 times greater than MT_CKD_1.0, although the reported strength was about half as large as specified in Cormier et al. (2005). Given the relative optical depths of the window foreign and self continua shown in Fig. 3, assuming a 2-4 times larger foreign continuum would have an appreciable effect on the self continuum absorption derived in a field study.

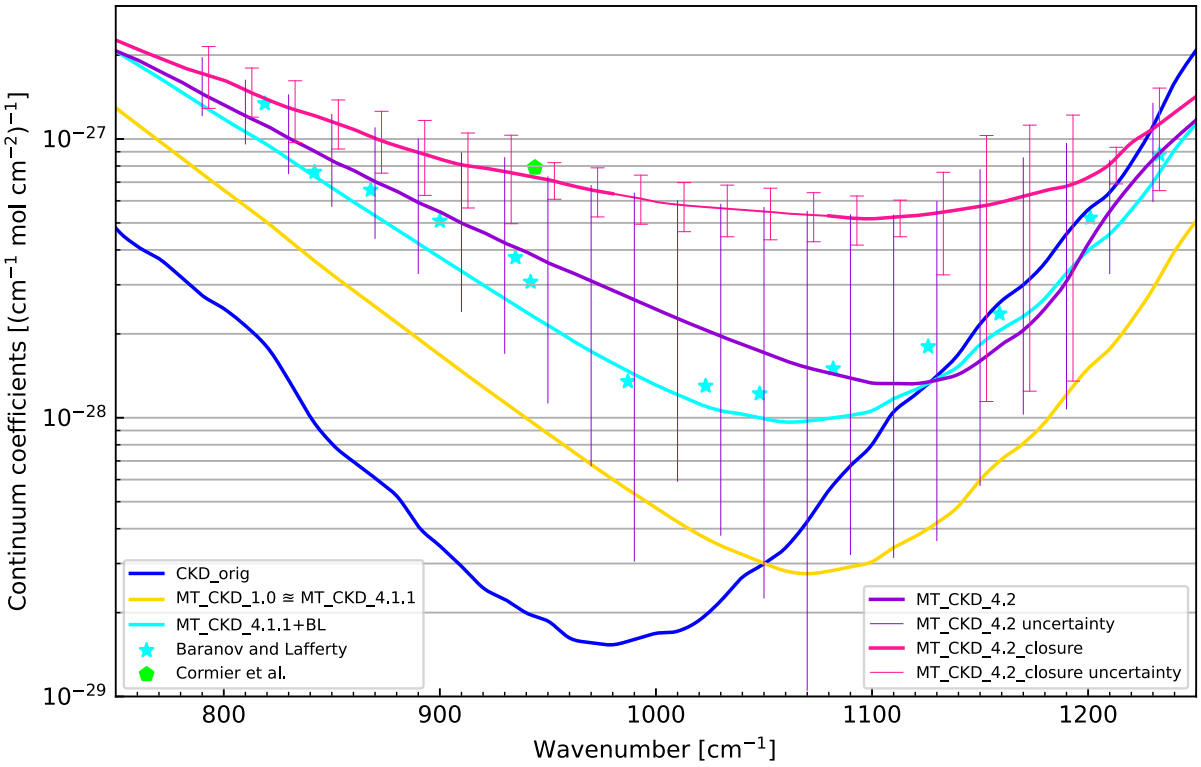

Fig. 6. Water vapor foreign continuum coefficients from 750-1250 cm^{-1} for the original version of the CKD model (blue curve), the current version of the MT_CKD model (v4.1.1, which is equivalent to MT_CKD_1.0, yellow curve), the laboratory results from Baranov and Lafferty (2012, cyan stars) and Cormier et al. (2005, green pentagon), and a version of MT_CKD (v4.1.1+BL, cyan curve) that was adjusted to be consistent with the Baranov and Lafferty (2012) results. The foreign continuum derived in this study, MT_CKD_4.2, is shown in purple, with associated uncertainty values shown with vertical lines without end caps. The pink curve shows the foreign continuum (MT_CKD_4.2_closure) needed to obtain radiative closure with the SGP observations used in this study. Error bars based on the SGP data set are pink vertical lines (slightly offset in the x-direction for clarity) with end caps.

Given that the window foreign continuum derived in Baranov and Lafferty (2012) is much larger than the corresponding foreign continuum values assumed in previous analyses of field observations, it is instructive to understand to what extent the self continuum values derived in previous field studies would have been affected had a stronger foreign continuum been utilized instead in these studies. To evaluate this, we modify the current version of MT_CKD such that the window foreign continuum coefficients are increased to be generally consistent with the Baranov and Lafferty (2012) values. This modified foreign continuum version is shown as MT_CKD_4.1.1+BL in Fig 6. We use this modified version to estimate (method described in Appendix 1) the change in the self continuum values that would have been obtained in three prior field studies had a greater foreign continuum been assumed rather than the values that actually were used in these studies. These reconsidered self continuum values are shown in Fig. 4d as MT_CKD_1.0_adj, CKD_2.1_adj, and Taylor_adj (which, respectively, are based off the studies of Turner et al., 2004, Westwater et al., 1995/Han et al., 1997, and Taylor et al., 2003). We also include on this figure the self continuum laboratory results of Cormier et al. (2005), Baranov et al. (2008), and Burch and Alt (1984), which improved upon the previous measurements by the Burch group.

The overall impression given by Fig. 4d is murkier than in Fig. 4c (or in Fig. 8 of Baranov et al., 2008), but the observational evidence clearly allows the possibility that the window self continuum is significantly weaker than in current MT_CKD. The diversity of values shown suggests, however, that there is no consensus for the strength of the window self continuum. The main motivation for this current study is to bring some clarity to this question of great importance.

3. Elements of the Comparison

Our analysis of water vapor continuum absorption in the infrared window is based on comparisons between clear-sky radiance measurements by the AERI and corresponding calculations by the Line-By-Line Radiative Transfer Model (LBLRTM; Clough et al., 2005) that utilize as input a combination of in situ measurements, retrieved quantities, and model output to specify the atmospheric properties in the radiating column above the AERI.

Our radiative closure analysis is based on observations taken at two sites operated by the ARM program. The primary data set is more than two years of observations (March 2016 - October 2018) from the ARM SGP site, the world's largest and most extensive climate research facility. The SGP site consists of in situ and remote-sensing instrument clusters and has been collecting data since it was established in 1993. Also used in this study are observations from the ARM Observations and Modeling of the Green Ocean Amazon (GoAmazon; Martin et al., 2016) campaign (MAO), held from January 2014 through November 2015 in Manaus, Brazil, at an altitude of about 50 meters. Due to MAO's tropical location the median PWV amount for the profiles used in our analysis is far greater than for SGP (Fig. 7) and provide an excellent dataset for validating the self and foreign continuum derived from SGP observations.

We provide here details about each of the three elements involved in this radiative closure study.

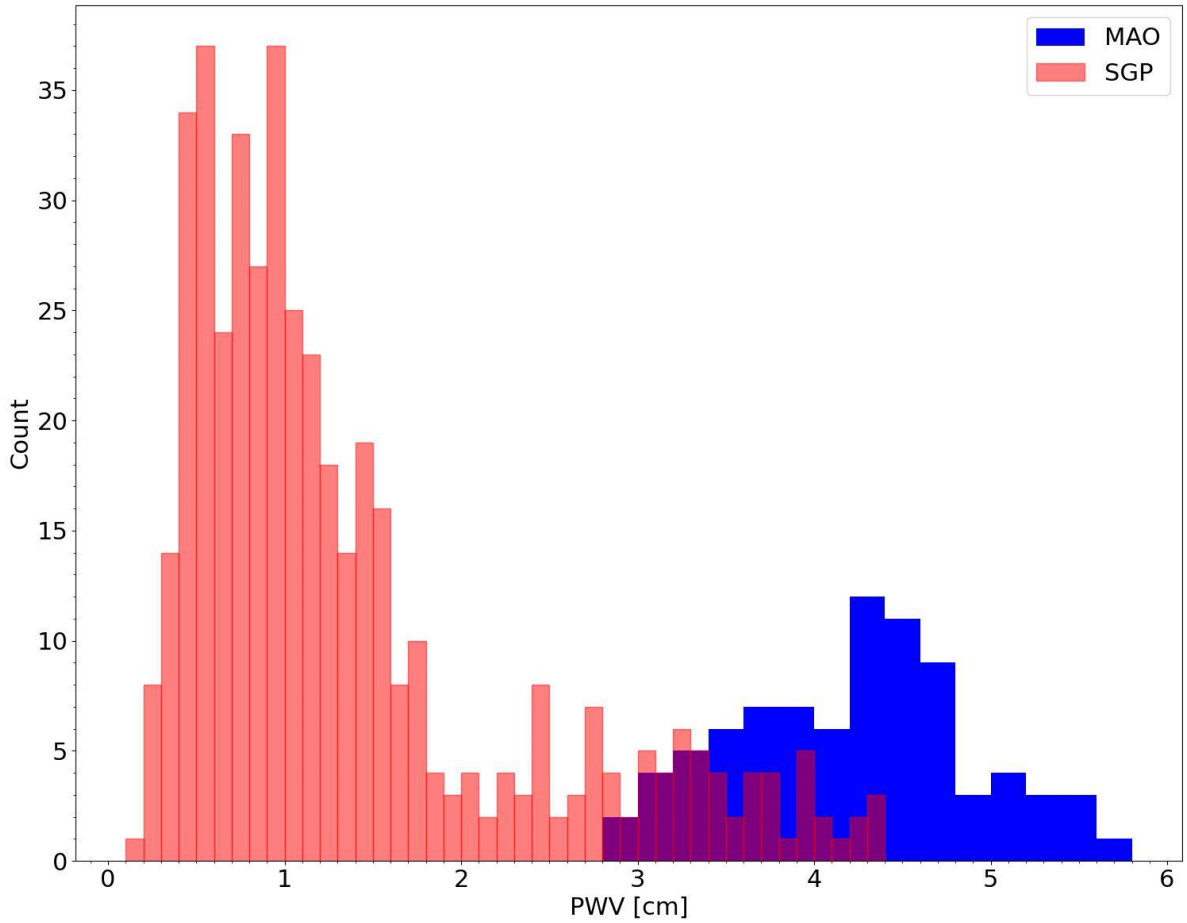

Fig. 7. Precipitable water vapor amounts for the cases used in this study.

3.1 Radiometric Measurements

The AERI, a Fourier transform infrared interferometer that was designed specifically for the ARM program (Turner et al., 2016), measures downwelling spectrally resolved infrared radiance from 550-3000 cm^{-1}. A zenith-looking AERI, deployed at an altitude of 320 m, has been providing operational radiance measurements at SGP since 1995, observing radiances emitted downward by the atmosphere for a large range of water vapor column amounts (PWVs). It uses two detectors to have sensitivity to radiance in the 3.3 to 19 μm band, and the maximum optical path delay provides a spectral resolution of 0.5 cm^{-1}. The instrument regularly views two well-characterized blackbodies, which are operated at ambient temperature and 60 °C, respectively. These blackbody observations, together with a correction for the detector's non-linearity, allows the instrument to measure downwelling spectral infrared radiance with a radiometric accuracy better than 1% of the ambient radiance. Additionally, a calibrated metrology laser and corrections for the finite field-of-

view of the instrument provides the spectral calibration for the observed radiance. Details on the instrument and its calibration method are provided in Knuteson et al. (2004a, b).

The signal observed from the sky is calibrated using the ambient and hot blackbody views using the complex arithmetic technique proposed by Revercomb et al. (1988). However, careful analysis has shown that there can still exist a slight positive bias to the observed sky radiance; this is most easily seen in extremely dry clear sky scenes (Delamere et al., 2010; Turner, 2003). Initially, the source of this bias was assumed to be something in the foreoptics (e.g., some scattered light), and Delamere et al. (2010) assumed that there was a small fraction (order 0.1%) of ambient radiation scattered into the sky observations. However, extensive analysis across multiple AERI systems, including a detailed examination during a particular low radiance condition, ruled out all contributions from the foreoptics (e.g., scattered radiation, polarization) and the Revercomb calibration method rules out phase issues. A new hypothesis was formulated suggesting that emission from the aft optics is not accounted for in the calibration. The functional form of an aft optics correction would be the same as used in Delamere et al. (2010), with the contribution from the "offending" temperature being that of the aft optics. For this study, the observations did not definitively support either an issue with the foreoptics or the aft optics, so no bias correction was applied.

Fig. 8 shows average AERI radiances from observations used in this study for different PWV ranges.

3.2 Model Calculations

Radiance calculations by LBLRTM_v12.15.1 are used in our radiative closure analysis, which focuses on the 780-1280 cm^{-1} region. Absorption line parameters used in these calculations utilize the line file version AER_v3.8.1 and continuum absorption is specified by MT_CKD_4.1.1 (for our baseline calculations). (These models and databases are available at https://github.com/AER-RC, the GitHub repository of the AER Radiation and Climate Group.) We also perform LBLRTM calculations for which the water vapor continuum is changed to MT_CKD_4.1.1+BL. All calculations used in this study include all relevant absorption due to water vapor, carbon dioxide

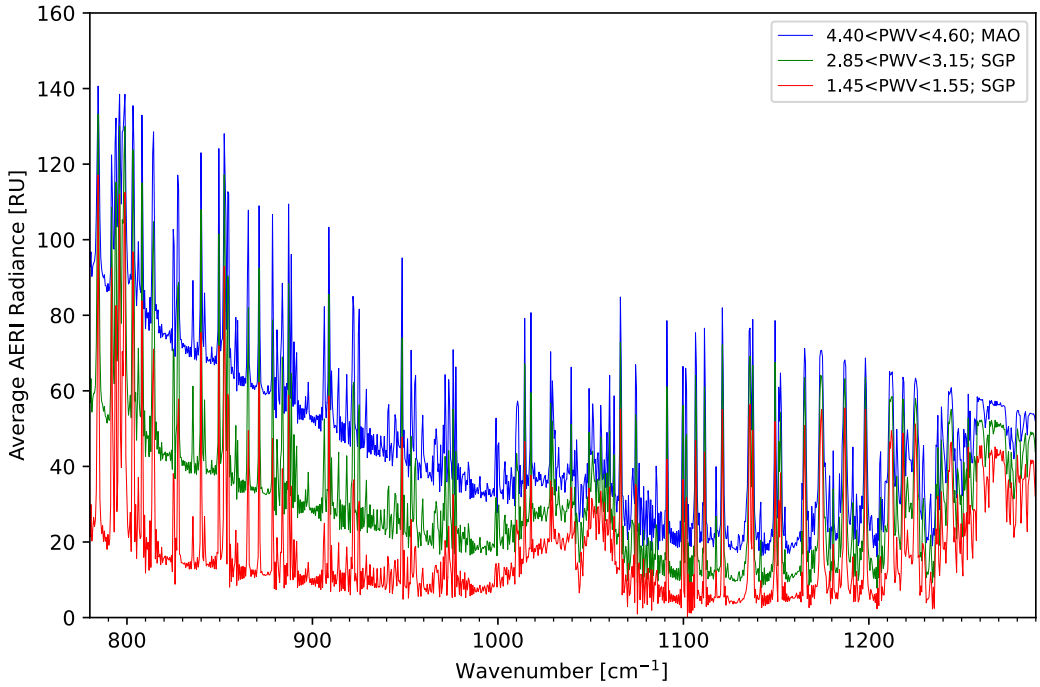

Fig. 8. Average AERI radiances used in this study from MAO (blue curve) and for two PWV bins at SGP (red and green curves). A "radiance unit" (RU) is 1 mW / (m^2 sr cm^{-1}).

(including first-order line coupling), ozone, nitrous oxide, methane (first-order line coupling), ammonia, CCl4, CFC-11, CFC-12, HNO_3, HCFC-22, and PAN.

The MT_CKD water vapor continuum model (Mlawer et al., 2023; Mlawer et al., 2012) provides water vapor self and foreign continuum coefficients (cm^2/molecule/cm^{-1}) every 10 cm^{-1} from 0-20,000 cm^{-1}. To obtain continuum coefficients in between the stored values, a cubic interpolation using the four closest stored values is performed. Absorption coefficients C_x (cm^2/molecule) can be obtained by multiplying the continuum coefficients $\tilde{C}_x$ by the radiation term R:

$$C(\nu, T, \rho_x) = \tilde{C}_x(\nu, T, \rho_x)\, R(\nu, T) \qquad (1)$$

where ν is the wavenumber, T is the temperature, the subscript 'x' denotes either 'self' or 'foreign', and the radiation term R is given by

$$R(\nu, T) = \upsilon \tanh\left(\frac{hc\upsilon}{2kT}\right), \qquad (2)$$

where h is Planck's constant, c is the speed of light, and k is Boltzmann's constant. The dependence on density implied by the notation for $\tilde{C}_x$ is given by

$$\tilde{C}_x(\nu, T, \rho_x) = \tilde{C}_x\left(\nu, T, \rho_{x,ref}\right)\left(\frac{\rho_x}{\rho_{x,ref}}\right) \quad (3)$$

where ρ is the density of the gaseous molecules interacting with water vapor in the respective process (i.e. water vapor for the self continuum; all gaseous molecules except for water vapor for the foreign continuum) and the reference density at which coefficients are stored corresponds to a pressure of 1013 mbar and a temperature of 296K. The optical depth of the self or foreign continuum is given by the product of the absorption coefficient C_x and the water vapor column amount W (molecules/cm^2):

$$\tau_x(\nu, T, \rho_x) = W(H_2O)\, C(\nu, T, \rho_x). \quad (4)$$

The temperature dependence of the self continuum coefficients in the MT_CKD model is given by

$$\tilde{C}_s(\nu, T) = \tilde{C}_s(\nu, 296K)\, (296/T)^{n(\nu)} \quad (5)$$

where n is a wavenumber-dependent dimensionless parameter and the density dependence of the coefficients has been suppressed for clarity. The foreign continuum coefficients are assumed to not be dependent on temperature.

More details about this formulation can be found in Mlawer et al. (2023).

3.3. Input to the Model

Multiple observations are used to create the profiles used as input to the model calculations. The foundation for the temperature and water vapor profiles are observations by radiosondes (hereafter sondes), which were usually launched four times daily during our study period at SGP and twice a day at MAO. However, sonde measurements are not directly used as input to the radiative transfer calculations in our analysis. The sonde launch location at SGP is ~250 m from where the AERI is deployed so its measured temperatures and humidity values in the lowest several hundred meters cannot provide the needed accuracy for our closure study, and sonde humidity measurements have

well known accuracy issues (Turner et al., 2016). For our study, we use the TROPoe (Turner & Löhnert, 2014) physical retrieval algorithm to retrieve profiles of temperature and humidity that provide closure with the sonde profiles, the AERI radiance observations between 538 and 722 cm^{-1} (i.e., regions of the spectrum wherein the water vapor line shape and continuum absorption have undergone validation (Delamere et al., 2010; Mlawer et al., 2019), and the brightness temperatures at 23.8 and 31.4 GHz from a microwave radiometer (MWR; Cadeddu et al., 2013). For this study, the TROPoe retrieval utilizes the latest version of the MT_CKD continuum (Mlawer et al., 2023) and the AER line file, ensuring that its water vapor spectroscopy from 538-722 cm^{-1} includes recent upgrades.

The TROPoe algorithm is a 1-dimensional variational retrieval approach using the optimal estimation framework. It has been extensively modified to include a wide number of measurements (with their uncertainties) from different instruments in the observation vector (Turner & Blumberg, 2019; Turner & Löhnert, 2021). A prior dataset is used to constrain the retrieval; for the SGP, sonde launches from over 10 years were used to create seasonal priors, whereas all the sondes launched during the Go-Amazon field campaign were used to create the single yearly prior for the MAO site. Ultimately, the retrieval finds the solution (i.e., the retrieved thermodynamic profiles) that provides the best fit with all the observations (i.e., sonde, AERI radiances, and MWR brightness temperatures) and the prior (within their uncertainties). The TROPoe retrieval is run at the sonde launch time.

The TROPoe profiles only extend to 17 km, as that is the maximum height of the prior dataset used to constrain the retrieval. Above 17 km, water vapor values are taken from reference atmospheric profiles (U.S. standard for SGP, tropical for MAO) (Anderson et al., 1986). For temperature, Modern-Era Retrospective analysis for Research and Applications, Version 2 (MERRA-2; Randles et al., 2017) profiles are used above 17 km.

Below, in the uncertainty analysis (section 4.5) of the water vapor continuum absorption parameters derived in this study, an alternative data set of temperature and water vapor profiles is also considered. This specification directly uses the sonde-measured temperature and water vapor profiles in which the sonde water vapor measurements are scaled such that agreement is attained

between the 23.8 GHz measurement of the collocated MWR and a corresponding radiative transfer calculation (Turner et al., 2016). This method to specify the thermodynamic profile has been previously used in similar radiative closure studies (e.g. Turner et al., 2004; Mlawer and Turner, 2016). For the SGP cases used in this study, the ratios of the PWV values of the TROPoe-derived and sonde profiles are shown in Fig. 9. Also shown in this figure are the ratios of the PWV values of the TROPoe-derived and MWR-scaled sonde profiles.

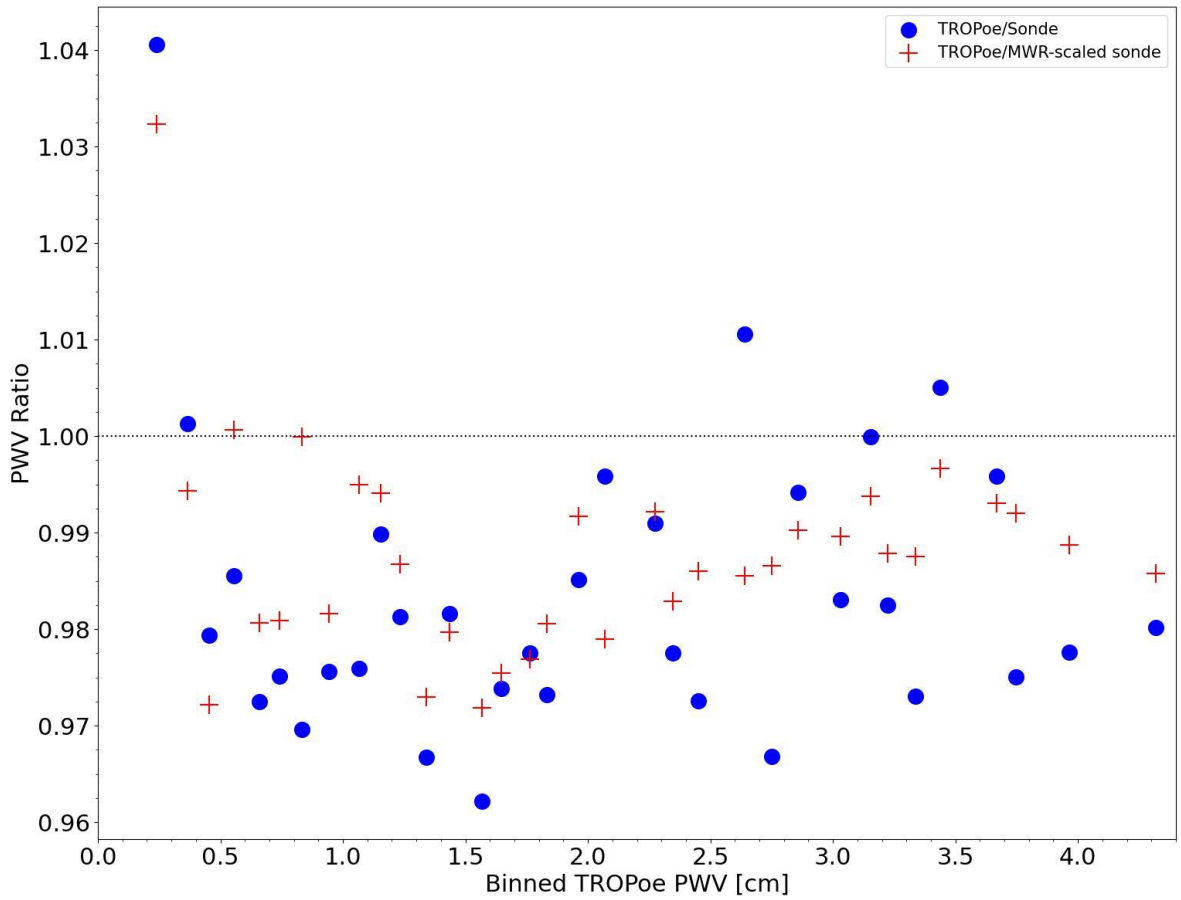

Fig. 9. Ratios of PWV derived from TROPoe retrieval to the sonde-measured (blue circles) and MWR-scaled (red plus symbols) PWVs at SGP.

The profiles of trace gas abundances that are used in the radiative transfer calculations are obtained from multiple sources. MERRA-2 profiles corresponding to the SGP and MAO locations are used to specify ozone. For CO_2, N_2O, CH_4, HCOOH, HNO_3, and PAN, monthly climatologies are used that were originally developed for the NASA Aura satellite project and updated over time by the Tropospheric Emission Spectrometer (TES; Worden et al., 2007) and TRopospheric Ozone and its Precursors from Earth System Sounding (TROPESS; Fu et al., 2013) teams. For four other

446 molecules (CCl4, CFC-11, CFC-12, and HCFC-22), abundance values from the NOAA
447 Halocarbons and other Atmospheric Trace Species (HATS) program
448 (https://gml.noaa.gov/hats/flask/flasks.html) are used. All other molecular profiles are specified
449 using the reference values stored in LBLRTM (U.S. standard atmosphere for SGP, tropical
450 atmosphere for MAO).
451
452 **4. Results of Measurement-Calculation Comparisons**
453 ***4.1. Case and channel selection***
454 More than 3000 sondes were launched at SGP during our study period. For each sonde, AERI
455 measurements within a 35-minute window associated with each sonde launch (t-5 to t+30 minutes)
456 are averaged. Given the large number of sondes and the many AERI channels in the targeted
457 spectral region (780-1280 cm^{-1}), we can be selective with respect to the AERI radiance
458 measurements we use in the study to minimize the possibility that our analysis is affected by
459 clouds, insensitivity to water vapor continuum absorption, and trace gas uncertainty.
460
461 To avoid cloud contamination, we remove from our analysis all cases where a cloud might be
462 contributing to the downwelling infrared radiance using two tests: the cloud liquid water path
463 retrieved by TROPoe is less than 2 g/m^2, and the magnitude of the standard deviation of the 900
464 cm^{-1} radiance observation over the 35-minute window is less than 0.3 RU. This initial screening
465 removes AERI spectra that fail either of these tests for the presence of clouds, resulting in 453
466 AERI spectra being identified as clear-sky observations.
467
468 Our analysis of the water vapor continuum focuses on AERI channel measurements that are
469 sensitive to the strength of water vapor continuum absorption. These spectral elements are
470 identified by evaluating the sensitivities of all AERI channels to a change in continuum strength.
471 We first compute the change in spectral radiances for all clear AERI cases due to a small
472 perturbation in the self continuum, then bin these sensitivity values in 10 cm^{-1} spectral bins and
473 five PWV ranges. For each spectral bin and PWV range, we classify each channel in all AERI
474 cases as either "sensitive" or "insensitive" by computing a threshold between the two classes based
475 on minimizing the combined variance in both classes (Otsu, 1979). AERI channels that are
476 classified as "sensitive" for at least 50% of the cases in at least three of the five PWV ranges are

used in the SGP analysis, and the other channels are not considered further in our retrieval of water vapor continuum coefficients.

Given the very low optical depths associated with the foreign continuum (Fig. 3), a small error in the specification of trace gas abundances can impact the determination of foreign continuum coefficients from the AERI measurements. Any such error in the foreign continuum may then cascade through the analysis, impacting the accuracy of the derived self continuum. To identify AERI channels that may be non-trivially impacted by inaccurate specification of trace gas abundances, the uncertainty for each abundance value is required. In this analysis, we use a conservative estimate of ~2 ppm for CO_2, while the uncertainty in the total column amount of N_2O is estimated as 1% and CH4 as 0.02 ppmv. For HNO_3 and PAN, the uncertainty was calculated as the standard deviation of the monthly values for this location in the climatologies. For NH_3 and HCOOH, we use estimated uncertainties of 50%. For ozone, following Wargan et al. (2017) the stratospheric and tropospheric uncertainties are estimated as 8% and 21%, respectively. For CCl4, CFC-11, CFC-12, and HCFC-22, the uncertainty is set to be consistent with the variance of the respective source value in the HATS database. Using the uncertainty values for all trace gases, a sensitivity study is performed corresponding to an AERI observation associated with a moderate PWV value (2.15 cm) and spectral differences are computed between a baseline calculation in which the trace gases are at their standard abundances and a perturbed calculation in which these abundances are increased by their respective uncertainties. The results from these calculations are shown in Fig. 10a. For a chosen uncertainty threshold value of 0.075 RU, we consider water vapor continuum coefficients derived at spectral points for which the sensitivity to trace gas abundances exceeds this threshold to be less reliable, while those AERI channels below this threshold and thus showing less sensitivity to trace gas uncertainty are considered more reliable. Certain figures in this paper (Figs. 10, 12, 13, and 14) distinguish between these two categories of AERI channels through the use of large circles (greater confidence) and small circles (lesser confidence). (The uncertainty threshold is significantly exceeded throughout the ozone band from 980-1080 cm^{-1} and radiative closure results in this spectral region are not presented in this study to avoid confusion.)

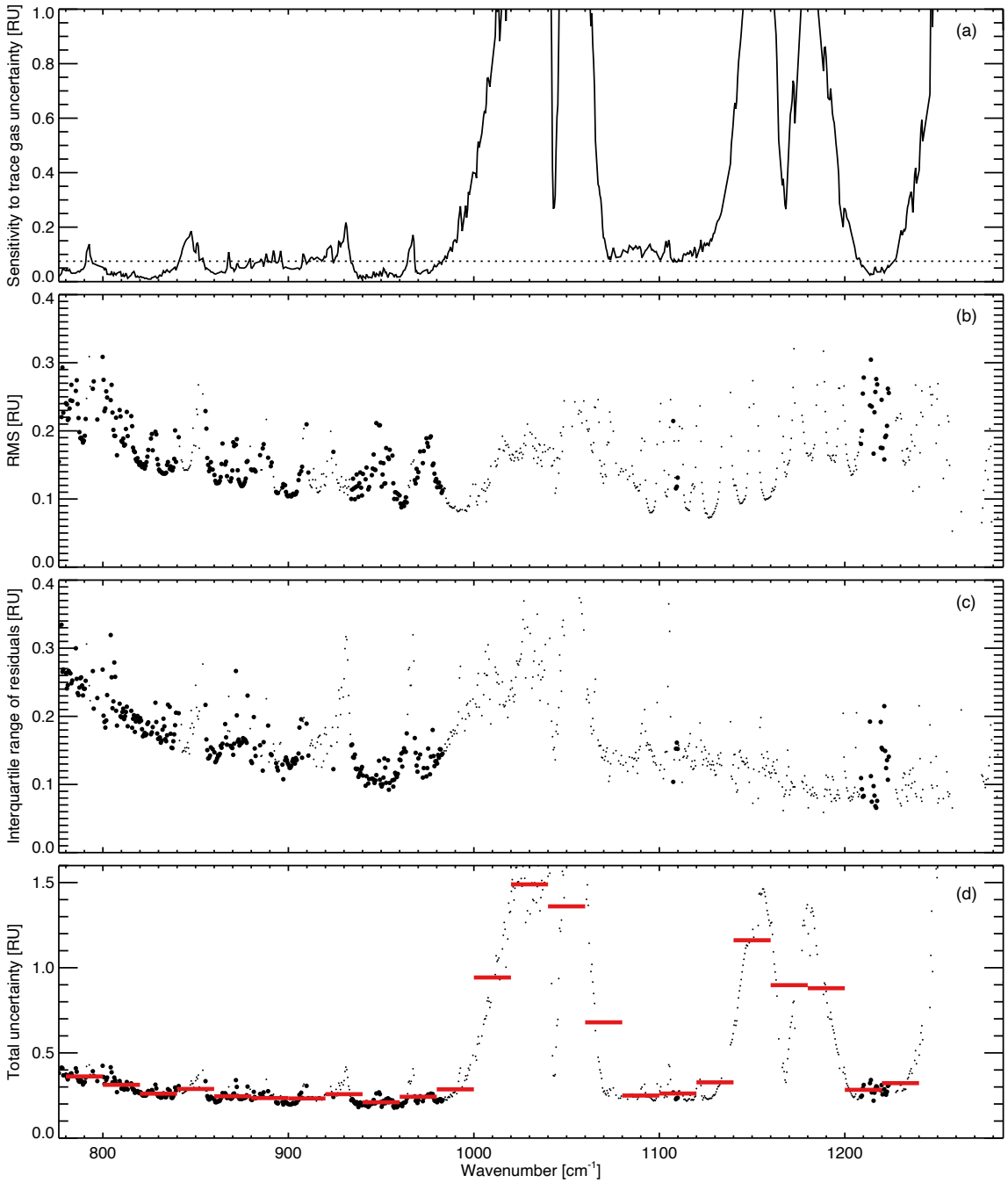

Fig. 10. For AERI channels from 780-1280 cm^{-1}: (a) Difference in calculated radiances due to the changes to abundances of trace gases described in the text. The analysis in this study at spectral locations for which this change is less than the horizontal dotted line shown are viewed with greater confidence; (b) RMS differences between radiances calculated with profiles utilized in this study and reasonable alternate profiles (as described in text); (c) Interquartile range of measurement-calculation differences for all PWV bins; (d) Total spectral uncertainty of measurement-calculation residuals (black circles) and RMS of uncertainties in 20 cm^{-1} regions (red horizontal lines).

4.2. Initial analysis

For each selected AERI channel, the residuals between the AERI radiance measurements and corresponding LBLRTM calculations are grouped into 0.1 cm PWV bins. Since the values of some residuals in each bin can differ greatly from the median residual in that bin, we eliminate the impact of possible outliers only considering the results in a PWV bin for cases that have a residual between the 25th and 75th quartiles. The mean of this "inner half" of cases is computed for all PWV bins (for each set of LBLRTM calculations considered in this study).

The behavior of these binned mean residuals as a function of PWV is shown in Fig. 11 for three AERI channels. Results are shown for LBLRTM calculations that use MT_CKD_4.1.1 (black) and MT_CKD_4.1.1+BL (green; description in section 2). The dependence of the residuals on PWV, fit with a quadratic function for each channel, indicates that the measurement data set is not consistent with the LBLRTM calculations for either of these specifications of self and foreign water vapor continuum absorption. Furthermore, the behavior of the residuals as a function of optical depth suggests that more atmospheric opacity is needed in the calculation for low PWV amount, while the opacity is overestimated for higher PWV values. Other channels in the infrared window show similar results.

The medians (over PWV bins) of the inner half mean residuals for calculation using MT_CKD_4.1.1 (black) and MT_CKD_4.1.1+BL (green) are shown in the top panel of Fig. 12 for each AERI channel analyzed. Although MT_CKD_4.1.1 appears to provide reasonable results, the results in this panel are misleading. As for the three channels shown in Fig. 11, a quadratic curve is fit to the values of binned mean residuals vs. PWV for all AERI channels. The linear and quadratic coefficients of the fit for each channel are shown in the bottom two panels, respectively, of Fig. 12. Reasonable overall agreement between the measured and calculated radiances would result in residuals that would have little dependence on PWV -- the values in each of the bottom two panels of Fig. 12 would be more-or-less zero (i.e. follow the panel's x-axis). This is not the case for either version of LBLRTM available prior to this study.

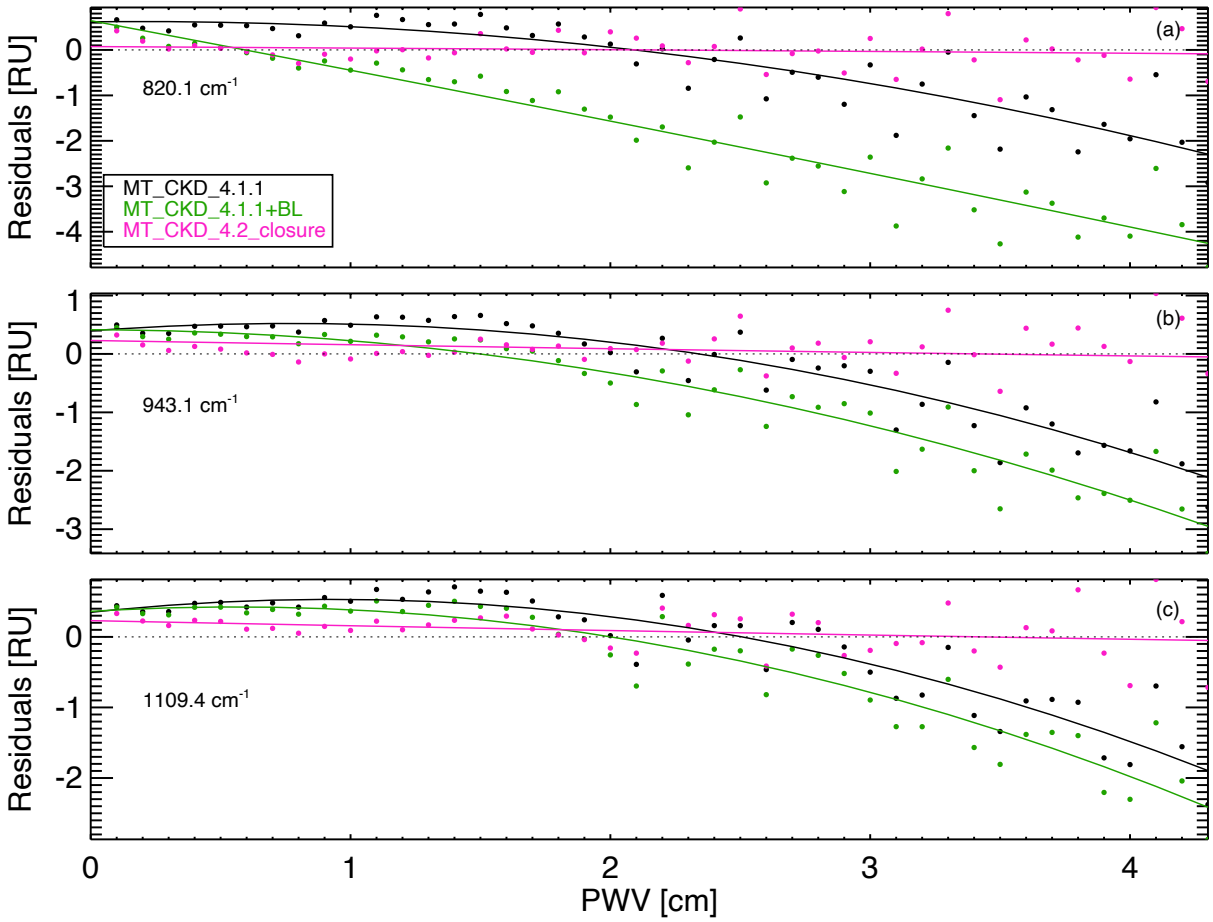

Fig 11. Residuals between AERI measurements at SGP and corresponding LBLRTM calculations as a function of PWV for three AERI channels in the infrared window. The black symbols are for LBLRTM calculations that use MT_CKD_4.1.1, the green symbols correspond to the use of MT_CKD_4.1.1+BL, and the pink symbols result from using the continuum derived in this study, MT_CKD_4.2_closure. Quadratic fits to these residuals are shown as curves in corresponding colors. Cases are binned by PWV and analyzed as described in the text.

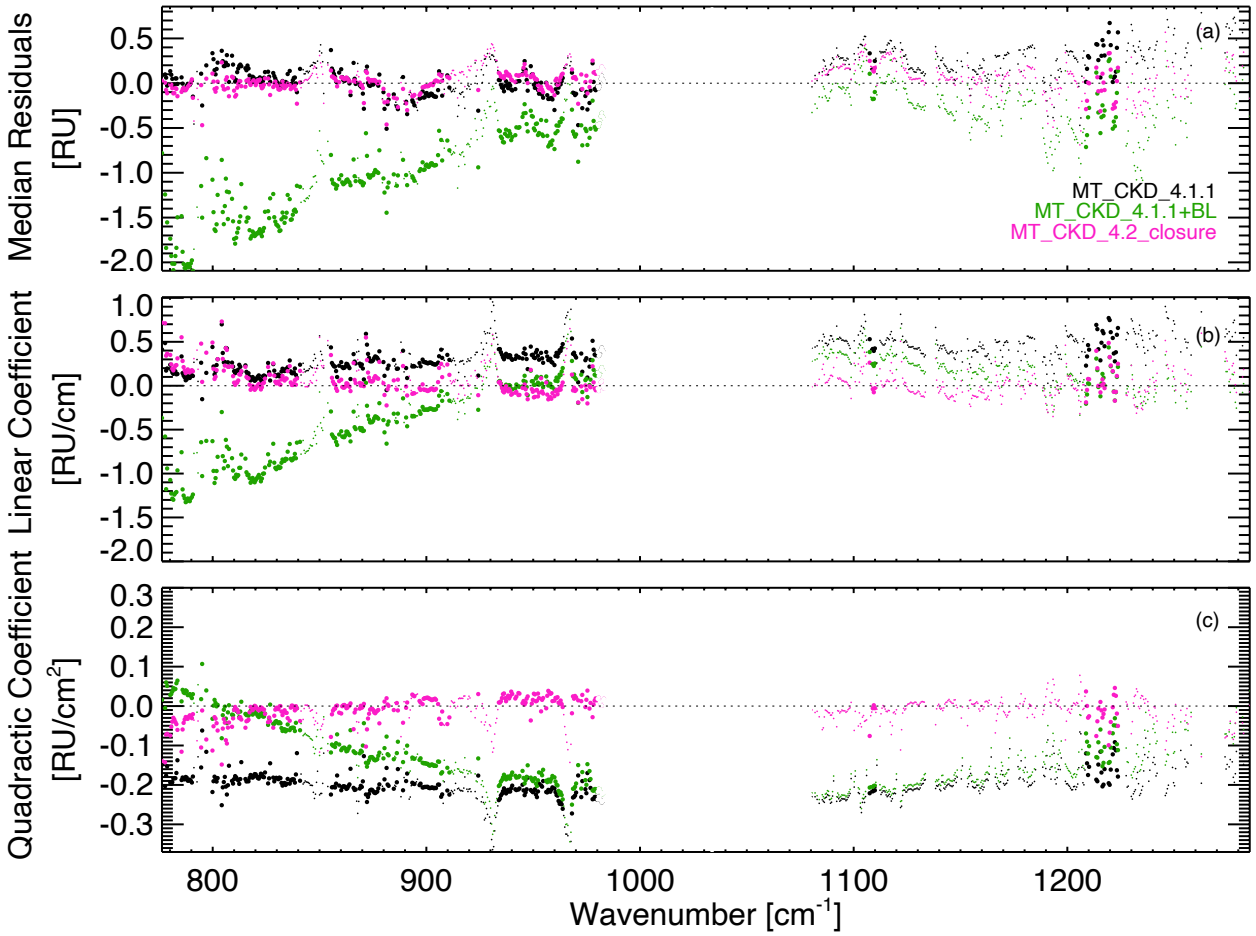

551 **Fig. 12.** Comparison between AERI measurements at SGP and corresponding LBLRTM calculations for
552 the spectral region 780-1280 cm^{-1}: (upper) Median of the PWV-binned residuals. The residual for each
553 spectral point in a PWV bin is computed as the mean of the "inner half" of all residuals in that bin, as
554 described in the text. The black symbols are for LBLRTM calculations that use MT_CKD_4.1.1, the green
555 symbols correspond to MT_CKD_4.1.1+BL, and the pink symbols result from using the continuum derived
556 in this study, MT_CKD_4.2_closure; (middle) Linear coefficient of the quadratic fit to the residuals as a
557 function of PWV; (bottom) Quadratic coefficient of the quadratic fit to the residuals as a function of PWV.
558 The distinction between large and small circles in all panels is explained in the text.
559

560 Since the foreign continuum depends linearly and the self continuum quadratically on the water
561 vapor amount, there is some validity in associating the behavior of the linear fit coefficient shown
562 in Fig. 12b with an inaccurate specification of the foreign continuum and the behavior of the
563 quadratic coefficient (Fig. 12c) with the self continuum. However, due to the dependence of each
564 on pressure, and hence on the water vapor profile and not simply on PWV, and the dependence of
565 the self continuum coefficients on temperature, such an association is not exact. A modification in
566 the specification of either continuum source will lead to changes in both the linear and quadratic

fit coefficients, so improvements to the results shown in Fig. 12 can follow only from a simultaneous analysis of the foreign and self continua.

4.3 Retrieval of Self and Foreign Continua

Our SGP AERI dataset, with its large number of cases and wide range of PWV values, is ideal for retrieving self and foreign continuum coefficients in the infrared window. The wide range of temperatures that characterize the water vapor profiles associated with these AERI observations also may possibly allow the derivation of coefficients that characterize the temperature dependence of the self continuum. Continuum properties determined in the analysis of SGP cases are then validated using AERI measurements from MAO. Due to the high PWV amounts for the MAO cases, this validation is especially informative with respect to the properties of the crucial self continuum.

The retrieval of water vapor continuum properties in the infrared window begins with baseline LBLRTM calculations of downwelling surface radiances for all the cases in the SGP AERI data set. These initial LBLRTM calculations utilize MT_CKD_4.1.1+BL (i.e. corresponding to the green results in Fig. 12), although the retrieval results are fairly insensitive to this choice. Using the measurement-calculation residuals, for each AERI channel between 780-1280 cm^{-1} a least-squares retrieval is performed of three independent variables -- two linear scale factors, one each for the self and foreign continuum coefficients used in the LBLRTM calculations, and a scale factor for the exponent of the self continuum temperature dependence. The sensitivities of the residuals to changes in the retrieved continuum properties (i.e. the Jacobian) used in the retrieval are obtained from additional sets of LBLRTM calculations in which each of these three properties is perturbed by a small amount. In the methodology, we apply the PWV binning discussed above. That is, at each spectral point a single residual and corresponding sensitivities are computed for each PWV bin by averaging the "inner half" of the residuals for all the cases in that bin. With this, each least-square retrieval operates on 43 (the number of PWV bins) measurement-calculation residuals. A three-variable retrieval is run to obtain scale factors for the self continuum, foreign continuum, and temperature exponent of the self continuum. Fig. 13 shows the results of this retrieval.

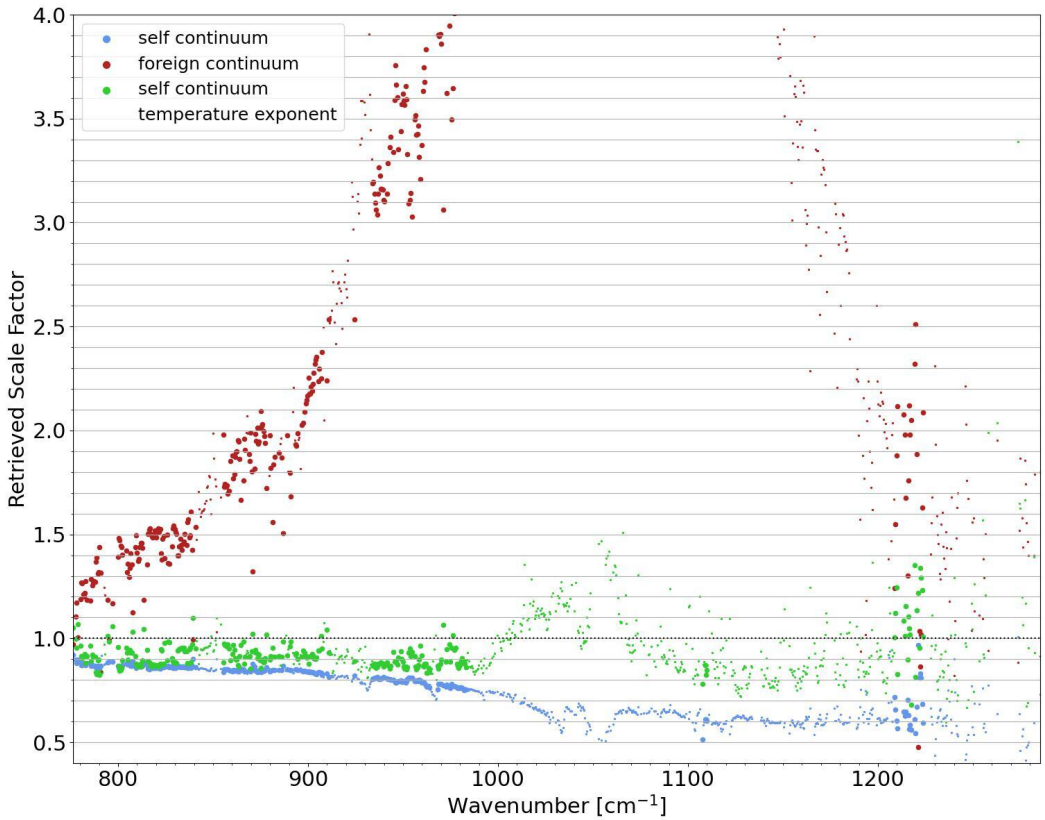

598 **Fig. 13.** Scale factor values (relative to MT_CKD_4.1.1+BL) obtained from the initial retrieval step
599 described in the text for the self continuum (blue), foreign continuum (red), and self continuum temperature
600 exponent (green). The distinction between large and small circles is the same as in Fig 12.
601

602 Using these results, an interim revised version of the MT_CKD water vapor continuum is created
603 by smoothing the retrieved spectral coefficients, interpolating through the ozone band region, and
604 blending the retrieved values into the continuum values in neighboring regions. Then the entire
605 retrieval process is repeated, including new sensitivity calculations using the interim MT_CKD
606 version. This process is iterated several times until the properties until no further smoothly varying
607 change in the continuum parameters could further improve the results (i.e. the median residuals
608 and the linear and quadratic coefficients of the fit of the residuals with respect to PWV).
609

610 The median values of the measurement-calculation residuals using the final retrieved continuum
611 coefficients and temperature dependence (MT_CKD_4.2_closure) are shown in pink in Fig. 12a.
612 As before, a quadratic function is fit to these residuals at each spectral point and the fit coefficients
613 are shown in Fig. 12b and c. Fig. 11 shows in pink the quadratic fit for MT_CKD_4.2_closure for
614 the same example AERI channels shown in this figure for prior versions of MT_CKD. These

figures indicate that the properties of the residuals between the SGP AERI measurements and LBLRTM residuals are greatly improved when MT_CKD_4.2_closure is used in the calculations compared to previous continuum versions. This improvement has resulted from increasing the atmospheric opacity for low PWV cases (roughly PWV < 2 cm) while decreasing it for higher PWVs.

4.4 Validation using AERI observations from MAO

As validation, LBLRTM calculations using several versions of MT_CKD are performed for the MAO AERI cases. The median residuals corresponding to these calculations are shown in Fig. 14. As for the SGP analysis above, these medians are computed from the inner half mean residuals of each PWV bin. (Each MAO PWV bin has a width of 0.2 cm.) As for SGP, no bias correction is applied to the MAO AERI measurements. (For the warm and moist conditions of MAO, any such correction would have only a small impact.) Due to the limited range of PWV values in the MAO dataset, quadratic functions are not fit to the residuals. It is clear from Fig. 14 that the residuals using MT_CKD_4.2_closure are greatly improved compared to previous continuum versions.

The self and foreign continuum coefficients retrieved from the SGP AERI measurements in this study are shown (MT_CKD_4.2_closure) in purple in Figs. 4d and pink in Fig. 6, respectively. The retrieved temperature exponents of the self continuum are shown in Fig. 5 (purple). Detailed discussion of these results is provided in section 5.

4.5 An adjustment to the retrieved foreign continuum

The continuum coefficient retrieval described above did not include the spectral region from 990-1070 cm^{-1}, which has significant ozone absorption. In Fig. 6, a reasonable spectral continuation of the AERI-derived coefficients across this region is shown with a thin pink curve segment. The overall flatness of the foreign continuum coefficients in the 900-1150 cm^{-1} region does not agree with the corresponding relative behavior of the coefficients derived by Baranov and Lafferty (2012) or that of MT_CKD_4.1.1, both of which have much smaller continuum coefficients in the middle of this region (~ 1070 cm^{-1}) than at its endpoints. For MT_CKD_4.1.1, this deep well is a

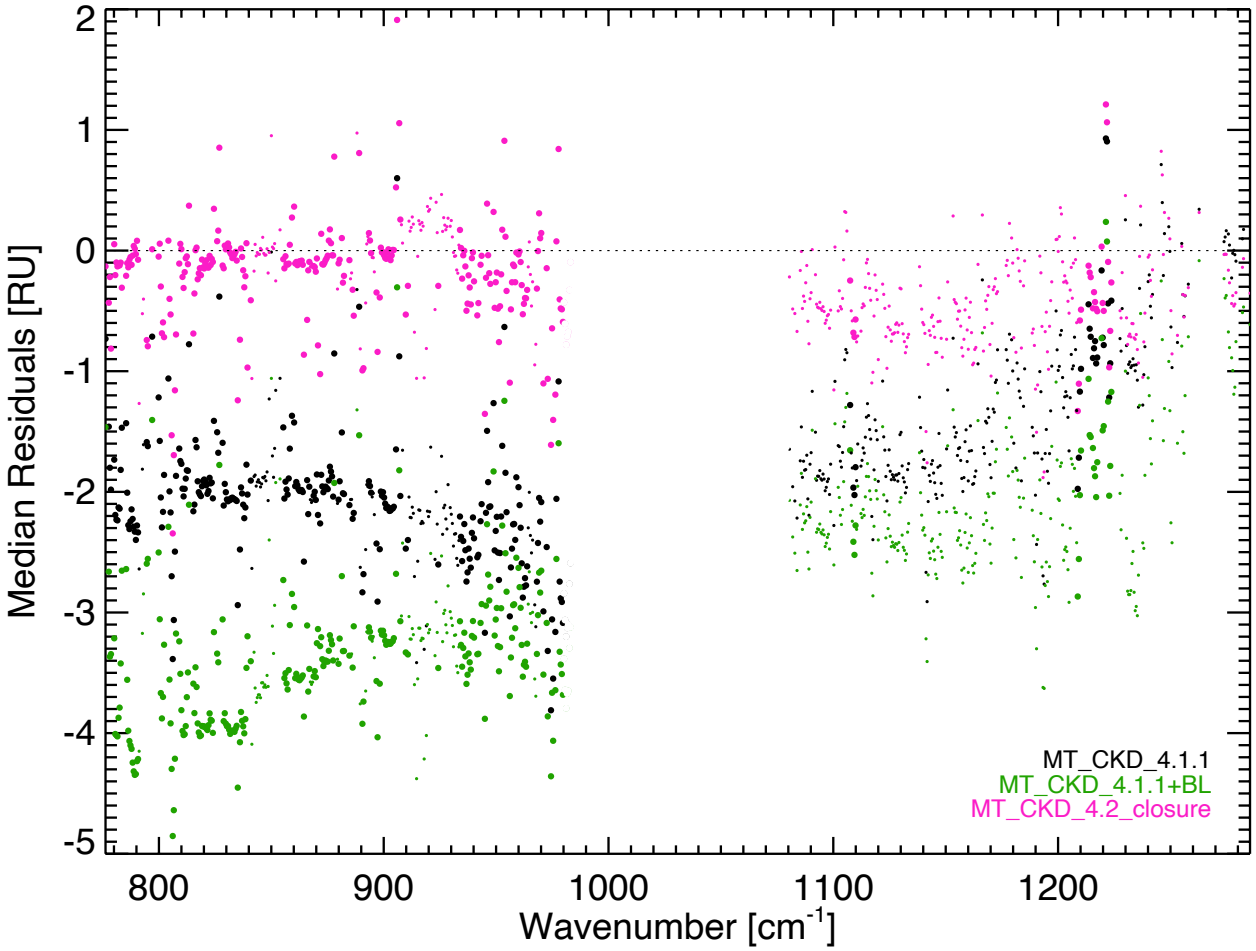

644 **Fig. 14.** Median of the PWV-binned residuals between AERI measurements at MAO and corresponding
645 LBLRTM calculations for the spectral region 780-1280 cm-1. The residual for each spectral point in a PWV
646 bin is computed as the mean of the "inner half" of all residuals in that bin, as described in the text. Residuals
647 are shown for MT_CKD_4.1.1 (black), MT_CKD_4.1.1+BL (green), and MT_CKD_4.2_closure (pink).
648 The distinction between large and small circles is the same as in Fig 12.
649

650 natural consequence of the assumption that the continuum in this region is due to the sum of
651 transitions centered hundreds of wavenumbers away from this window region (e.g. at 100 cm^{-1}),
652 with the continuum absorption from each transition decaying rapidly with increasing wavenumber
653 far (e.g. 800-1000 cm^{-1}) from its center. Based on its generally flat behavior from 900-1150 cm^{-1},
654 we conclude that the MT_CKD_4.2_closure (pink) curve in Figure 6 likely does not represent the
655 actual behavior of the foreign continuum in this region.
656
657 The optical depths in this region from the MT_CKD_4.2_closure foreign continuum are small.
658 Fig. 15a shows the derived foreign continuum optical depths at 980 cm^{-1} for all the cases in the

659 SGP data set. For a PWV of 2 cm, this optical depth is ~0.03. At SGP, if there existed an
660 atmospheric constituent with a small optical depth that scaled somewhat linearly with PWV, then
661 the impact in our analysis of such a constituent would be to inflate the derived foreign continuum
662 optical depth above the actual foreign continuum, and this artificial inflation would
663 disproportionately affect the derived foreign continuum most where it is smallest, i.e. the 980-1120
664 cm^{-1} region.
665
666 We now explore the possibility that the presence of aerosol in the skies over SGP can lead to such
667 an overestimation of the foreign continuum in our analysis. We obtain retrievals of aerosol optical
668 depth (AOD) with two markedly different approaches. We analyze periods coincident with the
669 daytime cases in our data set, and assume that the daytime result are representative of the entire
670 data set.
671
672 The first approach is to retrieve aerosol optical depth (AOD) and aerosol refractive index (RI)
673 within one hour of the AERI observations at SGP used in our analysis from the Aerosol Robotic
674 Network (AERONET; Dubovik & King, 2000). We estimate the AOD at ~1000 cm^{-1} (10 μm) from
675 AERONET observations at shortwave infrared (longest wavelength observed is 1640 nm) and
676 visible wavelengths coupled with assumptions about aerosol composition. We assume that the
677 AOD at longer wavelengths is dominated by contributions from an external mixture of coarse-
678 mode aerosols composed of deliquescent aerosol (produced through hygroscopic growth) and
679 mineral dust. The RI of deliquescent aerosol converges with that of water, 1.3 at 1640 nm and 1.2
680 +0.05i at 10 μm. The RI of dust depends on the composition, which is assumed to be iron-
681 oxide/hematite, a common soil component for the SGP region, having an index of refraction of
682 about 1.6 at 1640 nm and 2+0.02i at 10 μm. We allow the retrieved real part of the RI which spans
683 the range from 1.3 to 1.6 um to dictate the relative fraction of deliquescent aerosol to dust, and
684 thus infer the effective RI of the external mixture at 10 μm. Lastly, we use Mie scattering theory
685 to extend the measured AOD from shorter wavelengths out to ~10 μm. Clearly, the deliquescent
686 components should have a positive dependence on relative humidity and PWV, a fact that is borne
687 out in Fig. 15b. It is also intriguing and comfortingly consistent that the aerosol Angstrom exponent

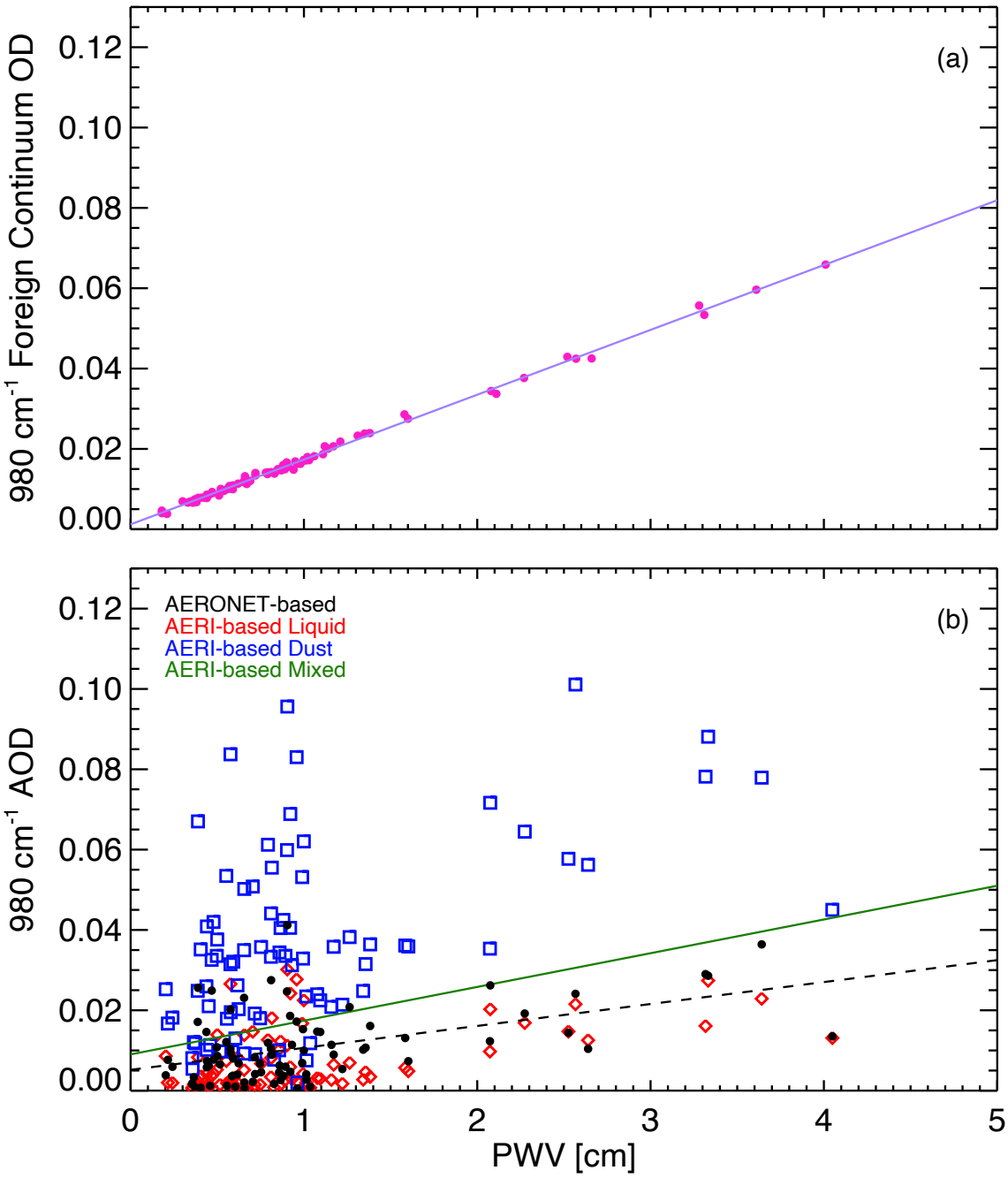

688 **Fig 15**. As a function of PWV for the daytime SGP AERI cases analyzed in this study: (a) Foreign
689 continuum optical depths from MT_CKD_4.2_closure; (b) Aerosol optical depths at 980 cm^{-1} derived from
690 AERONET measurements assuming a combination of a deliquescent aerosol and mineral dust (black points
691 with dashed black fitted line), retrievals from AERI observations at 2500-2860 cm^{-1} assuming a hydrated
692 sulfate aerosol (modeled as liquid, red diamonds), retrievals from AERI observations at 2500-2860 cm^{-1}
693 assuming montmorillonite spheres (dust, blue squares), and a 74/26 combination of the liquid and dust
694 aerosol assumptions, respectively (green linear fit, individual values not shown for figure clarity). Positive
695 correlation with PWV is seen for all modeled aerosols.

696 which typically varies between +2 to 0 for shorter wavelengths that are observed by the AERONET
697 system, to be moderately negative (-0.65) over the 1000-1100 cm^{-1} spectral range, driven by
698 changes in the refractive indices that vary notably in the longer wavelength range while being
699 virtually constant at shorter wavelengths.
700
701 The AODs values obtained from this analysis are shown as black circles in Fig. 15b. The results
702 in Fig. 15 show the estimated aerosol optical depth at 980 cm^{-1} is approximately half of the derived
703 foreign continuum optical depth. The aerosol optical depths scale reasonably linearly with PWV,
704 a consequence of the hygroscopicity of ambient aerosol whereby aerosols increase in size through
705 uptake of water vapor from the atmosphere, supporting the inference that the presence of aerosols
706 could have impacted our retrieval of foreign continuum coefficients.
707
708 The second approach to retrieve AOD uses the downwelling radiance observations made by the
709 AERI in the 2500-2860 cm^{-1} (3.5-4.0 μm) spectral region. Since at 2500-2860 cm^{-1} the
710 downwelling AERI radiance observation is dominated by scattered solar radiation during the
711 daytime, in this analysis we use only the daytime AERI samples that coincide with the AERONET
712 observations used in the first approach. We apply the physical-iterative Mixed-phase Cloud
713 Retrieval Algorithm (MIXCRA; Turner, 2005) to these AERI observations assuming that the
714 "cloud" was composed of aerosol particles (as was done in Turner 2008). We apply MIXCRA
715 with two distinct assumptions for aerosol type, one modeling the aerosol as liquid droplets
716 (representing a hydrated sulfate aerosol, shown as red diamonds in Fig. 15b) and the other
717 assuming montmorillonite spheres (i.e. dust, blue squares in Fig. 15b). The Interagency Monitoring
718 of Protected Visual Environments (IMPROVE; Malm et al., 1994) project provides measurements
719 of the mass of sulfate and soil particles that have diameters less than 2.5 μm. Using IMPROVE
720 data from Stilwell, OK (the closest IMPROVE site to ARM SGP during 2016-2018), over our
721 analysis period the mean ratio of the sulfate (liquid) aerosol mass to the sum of the sulfate and soil
722 mass was 0.74. We thus estimate the AOD at 980 cm^{-1} using $0.74 * AOD_{liquid} + 0.26 * AOD_{dust}$,
723 which yields somewhat higher AOD results (green line in Fig. 15b) as a function of PWV as the
724 first method that was based on AERONET observations.
725

These AOD estimates establish that it is plausible that the presence of aerosols has impacted the determination of the MT_CKD_4.2_closure foreign continuum coefficients shown in Fig. 6. However, the assumptions about aerosol properties made in the analyses above are quite speculative and the actual aerosol optical depths in the infrared window may differ significantly from those we derived. The possibility that our continuum coefficient retrieval has been impacted by aerosols leaves us with two choices, each of which has positive aspects and flaws. We could ignore this likely contamination of our derived foreign continuum (MT_CKD_4.2_closure in Fig. 6) and its problematic flat spectral behavior, and provide these foreign continuum coefficients in the next release of MT_CKD. This choice, when used in concert with our derived self continuum, would provide radiative closure with the AERI observations used in this study, but likely only because the water vapor continuum in this region inappropriately included some absorption that is actually due to aerosols. The other choice is to use the analysis above to make an estimate of the aerosol contribution to the derived foreign continuum, subtract this initial estimate of this aerosol contamination from MT_CKD_4.2_closure, and then use the MT_CKD line shape methodology (Mlawer et al., 2012) to compute foreign continuum coefficients that are in reasonable agreement with this difference. By construction, this option will have relative spectral behavior in the middle of the window that is similar to the behavior in MT_CKD_4.1.1 (also similar to that measured by Baranov and Lafferty, 2012), but will no longer provide closure with the AERI measurements since calculations using this foreign continuum would be missing optical depth unless a user explicitly included longwave aerosols in their calculation. Another drawback of this approach stems from the realization that any estimate of aerosol absorption in the infrared window would be highly uncertain, which would lead to significant uncertainty in the foreign continuum derived after the aerosol contribution is removed from the MT_CKD_4.2_closure foreign continuum.

Given this difficult choice, we feel that it is important for the MT_CKD continuum model to provide our best estimate of the actual foreign continuum despite the inherent uncertainty of the approach used to derive it. Therefore, we choose to derive the new foreign continuum for MT_CKD_4.2 by accounting for the estimated contribution of aerosols. Given that the use of MT_CKD_4.2 will not result in radiative closure, we will also provide the MT_CKD_4.2_closure foreign continuum as an alternate foreign continuum choice for users of MT_CKD.

In Appendix 2, we discuss the approach used to derive a specification of the foreign continuum in the infrared window that is consistent with both a) the closure analysis described in section 3.2 interpreted in light of the aerosol absorption analysis above (i.e. in Fig. 15b) and b) the relative spectral behavior of the foreign continuum in this region given by the MT_CKD line shape calculation. This derivation uses the MT_CKD line shape formalism to compute foreign continuum coefficients from 780-1250 cm^{-1} that, once subtracted from the coefficients in MT_CKD_4.2_closure, is roughly consistent with the properties (AOD and Angstrom exponent in the infrared window) of the aerosol absorption derived from the AERONET measurements.

The foreign continuum coefficients (labeled as MT_CKD_4.2) that result from this aerosol-removing procedure are shown as a purple curve in Fig. 6. Since a similar line shape formalism was used to derive these coefficients as was done for MT_CKD_1.0 (virtually the same as MT_CKD_4.1.1), the MT_CKD_4.2 coefficients also have a minimum near 1100 cm^{-1}. The spectral behavior of the MT_CKD_4.2 coefficients now more closely resemble the Baranov and Lafferty (2012) measurements than the derived coefficients before the assumed impact of aerosols was accounted for. This agreement with an independent measurement of foreign continuum absorption provides a measure of confidence that the aerosol adjustment has some validity.

Given the modification made to the foreign continuum to obtain MT_CKD_4.2 from MT_CKD_4.2_closure, a few observations are worth pointing out. First, calculations using MT_CKD_4.2 do not provide radiative closure with either the SGP or MAO AERI observations. As shown in Fig. 12, impressive agreement between the observations and calculations is obtained using MT_CKD_4.2_closure, but this closure to some extent is due to the assumed inclusion of the radiative effects of aerosols in that continuum version. Removing that contribution, as has been done to construct MT_CKD_4.2, destroys that radiative closure. Therefore, a comparison between the observations and calculations using MT_CKD_4.2 is not informative and we do not include those results on Fig. 12. Second, the strong agreement shown in Fig. 14 between the MAO AERI measurements and calculations using MT_CKD_4.2_closure occurs even though that continuum version is assumed to include the impact of aerosols at SGP. This is possibly due to reasonably similar aerosol loading at SGP and MAO, both continental sites, and the reduced relative radiative impact of aerosols at MAO compared to SGP given the higher PWV amounts at MAO. Third,

some consideration should be given to the results for MT_CKD_4.1.1 and MT_CKD_4.1.1+BL in Fig. 12 in light of the need for the aerosol adjustment detailed above. In both cases, the foreign coefficients in the infrared window in these continuum versions were not derived from field studies, so they could not have been impacted by aerosols in the same way that the MT_CKD_4.2_closure coefficients are assumed to have been. The window self continuum used in these calculations (the same in both versions) was derived by Turner et al. (2004), a radiative closure field study at SGP. It is reasonable that atmosphere opacities in this previous study were affected by a similar aerosol loading as in the current study, and that the self continuum coefficients derived in Turner et al. (2004) implicitly include the radiative effects of the aerosols. Therefore, no further adjustment to these versions is needed to evaluate the behavior of their associated residuals, and it is fair to compare them to those obtained using MT_CKD_4.2_closure, as is done in Fig. 12.

4.6 Uncertainty analysis

The determination of the uncertainties in our retrieved values of self continuum coefficients, foreign continuum coefficients, and the temperature dependence of the self continuum in the infrared window is challenging. Consideration must be given to typical uncertainties in radiative closure studies, such as those due to the radiometric instrument and the specification of the atmospheric profile, as well as complexities in this study such as the consideration of the role of aerosols in the derivation of the foreign continuum. We here provide an analysis of key sources of uncertainty in our derived continuum values.

Our uncertainty analysis is based on the realization that the set of retrieved continuum values (self, foreign, and temperature dependence of self) in MT_CKD_4.2_closure at a spectral point is not the only combination of continuum values that would provide suitable agreement between the observed and calculated radiances. The retrieved values in most small spectral windows (e.g. 10 cm^{-1}, the spacing at which MT_CKD stores continuum coefficients) show some variability (see Fig. 13), as do the final residuals shown in Fig. 12. Therefore, we must consider to what extent the retrieved continuum values can be modified while maintaining "good agreement" between the measurements and calculations. How we define "good agreement" must reflect the uncertainties in both the measurements and calculations. Therefore, we must first analyze individual factors that

lead to uncertainty in the spectral residuals, and then combine these factors to get a total spectral uncertainty. Then, at each spectral point the total uncertainty in the radiance residuals provides a foundation for evaluating other sets of possible retrieved continuum values – if the residuals generally stay within this uncertainty for all PWV bins for a given set of continuum values, then these alternate values are considered plausible. Using this approach, we can find limits past which good agreement is no longer possible, therefore defining the uncertainty in each continuum parameter.

Sources of uncertainty in the radiance residuals arise from the uncertainty in a) the specification of trace gas abundances, b) the temperature and water vapor profiles, and c) the AERI radiance measurements. The method used to determine the uncertainty due to the trace gas specification is discussed above and is shown in Fig. 10a. The uncertainty due to temperature and water vapor profiles is evaluated through the use of a reasonable alternate specification of these profiles, given by sonde measurements in which the measured water vapor profile has been scaled to attain agreement with the brightness temperature measured by a collocated microwave radiometer. This approach to specifying the temperature and water vapor profiles in radiative closure studies has often been utilized in past analyses (e.g. Turner et al., 2004; Mlawer and Turner, 2016; Turner et al., 2016). Fig. 10b shows the spectral RMS differences between calculations that use these alternate profiles and those that use the profiles employed in the analysis described above. Finally, the AERI uncertainty is assigned a value of 0.1 RU based on the random error spectra of the instrument, as estimated by the calibration equation used in its processing (Revercomb et al., 1988; Knuteson et al, 2004b).

In addition to these contributions to the uncertainty in the residuals, it is clear from Fig. 11 that the variability of the final (pink) residuals as a function of PWV adds an additional challenge in determining what constitutes agreement between measurements and calculations for given continuum parameters. To account for this uncertainty, we compute the interquartile differences of the binned residuals for each spectral point, which is shown in Fig. 10c, and include this as an additional term in the uncertainty calculations.

We assume that these four sources of uncertainty in the residuals are independent and add these values in quadrature at each spectral point to get the spectrum of total uncertainty, shown as balck circles in Fig. 10d. Given that the determination of continuum coefficients enforces a degree of spectral smoothness on the coefficients, rather than considering the spectral uncertainty shown in Fig. 10d we group the uncertainty values in 20 cm^{-1} intervals. We take a conservative approach in assigning the final uncertainty value in each interval by using the RMS of the spectral values, which are also shown in Fig. 10d.

Now we compute alternate sets of continuum coefficients at each spectral point to determine the maximum that each continuum coefficient can be perturbed while keeping the residuals as a function of PWV within the uncertainty in the residuals computed above. We illustrate this procedure for the self continuum. First, all self continuum coefficients in MT_CKD_4.2_closure are increased, in turn, by 5,10, 20, and 30%. For each perturbation, we then follow the procedure detailed in Sec. 4.2 to derive optimal spectral values for the foreign continuum and the temperature dependence of the self continuum. For illustration, quadratic fits to the resulting residuals from these optimal perturbations are shown in Fig. 16 as a function of PWV for all spectral elements in the 20 cm^{-1} bins that contain the wavenumbers in Fig. 11, as well as the 1200-1220 cm^{-1} bin. (The wavenumber corresponding to each curve shown is not identified since this analysis is being performed collectively for the spectral elements grouped in each interval.) As an example, Fig. 16b shows that, for the 940-960 cm^{-1} region, the coefficients obtained starting with a 5% perturbation to the self continuum result in the residuals staying within the unshaded region, which corresponds to the radiance uncertainty in this region. That is, a 5% perturbation to the self continuum results in measurement-calculation agreement (as defined above). In contrast, the curves corresponding to a 10% perturbation do not remain withing the unshaded region, so a 10% change to the self continuum does not lead to agreement. Based on the set of perturbation calculations, for this spectral region we determine that the self continuum uncertainty is 7%. We perform this analysis for all 20 cm^{-1} bins – the resulting self continuum uncertainty values are shown as thin purple error bars on the MT_CKD_4.2 curve in Fig. 4.

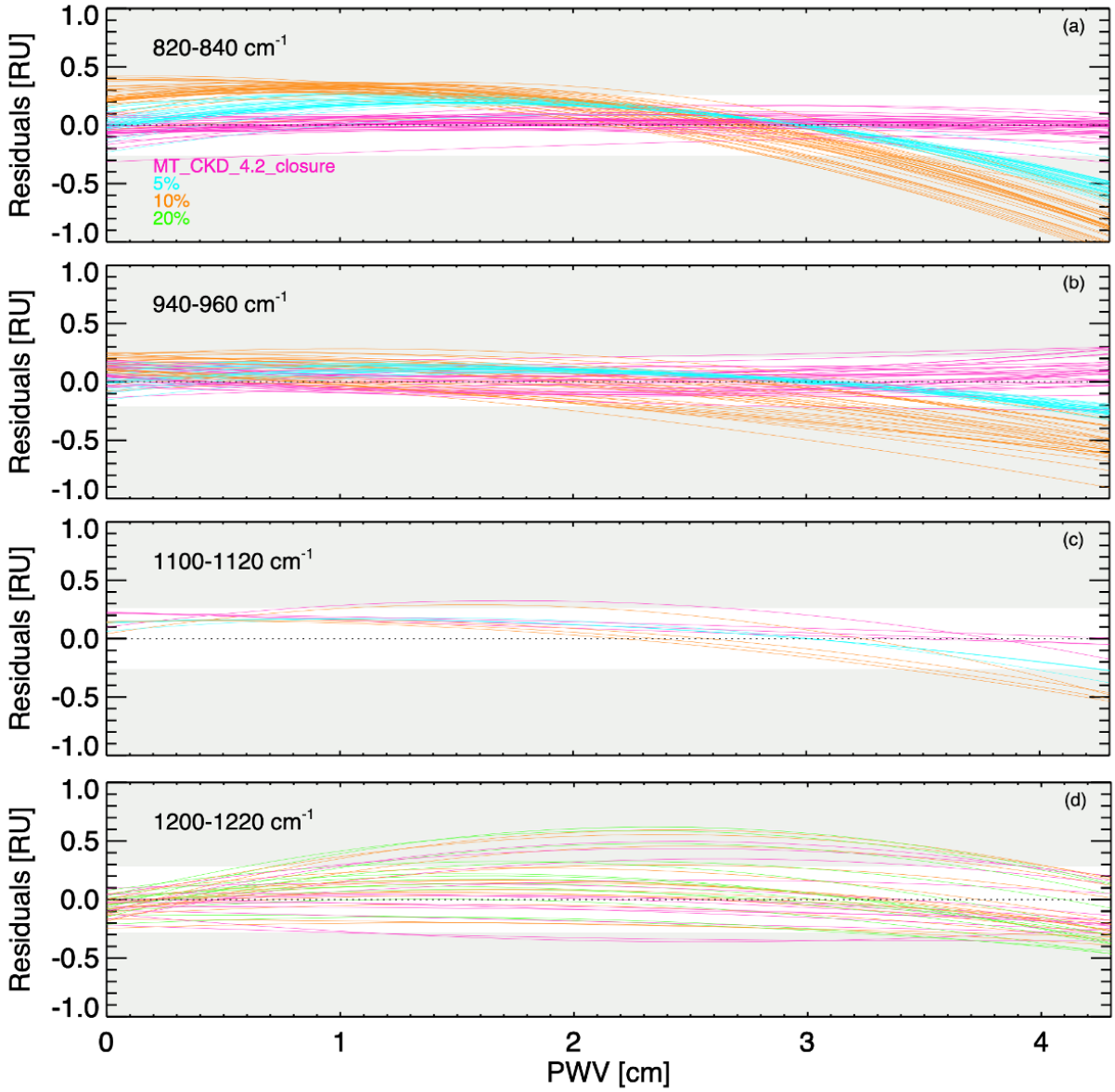

878 **Fig. 16.** For four example 20 cm^{-1} spectral regions, quadratic fits to the residuals are shown for
879 MT_CKD_4.2 closure (pink) and variations in which the self continuum has been increased by 5% (cyan),
880 10% (orange), and 20% (green), with the foreign continuum and self continuum temperature dependence
881 rederived for each perturbation (as described in text). Curves are shown for the spectral elements
882 corresponding to the large circles in Fig. 12 and not all colored curves are shown on all panels for clarity.
883 The regions shaded gray on each panel are outside of the total uncertainty for the respective panels. The set
884 of colored curves that do not typically stay within the unshaded region shows that the corresponding
885 perturbation to the self continuum is greater than the self continuum uncertainty in these regions.
886

887
888 We repeat this procedure starting with a series of foreign continuum perturbations, determining
889 optimal spectral values for the self continuum and the temperature dependence of the self for each
890 perturbation. An analysis similar to the one described above for the self continuum results in the
891 foreign continuum uncertainty values shown in Fig. 6 for MT_CKD_4.2_closure in the 20 cm^{-1}
892 spectral bins. Note that in some spectral regions (primarily the ozone-dominated region from 980-
893 1080 cm^{-1}) this method is not able to determine a reliable uncertainty value for the foreign
894 continuum due to the large uncertainty in the residuals and combined behavior of the self and self
895 temperature dependence in response to the foreign perturbations. In this region, we compute an
896 uncertainty by combining the uncertainty at its boundaries (i.e. 970 and 1090 cm^{-1}) with the
897 difference in continuum values resulting from alternate reasonable ways to span the gap in
898 retrieved (i.e MT_CKD_4.2_closure) foreign continuum values from 980-1080 cm^{-1}. We discuss
899 below the uncertainty associated with the MT_CKD_4.2 foreign continuum coefficients.
900
901 Finally, we follow this procedure beginning with a series of perturbations to the temperature
902 dependence of the self continuum, determining optimal spectral values for the self and foreign
903 continuum. However, in all spectral bins this method is not able to derive reliable estimates of the
904 uncertainty in the self temperature dependence. Even though the AERI datasets used in our study
905 are not able to effectively constrain the self continuum temperature dependence, below we
906 consider the results of other studies to determine rough estimates of the uncertainty in the
907 MT_CKD_4.2 temperature dependence parameters.
908
909 The continuum parameters derived from the AERI measurements are not independent – for
910 example, an increase in the derived self continuum value at a spectral point would necessitate a
911 lower associated foreign continuum value in order to maintain overall radiative closure at that
912 point. Therefore, for the uncertainty analysis it is informative to understand how these two
913 continuum values co-vary. We therefore perform a retrieval of the foreign continuum value for a
914 small perturbation to the self continuum (with the temperature dependence kept fixed). Fig. 17
915 shows the ratio of the foreign and self continuum changes in these retrievals for the window region.
916 Consideration of the uncertainty in either of these quantities should be done in the context of their
917 combined behavior.

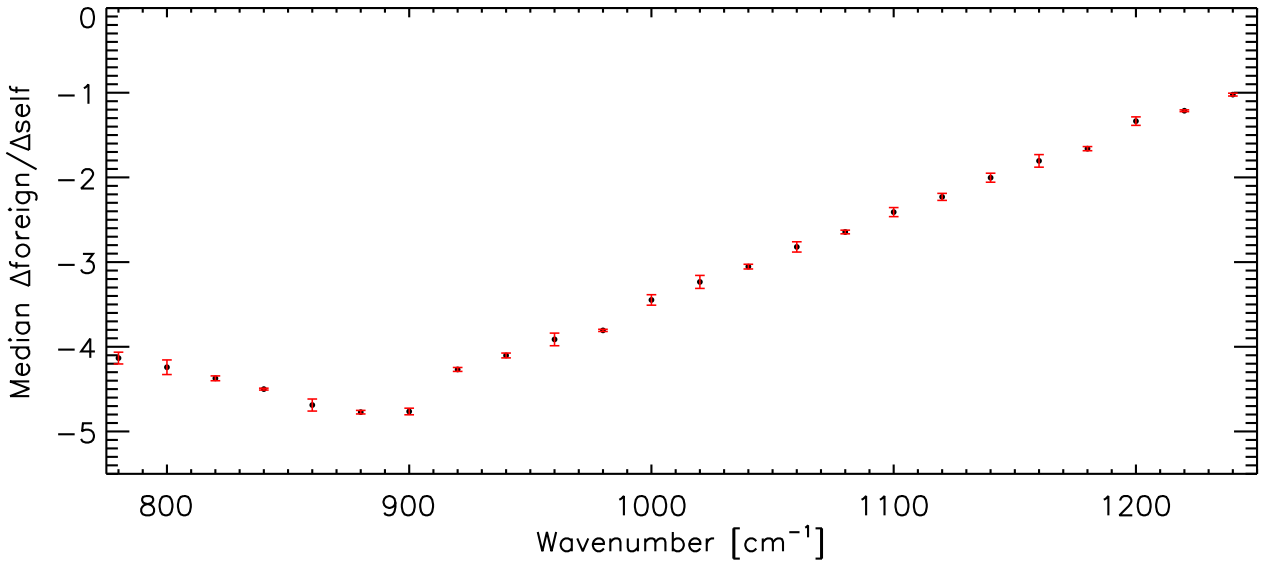

Figure 17. Ratio of change in derived foreign continuum value to a small perturbation in the self continuum value.

The derivation above of uncertainty values for the MT_CKD_4.2_closure foreign continuum coefficients does not directly apply to the MT_CKD_4.2 foreign continuum, which was derived using information other than the AERI measurements at SGP and MAO. The method used to derive these foreign continuum coefficients was quite speculative, involving a) the MT_CKD_4.2_closure foreign continuum coefficients, b) 'best guess' estimates of the aerosol optical properties in the infrared window, and c) a calculation using the MT_CKD line shape formulation constrained to foreign continuum values outside the infrared window and those inferred in the window from a) and b). The highly conjectural nature of this approach presents large challenges from using it alone to determine reasonable uncertainty estimates. Instead, we use all available information (MT_CKD_4.2 closure uncertainties, analysis of the method used to derive MT_CKD_4.2 foreign continuum, and the laboratory measurements shown in Fig. 6) to provide users of MT_CKD with a rough estimate of the uncertainty of MT_CKD_4.2 in specifying water vapor foreign continuum absorption in this region. The upper limit of the uncertainty must reflect the possibility that the impact of aerosols on the derivation of foreign continuum is negligible, so the corresponding uncertainty values are determined by the difference between MT_CKD_4.2 and MT_CKD_4.2_closure (accounting for its own uncertainty). Reassuringly, even though this uncertainty estimate did not consider the single-frequency measurement of Cormier et al. (2005), the upper envelope of the MT_CKD_4.2 uncertainty estimates (shown with

939 thin purple vertical bars in Fig. 6) allow the possibility that the foreign continuum is as great as
940 that value. With respect to the lower limit of the MT_CKD_4.2 uncertainty, we explicitly consider
941 the results from the Baranov and Lafferty (2012) study, which is generally lower than the
942 MT_CKD_4.2 coefficients but clearly represent possibly valid values. We compute the uncertainty
943 by adding in quadrature: a) the difference between MT_CKD_4.2 and MT_CKD_4.1.1+BL and
944 b) the uncertainty in the coefficients determined in Baranov and Lafferty (2012). The resulting
945 MT_CKD_4.2 uncertainty estimates are generally consistent with the results we would have
946 attained in our study had we adjusted the MT_CKD_4.2_closure coefficients to account for the
947 impact of aerosol optical depths somewhat greater than we actually assumed (i.e. consistent with
948 the relative aerosol loading of the green line compared to the black line in Fig. 15b). In Fig. 6, we
949 denote MT_CKD_4.2 foreign continuum uncertainty estimates with open-ended vertical lines to
950 contrast the broader perspective used to determine these values with the AERI-based uncertainty
951 estimates used for the MT_CKD_4.2_closure foreign coefficients, which are denoted as (pink)
952 vertical lines with end caps. To conclude, MT_CKD users should be aware of possible
953 considerable uncertainties when utilizing MT_CKD_4.2 foreign continuum coefficients.
954
955 With a similar perspective, we also consider all available information to determine rough
956 uncertainty estimates for the MT_CKD_4.2 temperature dependence exponents, which are not able
957 to be effectively constrained by the AERI measurements used in this study. The upper limit of the
958 uncertainty needs to include the (refit) values from the Burch and Alt (1984) study (accounting for
959 that study's uncertainty) since we view its results with confidence due to the close agreement of
960 its derived self continuum coefficients with those from the current study. (See Fig. 4.) When
961 considering the lower limit of possible values of the temperature dependence exponents, we do not
962 consider the values derived by Baranov et al. (2008) with great confidence since the self continuum
963 coefficients determined in that work do not agree with those derived in the current study. As a
964 result, there is little information to go on to constrain the lower uncertainty limit. We therefore
965 define the uncertainty bars to be equal in the positive and negative directions (adjusted to ignore
966 the bump in the MT_CKD_4.2 exponents centered at 780 cm^{-1}).
967
968 **5. Analysis of MT_CKD_4.2**

969 Fig. 4a shows the final self continuum coefficients (MT_CKD_4.2) derived in this study along
970 with previous versions of the continuum model. With MT_CKD_4.1.1 used as a reference, Fig. 4d
971 shows the relative spectral behavior of MT_CKD_4.2 (and its uncertainty), the most recent
972 laboratory measurements from three groups, previous versions of CKD and MT_CKD based on
973 field studies that have been adjusted (as described in section 2) to account for a larger foreign
974 continuum than utilized in their respective original derivations, and the similarly adjusted results
975 from the field study by Taylor et al. (2003). Although these self continuum specifications do not
976 all agree, it can be argued the evidence clearly suggests that MT_CKD_4.1.1 is too strong across
977 the entire infrared window. For wavenumbers less than 900 cm^{-1}, most of the results shown agree
978 that the self continuum is 8-15% weaker than MT_CKD_4.1.1. Exceptions to this are the study of
979 Baranov et al. (2008) and the adjusted coefficients of CKD_2.1, which is based on the Westwater
980 et al. (1995) study. The adjustment made to CKD_2.1 only accounts for a change in the foreign
981 continuum, but another significant bias in the Westwater et al. (1995) results likely is present. The
982 type of sonde used in the calculations in that study to specify the water vapor fields were
983 subsequently shown to have a dry bias of 4-8% due to contamination of the relative humidity
984 sensor by the packaging (Wang et al. 2002; Turner et al. 2003). Given the squared dependence of
985 the self continuum on water vapor abundance, a rough estimate suggests that the self continuum
986 coefficients derived in that study were likely too high by at least 8%. As a result, the CKD_2.1_adj
987 curve in Fig. 4d likely needs to be shifted downward by that amount to account for this bias. Given
988 that, all results shown in Fig. 4d for 780-900 cm^{-1} exhibit agreement except for a single outlier
989 result by Baranov et al. (2008). The good agreement of these self continuum specifications persists
990 over the rest of infrared window with the exception of MT_CKD_1.0_adj, which is based on the
991 adjusted results of the Turner et al. (2004) study. It is encouraging that the accurate cavity ring
992 down measurement by Cormier et al. (2005) agrees within the tight uncertainty bound of the
993 current study. In spectral regions in which the uncertainty estimates of the current study are small,
994 the results of the current study are in agreement with all laboratory measurements by Burch and
995 Alt (1984) and most of the adjusted values from the Taylor et al. (2003) field analysis.
996
997 The MT_CKD_4.2 foreign continuum coefficients, which have been adjusted to account for the
998 presence of aerosols at SGP as described above, are shown in Fig. 6. Since its behavior near its
999 minimum results from a similar line shape calculation as MT_CKD_1.0, it is not surprising that

1000 the shapes of these two continuum versions are similar in this region. However, MT_CKD_4.2 is
1001 ~5 times greater than its predecessor in the 960-1150 cm^{-1} region, and 2-4 times greater in the
1002 regions of the infrared window outside this minimum region, i.e. where the continuum is stronger
1003 and the AERI observations provide a greater constraint. In these regions, the MT_CKD_4.2
1004 uncertainty estimates do not include the MT_CKD_1.0 (equivalent to MT_CKD_4.1.1)
1005 coefficients. Despite the quite speculative approach used to adjust the derived foreign continuum
1006 for aerosols, there is some correspondence of these continuum values with the Baranov and
1007 Lafferty (2012) experimental values. By construction, the MT_CKD_4.2 uncertainty estimates
1008 include the Baranov and Lafferty (2012) values.
1009
1010 The self continuum temperature dependence exponents derived in this study are shown in Fig. 5.
1011 As can be seen in Fig. 13, the retrieval of this exponent for 780-980 cm^{-1} shows less variability
1012 than at higher wavenumbers in the region analyzed. Also shown in Fig. 5 are the exponents in
1013 MT_CKD_4.1.1 as well as values derived from the laboratory studies of Baranov et al. (2008),
1014 Cormier et al. (2005), and Burch and Alt (1984). (It is important to note that the exponents shown
1015 on this figure for these studies are for the continuum coefficients as defined in MT_CKD, which
1016 are specified for a reference density and do not include the radiation term.) The Burch and Alt
1017 (1984) study is represented by two sets of alternate temperature exponent values, one based on the
1018 data in the table provided in that work associated with its Fig. 2 and one based on our analysis of
1019 the plotted values in its Fig. 2. It is clear from Fig. 5 that there is no consensus between the
1020 specifications of the self continuum temperature exponents that are displayed. The MT_CKD_4.2
1021 values are in excellent agreement at the single location analyzed in Cormier et al. (2005) and are
1022 closer than MT_CKD_4.1.1 to the Baranov et al. (2008) values in the region where the AERI
1023 analysis is most definitive. Above 980 cm^{-1}, the MT_CKD_4.2 exponents diverge from the
1024 Baranov et al. (2008) values, but there is some suggestion in Fig. 13 that a justifiable choice could
1025 have been made to decrease the MT_CKD_4.2 exponents further, thereby bringing them in closer
1026 agreement to Baranov et al. (2008). Our inability to determine uncertainty values for the exponents
1027 based on the AERI analysis alone reflects that a wide range of exponent values are able (after
1028 adjustments to the self and foreign coefficients) to provide radiative closure with the observations
1029 within the uncertainty in the residuals. Therefore, the exponent values shown in Fig. 5 should be

considered numerical values that optimize the radiative closure results rather than an attempt at a definitive determination of the spectral behavior of a physical quantity.

6. Impact

6.1 Broadband fluxes and heating rates

The impact of the modified water vapor continuum in MT_CKD_4.2 on broadband radiative fluxes (Fig. 18) depends strongly on the moisture content of a profile. (See Table 1 for PWV values.) For dry winter profiles, the continuum modifications cause a modest decrease in upward flux and an increase in downward flux from the increased opacity due to the larger foreign continuum, which outweighs the decrease in the self continuum. The difference in downwelling flux sharply increases at ~800 mb for the tropical or summer profiles (Fig. 18d). In the tropical atmosphere, for example, the downwelling flux at the surface decreases by more than 4 W/m^2 as a result of the overall decrease in atmospheric opacity in the IR window caused by the 10-30% decrease in the dominant water vapor self continuum. The magnitude of the change in upwelling flux (Fig. 18c) due to the use of MT_CKD_4.2 is much smaller than for the downwelling flux since the radiating temperature of lower atmosphere, the region in which the self continuum emits radiation, does not differ too greatly from the surface temperature. Therefore, decreased absorption of surface-emitted radiation by the self continuum in MT_CKD_4.2 is partially compensated by its decreased emission of the lower atmosphere at a (typically) slightly lower temperature. Nevertheless, the upwelling radiation does increase by ~0.7 W/m^2 in the mid-troposphere and 0.5 W/m^2 at the top of the tropical atmosphere, with smaller but still notable increases for atmospheres with moderate PWV values.

The analysis in this study shows that the total atmospheric opacity in the infrared window is less than had previously been thought, but the exact partitioning between the water vapor continuum and aerosols, i.e. the difference between MT_CKD_4.2 and MT_CKD_4.2_closure, is quite uncertain. Fig. 19, which shows the analogous results to those in Fig. 18 for calculations using MT_CKD_4.2_closure, may better reflect the impact on fluxes resulting from this study since all sources of opacity in the infrared window are accounted for. In drier conditions the increase in atmospheric opacity in MT_CKD_4.2_closure results in an increase in downwelling flux at the surface, consistent with the change in the measurement-calculation residuals (e.g. Fig. 11) for

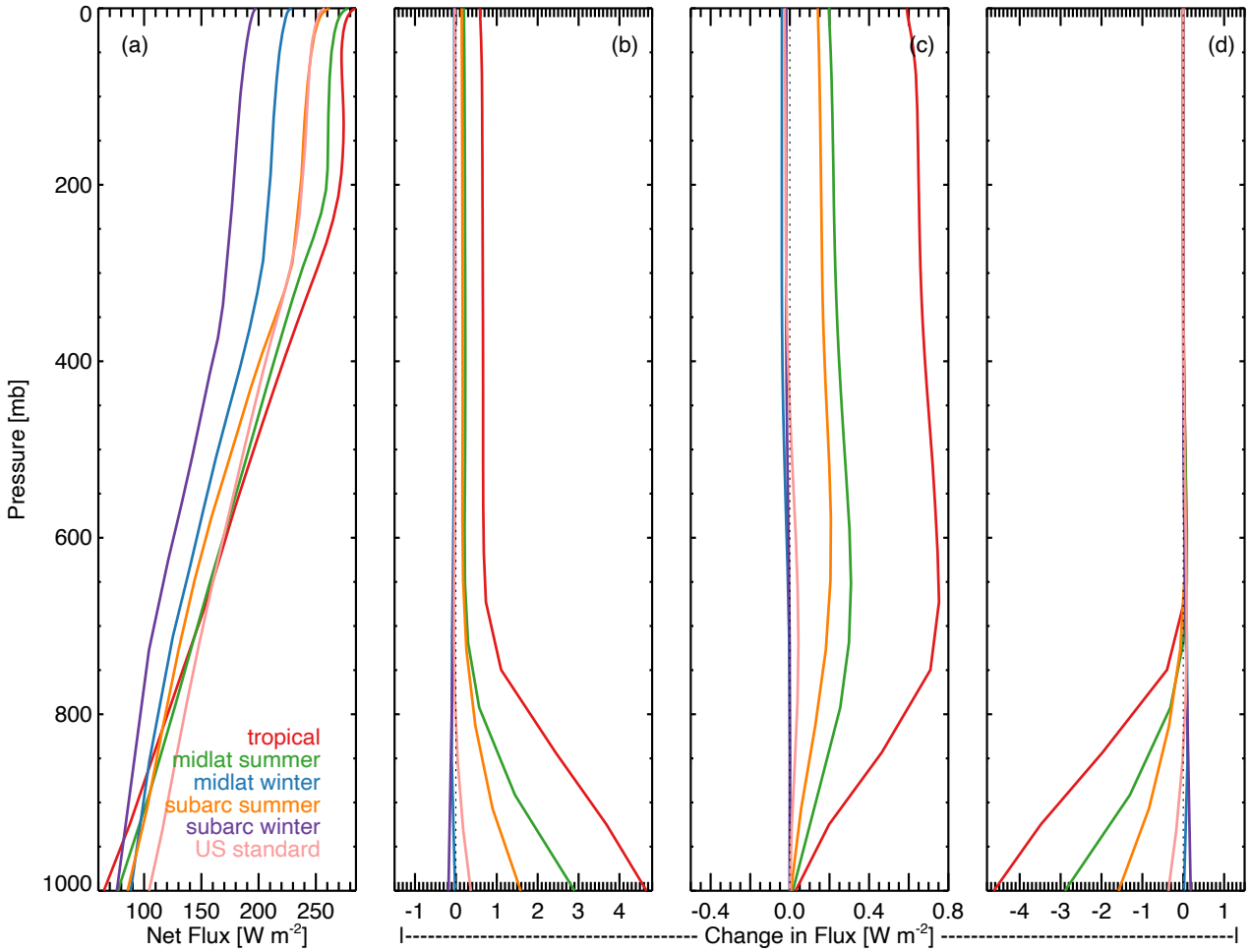

Fig. 18. For six standard atmospheres: (a) longwave net flux from LBLRTM calculations using MT_CKD_4.1.1; (b) Difference in net flux between calculations that use MT_CKD_4.2 and calculations that use MT_CKD_4.1.1; (c) Difference in upward flux between MT_CKD_4.2 and MT_CKD_4.1.1; (d) Difference in downward flux between MT_CKD_4.2 and MT_CKD_4.1.1.

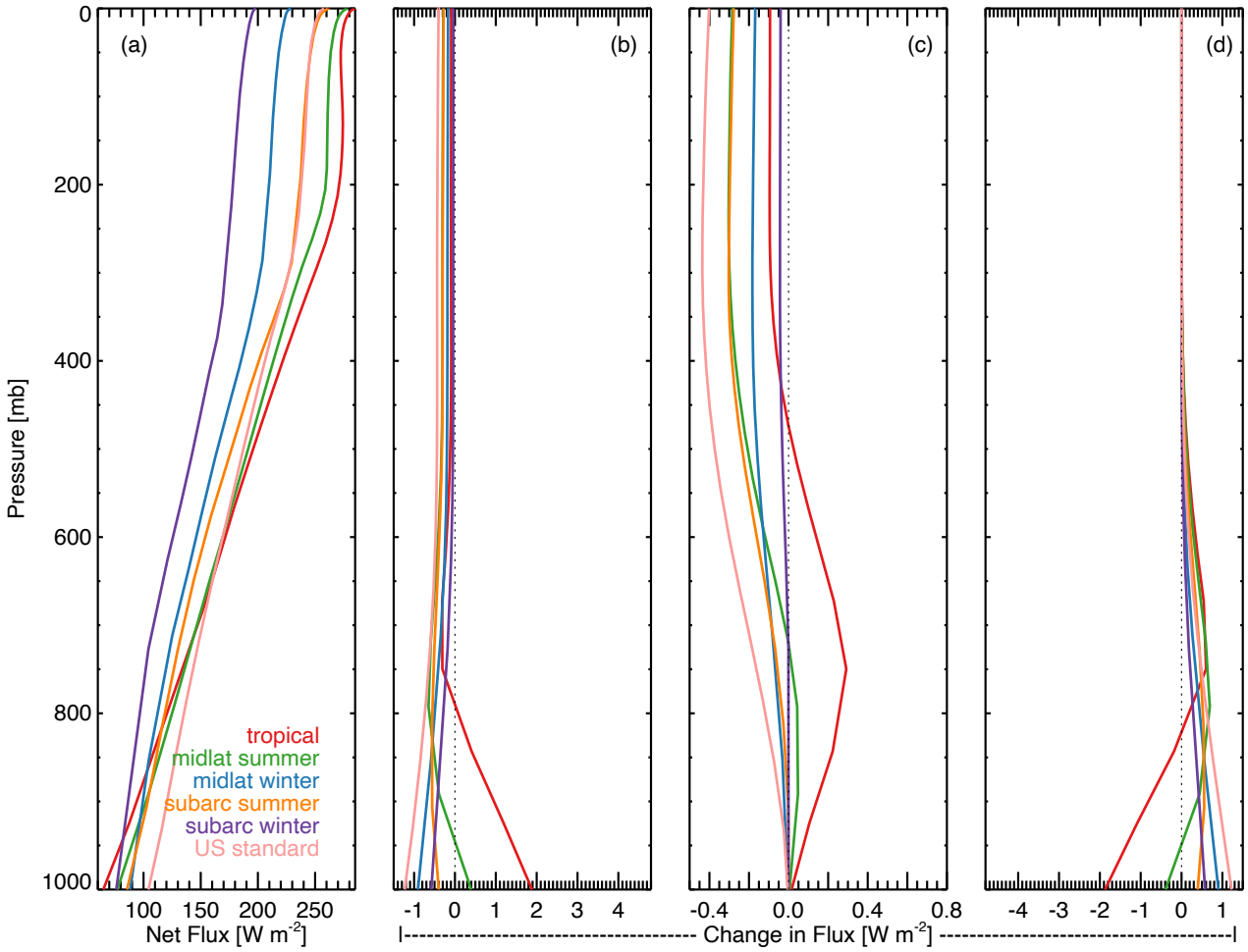

1066 **Fig. 19**. Same as Fig. 18, but differences in (b) through (d) are for calculations that use
1067 MT_CKD_4.2_closure and those that use MT_CKD_4.1.1.
1068

similarly low PWVs. For higher PWV cases, the decreased overall absorption, driven by the decrease in the optical depth of the dominant self continuum, results in a decrease in surface downwelling flux. For upwelling flux at TOA, all cases shown in Fig. 19 show a decrease due to the continuum changes. Even for moist cases in which the magnitude of the increase in foreign continuum optical depth is less than the decrease in the self continuum, the change in foreign continuum results in an upwelling flux difference of larger magnitude since foreign continuum emission occurs higher in the atmosphere, i.e. at temperatures that differ more with respect to the surface temperature than the self continuum emission temperature. Crucially, the impact on fluxes may be very different when the aerosol properties (*e.g.* loading) differ greatly from the aerosols at the location analyzed in this study since the presumed contribution of aerosols is included in the foreign continuum in these calculations.

Fig. 20 shows the difference in longwave heating rates due to modifications in MT_CKD_4.2. The largest changes occur in moist atmospheres, with the heating rates increasing (less cooling) by ~5% in the lower layers of the atmospheres. Fig. S1 presents analogous results for MT_CKD_4.2_closure.

6.2 Top of the atmosphere brightness temperature

Fig. 21 shows the change in the brightness temperature at the top of the atmosphere between LBLRTM calculations that use MT_CKD_4.2 and those that use MT_CKD_4.1.1. These differences increase with the PWV of the atmospheric profile, with maximum of ~+0.3 K for the tropical atmosphere, and do not show a great deal of spectral variability throughout the infrared window. This suggests that use of the new continuum version will lead to a non-trivial change in surface temperatures retrieved using satellite radiances in the infrared window. Fig. S2 provides analogous results for MT_CKD_4.2_closure. For all but the moistest of the profiles shown, the change in brightness temperature is negative due to the additional absorption provided by the aerosol assumed to be included in the foreign continuum.

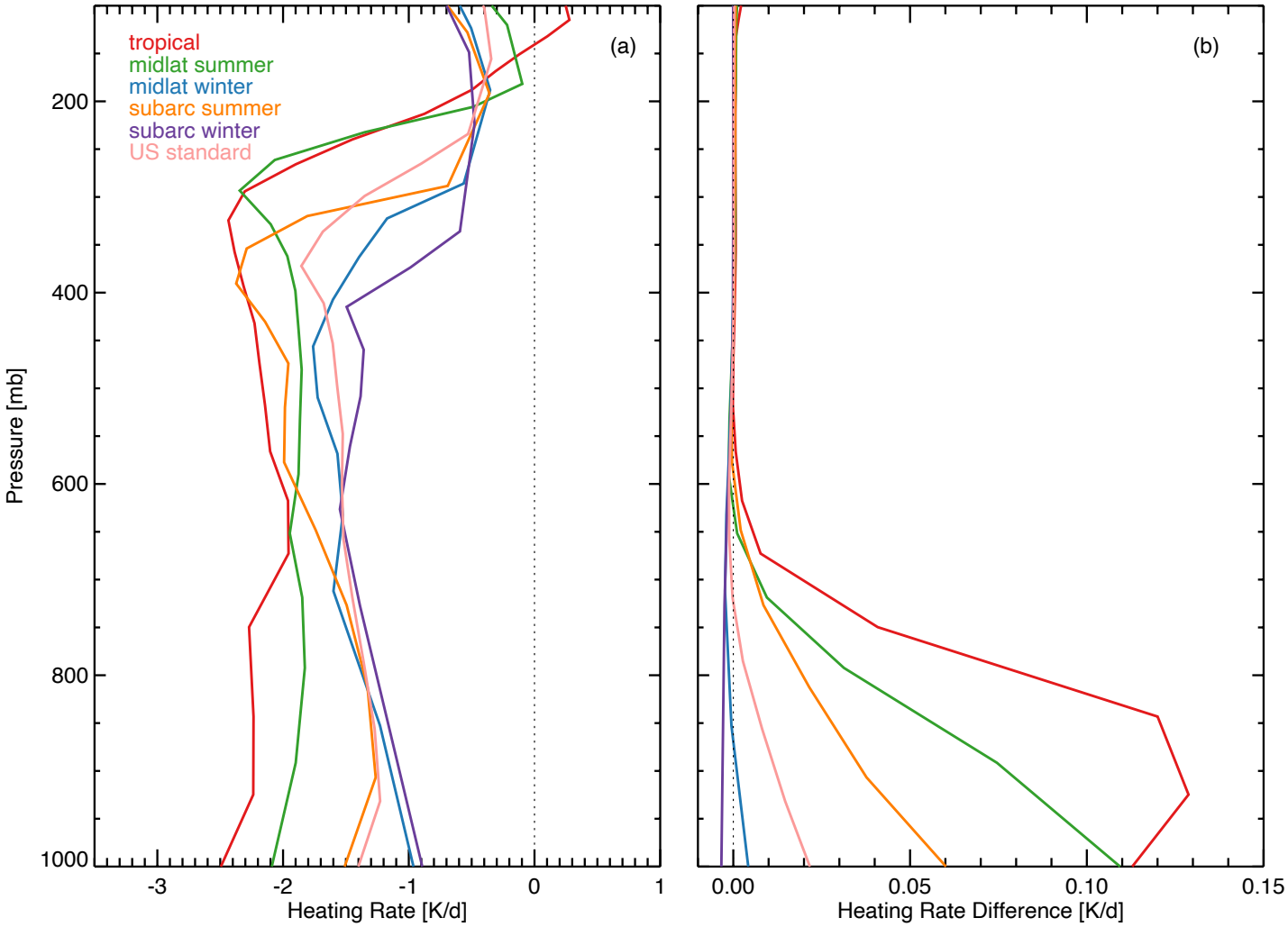

1097 **Fig. 20.** For six standard atmospheres: (a) longwave heating rates from LBLRTM calculations using
1098 MT_CKD_4.1.1 and (b) difference in heating rates between calculations that use MT_CKD_4.2 and
1099 calculations that use MT_CKD_4.1.1.
1100

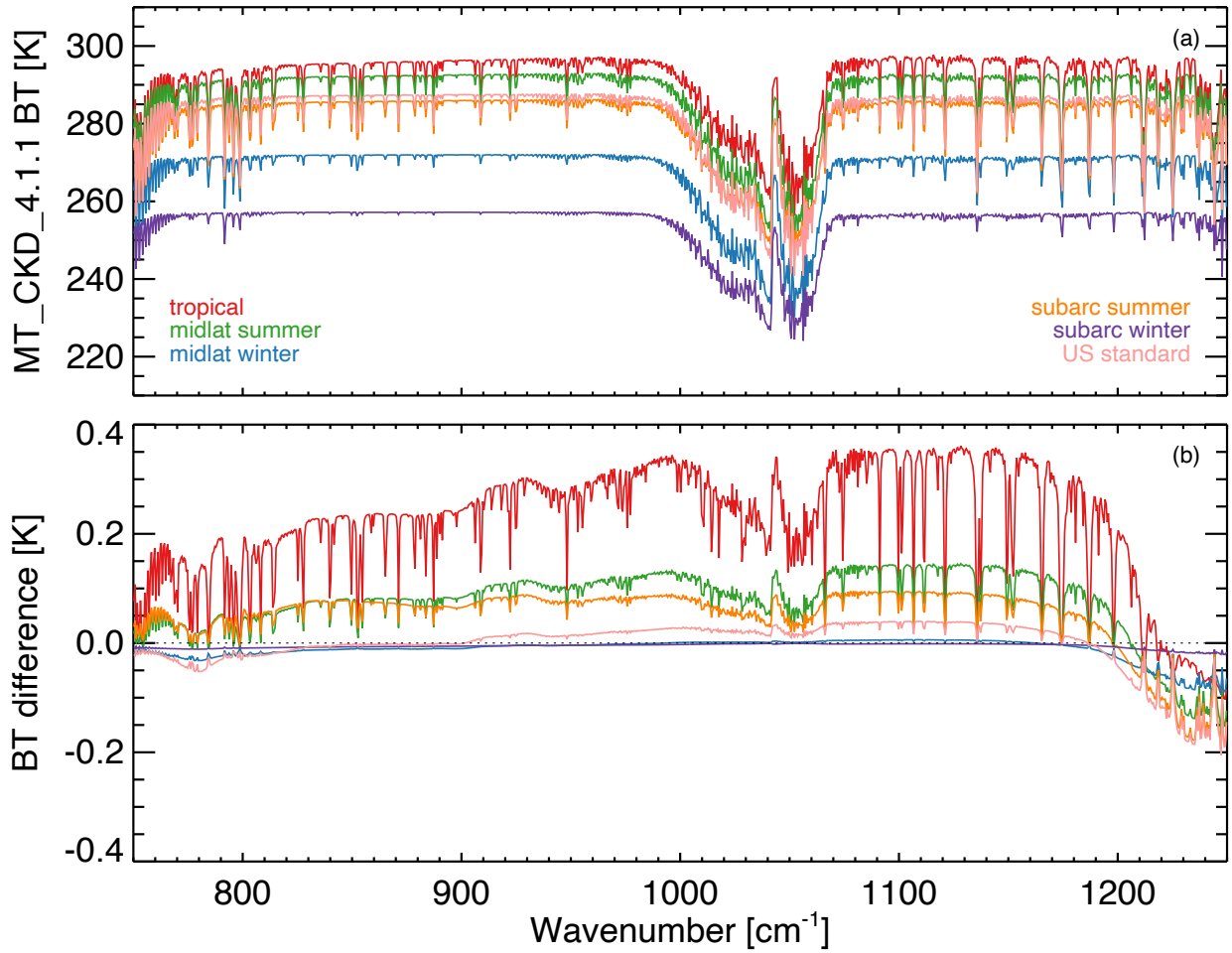

Fig. 21. For six standard atmospheres: (a) brightness temperatures calculated with LBLRTM with MT_CKD_4.1.1 and (b) brightness temperature differences between calculations that use MT_CKD_4.2 and calculations that use MT_CKD_4.1.1.

5.3 Climate considerations

Since only a small fraction of the radiative forcing due to carbon dioxide and methane occurs in the infrared window, the change in the water vapor continuum derived in this work will result in an insignificant change in these forcings. Therefore, no relevant results are shown here.

We assess the impact of the new continuum and resulting opacity change in the infrared window on climate feedbacks with radiative calculations for idealized atmospheric profiles (see, e.g. Koll and Cronin, 2018) using a range of surface temperatures from 240-340K (in 5K increments). Atmospheric temperatures follow a moist adiabat until reaching 220K (defined as the tropopause); temperatures above the tropopause are fixed at 220K. Relative humidity in the troposphere is 75%

and carbon dioxide and ozone concentrations are based on the U.S. Standard atmosphere (ozone concentrations are zero above the tropopause and rescaled in the troposphere to ensure the same total column amount at all surface temperatures). The change in flux between consecutive surface temperatures is interpreted as the climate feedback. Fig. 22 shows this feedback as determined with the existing water vapor continuum (v4.1.1, dashed curves) and with the newly derived continuum (v4.2, solid curves). Differences are shown in the lower panels. Changes to the continuum, and the resulting decrease in atmospheric opacity in the infrared window, induce an increase in climate feedback of ~5% at current surface temperature (~290K), rising to greater than 10% for a surface temperature of ~300K.

The colored curves in Fig. 22 show the contributions of key spectral regions to the total climate feedback. (For this figure, we have slightly expanded the spectral region defined as the window to include the entire region in which the continuum has been modified in this study.) At current Earth temperatures, the infrared window (green) is the spectral region with by far the largest climate feedback. Secondary contributions to the total climate feedback are also provided by infrared water vapor absorption bands, the CO_2 ν_2 band at 15 μm (600-750 cm^{-1}), and the main infrared ozone band at 9.6 μm (1000-1070 cm^{-1}). The climate feedback in the infrared window region decreases with surface temperature due to the increase in atmospheric opacity in moister atmospheres. This opacity increase is rapid due to the dominant role of the water vapor self continuum in the window region and its quadratic dependence on water vapor concentration. The decrease in the climate feedback in the infrared window for higher surface temperatures is partially compensated for by increases in the climate feedback in water vapor absorption bands and the CO_2 band, which has the largest contribution for surface temperatures larger than ~307K.

Fig. 22 shows the significant increase in climate feedback in the infrared window due to the continuum changes derived in this study. The reduced opacity in the revised water vapor continuum results in the climate feedback in the infrared window becoming negative at a temperature 3K greater than before this revision. Our calculations do not extend to sufficiently high temperatures for the climate feedback for the complete longwave region (black curve) to become negative (i.e. runaway greenhouse), but Fig. 22 suggests that the revised continuum implies that runaway greenhouse conditions will occur on Earth at a slightly higher temperature

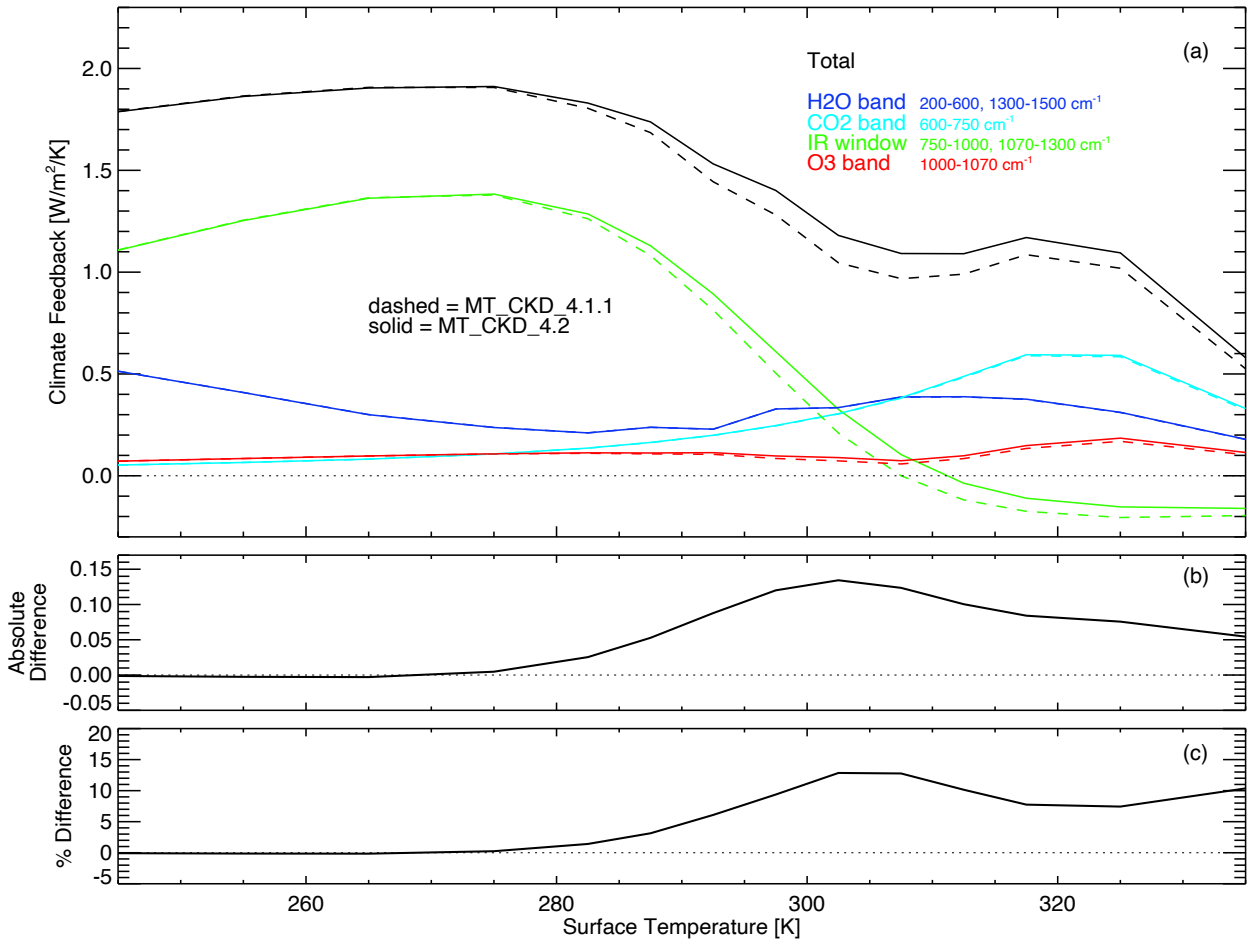

1146 **Fig 22.** As a function of surface temperature in moist adiabat profiles (as described in text), (a) climate
1147 feedback for full longwave region (black), water vapor absorption bands (blue), CO_2 ν_2 band (cyan),
1148 infrared window (green), and ozone band (red). Solid curves use revised continuum (MT_CKD_4.2) in the
1149 calculations while dashed curves use previous continuum (MT_CKD_4.1.1); (b) for full longwave, climate
1150 feedback differences between calculations using MT_CKD_4.2 and MT_CKD_4.1.1; and (c) percentage
1151 differences in climate feedback between calculations using MT_CKD_4.2 and MT_CKD_4.1.1. Climate
1152 feedback is defined as the change in TOA flux per unit change in surface temperature.
1153

than had been previously thought. (Analogous results to those presented in Fig. 22 can be seen in Fig. S3 for MT_CKD_4.2_closure.)

Fig. 23 shows spectrally-resolved climate feedbacks computed with MT_CKD_4.2 (panel b) and the difference with respect to MT_CKD_4.1.1 (panel c); analogous results for MT_CKD_4.2_closure are shown in Fig. S4. Since the changes to the continua decrease absorption due to the self continuum, which is the dominant source of opacity in this region, with the new continuum the climate feedback is increased throughout the vast majority of the infrared window region. The exception is in the region 1200-1300 cm^{-1} for low surface temperatures (i.e. lower PWV values) where, under these conditions, the increased absorption due to the revised foreign continuum can outweigh the impact of the reduced self continuum, leading to a decrease in opacity and a slight increase in climate feedback. Fig. 23c indicates that the change in climate feedback varies spectrally and with surface temperature, a result of the varying spectral behavior of the continuum changes and atmospheric opacity for the different surface temperatures. Additional discussion about the climate feedback results in Figs. 22 and 23 is provided in the supplementary material.

Changes resulting from the new continuum formulation to the surface net radiative flux (defined positive upwards), key to processes such as evaporation, are shown in Fig. 24 as a function of surface temperature for these moist adiabat calculations; spectral results are shown in Fig. S5. Analogous results for MT_CKD_4.2_closure are shown in Fig. S6 and Fig. S7, respectively. The results in Fig. 24 reflect a balance between the increase in upwelling surface flux with increasing surface temperature and an increase in downwelling surface flux due to the increased atmospheric temperature and water vapor loadings associated with the increased surface temperature. At low surface temperature, the low water vapor amounts lead to the former term being larger, so the "surface climate feedback" shown is positive. When the surface temperature is larger than 270K, the impact of the increase in atmospheric opacity associated with a greater surface temperature becomes increasing large, leading to a negative surface climate feedback. The magnitude of this feedback, dominated by the infrared window region, continues to increase with surface temperature until ~300K. At higher temperatures, the most opaque part of this region (~800 cm^{-1}) has become sufficiently opaque so that its surface net flux is small and, therefore, the change in

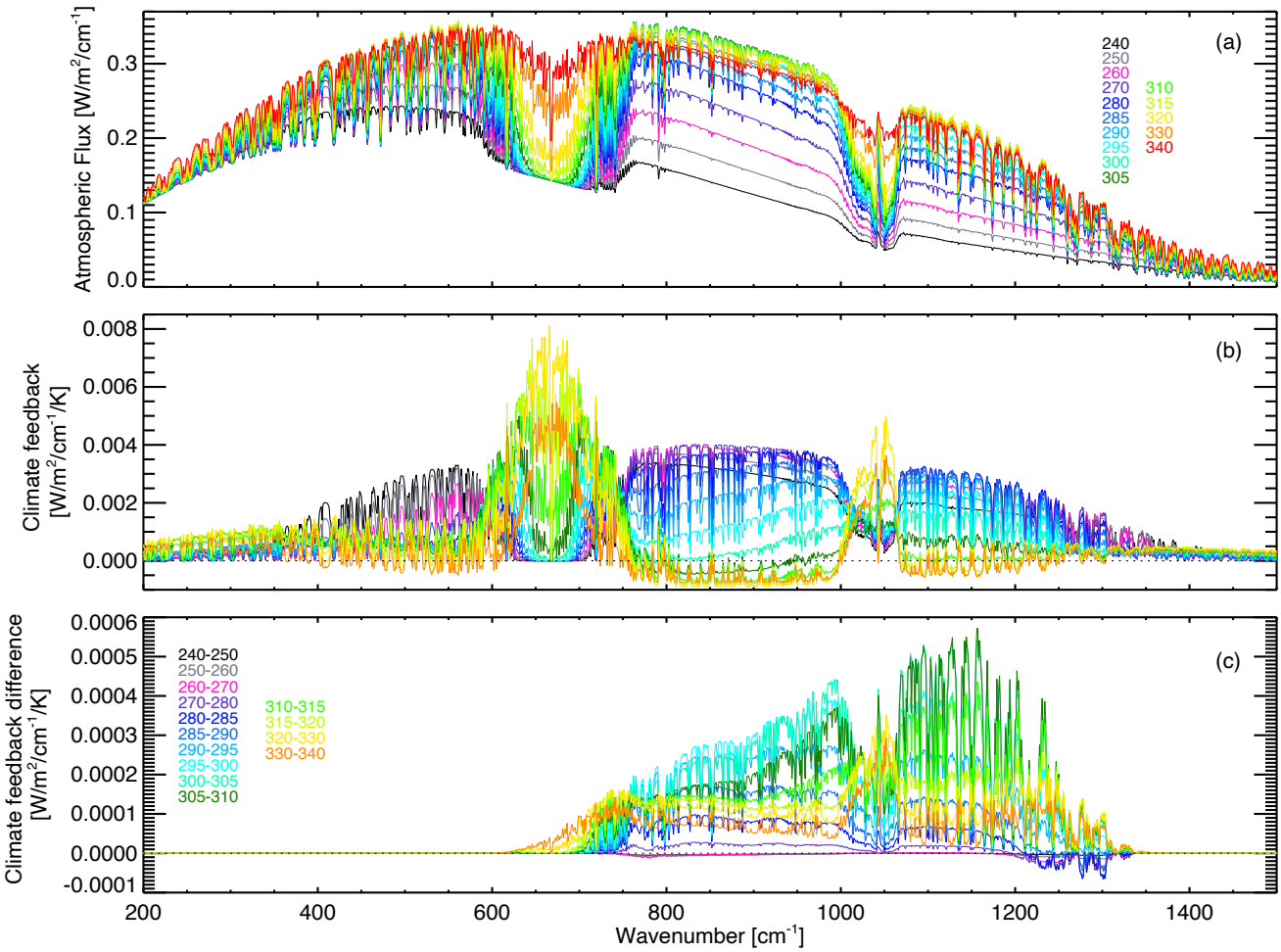

1185 **Fig 23.** For various surface temperatures (colored curves) in moist adiabat profiles (as described in text):
1186 (a) TOA longwave flux calculated using MT_CKD_4.2; (b) spectral behavior of climate feedback
1187 calculated for the temperature ranges denoted on panel (c); and (c) spectral climate feedback differences
1188 between calculations using MT_CKD_4.2 and MT_CKD_4.1.1.

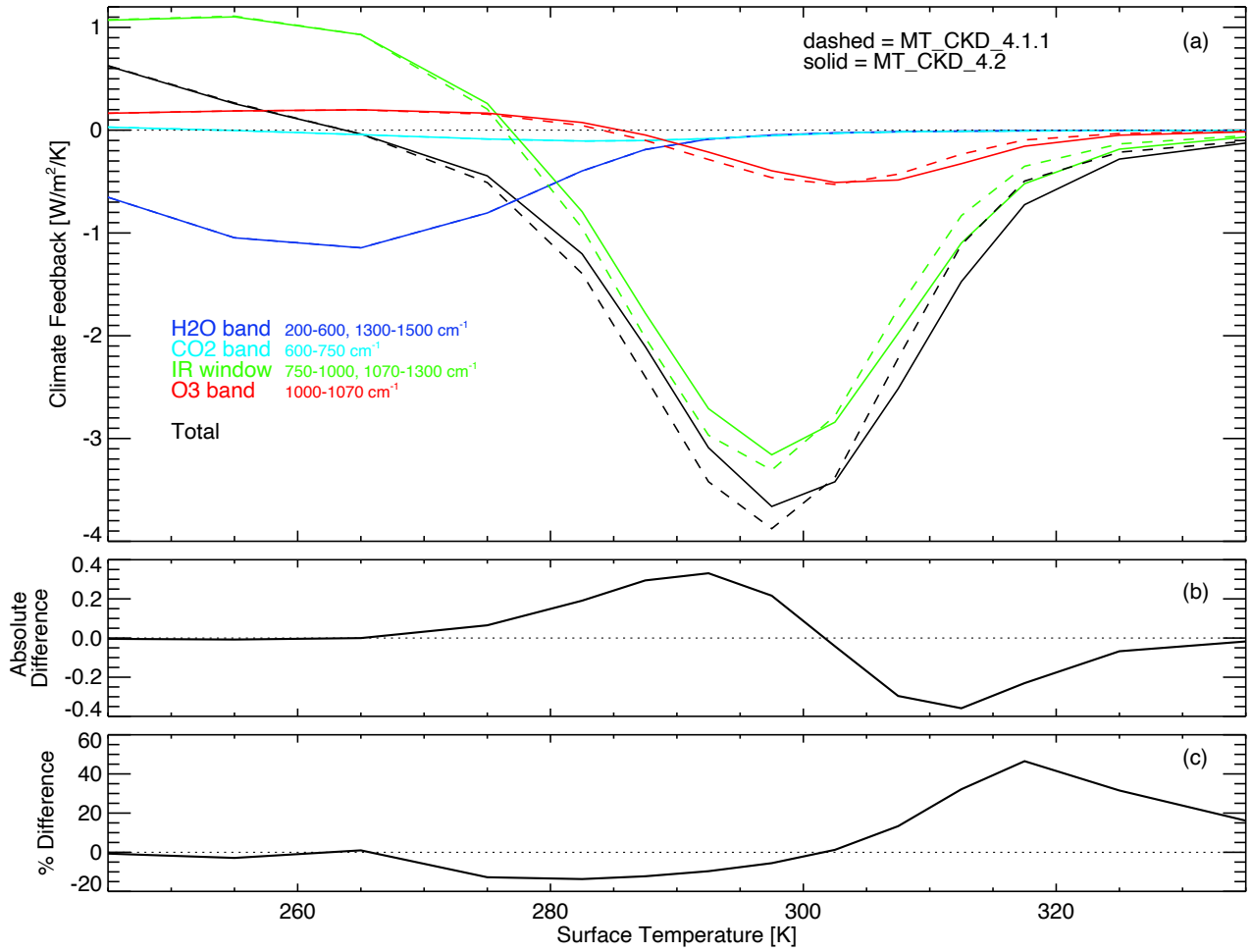

Fig 24. Similar to Fig. 22 but for the surface instead of TOA. Surface climate feedback is defined as the change in surface net flux (defined as positive upward) per unit change in surface temperature.

surface net flux values resulting from a change in surface temperature decreases. These spectral regions stop contributing appreciably to the surface climate feedback, and the overall magnitude starts to decrease. This trend continues as the surface temperature increases until the surface net flux approaches zero, as does the surface climate feedback.

The impact of the changes to the infrared window continuum is to decrease the magnitude of the surface climate feedback for lower surface temperatures, where the trend in surface climate feedback is due to the increase in surface downwelling flux due to the increased atmospheric opacity – the decrease in the self continuum slows down this trend. Conversely, for higher temperatures, the decrease in self continuum opacity decelerates the trend of the surface net flux approaching zero, thereby leading to an increase in the magnitude of the surface climate forcing.

For completeness, the Supplemental Materials includes analogous figures (both for MT_CKD_4.2 and 4.2_closure) for the atmospheric net flux (TOA minus surface net flux) for the moist adiabat calculations, change in atmospheric net flux due to the change in surface temperature ("atmospheric climate feedback"), and changes in this feedback due to the revised water vapor continuum in the infrared window (Figs. S8-S11).

7. Conclusion and discussion

This study provides a new determination of the strength of water vapor continuum absorption in the infrared atmospheric window, which, despite its importance to climate, has not been the subject of many observational studies in the last two decades. Our results are consistent with several recent analyses that indicate that the self continuum, the dominant source of atmospheric absorption in this spectral region, is too strong in MT_CKD_4.1.1. In general, the weaker self continuum derived here results in an overall increase in atmospheric transparency in the window in MT_CKD_4.2 compared to MT_CKD_4.1.1. However, the transparency in atmospheres with low amounts of water vapor, which is high, may slightly decrease due to the increase in foreign continuum absorption derived in this study. These continuum changes lead to a significant decrease in downwelling longwave flux at the surface for moist atmospheres as well as a modest increase in OLR. The increased fraction of surface-leaving radiation that escapes to space leads to a notable increase (~5-10%) in the clear-sky climate feedback.

The diversity of the continuum values derived in previous studies is striking, and the high uncertainty of some of the continuum values we have derived means that our study cannot resolve all remaining uncertainties of significance to Earth's radiative budget and climate. This is especially the case for the foreign continuum and the temperature dependence of the self continuum, but also for the self continuum in certain spectral regions (e.g. 1150-1200 cm^{-1}). This reality points to the need for further accurate laboratory studies of the water vapor continuum in the atmospheric window. Within the last year, an important step in this direction has occurred. Motivated by a presentation of preliminary results from this study (Mlawer et al., 2022), the Campargue group at the University of Grenoble Alpes undertook a measurement of the self continuum at ~1185 cm^{-1} using the accurate technique of optical feedback cavity ring down

spectroscopy. The results of this study (Fournier et al., 2023; F23) are consistent with our result that there is a need for a significant reduction in the strength of the MT_CKD_4.1.1 self continuum in this region, although the decrease derived in our study is greater than in F23. The two results agree within the uncertainties associated with our determination of the self continuum in this region. Measurements of the self continuum were performed in F23 over a limited range of temperatures (296-308 K), which resulted in the determination that the temperature dependence is much weaker than the value we have implemented in MT_CKD_4.2. Given that our study determined that the self continuum temperature dependence could assume a wide range of values while still allowing radiative closure with AERI measurements, this is not surprising. There is a clear need for additional accurate laboratory studies of the self continuum across the full atmospheric window, as well as its temperature dependence and the strength of foreign continuum absorption.

The foreign continuum analysis in this study also demonstrates the need for further laboratory studies of this source of atmospheric absorption. In this study, we posit that our derivation of foreign continuum absorption includes a contribution from aerosols and determine the spectrally dependent fraction of the absorption due to the foreign continuum vs. aerosols through a highly speculative approach. Despite the resulting substantial uncertainty inherent our methodology, our results point out the possibly important role that aerosol absorption may play in the longwave radiative budget, which we hope will prompt further study.

Appendix 1

The method to estimate the "adjusted" self continuum values shown in Fig. 4d for three previous field studies is described here. Using the SGP dataset described in Section 3, we retrieved self continuum values (see section 4.2 for the description of the methodology) using the MT_CKD_4.1.1+BL foreign continuum. For our reconsideration of the Turner et al. (2004) study, we used the entire dataset to estimate the change in derived self continuum values due to the modified foreign continuum, while for the tropical analyses upon which CKD_2.1 was based (Westwater et al., 1995; Han et al., 1997) we used only the most moist cases in the SGP dataset. These revised self continuum values are shown in Fig. 4d as MT_CKD_1.0_adj and CKD_2.1_adj, respectively. Also shown in this figure are the self continuum values derived in a field study by Taylor et al. (2003), which assumed the CKD_2.4 foreign continuum, and corresponding self continuum values that are estimated as the values that would have been obtained had the larger MT_CKD_4.1.1+BL foreign continuum values been assumed instead (denoted as "Taylor_adj").

Appendix 2

Based on a) the foreign continuum value at 980 cm^{-1} from a revised line shape fit (similar to the one used to derive MT_CKD_1.0 as described in Mlawer et al., 2012) applied to the foreign continuum coefficients in MT_CKD_4.1.1 from 500-800 cm^{-1} and b) the value of the foreign continuum at 980 cm^{-1} in MT_CKD_4.2_closure, we estimate that the actual foreign continuum is a little more than half of the retrieved foreign continuum at 980 cm^{-1}, and assume that aerosols are responsible for the remaining fraction. This split between foreign continuum and aerosol is weighted more to the foreign continuum than is implied by Fig. 15, but is within the uncertainty of the aerosol optical depth estimates in panel b of that figure. The first step in the procedure to account for the estimated impact of aerosols on the derived spectral foreign continuum coefficients is to compute the spectral fraction of the derived continuum due to aerosol optical depths. To do this, the spectral dependence of the aerosol optical depth is assumed to be given by a derived Angstrom exponent of -0.647 while the combined foreign and aerosol optical depth is given by MT_CKD_4.2_closure. Using this ratio, the estimated aerosol contribution is removed from the derived foreign continuum coefficients, yielding an estimate of the actual foreign continuum coefficients (i.e. with aerosol removed). It is important to note that since no coefficients were derived from 990-1070 cm^{-1}, this gap remains in these estimated pure continuum coefficients.

These coefficients are then used as constraints in a new fit of the same line shape formalism that was used to derive MT_CKD_1.0. The new fit is aimed at providing values for the foreign continuum in the gap as well as in neighboring spectral regions that are impacted greatly by aerosols (given our assumption) and, therefore, the derived foreign continuum coefficients in those regions cannot be considered very definitive (e.g. 1080-1150 cm^{-1}). The main priorities in the fitting effort are to match the following properties of the constraining foreign continuum coefficients: a) the overall slope of the coefficients from 800-980 cm-1 and b) the coefficient values in spectral regions closest to the gap in which the actual foreign continuum value are thought to be responsible for more than 60% of the AERI-derived foreign continuum coefficients (960-980 $cm^{-1}$and 1220-1230 cm^{-1}). The continuum coefficients resulting from this fit are the final foreign continuum coefficients in the targeted spectral region; in neighboring spectral regions the coefficients from the fit are smoothly merged with the constraining coefficients (i.e. AERI-derived), resulting in the final foreign water vapor coefficients from this AERI analysis (780 - 1250 cm^{-1}). In spectral regions just outside of this range, these coefficients are transitioned into the existing MT_CKD_4.1.1 foreign continuum coefficients in spectral regions (< 600 cm^{-1}, > 1400 cm^{-1}) in which the coefficients have been determined in previous observation-based analyses.

Acknowledgements

The primary support for this project at AER was provided by Atmospheric Systems Research (ASR) program of the U.S. Department of Energy under contract number DE-SC0018296. Additional support for the analysis and dissemination of the results were provided by the NASA U.S. Participating Investigator program under contract number 80NSSC21K1038 and the National Science Foundation under award number 1916927. Support at NOAA was provided by ASR contract 89243019SSC000034. We thank the DOE Atmospheric Radiation Measurement program for the observations upon which this study is based and for their excellent data archive. AER authors are indebted to Karen Cady-Pereira, Matt Alvarado, and Rick Pernak for helpful advice. Part of this research was carried out at the Jet Propulsion Laboratory, California Institute of Technology, under a contract with NASA (80NM0018D0004).

Open Research

Data availability.

All SGP and MAO observations used in this study were obtained from https://www.arm.gov/data. The LBLRTM radiative transfer model can be accessed from https://github.com/AER-RC/LBLRTM and the MT_CKD continuum model from https://github.com/AER-RC/MT_CKD. The LBLRTM input files derived from ARM observations that are used in this study can be found in a tar file that can be downloaded from Zenodo (https://zenodo.org/records/10909710). The Zenodo file also contains all aerosol-related data used in our analysis, as well as the code (Python) used to retrieve the self and foreign continuum coefficients and the self continuum temperature exponents from the measurement-calculation residuals. Additional supporting information is also available in this tar file. All analysis and plots were executed using Python 3.9.7 and IDL Version 8.4.

Supporting information

Additional text and data can be found in *mlawer_ir-window_supporting_information.pdf*.

References

Anderson, G. P., Clough, S. A., Kneizys, F. X., Chetwynd, J. H., & Shettle, E. P. (1986). AFGL atmospheric constituent profiles (0.120 km). (No. AFGL-TR-86-0110). Air Force Geophysics Lab, Hanscom, AFB, MA. Retrieved from http://www.dtic.mil/docs/citations/ADA175173

Baranov, Y.I., Lafferty W.J., Ma Q., & Tipping R.H. (2008). Water vapor continuum absorption in the 800-1250 cm^{-1} spectral region at temperatures from 311 to 363K. *J Quant Spectrosc Radiat Transf*., 109, 2291–2302.

Baranov, Y.I & Lafferty W.J. (2012). The water vapor self- and water–nitrogen continuum absorption in the 1000 and 2500 cm^{-1} atmospheric windows. *Philos Trans R Soc A*, 370, 2578–2589.

Burch, D.E. (1982). Continuum absorption by H2O. *AFGL-TR-81-0300*. 46 pp. Air Force Geophys. Lab., Hanscom AFB, MA. http://dx.doi. org/10.1117/12.931899

Burch, D.E. & Alt, R.L. (1984). Continuum absorption by H_2O in the 700-1200 cm^{-1} and 2400-2800 cm^{-1} windows. *AFGL-TR-84-0128*, 32 pp., Air Force Geophys. Lab., Hanscom AFB, MA.

Cadeddu, M. P., Liljegren, J. C., & Turner, D. D. (2013). The Atmospheric radiation measurement (ARM) program network of microwave radiometers: instrumentation, data, and retrievals. *Atmos. Meas. Tech.,* 6, 2359–2372. https://doi.org/10.5194/amt-6-2359-2013

Clough, S.A., Kneizys, F.X., & Davies, R.W. (1989). Line shape and the water vapor continuum. *Atmos. Res*., 23, 229. https://doi.org/10.1016/0169-8095(89)90020-3

Clough, S.A., Shephard, M.W., Mlawer, E.J., Delamere, J.S., Iacono, M.J., Cady-Pereira, K., Boukabara, S., & Brown, P.D (2005). Atmospheric radiative transfer modeling: A summary of the AER codes. *J. Quant. Spectrosc. Radiative Trans*., 91, 233-244.

Cormier J.G., Hodges J.T., & Drummond, J.R. (2005). Infrared water vapour continuum absorption at atmospheric temperatures. *J. Chem. Phys.,* 122:114309. http: //doi.org/10.1063/1.1862623

Cormier, J.G, Ciurylo, R., & Drummond, J.R. (2002). Cavity ringdown spectroscopy measurements of the infrared water vapor continuum. *J. Chem. Phys*., 116, 1030.

Delamere, J.S., Clough, S.A., Payne, V., Mlawer, E.J., Turner, D.D., & R. Gamache (2010). A far-infrared radiative closure study in the Arctic: Application to water vapor. *J. Geophys. Res*., 115, D17106. doi:10.1029/2009JD012968

Dubovik, O. & King, M.D. (2000). A flexible inversion algorithm for retrieval of aerosol optical properties from Sun and sky radiance measurements. *J. Geophys. Res.*, 105, 20,673-20,696.

Feng, J., Paynter, D., & Menzel, R. (2023). How a stable greenhouse effect on Earth is maintained under global warming. *Journal of Geophysical Research: Atmospheres*, 128, e2022JD038124. https://doi.org/10.1029/2022JD038124

Fournier, Q., Kassi, S., Mondelain, D., Fleurbaey, H., Georges, R., & Campargue, A. (2024), The water vapor self-continuum absorption at 8.45 μm by optical feedback cavity ring down spectroscopy. *J. Quant. Spectr. Rad. Trans.,* 315. http://dx.doi.org/10.2139/ssrn.4607109

Fu, D., Worden, J.R.. Liu, X., Kulawik, S.S., Bowman, K.W. & Natraj, V. (2013). Characterization of ozone profiles derived from Aura TES and OMI radiances. *Atmos. Chem. Phys.*, 13(6), 3445–3462. doi:10.5194/acp-13-3445-2013

Han, Y., Shaw, J.A., Churnside, J.H., Brown, P.D., & Clough, S.A. (1997). Infrared spectral measurements in the tropical Pacific atmosphere. *J. Geophys. Res.*, 102, 4353-4356.

Harries, J., Carli, B., Rizzi, R., Serio, C., Mlynczak, M., Palchetti, L., et al. (2008), The far-infrared Earth, *Rev. Geophys.*,46, RG4004. doi:10.1029/2007RG000233

Jeevanjee, N., Koll, D. D., & Lutsko, N. (2021). "Simpson's law" and the spectral cancellation of climate feedbacks. *Geophysical Research Letters*, 48(14), e2021GL093699. https://doi.org/10.1029/2021gl093699

Koll, D. D., Jeevanjee, N., & Lutsko, N. J. (2023). An analytic model for the clear-sky longwave feedback. *Journal of the Atmospheric Sciences*, 80(8), 1923-1951.

Koll, D. D., & Cronin, T. W. (2018). Earth's outgoing longwave radiation linear due to H_2O greenhouse effect. *Proceedings of the National Academy of Sciences*, 115(41), 10293–10298. https://doi.org/10.1073/pnas.1809868115

Knuteson, R.O, Revercomb. H.E., Best, F.A., Ciganovich, N.C., Dedecker, R.G., Dirkx, T.P., et al. (2004a) Atmospheric Emitted Radiance Interferometer. Part I: Instrument design. *J. Atmos. Oceanic Technol.*, **21**, 1763-1776. https://doi.org/10.1175/JTECH-1662.1

Knuteson, R.O, Revercomb. H.E., Best, F.A., Ciganovich, N.C., Dedecker, R.G., Dirkx, T.P., et al. (2004b): Atmospheric Emitted Radiance Interferometer. Part II: Instrument performance. *J. Atmos. Oceanic Technol.*, **21**, 1777-1789. https://doi.org/10.1175/JTECH-1663.1

McKim, B. A., Jeevanjee, N., & Vallis, G. K. (2021). Joint dependence of longwave feedback on surface temperature and relative humidity. *Geophysical Research Letters*, 48(18), e2021GL094074. https://doi.org/10.1029/2021gl094074

Martin S.T., Artaxo, P., Machado, L., Manzi, A.O.,Souza, R.A., Schumacher, C. et al. (2016). The Green Ocean Amazon Experiment (GoAmazon2014/5) Observes Pollution Affecting Gases, Aerosols, Clouds, and Rainfall over the Rain Forest. *Bulletin of the American Meteorological Society*, 98(5), 10.1175/bams-d-15-00221.1

Malm, W. C., Sislerm J. F., Huffmann, D., Eldred, R. A., & Cahill, T. A. (1994). Spatial and seasonal trends in particle concentration and optical extinction in the United States. *J. Geophys. Res.*, 99, 1347–1370. https://doi.org/10.1029/93JD02916

Mlawer, E.J. & Turner, D.D. (2016). Spectral radiation measurements and analysis in the ARM program. *Meteorol Monogr*, 57 14.1-14.17. doi:10.1175/ AMSMONOGRAPHS-D-15-0027.1

Mlawer, E.J., Cady-Pereira, K.E., Mascio, J., & Gordon, I.E. (2023). The inclusion of the MT_CKD water vapor continuum model in the HITRAN molecular spectroscopic database. *J. Quant. Spectr. Rad. Trans.,* 306. https://doi.org/10.1016/j.jqsrt.2023.108645

Mlawer, E.J., Payne, V.H., Moncet. J.-L., Delamere, J.S., Alvarado, M.J., Tobin, D.C (2012). Development and recent evaluation of the MT_CKD model of continuum absorption. *Philos Trans R Soc A*, 370, 2520–56. doi:10.1098/rsta. 2011.0295

Mlawer, E.J., Taubnam, S.J., Brown, P.D., Iacono, M.J., and Clough, S.A. (1997). RRTM, a validated correlated-k model for the longwave. *J. Geophys. Res*., 102, 16663-16682.

Mlawer, E.J., Turner, D.D., Paine, S.N., Palchetti, L., Bianchini, G., Payne, V.H., et al. (2019). Analysis of water vapor absorption in the far-infrared and submillimeter regions using surface radiometric measurements from extremely dry locations. *J Geophys Res Atmos,* 124,8134–60. doi:10.1029/2018JD029508

Otsu, N. (1979). A threshold selection method from gray-level histograms. *IEEE Transactions on Systems, Man, and Cybernetics*. 9 (1): 62–66. doi:10.1109/TSMC.1979.4310076. S2CID 15326934

Randles, C. A., da Silva, A. M., Buchard, V., Colarco, P. R., Darmenov, A., Govindaraju, R., et al. (2017). The MERRA-2 Aerosol Reanalysis, 1980 onward. Part I: System description and data assimilation evaluation. *J. Climate*, 30(17), 6823–6850. https://doi.org/10.1175/JCLI-D-16-0613.1

Revercomb, H.E., Buijs, H., Howell, H.B., LaPorte, D.D., Smith, W.L., and Sromovsky, L.A. (1988). Radiometric calibration of IR Fourier transform spectrometers: Solution to a problem with the high-resolution interferometer sounder. *Appl. Opt.*, 27, 3210-3218.

Revercomb, H.E., Turner, D.D., Tobin, D.C., Knuteson, R.O., Feltz, W.F., Barnard, J. et al. (2003) The Atmospheric Radiation Measurement Program's water vapor intensive observation periods: overview, initial accomplishments, and future challenges. *Bull. Amer. Meteor. Soc.*, **84**, 217-236

Seeley, J. T., & Jeevanjee, N. (2021). H_2O windows and CO_2 radiator fins: A clear-sky explanation for the peak in equilibrium climate sensitivity. *Geophysical Research Letters*, 48(4), e2020GL089609. https://doi.org/10.1029/2020gl089609

Shephard, M.W., Goldman, A., Clough, S.A., Mlawer, E.J. (2003) Spectroscopic improvements providing evidence of formic acid in AERI-LBLRTM validation spectra. *J. Quant. Spectr. Rad. Trans.,* 82, 383-390. https://doi.org/10.1016/S0022-4073(03)00164-X.

Simpson, G. (1928). Some studies in terrestrial radiation. *Memoirs of the Royal Meteorological Society*, 2(16), 69–95.

Sisterson, D.L, Peppler, R.A., Cress, T.S., Lamb, P.J., and Turner, D.D. (2016). The ARM Southern Great Plains (SGP) site. *The Atmospheric Radiation Measurement Program: The First 20 Years*, *Meteor. Monograph. Amer. Meteor. Soc.,* 57, 6.1-6.14, DOI:10.1175/AMSMONOGRAPHS-D-16-0004.1

Slingo, A. and Webb, M.J. (1997), The spectral signature of global warming. *Quarterly Journal of the Royal Meteorological Society*, 123(538), 293–307. https://doi.org/10.1002/qj.49712353803

Taylor, J.P., Newman, S.M., Hewison, T.J., & McGrath, A. (2003). Water vapour line and continuum absorption in the thermal infrared – reconciling models and observations *Quart. J. Roy. Meteorol. Soc.,* 129 (2003),2949-2969. 10.1256/qj.03.08

Turner, DD., 2003: Microphysical properties of single and mixed-phase Arctic clouds derived from ground-based AERI observations. Ph.D. Dissertation, University of Wisconsin-Madison, 167 pp. Available from https://search.library.wisc.edu/catalog/999951770902121

Turner, D.D. (2005). Arctic mixed-phase cloud properties from AERI-lidar observations: Algorithm and results from SHEBA. *J. Appl. Meteor.,* 44, 427-444.

Turner, D.D. (2008). Ground-based retrievals of optical depth, effective radius, and composition of airborne mineral dust above the Sahel. *J. Geophys. Res.,* 113, E00E03, doi:10.1029/2008JD010054

Turner, D.D., Tobin, D.C., Clough, S.A., Brown, P.D., Ellingson, R.G., Mlawer, E.J. et al. (2004). The QME AERI LBLRTM: A closure experiment for downwelling high spectral resolution infrared radiance. *J. Atmos. Sci*., 61, 2657-2675.

Turner, D.D. & Blumberg, W.G. (2019). Improvements to the AERIoe thermodynamic profile retrieval algorithm. *IEEE Selected Topics Appl. Earth Obs. Remote Sens.*, 12, 1339-1354, doi:10.1109/JSTARS.2018.2874968

Turner, D.D. & Ellingson, R.G. Eds., 2016: *The Atmospheric Radiation Measurement (ARM) Program: The First 20 Years*. Meteor. Monograph, **57**, American Meteorological Society

Turner, D. D. & Löhnert, U. (2014). Information content and uncertainties in thermodynamic profiles and liquid cloud properties retrieved from the ground-based Atmospheric Emitted Radiance Interferometer (AERI). *J. Appl. Meteor. Climatol.*, **53**, 752-771, doi:10.1175/JAMC-D-13-0126.1

Turner, D.D. & Löhnert, U. (2021). Ground-based temperature and humidity profiling: Combining active and passive remote sensors. *Atmos. Meas. Technol*., 14, 3033-3048, doi:10.5194/amt-14-3033-2021

Turner, D.D. & Mlawer, E.J. (2010). Radiative heating in underexplored bands campaigns (RHUBC). *Bull. Amer. Meteor. Soc*., *91*, 911-923. doi:10.1175/2010BAMS2904.1.

Turner, D.D., Lesht, B.M. Clough, S.A., Liljegren, J.C., Revercomb, H.E., & Tobin, D.C. (2003). Dry bias and variability in Vaisala radiosondes: The ARM experience. *J. Atmos. Oceanic Technol.*, **20**, 117-132.

Turner, D.D., Mlawer, E.J. & H.E. Revercomb (2016). Water vapor observations in the ARM program. *The Atmospheric Radiation Measurement Program: The First 20 Years*. Meteor. Monograph, 57, Amer. Meteor. Soc., 13.1-13.18, doi:10.1175/AMSMONOGRAPHS-D-15-0025.1

Wang, J., Cole, H.L., Carlson, D.J., Miller, E.R. & Beirle, K. (2002). Corrections of humidity measurement errors from the Vaisala RS80 radiosonde – application to TOGA COARE data. *J. Atmos. Oceanic Technol.*, **19**, 981-1002

Wargan, K., Labow, G., Frith, S., Pawson, S., Livesey, N., & Partyka, G. (2017). Evaluation of the ozone fields in NASA's MERRA-2 reanalysis. *Journal of Climate*, 30, 2961–2988. https://doi.org/10.1175/JCLI-D-16-0699.1

Westwater, E., Churnside, J., Shaw, J., Snider, J.B., Gage, K.S., Han, Y., Ecklund, W. et al. (1995). Ground-based remote sensor observations during the PROBE experiment in the tropical western Pacific. 882 - 886 vol.2. 10.1109/IGARSS.1995.521086

Worden, H.M., Logan, J.A., Worden, J.R., Beer, R., Bowman, K., Clough, S.A. et al. (2007). Comparisons of Tropospheric Emission Spectrometer (TES) ozone profiles to ozonesondes: Methods and initial results, *J. Geophys. Res.,* 112, D03309. doi:10.1029/2006JD007258

S.1 Discussion of figures related to climate feedback

Section 5.3 presents results of climate feedback calculations related to the revision to the water vapor continuum made in this study. Here we discuss information about these calculations unrelated to the continuum revision. This discussion has been inspired by and is complementary to many excellent recent studies on spectral aspects of climate feedback, including Feng et al. (2022), Koll et al. (2022), Jeevanjee et al. (2021), McKim et al. (2021), and Seeley and Jeevanjee (2020).

Detailed spectral information related to climate feedback considerations can be seen in Fig. 23, where panel (b) shows the spectral results underlying the climate feedback results shown as solid curves (for MT_CKD_4.2) for the various spectral regions in Fig. 22a, while panel (c) shows the spectral differences due to the revised continuum (corresponding to the results in Fig. 22b). (Analogous results to those presented in Fig. 23 can be seen in Fig. S4 for MT_CKD_4.2_closure.)

- For the lowest temperature range shown (240-250K, black/grey), Fig. 23b indicates that significant contributions to the climate feedback occur in the far-infrared (200-600 cm^{-1}) and infrared window. At these temperatures, the far-infrared is semi-transparent (Mlawer et al., 2019; Turner & Mlawer, 2010; Harries et al., 2008) and acts as a partial window, allowing some surface radiation to escape to space. As a result, there is a significant increase in the radiation emitted to space in both this region and the infrared window as the surface temperature increases.
- As the surface temperature increases to ~280K, the relative contributions of these two spectral regions to climate feedback is modified, with an increase in the window region and a decrease in the far-infrared. As shown in Fig. 22, these changes are of roughly equal magnitude and the total climate feedback stays fairly constant over this temperature range. As the temperature increases in this range, in the infrared window there is an increase in the climate feedback in the most transparent part of the region (950-1000, 1070-1300 cm^{-1}) since almost all of the surface radiation reaches the top of the atmosphere. In the less transparent part of the window (750-950 cm^{-1}), for surface temperatures above 260K the impact of the greater atmospheric absorption of the increasingly moist atmosphere begins to outweigh the increased surface radiation, and the climate feedback begins to decrease, although it is still quite significant. In contrast, for these surface temperatures the opacity of the far-infrared (200-600 cm^{-1}) is too

large (due to increased PWV values) to be considered a window and most of the surface radiation does not reach the TOA. As has been shown previously (e.g. Slingo and Webb, 1997, and Simpson, 1928), the outgoing radiation in the far-infrared under these conditions stays fairly constant with increasing surface temperatures since the impact of higher tropospheric temperatures is counterbalanced by the higher altitudes at which radiation emitted by the atmosphere can escape to space.

- As the surface temperature increases to 300K, the climate feedback across the entire infrared window decreases with surface temperature due to the rapidly increasing opacity due to self continuum absorption (proportional to square of water vapor abundance), although the climate feedback itself still remains positive throughout this region. This decrease is mitigated somewhat by increases in the climate feedback in the far-infrared, demonstrating that the counterbalancing mentioned above is only approximate, and in the CO_2 region (600-750 cm^{-1}). The behavior in the far-infrared can be seen in Fig. 23b, as well as in an expanded view in Fig. S12a, which demonstrates that the modest increase in climate forcing in this temperature regime occurs both in spectral locations dominated by absorption lines and in microwindows between lines. For one far-infrared microwindow, Fig. S13 shows the cumulative tropospheric optical depth downward from the tropopause as a function of layer temperature for the surface temperature values analyzed. The temperatures at which the cumulative optical depth reaches unity (i.e. roughly the temperature of emission to space) modestly increases with surface temperature, resulting in positive climate feedback values at this spectral location. The rate of this increase results in an increasing climate feedback for surface temperatures below ~305K, although it decreases at higher temperatures. The opaque region CO_2 region exhibits somewhat different behavior. In this region, the cumulative optical depth from the tropopause downward is a fairly constant function of pressure (not shown). Therefore, in the part of this region in which the outgoing radiation is from the troposphere (e.g. see 600-620 cm^{-1} in Fig. S12b), the positive climate feedback does not change too dramatically from 280-310K. In the more opaque part of the band (640-680 cm^{-1}), the climate feedback tends toward zero since the emission to space for all surface temperatures originates in the stratosphere, which is defined to be isothermal (at 220K) in these calculations.
- At surface temperatures just greater than 300K, the climate feedback in the more opaque part of the infrared window (750-1000 cm^{-1}) becomes negative while the more transparent region

(1070-1300 cm^{-1}) remains at a small positive value. When the surface temperature exceeds 310K, the entire window has negative climate feedback. As is the case for lower surface temperatures, the CO_2 region compensates for some of this decrease. As can be seen in Fig. S12b, most of this increase occurs in the center of this band (640-680 cm^{-1}), although it is unclear to what extent this calculated behavior is physically realistic since the isothermal stratosphere becomes quite thin (i.e. less air, so less CO_2) for higher surface temperatures, leading to increased emission to space from the troposphere. In the far-infrared, for these higher temperatures the climate feedback shows a slight decrease, with a climate feedback increase in more opaque parts of this region and a larger decrease in the less opaque regions, which have negative climate feedback for surface temperatures greater than 330K.

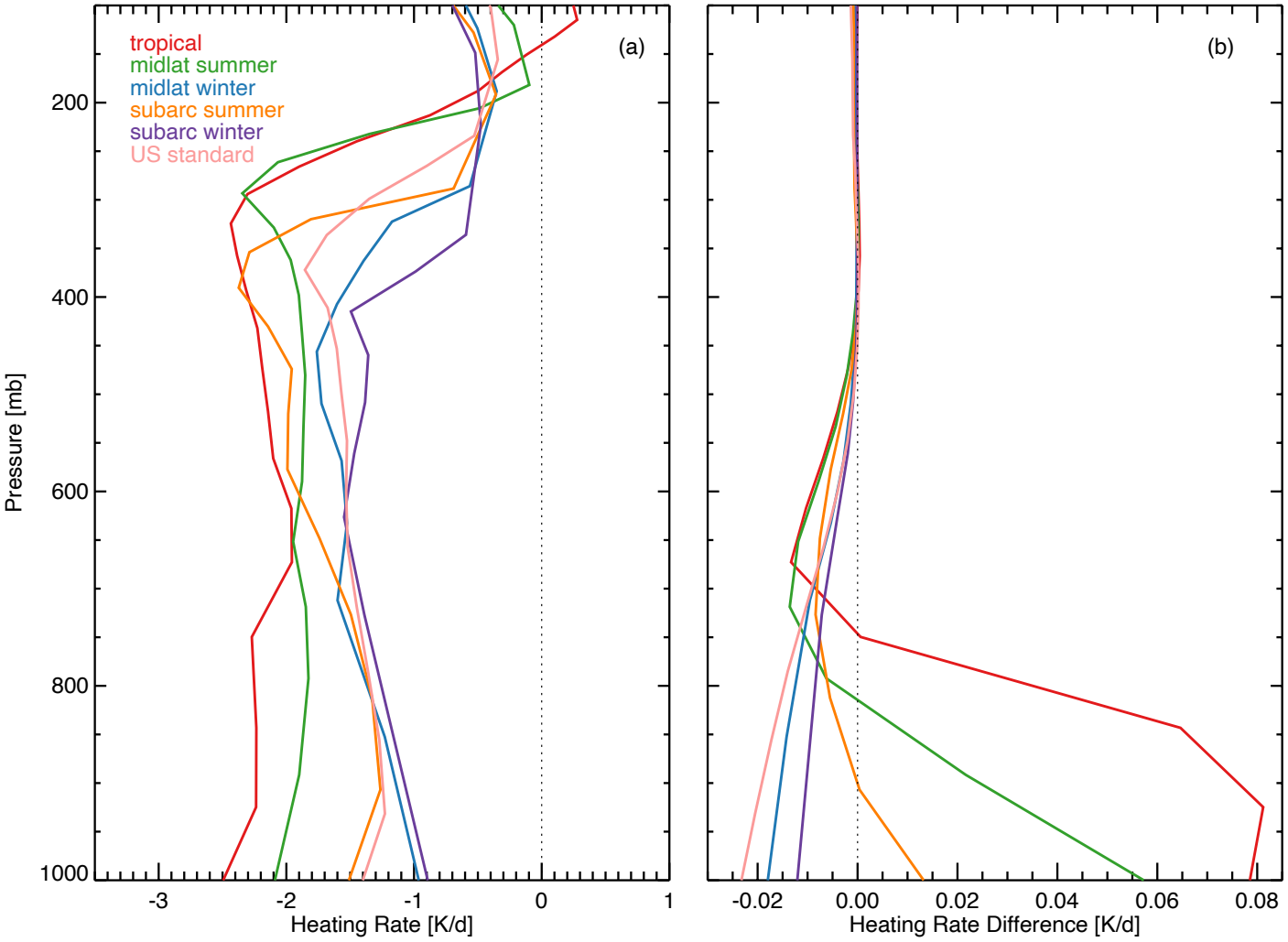

Fig. S1. For six standard atmosphere, (a) longwave heating rates from LBLRTM calculations using MT_CKD_4.1.1 and (b) difference in heating rates between calculations that use MT_CKD_4.2_closure and calculations that use MT_CKD_4.1.1. Comparable to Fig. 20.

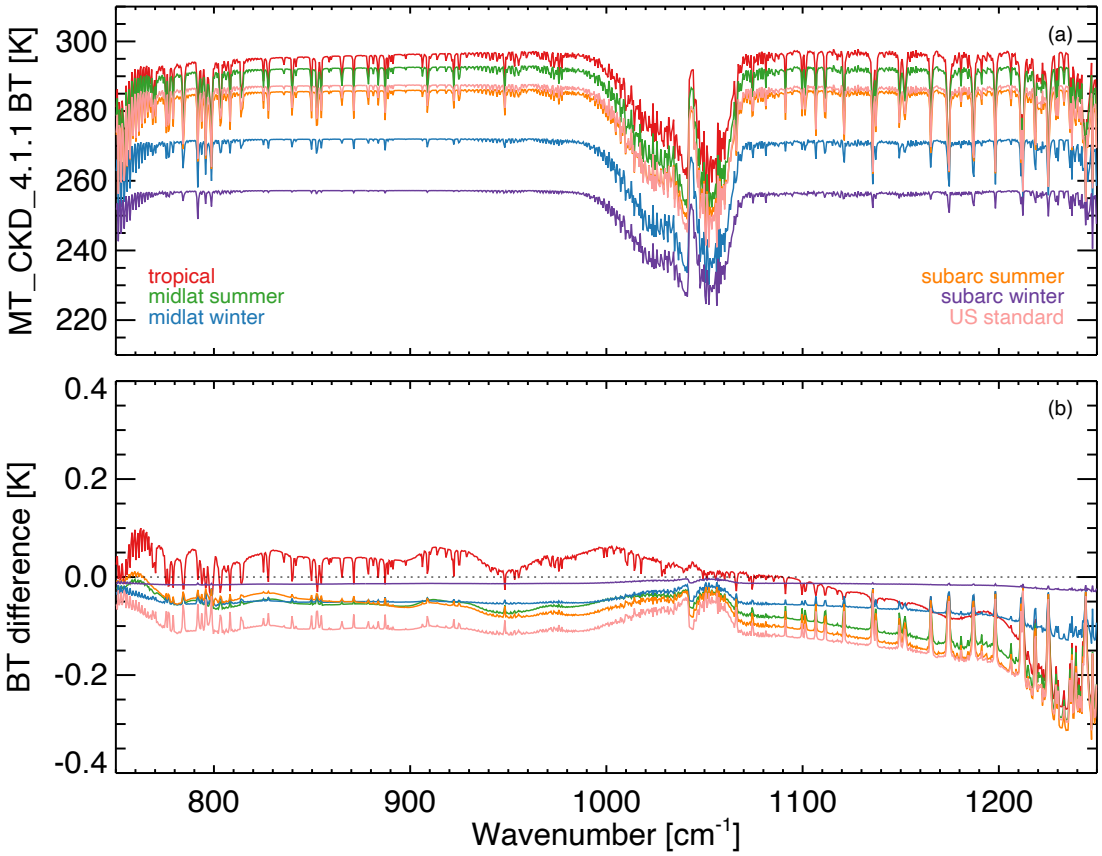

Fig. S2. For six standard atmospheres, (a) brightness temperatures calculated with LBLRTM with MT_CKD_4.1.1 and (b) brightness temperature differences between calculations that use MT_CKD_4.2_closure and calculations that use MT_CKD_4.1.1. Comparable to Fig. 21.

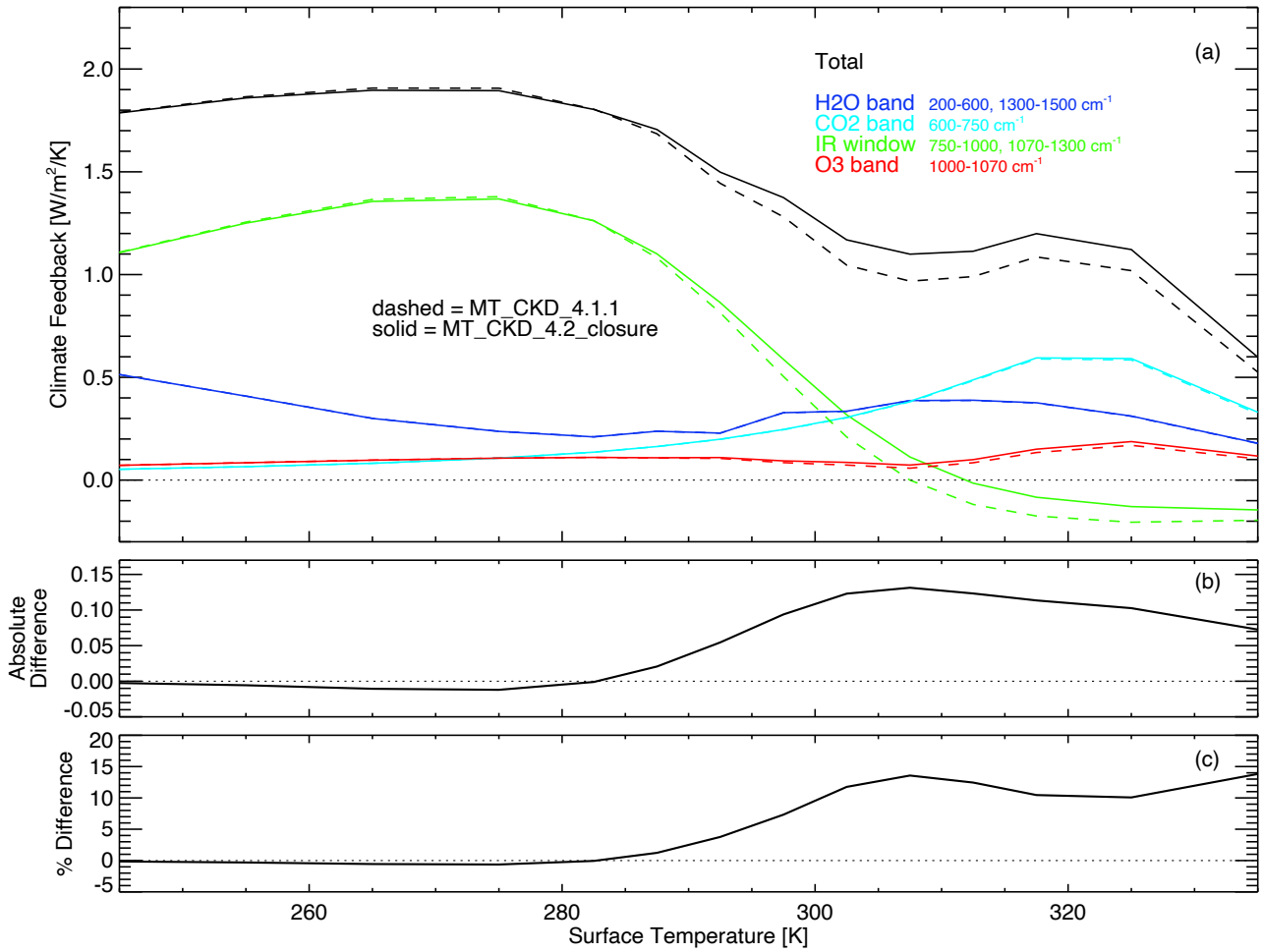

Fig. S3. As a function of surface temperature in moist adiabat profiles (as described in text): (a) climate feedback for full longwave region (black), water vapor absorption bands (red), CO_2 ν2 band (cyan), infrared window (green), and ozone band (red). Solid curves use revised continuum (MT_CKD_4.2_closure) in the calculations while dashed curves use previous continuum (MT_CKD_4.1.1); (b) for full longwave, climate feedback differences between calculations using MT_CKD_4.2_closure and MT_CKD_4.1.1, and (c) percentage differences in climate feedback between calculations using MT_CKD_4.2_closure and MT_CKD_4.1.1. Climate feedback is defined as the change in TOA flux per unit change in surface temperature. Comparable to Fig. 22.

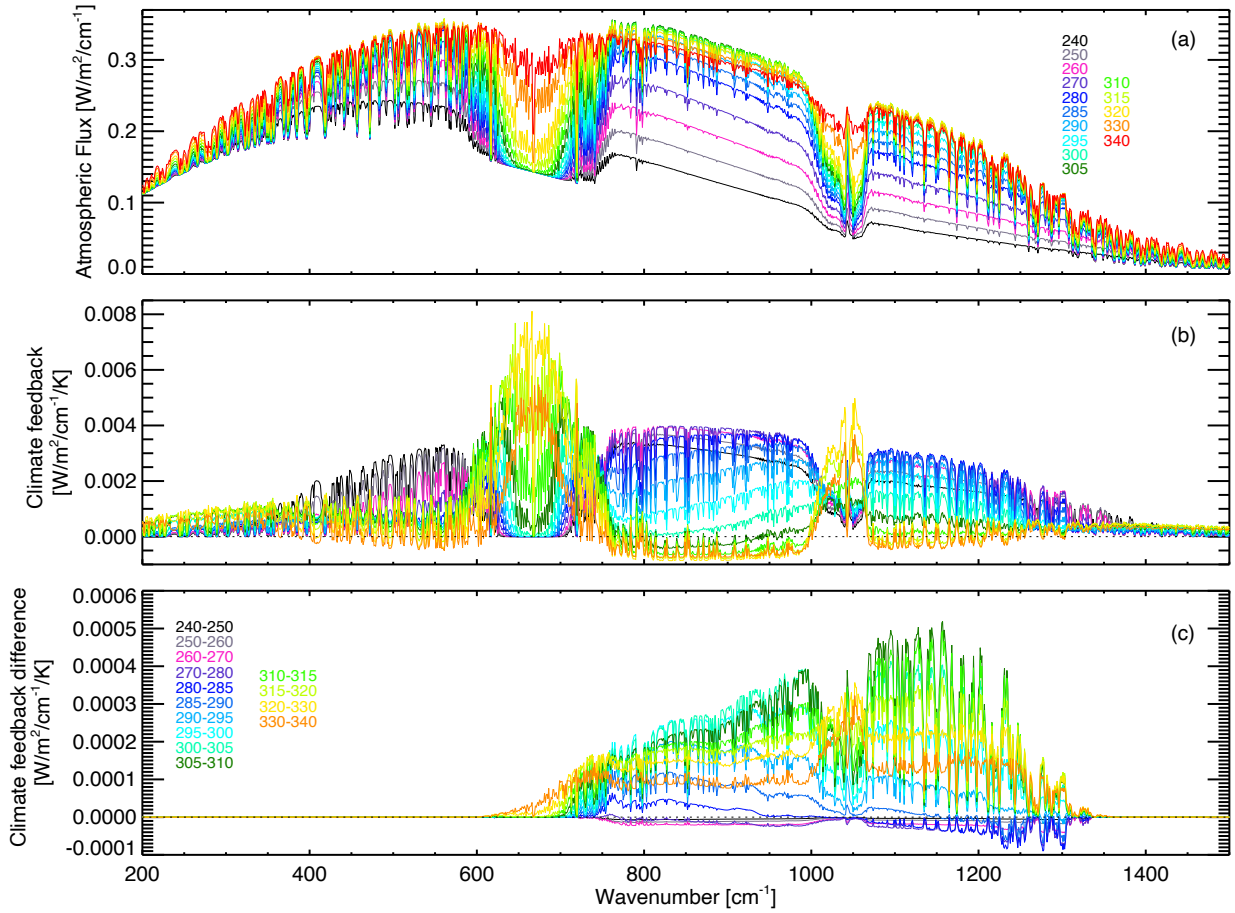

Fig. S4. For various surface temperatures (colored curves) in moist adiabat profiles (as described in text), (a) TOA longwave flux calculated using MT_CKD_4.2_closure, (b) spectral behavior of climate feedback calculated for the temperature ranges denoted on panel (c), and (c) Spectral climate feedback differences between calculations using MT_CKD_4.2_closure and MT_CKD_4.1.1. Comparable to Fig. 23.

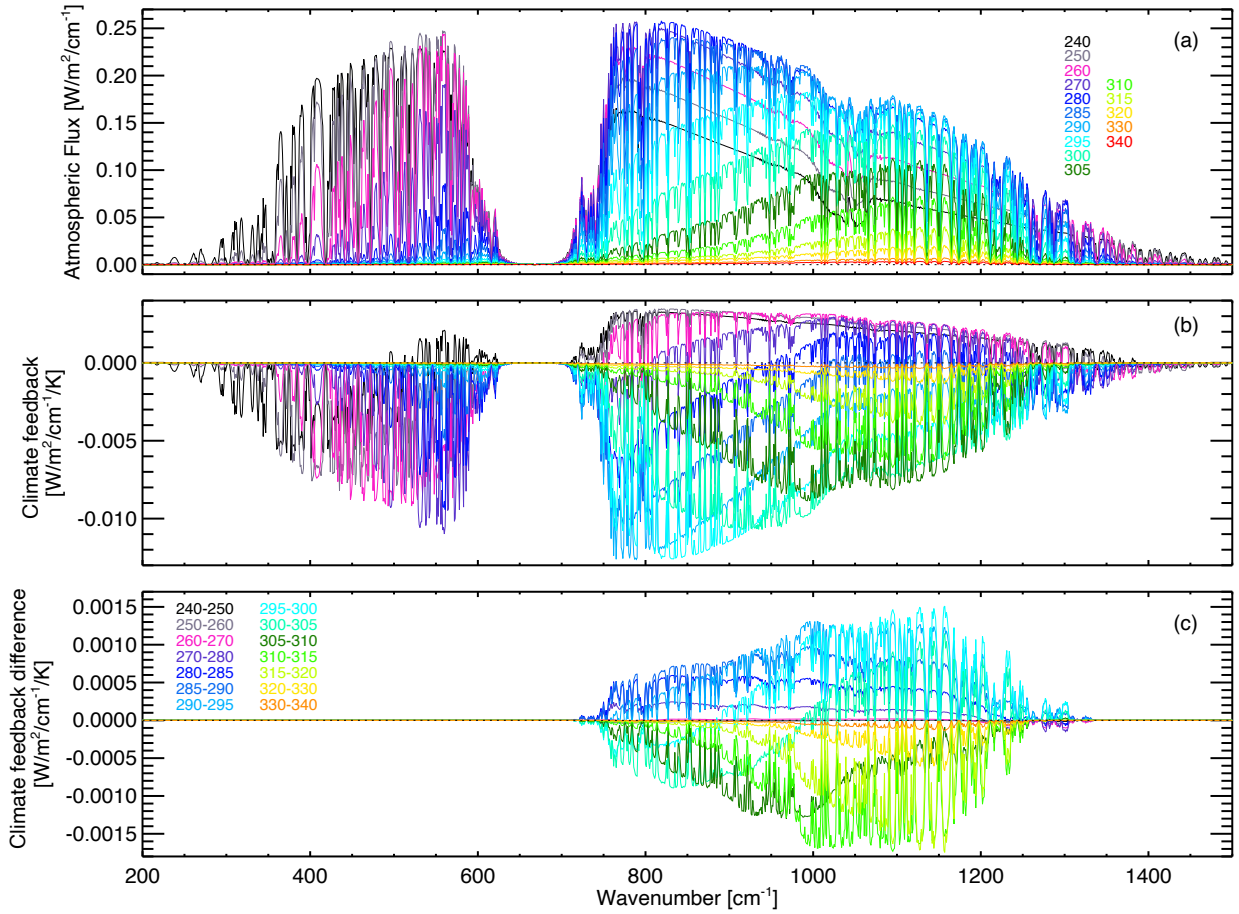

Fig. S5. For various surface temperatures (colored curves) in moist adiabat profiles (as described in text), (a) surface net flux calculated using MT_CKD_4.2, (b) spectral behavior of surface climate feedback calculated for the temperature ranges denoted on panel (c), and (c) spectral surface climate feedback differences between calculations using MT_CKD_4.2 and MT_CKD_4.1.1.

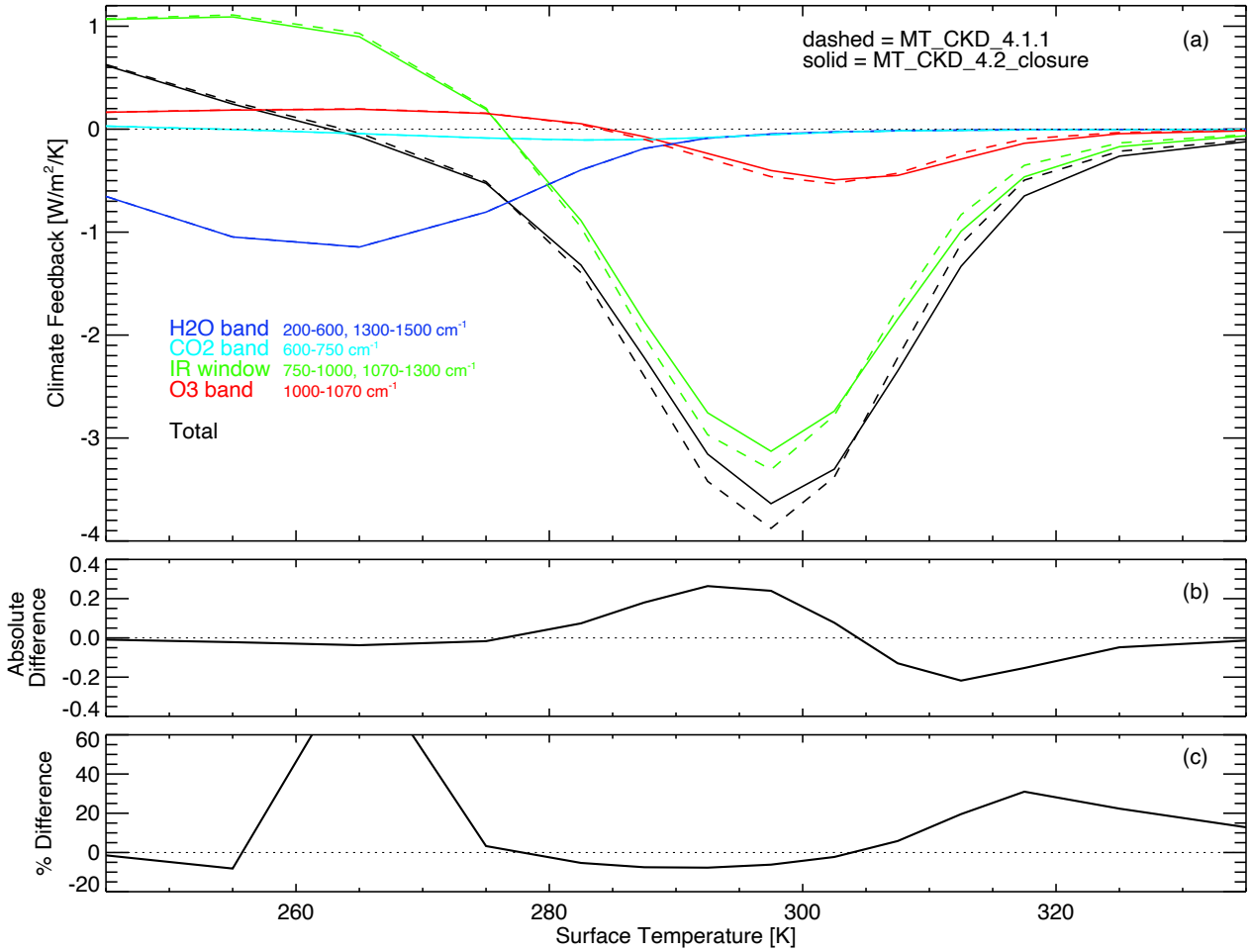

Fig. S6. Comparable to Fig. 24 but for MT_CKD_4.2_closure instead of MT_CKD_4.2.

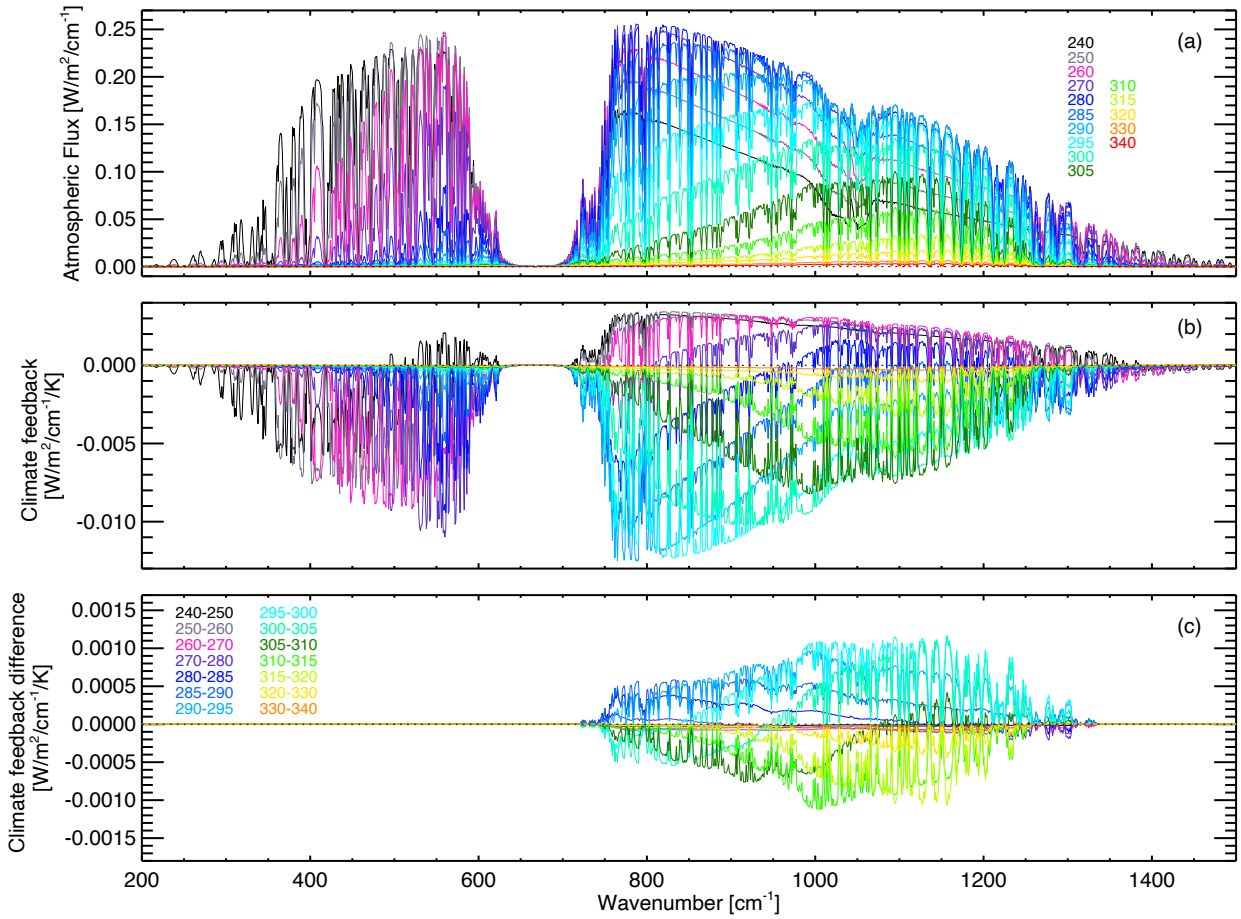

Fig. S7. Comparable to Fig. S5 but for MT_CKD_4.2_closure instead of MT_CKD_4.2.

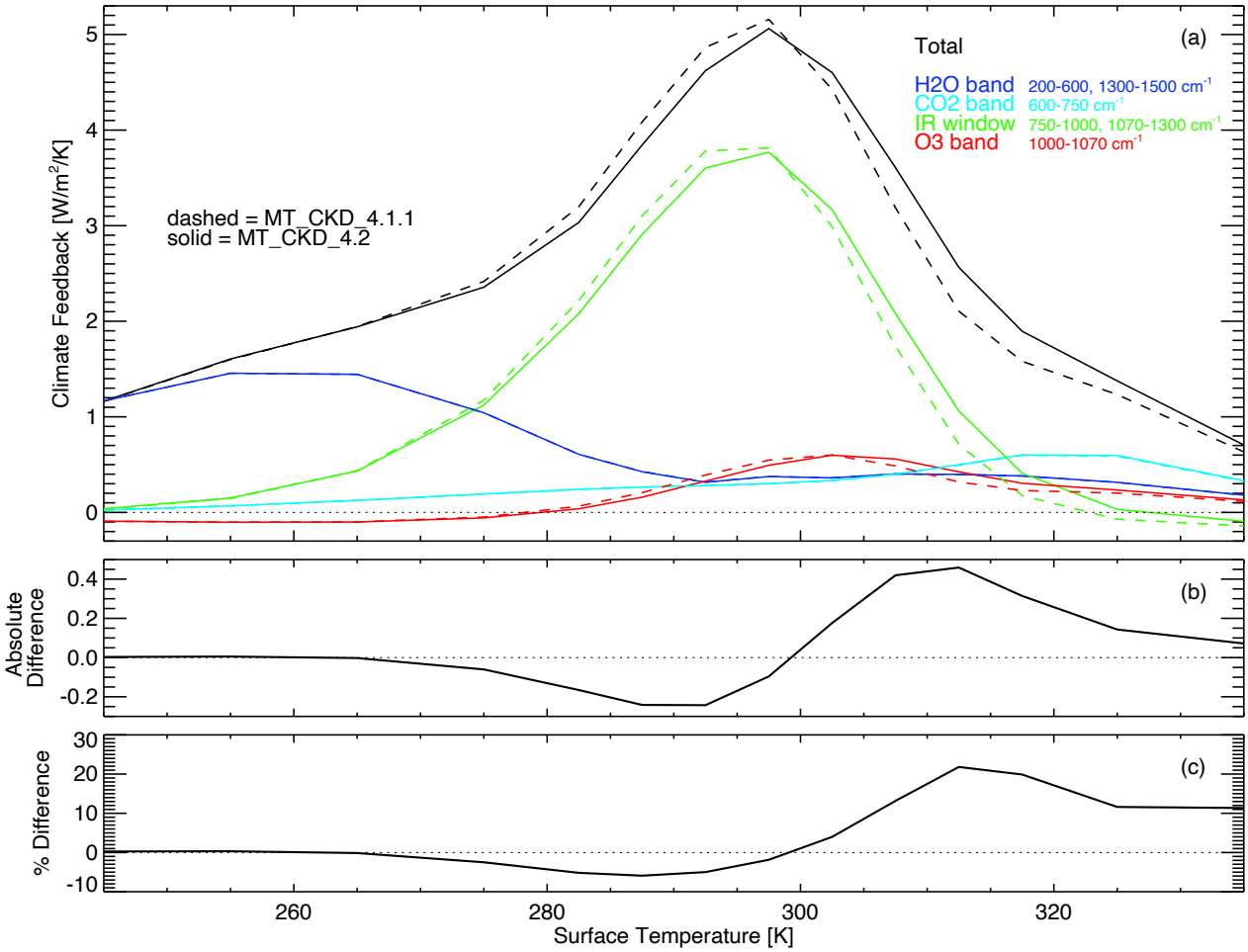

Fig. S8. As a function of surface temperature in moist adiabat profiles (as described in text), (a) atmospheric climate feedback for full longwave region (black), water vapor absorption bands (blue), CO_2 ν_2 band (cyan), infrared window (green), and ozone band (red). Solid curves use revised continuum (MT_CKD_4.2) in the calculations while dashed curves use previous continuum (MT_CKD_4.1.1); (b) for full longwave, atmospheric climate feedback differences between calculations using MT_CKD_4.2 and MT_CKD_4.1.1, and (c) percentage differences in atmospheric climate feedback between calculations using MT_CKD_4.2 and MT_CKD_4.1.1. Atmospheric climate feedback is defined as the difference between climate feedback (i.e. TOA) and surface climate feedback.

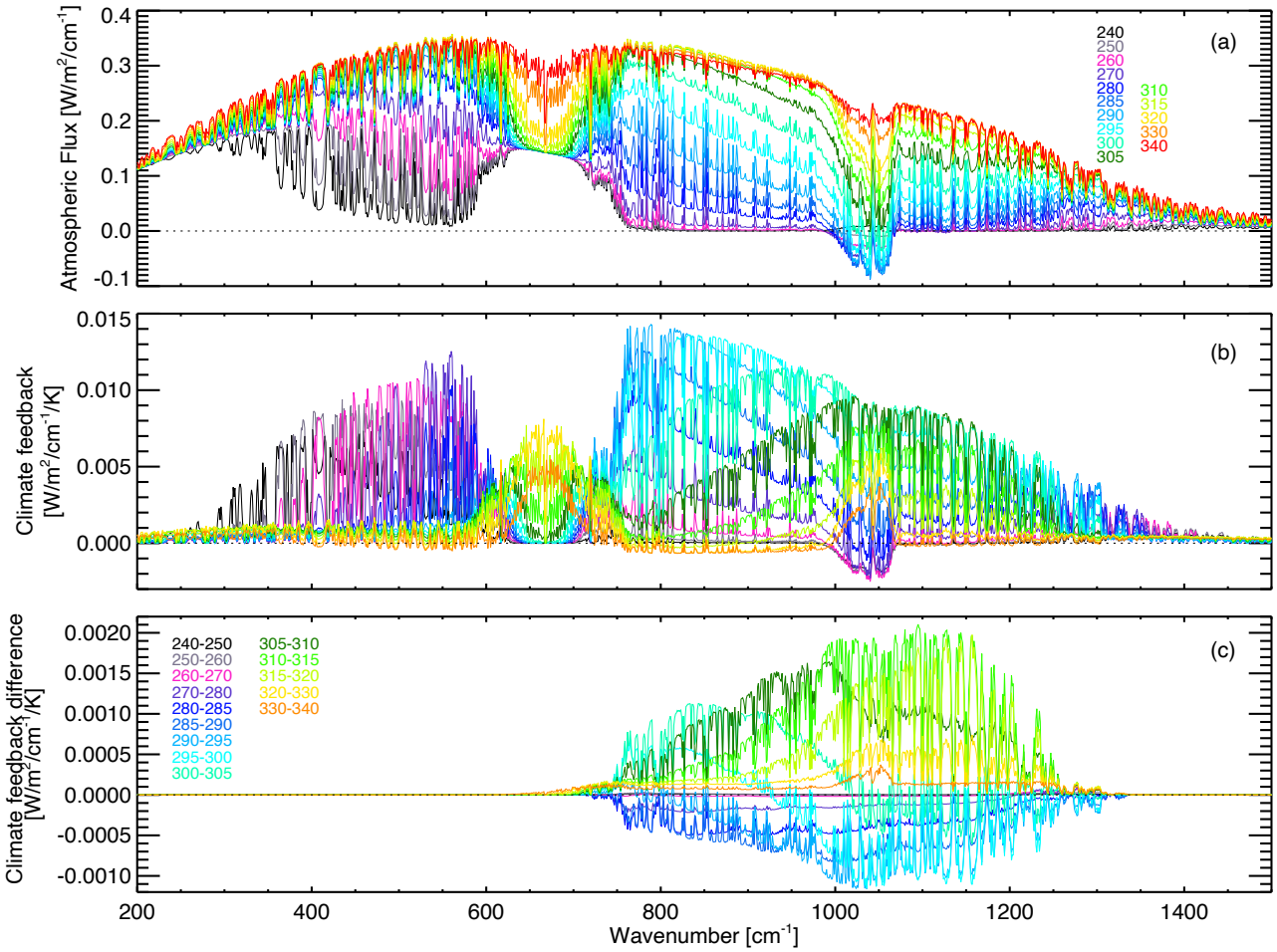

Fig. S9. Similar to Fig. S5 but for the atmospheric flux (a) and atmospheric climate feedback (b,c) instead of the surface flux and feedback, respectively.

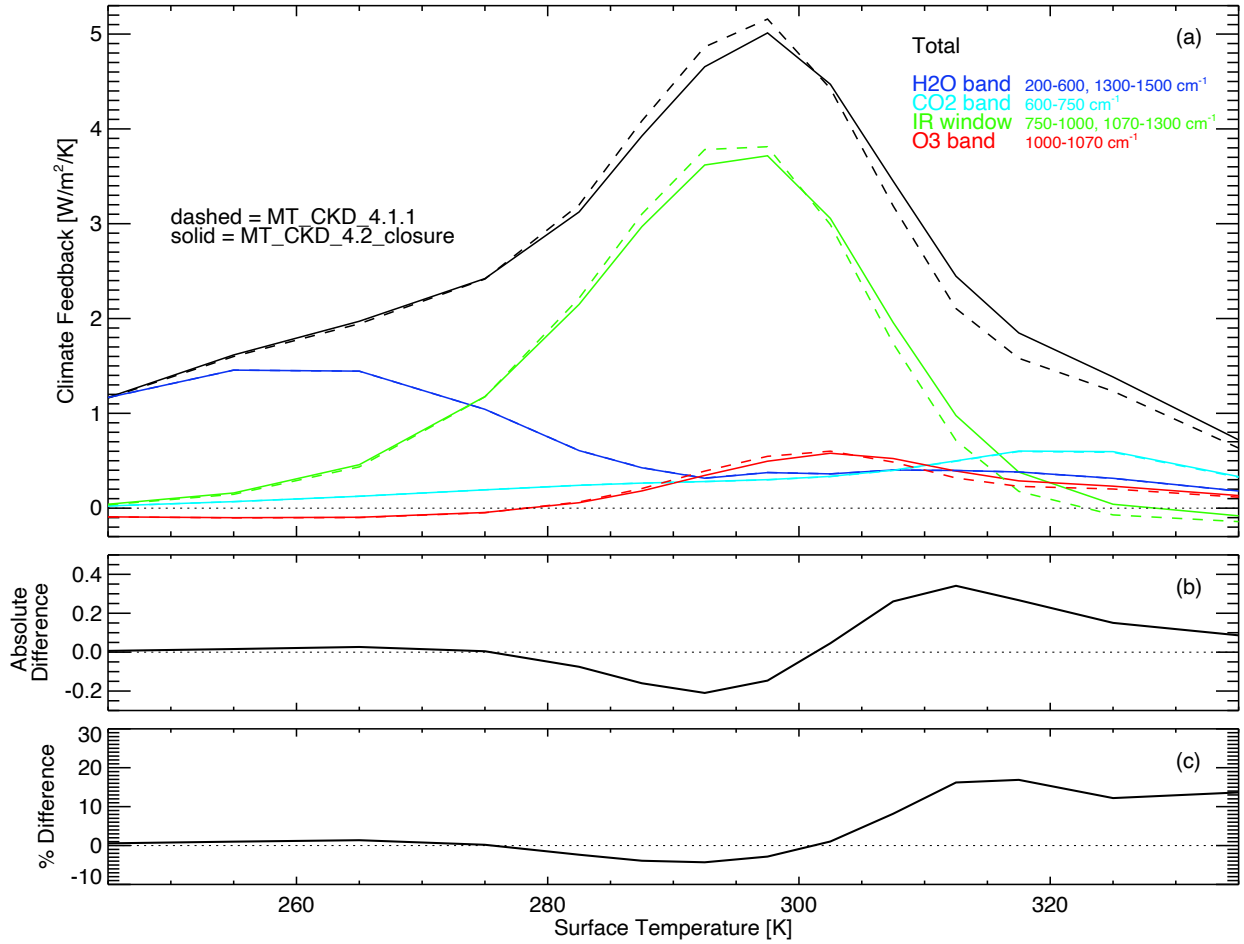

Fig. S10. Similar to Fig. S8 but using MT_CKD_4.2_closure instead of MT_CKD_4.2.

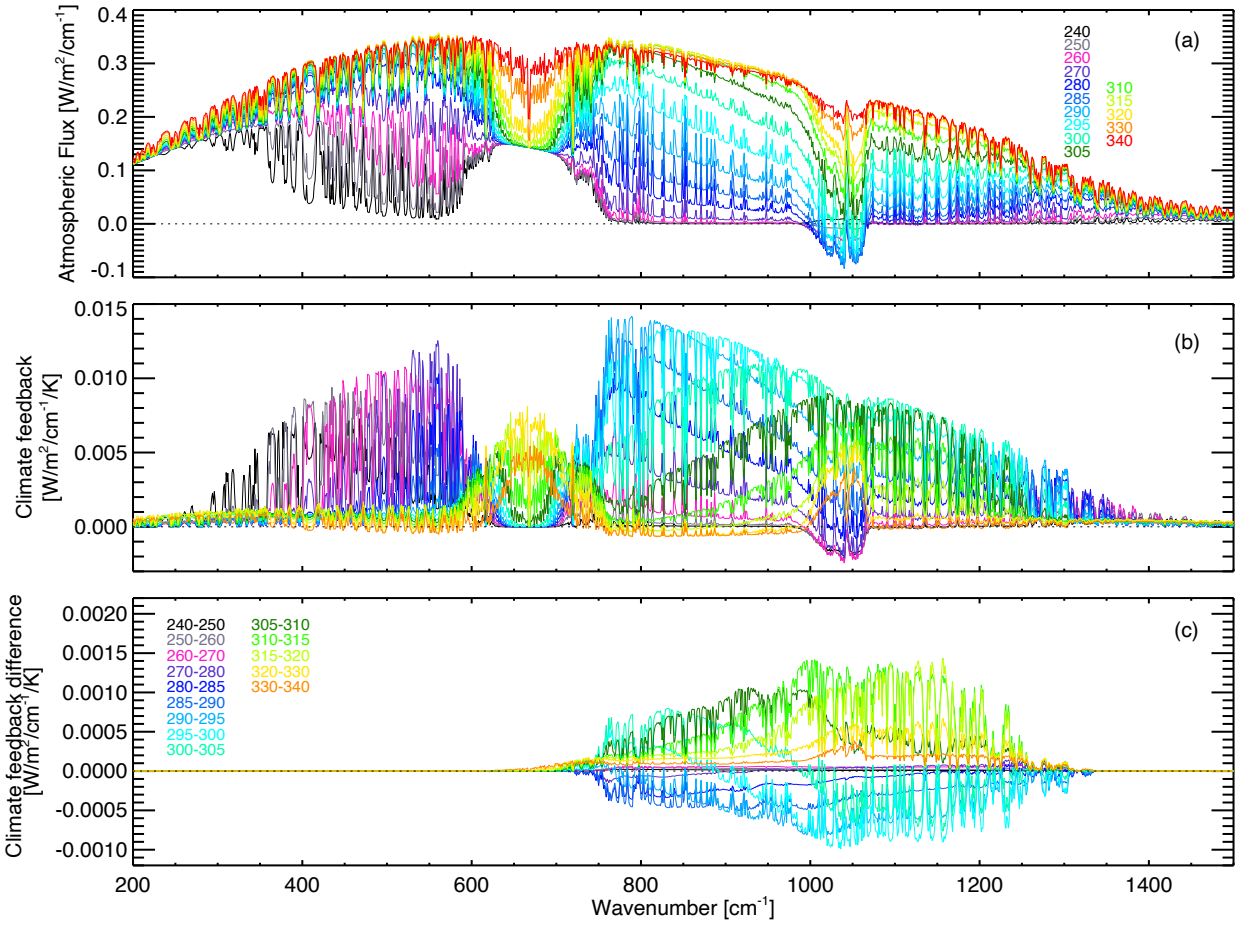

Fig. S11. Similar to Fig. S9 but using MT_CKD_4.2_closure instead of MT_CKD_4.2.

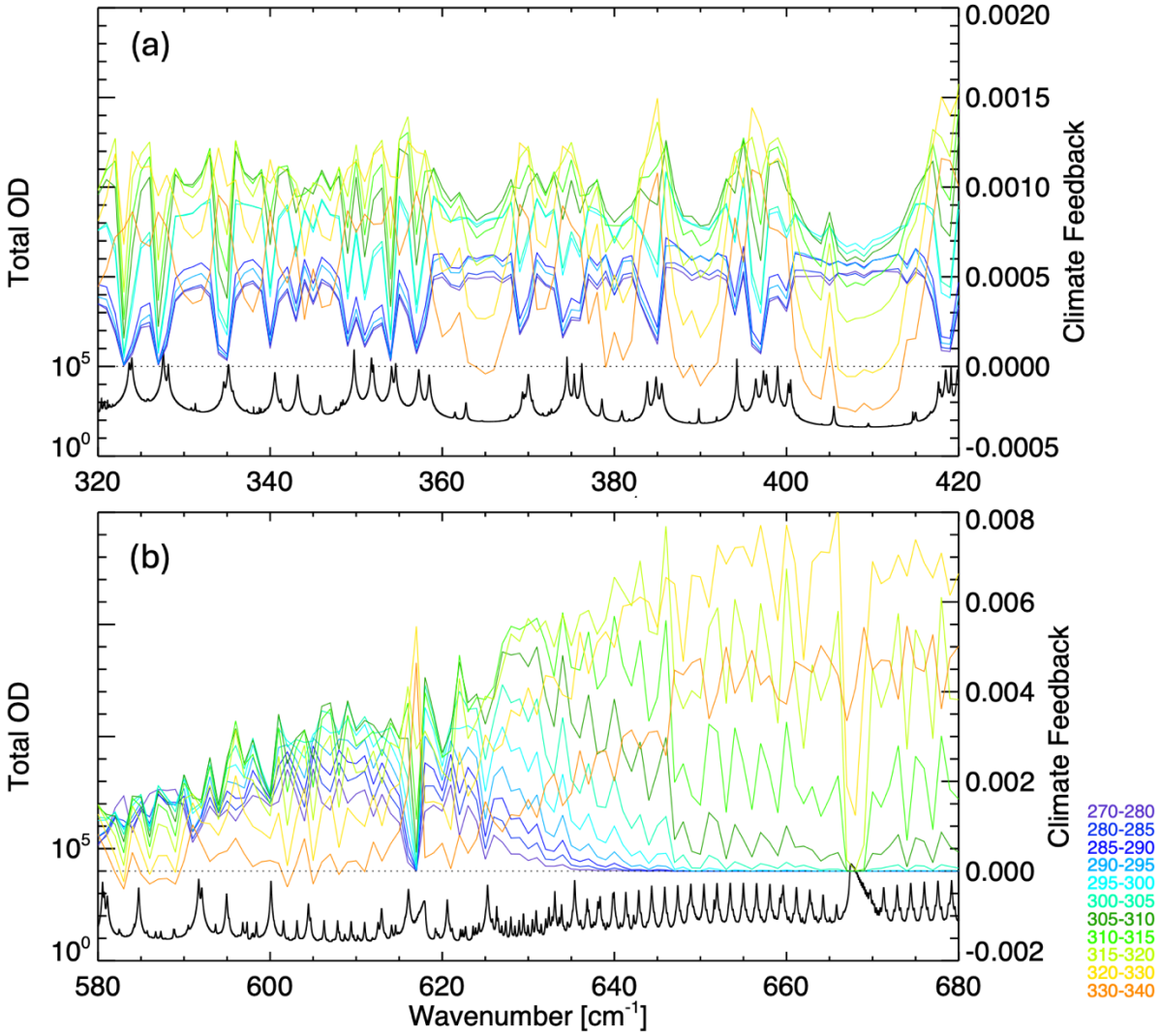

Fig. S12. (a) For 320-420 cm^{-1}, climate feedback ($W/m^2/cm^{-1}/K$, right axis) calculated for LBLRTM calculation using MT_CKD_4.2 for various temperature ranges (colored curves) in moist adiabat profiles (as described in text). Black curves show the optical depths (left axis) for a sample profile; (b) Same as (a) except for the 580-680 cm^{-1} spectral range.

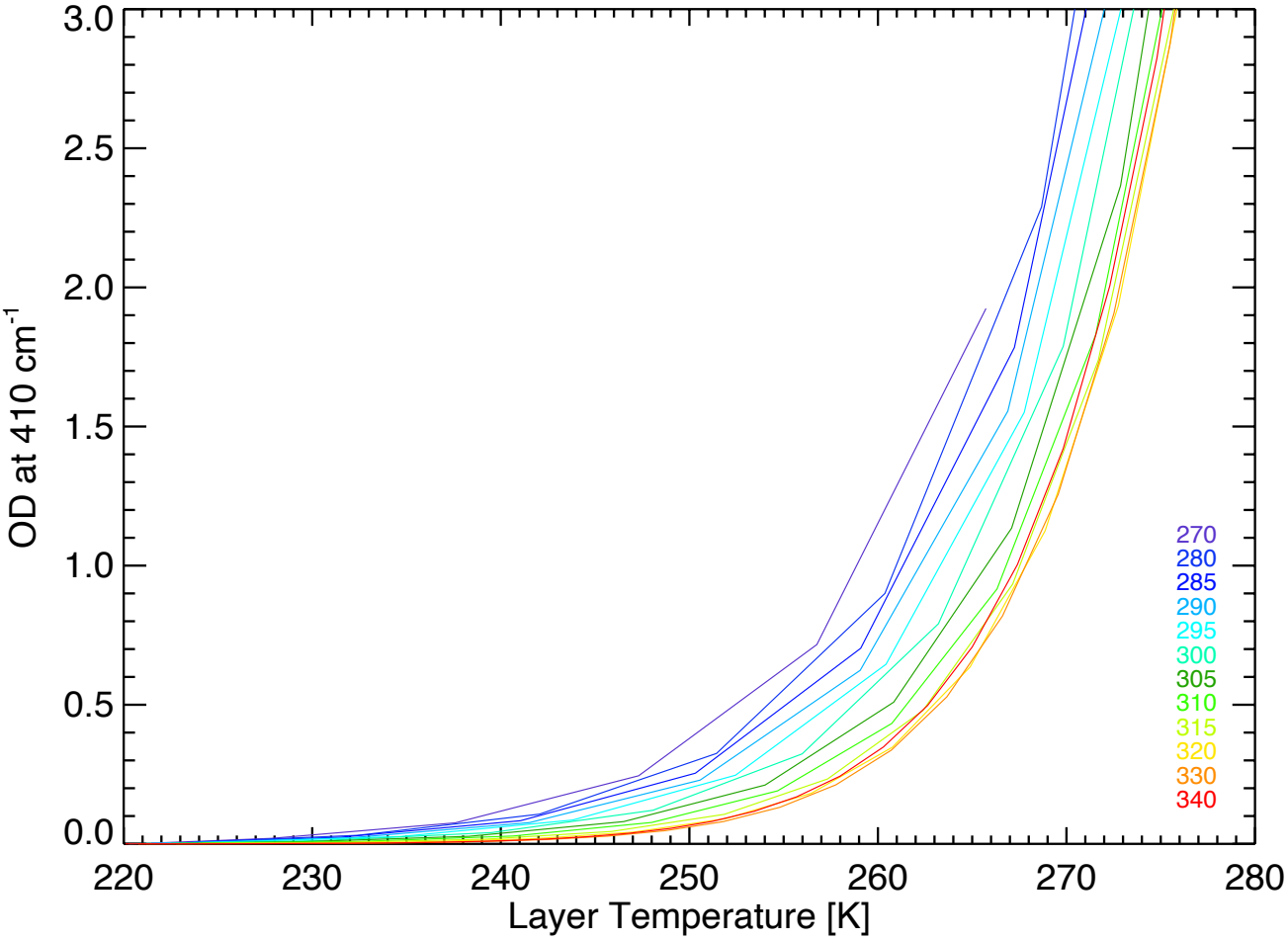

Fig. S13. Cumulative optical depth at 410 cm^{-1} from the tropopause (220K) as a function of atmospheric temperature for various surface temperatures in moist adiabat profiles (as described in text).